

Measurement of Polarized Parton Distributions With Spin-dependent Deep-inelastic Scattering

by

Bryan Eldon Tipton

B.S. with Honors, Physics
The Pennsylvania State University
June 1994

Submitted to the Department of Physics
in partial fulfillment of the requirements for the degree of

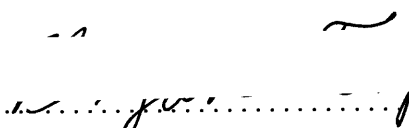
Doctor of Philosophy

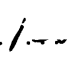
at the

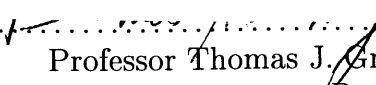
MASSACHUSETTS INSTITUTE OF TECHNOLOGY

September 1999

© Massachusetts Institute of Technology 1999

Signature of Author 
Department of Physics
September 1999

Certified by 
Professor Robert P. Redwine
Professor of Physics
Thesis Supervisor

Accepted by 
Professor Thomas J. Greytak
Professor
Associate Department Head for Education

Measurement of Polarized Parton Distributions With Spin-dependent Deep-inelastic Scattering

by

Bryan Eldon Tipton

Submitted to the Department of Physics
on September 1999, in partial fulfillment of the
requirements for the degree of
Doctor of Philosophy

Abstract

This thesis reports the first polarized parton distributions extracted from HERMES 1995, 1996, and 1997 data. HERMES is an experiment located at the DESY laboratory in Hamburg, Germany. The experiment scatters a polarized positron beam at 27.5 GeV/c momentum from polarized ^1H and ^3He internal gas targets in order to measure double-spin asymmetries in the deep inelastic region. This work reviews the theoretical motivations for the study of polarized deep inelastic scattering and details the setup of both the HERMES experiment and the Transverse Polarimeter at HERA.

The asymmetries of HERMES deep inelastic events with inclusive positrons and semi-inclusive hadrons and pions are then presented. In the framework of the Quark-Parton Model, the polarized quark distributions $\Delta u_v(x)$, $\Delta d_v(x)$, and $\Delta \bar{u}(x)$ are extracted in the kinematic region $0.023 < x < 0.6$ and $1 \text{ GeV}^2 < Q^2 < 10 \text{ GeV}^2$. The extracted values for the measured region integrals are $\Delta u_v = 0.525 \pm 0.046 \pm 0.078$, $\Delta d_v = -0.23 \pm 0.10 \pm 0.14$, and $\Delta \bar{u} = -0.003 \pm 0.021 \pm 0.030$.

Thesis Supervisor: Professor Robert P. Redwine
Title: Professor of Physics

Acknowledgements

A benefit of working with a large collaboration of physicists is the wide range of individuals whom one has the fortune of knowing. This makes the graduate school experience interesting but the acknowledgement section of the thesis lengthy. I'll try to be brief, but I apologize to many people left out of this list of acknowledgements.

I would first like to thank my advisor, Bob Redwine, for giving me the opportunity to work on HERMES and for overseeing a successful Ph.D. Bob always had wise advice, sharp insight, and kind words whenever we had discussions. I would also like to thank Richard Milner for his guidance through the HERMES project and for making sure I did not get lost while I stayed in Germany. I am grateful to a number of senior physicists in HERMES who have provided me with role models for success in science and in life. In particular, Wolfgang Lorenzon, Peter Schuler, and Michael Spengos taught me the skills to approach my first major research project as a graduate student, the Transverse Polarimeter. In my subsequent involvement in HERMES data analysis, I received help and guidance from Antje Bruell and Art Mateos who impressed me with their physics skills and with their ability to balance work with significant play.

In the analysis for this thesis, I worked closely with Marc-Andre Funk and Michael Ruh, and I want to thank both of them for stimulating discussion, inexhaustible patience, and dogged persistence in seeing our efforts to fruition. MAF was the first to document the analysis procedure comprehensively; in the process, he solved a large number of problems for which I am grateful. I would also like to thank Michael Düren and Michael Ruh for their tremendous efforts to bring these results to publication. The group of people involved in the analysis described in this thesis was very large and many other folks contributed significantly. The inclusive group, with Andreas Gute, Delia Hasch, and Uta Stösslein, has performed numerous service tasks for the rest of HERMES. In the semi-inclusive analysis group, I am grateful for the collaboration and help of Balijeet Bains, Marc Beckmann, Andrea Dvoredsky, Michael McAndrew, Holger Ihssen, and Naomi Makins. I also thank Bernd Braun, Michael Dueren, MAF, Phil, Ralf Kaiser, Norbert Meyners, Steve Pate, Michael Ruh, and Wolfgang Wander for providing directly or indirectly figures or figure templates used in the thesis. Finally, I was very lucky in my research to have three other MIT students in nearly the same year and project, to share experiences and perspectives. It was a pleasure to share the MIT HERMES office with such a relaxed group, including Jeff Martin, Taek-su Shin, Mark Sutter, and (honorary member) Nik Gregory.

On the lighter side, the HERMES ski team (Antje, Andrea, Eric Belz, and Greg Rakness among others) deserves credit for challenging me to test my skills at Breckenridge, Lake Louise,

and Lake Tahoe. As a fellow snowboarder, Ed Kinney further encouraged my snowboarding development. I owe Mark, Jeff, Taek-su, Wolfgang, Felix Dashevskiy, and Vitaly Ziskin for reminding me of the critical importance of regular coffee and off-site meeting attendance. Bob, Antje, Krishna Rajagopal, Kevin Mcilhany, Twiggy Chan, and Yvonne Tipton combed through pieces this manuscript; I appreciate their attempts to streamline my sometimes awkward writing style. Kevin also has my gratitude for teaching me the finer points of racquetball and providing numerous entertaining discussions.

I would like to thank my parents and family (Mom, Dad, Lin, and Lib) for their understanding and support during the doctoral studies. Finally, I am deeply grateful for the tremendous warmth and caring of Twiggy Chan, with whom the last year of my MIT experience was a joy.

Contents

1	Introduction	19
2	Theory	22
2.1	Deep-Inelastic Scattering	22
2.1.1	Inclusive Deep-Inelastic Scattering	23
2.1.1.1	The Quark-Parton Model and DIS	28
2.1.1.2	Quantum Chromodynamics and DIS	31
2.1.1.3	OPE and DIS	35
2.1.2	Semi-Inclusive DIS	36
2.1.3	Fragmentation Models	39
2.1.3.1	Independent Fragmentation	39
2.1.3.2	String Model	40
2.1.3.3	Cluster Model	41
2.1.4	Measurements in Polarized Deep-Inelastic Scattering	41
2.1.4.1	Polarized Observables in the QPM	41
2.1.4.2	Further Access to Nucleon Spin	44
2.1.4.3	Previous Experiments in Polarized DIS	45
2.2	Nucleon Spin Structure	47
2.2.1	Constituent Quark Model	47
2.2.2	Relativistic Quark Model	49
2.2.3	Current Algebra	49
2.2.4	Perturbative QCD	52
2.2.5	Impact of Inclusive DIS Measurements	53
2.2.6	Sea Polarization	55
2.2.7	Gluon Polarization	56
2.2.8	$SU(3)_{\text{flavor}}$ Symmetry Breaking	58
2.2.9	Lattice Gauge Theory	59
2.3	Summary	59

3	The HERMES Experiment	61
3.1	The HERA Accelerator	62
3.1.1	Positron Beam Polarization at HERA	64
3.2	The Internal Target	68
3.2.1	The ^3He Target	70
3.2.2	The H-D Target	72
3.2.3	The Unpolarized Gas Feed System	74
3.3	The Spectrometer	75
3.3.1	The Tracking System	75
3.3.1.1	The Vertex Chambers	77
3.3.1.2	The Drift Vertex and Front Chambers	78
3.3.1.3	The Spectrometer Magnet	79
3.3.1.4	The Magnet Chambers	79
3.3.1.5	The Back Chambers	80
3.3.1.6	Performance of the Tracking System	80
3.3.2	The Particle Identification Detectors	80
3.3.2.1	The Čerenkov Counter	82
3.3.2.2	The Transition Radiation Detector	82
3.3.2.3	The Hodoscopes	83
3.3.2.4	The Calorimeter	84
3.3.2.5	Performance of the PID system	84
3.3.2.6	The Luminosity Monitor	85
3.3.3	The Gain Monitoring System	85
3.3.4	The Trigger	85
4	Polarimetry at HERA	87
4.1	Polarized Compton Scattering	88
4.1.1	Extracting Beam Polarization Observables	91
4.2	The Transverse Polarimeter	93
4.2.1	The Polarimeter Setup	93
4.2.1.1	The Optical System	93
4.2.1.2	The HERA Beam	94
4.2.1.3	Backscattered Photon Detection	96
4.2.1.4	The Data Acquisition and Control Systems	97
4.2.2	The Transverse Polarization Measurement	98
4.2.2.1	Other Measured Parameters	102
4.2.3	A Polarimeter Monte Carlo	102

4.2.4	The Transverse Polarimeter Operation	103
4.2.4.1	Gain Calibration	103
4.2.4.2	Position Calibration	105
4.2.4.3	Scale Calibration and Monitoring	107
4.2.4.4	Beam Size Effects	110
4.2.4.5	Other Dependences	110
4.2.4.6	Calibration Without Beam	111
4.2.4.7	Online Monitoring and Slow Control	111
4.2.5	Asymmetry Fitting	112
4.2.6	TPOL Performance 1995-97	115
4.2.7	Improving the TPOL Performance	116
4.2.7.1	The Vertical Rate Asymmetry	116
4.2.7.2	Unpolarized Cross-section Fits	117
4.3	The Longitudinal Polarimeter	120
5	The Data Analysis	122
5.1	Data Processing	123
5.1.1	The Organization of the Data	123
5.1.2	The Data Production and Analysis	124
5.1.3	The Reconstruction of Tracks	125
5.2	Data Quality Selection	127
5.2.1	Fill and Run Quality	127
5.2.2	Burst and Record Quality	127
5.2.2.1	Beam Conditions	129
5.2.2.2	Target Conditions	129
5.2.2.3	Luminosity	129
5.2.2.4	Data Acquisition	131
5.2.2.5	Tracking	132
5.2.2.6	Particle Identification Conditions	133
5.2.2.7	Overall Data Collection Efficiency	133
5.2.2.8	Record Quality Summary	133
5.3	Event Selection	133
5.3.1	Particle Identification	136
5.3.1.1	Electron and Hadron Separation	136
5.3.1.2	Pion Separation	139
5.3.2	Selection of DIS Events	139
5.4	Formation of the Asymmetries	141

5.5	Corrections to the Raw Asymmetries	143
5.5.1	Background Corrections	143
5.5.2	Smearing Corrections	144
5.5.3	Radiative Corrections	145
5.5.4	Comment on Acceptance Corrections	147
5.6	Statistical Uncertainties on the Asymmetries	148
5.6.1	The Statistical Correlation	149
5.7	Systematic Uncertainties in the Asymmetries	150
5.7.1	Beam Polarization Uncertainty	151
5.7.2	Target Polarization Uncertainty	151
5.7.3	Yield Fluctuations	152
5.7.4	Smearing and Radiative Corrections	153
5.7.5	Model for g_2	154
5.7.6	The uncertainty in R	154
5.8	The Final Asymmetries	155
5.9	Summary	161
6	The Extraction of Polarized Parton Distributions	162
6.1	The Purity Model	162
6.2	Generating the Purities	165
6.2.1	Unpolarized Parton Distributions	166
6.2.2	Fragmentation Models	168
6.2.3	Acceptance	171
6.2.4	Purity Results	171
6.3	Models of Quark Polarization	173
6.4	Corrections for Nuclei	177
6.5	Monte Carlo Studies of the Extraction Procedure	179
6.6	Uncertainties on the Extracted Polarizations	181
6.6.1	Propagation of Asymmetry Uncertainties	181
6.6.2	The Purity Systematic Uncertainty	182
6.6.3	The Unpolarized Sea Model Uncertainty	182
6.7	Results as a function of x	183
6.7.1	The Quark Polarization Extraction	185
6.7.2	The Parton Distribution Extraction	185
6.7.3	Comparison of Models of the Sea	190
6.8	Determining Moments of the Distributions	192
6.9	Results for the Integrals	194

7	Conclusions	197
A	Tables of Results	199
B	Nuclear Corrections with Quark Polarizations	209

List of Figures

2-1	The One Photon Exchange Approximation in DIS	23
2-2	Definition of Angles in Inclusive DIS	26
2-3	Unpolarized Quark Distributions in the Proton	30
2-4	The $F_2^p(x, Q^2)$ Structure Function	32
2-5	QCD Corrections to DIS	34
2-6	Evolution of the Scattering in QCD	36
2-7	World Data on $A_1(x, Q^2)$ for the proton	45
2-8	World Data on the $g_1(x)$ Structure Functions	46
3-1	The HERA Ring	63
3-2	The Operation of the Spin Rotators at HERA	67
3-3	The Rise of HERA Positron Beam Polarization	68
3-4	Schematic of the HERMES Target Region	69
3-5	Event Distribution in the Target Cell	69
3-6	Operation of the ^3He Target	72
3-7	Diagram of the H-D Target	73
3-8	Diagram of the HERMES Spectrometer	76
3-9	Orientation of Planes in the Tracking system	76
3-10	Schematic of a Drift Cell in the Vertex Chamber	78
3-11	Efficiencies in the Front and Back Chambers	79
3-12	The Four HERMES Particle Identification Detectors	81
4-1	The Kinematics of Compton Scattering	88
4-2	The Energy and y Distributions of Backscattered Photons.	91
4-3	A Schematic of the TPOL Layout	95
4-4	The TPOL Calorimeter	97
4-5	The $\eta(y)$ Transformation	99
4-6	Measured Photon Spectra in E and η	100
4-7	The Analyzing Power, $\Pi_P(E_\gamma)$	101

4-8	Relative Voltage Calibration Spectra	104
4-9	Measurement Dependence on the Absolute Gain Calibration	105
4-10	The Calorimeter Vertical Centering Response Functions	106
4-11	Measurement Dependence on y_{center}	107
4-12	The Bunch Dependence of the Beam Polarization	109
4-13	Measurement Dependence on the Photon Focus	111
4-14	The TPOL Online Monitor	113
4-15	The Functions $\frac{\Sigma'_1}{\Sigma_0}(\eta)$ and $\frac{\Sigma_{2Y}}{\Sigma_0}(\eta)$	114
4-16	Polarization Asymmetry Fitting	114
4-17	Comparison of the Mean Shift and Vertical Rate Methods	118
4-18	Schematic Diagram of a Compton Cross-section Fit.	119
4-19	Comparison of Longitudinal and Transverse Polarimeter Measurements	120
5-1	Schematic Representation of the HERMES Data Chain	124
5-2	The Tresearch Method for Finding Particle Trajectories	125
5-3	Distributions of Burst Information at HERMES	128
5-4	Responses of the Particle Identification detectors	136
5-5	Particle Identification Distributions	138
5-6	Distribution of DIS Events in x and Q^2	140
5-7	Feynman Diagrams for Radiative Corrections	146
5-8	Estimated Acceptance Corrections for Proton Asymmetries	147
5-9	Comparison of 1996 and 1997 Proton Asymmetries	156
5-10	Inclusive Deep-Inelastic Scattering Structure Function Ratios	158
5-11	Semi-inclusive ^3He Asymmetries	159
5-12	Semi-inclusive Proton Asymmetries	160
6-1	The Purity Generation	166
6-2	The R and γ Correction to Unpolarized PDFs.	167
6-3	HERMES Fragmentation Functions	169
6-4	The Fitted String Model	170
6-5	The Čerenkov Response to Pions	172
6-6	Inclusive and Semi-inclusive Hadron Purities	173
6-7	Semi-inclusive Pion Purities	174
6-8	Monte Carlo Inversion with Purities	180
6-9	The Fitted Quark Polarizations	184
6-10	Extracted Valence and Sea Quark Helicity Densities Compared to SMC	186
6-11	Breakdown of Systematic Uncertainty Contributions	187

6-12 Comparison of the Extraction to World Parameterizations	189
6-13 The Extracted Non-singlet Quark Distribution	190
6-14 Comparison of Sea Models in the Extraction	193

List of Tables

2.1	Definition of Useful Variables in DIS	24
2.2	A Comparison of Experiments in Polarized DIS	47
2.3	World Integrals of $g_1(x)$	54
2.4	Lattice Results for Nucleon Spin Structure	59
3.1	HERA Beam Parameters	64
3.2	Comparison of the ^3He and ^1H Targets	70
3.3	Tracking Chamber Parameters	77
4.1	Parameters for a Fit to $\eta_V(y)$	99
4.2	Comparison of C_{Table} Parameters	108
4.3	A Summary of Transverse Polarimeter Performance	115
4.4	Systematic Uncertainties for a Monte Carlo Calibration	118
5.1	Beam and Target Conditions Data Quality Selection.	130
5.2	Data Acquisition Quality Selection	132
5.3	Spectrometer Performance Data Quality Selection	134
5.4	A Summary of the Final Burst Selection.	134
5.5	Track Selection for DIS Events	135
5.6	Particle Multiplicities for Each Year.	141
5.7	Definition of x Binning	143
5.8	Smearing Corrections for the Proton Asymmetries	144
5.9	Radiative Corrections to the Inclusive Asymmetries	146
5.10	Acceptance Corrections to the Asymmetries	148
5.11	Systematic Uncertainties from Yield Fluctuations in 1995	153
5.12	The Uncertainty in R	155
5.13	The Compatibility of the 96 and 97 Asymmetries.	157
6.1	JETSET Fragmentation Parameters	170
6.2	Parameters for a Fit to the Parton Distributions	188

6.3	Measured Region Integrals Compared to SMC	195
6.4	First Moments Compared to SU(3) Symmetry Analysis Results	195
6.5	Valence Quark Distribution Moments Compared to Lattice QCD Results	196
A.1	Average Values of Kinematic Variables	200
A.2	The Experimental Asymmetries Without Corrections.	201
A.3	The Structure Function Ratios, $\frac{g_1^h}{F_1^h}$	202
A.4	Proton Asymmetry Correlations	203
A.5	Helium Asymmetry Correlations	203
A.6	Extracted Valence and Sea Quark Polarizations versus x	204
A.7	Extracted Valence and Sea Quark Distributions Versus x	204
A.8	Correlations Among the Quark Polarizations	205
A.9	Contributions to the Systematic Uncertainty in the Extraction	206
A.10	First Moments of the Polarized Quark Distributions	207
A.11	Second Moments of the Polarized Quark Distributions	207
A.12	Correlations Among the First Moments	208
A.13	Correlations Among the Second Moments	208

Chapter 1

Introduction

The study of matter entails the understanding of its internal structure. The separation of atoms into electrons and nuclei was discovered by Rutherford and collaborators in 1911. The nucleon component of nuclei began to be appreciated after Chadwick's discovery of the neutron in 1932. Studies of hadron spectra in the 1950s revealed clues to the substructure of the nucleons. Gell-Mann [1] and Zweig [2] proposed a model suggesting hadrons are composed of three quarks in order to classify this spectra. Quark properties, such as flavor, spin, and charge, determine different hadron identities.

While useful in classifying hadrons, quarks remained a mathematical curiosity until the advent of deep-inelastic scattering. The SLAC-MIT experiments in the late 1960s discovered a scaling property of the high electron scattering cross-sections, which implied that the individual parts of the proton, called "partons," were probed. Subsequent study in nucleon structure merged the quark and parton interpretations and culminated in the field theory of the strong force, Quantum Chromodynamics (QCD). In QCD, quarks interact strongly with each other by exchanging electrically neutral gluons. Six flavors of quarks are observed in nature: u and d quarks are the basic components of nucleons, while s , c , b , and t quarks are observed in various high energy experiments.

The march to higher energies and smaller distance scales has continued in particle physics, illuminating vacuum state structure in the universe during the past twenty years. Many important questions in nucleon structure remain unanswered. QCD tells us that the interactions among quarks and gluons become weaker at higher energies. The weakness of the interactions allows their calculation by perturbative approximations. Perturbative QCD is thus successful

in describing strong forces in high energy laboratories. At low energies, these perturbative techniques fail, and calculations with QCD become complex. For example, the rigid confinement of quarks inside hadrons is suggested by the features of QCD, but it has not been shown to follow rigorously from the theory.

The study of the non-perturbative structure of QCD is an aim in this thesis. The strong force is probed by understanding its role in generating the nucleon intrinsic spin. Studies of spin are significant as spin angular momentum plays a special role in quantum mechanics: the symmetry property of each wavefunction in the theory is determined by its total spin quantization. A nucleon possesses one half spin in units of \hbar . If the nucleon is a composite collection of partons, how do we understand the origin of this spin? Answering this question may yield surprisingly sensitive tests of nucleon structure models.

As each quark has spin one half, one might imagine that the nucleon spin results from a simple sum of the spins of its three valence quarks. This naive view was upset by the results of the EMC experiment in 1987 [3]. That experiment indicated that little of the proton spin comes from its quarks' spins. Models of nucleon structure offer other sources of the nucleon spin: the spin alignments of sea and valence quarks may cancel in a complicated fashion, or gluon intrinsic spin and parton orbital angular momentum play important roles. As no rigorous conclusion may yet be calculated from QCD, experimental measurements of nucleon spin structure are needed to distinguish among these interpretations.

Polarized deep-inelastic scattering (DIS) provides the tool to study nucleon spin structure in this thesis. In the Quark-Parton Model, the deep-inelastic scattering rate is proportional to linear combinations of quark spin contributions to the nucleon spin. The total positron scattering rate is sensitive to a charge weighted sum of the contributions from all quark flavors. When a hadronic fragment of the proton is also detected, a different mixture of quark contributions determines this semi-inclusive process. A statistical analysis of all deep-inelastic scattering reactions can separate the spin contribution of each quark flavor.

The HERMES (HERa MEasurement of Spin) experiment was designed to optimize such studies. The experiment is located at the Deutsches Elektronen Synchrotron (DESY) laboratory in Hamburg, Germany. DESY's Hadronen Elektronen Ring Anlage (HERA) circulates a 27.5 GeV, naturally polarized positron beam. The HERMES target contains polarized nuclei in the positron path, allowing deep inelastic interactions. A large acceptance spectrometer behind the target detects the forward going positron and hadronic fragments from these interactions.

HERMES has been taking data since 1995, and this thesis reports on an analysis of polarized data taken through 1997. During these years, 2.1 and 2.3 million DIS events on polarized $^3\vec{\text{H}}\text{e}$ (1995) and $^1\vec{\text{H}}$ (1996-7) targets, respectively, were collected and analyzed. This work will explain how cross-section asymmetries in these targets constrain the spin contributions of valence and sea quarks inside the nucleon.

The thesis is divided into seven chapters. Chapter 2 reviews the theoretical framework of polarized deep-inelastic scattering and its interpretation in the Quark-Parton Model and Quantum Chromodynamics. A number of predictions for the nucleon spin structure and recent experimental results in this field are reviewed. Chapter 3 describes the HERMES experiment. In Chapter 4 the specific detector responsibility of the author, the Transverse Polarimeter, is detailed. Chapter 5 explains the analysis of the HERMES 1995-7 data to extract polarized DIS asymmetries on the nucleon. Finally, these asymmetries are analyzed in the framework of the Quark-Parton Model in Chapter 6. Polarized quark distributions as a function of x_{Bjorken} are presented and the total spin fractions of the quark flavors in the nucleon are estimated. These results are compared to the previous determinations described in Chapter 2. The conclusions of these studies are summarized in Chapter 7.

Chapter 2

Theory

A discussion of the theoretical foundation of this work may be separated into two parts, explaining what is being studied and what tools are used to study it. This chapter considers these questions in the reverse order. It begins with a review of the deep-inelastic scattering process, emphasizing its sensitivity to the nucleon structure. The measurement of polarized cross-section asymmetries may be directly related to spin degrees of freedom inside the nucleon. The deep-inelastic formalism conveniently lays the groundwork for the second topic of the chapter, the spin structure of the nucleon. The discussion reviews the current understanding of the spin structure of the nucleon, emphasizing a few important models of this structure and their ambiguities. Polarized DIS measurements are shown to constrain these models strongly, motivating the investigations in this thesis.

2.1 Deep-Inelastic Scattering

Deep-inelastic scattering is the scattering of a lepton from a nucleon at energies at which the nucleon breaks apart incoherently. The lepton may interact via photon exchange with the charged components inside the nucleon. With large interaction energies, a struck quark may be propelled rapidly from the nucleon and form a hadronic fragment. Electromagnetic interactions of leptons are relatively well understood, allowing physicists to isolate the quark properties in these studies. DIS is a useful probe of the strong interaction inside the nucleon. The physical picture is made exact below, laying out the basic framework for this thesis.

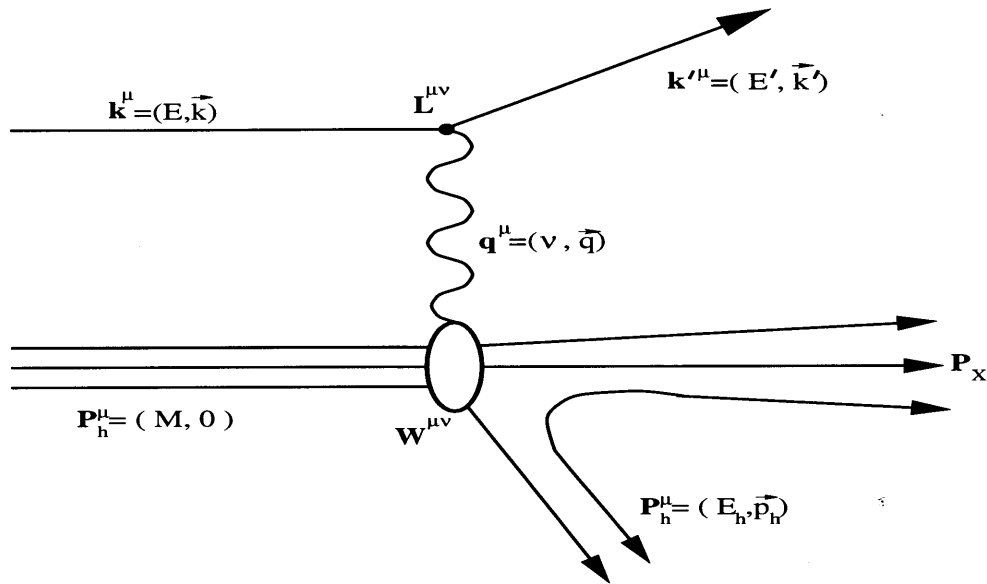


Figure 2-1: The leading order diagram contributing to deep-inelastic scattering.

2.1.1 Inclusive Deep-Inelastic Scattering

DIS reactions may be classified by what part of the final state is actually detected. The inclusive reaction involves the detection of the lepton after the scattering:

$$l + N \rightarrow l' + X.$$

In the most general case, the other reaction products, X , are ignored. In the HERMES energy region, the process is dominated by exchange of one virtual photon. Multi-photon exchange corrections are suppressed by the fine structure constant $\alpha_{EM} \sim \frac{1}{137}$. Weak boson exchange contributions are also heavily suppressed, as the experimental energy transfers are small compared to the weak boson masses.

A Feynman diagram for the one photon exchange process is shown in Figure 2-1, and a legend of variables used in this discussion is listed in Table 2.1. The fundamental relation for scattering studies is the differential cross-section in the measured variables. This cross-section is proportional to the probability of scattering, or equivalently to the particle detection rate measured in the experiment. For one photon exchange, one may generally form the differential

Experimental Observables	
Positron:	
k^μ	$= (E, \vec{k})$ The four-momentum of the incident positron.
k'^μ	$= (E', \vec{k}')$ The four-momentum of the scattered positron.
(θ, ϕ)	The polar and azimuthal scattering angles of the positron in the lab frame.
h	The incident positron helicity.
Hadron:	
P^μ	$\stackrel{\text{lab}}{=} (M, \vec{0})$ The four-momentum of the target nucleon.
S^μ	$\stackrel{\text{lab}}{=} (0, \vec{S})$ The four-vector spin of the target nucleon.
α	$= \cos^{-1} \left(\frac{\vec{S} \cdot \vec{k}}{ \vec{S} \vec{k} } \right)$ The polar angle between nucleon spin and positron momentum in the lab frame.
P_h^μ	$= (E_h, \vec{P}_h)$ The four-momentum of a detected final state hadron h .
Derived Variables	
Inclusive DIS:	
ν	$= E - E'$ The laboratory energy of the virtual photon.
\vec{q}	$= \vec{k} - \vec{k}'$ The laboratory three-momentum of the virtual photon.
q^μ	$= (\nu, \vec{q}) = k^\mu - k'^\mu$ The four-momentum of the virtual photon.
Q^2	$\equiv -q^\mu q_\mu$ The squared (positive) invariant mass of the virtual photon.
	$\stackrel{\text{lab}}{=} 4EE' \sin^2 \frac{\theta}{2}$
W^2	$\equiv (P + q)^2$ The squared invariant mass of the final hadronic system.
	$\stackrel{\text{lab}}{=} M^2 + 2M\nu - Q^2$
x	$\equiv \frac{Q^2}{2P \cdot Q} \stackrel{\text{lab}}{=} \frac{Q^2}{2M\nu}$ The Bjorken scaling variable.
y	$\equiv \frac{P \cdot q}{P \cdot k} \stackrel{\text{lab}}{=} \frac{\nu}{E}$ The fractional energy transfer of the photon.
Semi-inclusive DIS:	
P_L	$\equiv \vec{P}_h \cdot \frac{\vec{q}}{ \vec{q} } \Big _{\text{cm}}$ The longitudinal momentum of a hadron h in the frame of the photon-nucleon center-of-mass.
P_T	$= \sqrt{\vec{P}_h^2 - P_L^2}$ The hadron transverse momentum in the c.m. frame.
x_F	$\equiv \frac{P_L}{ \vec{q} } \approx \frac{2P_L}{W}$ The Feynman scaling variable.
z	$\stackrel{\text{lab}}{=} \frac{E_h}{\nu}$ The fraction of the photon energy carried by hadron h .

Table 2.1: A legend of variables used in deep-inelastic positron-nucleon scattering.

cross-section in terms of the lepton and hadron tensors [4];

$$\frac{d^2\sigma}{d\Omega dE'} = \frac{\alpha_e^2}{2Mq^4} \frac{E'}{E} L_{\mu\nu} W^{\mu\nu}, \quad (2.1)$$

$$= \frac{\alpha_e^2}{2Mq^4} \frac{E'}{E} \left\{ L_{\mu\nu}^S W_S^{\mu\nu} + L_{\mu\nu}^A W_A^{\mu\nu} \right\}, \quad (2.2)$$

where $q^\mu = k^\mu - k'^\mu$ is the 4-momentum transfer to the target nucleon. For the studies in this thesis, the scattering leptons are positrons. The energies involved are far greater than the positron mass, $E, E' \gg m_e$, justifying neglect of positron mass terms in the cross-section. Equation (2.2) is valid in the specific Lorentz frame of the fixed target, in which the nucleon is nearly at rest.

The key physics studied with deep-inelastic scattering is contained in the lepton and hadron tensors, $L^{\mu\nu}$ and $W^{\mu\nu}$, which derive from the matrix element representing the one photon exchange process. The lepton tensor represents the emission of a photon by a lepton, while the hadron tensor models the photon absorption on a nucleon. For the study of polarized beams and targets, the lepton and hadron tensors are typically separated into symmetric and anti-symmetric pieces under parity transformation, as in Eq. (2.2). As electromagnetic interactions conserve parity, only terms of like symmetry may contribute to the matrix element.

Calculation of the lepton current tensor is straightforward due to the point-like nature of the positron [5].

$$\begin{aligned} L^{\mu\nu}(k, h; k') &= \sum_{s'} \bar{u}(k, s) \gamma^\mu u(k', s') \bar{u}'(k', s') \gamma^\nu u(k, s), \\ &= 2 \left\{ k^\mu k'^\nu + k^\nu k'^\mu - g^{\mu\nu} (k \cdot k') \right\} + 2h \left\{ i\epsilon^{\mu\nu\alpha\beta} k_\alpha k'_\beta \right\}, \\ &= 2L_S^{\mu\nu} + 2h L_A^{\mu\nu}. \end{aligned} \quad (2.3)$$

The initial positron helicity in polarized scattering is represented in h . The final positron helicity is not detected and is summed in the expression.

Nucleons do not behave like point particles, and the understanding of their detailed structure is the aim of this work. $W^{\mu\nu}$ sums over all possible final states, “ X ,” by virtual photoab-

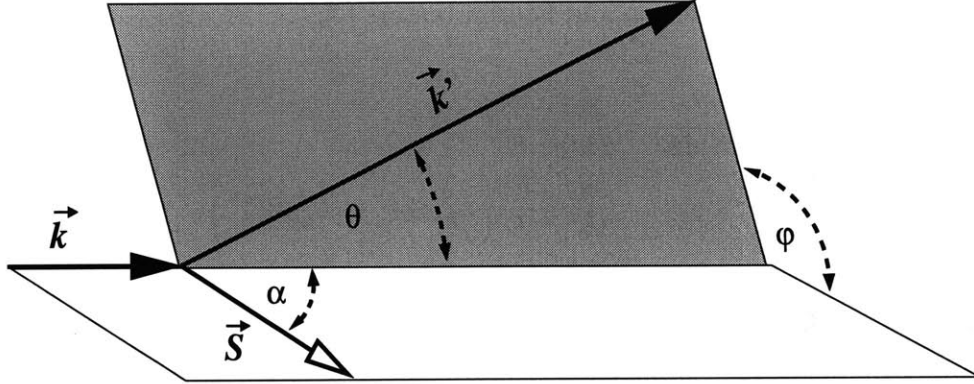


Figure 2-2: Definition of angles in inclusive deep-inelastic scattering.

sorption on a nucleon [4].

$$W^{\mu\nu}(P, S; X) = \frac{1}{4\pi} \sum_X \langle P, S | J^\mu | X \rangle \langle X | J^\nu | P, S \rangle \delta^4(P + q - P_X), \quad (2.4)$$

where J^μ represents the proton current. Arguments including current conservation, Lorentz invariance, parity invariance, time reversal invariance, and hermiticity constrain a general form for this tensor:

$$W_S^{\mu\nu}(P, S; X) = W_1 \left[2M \left(\frac{q_\mu q_\nu}{q^2} - g^{\mu\nu} \right) \right] + W_2 \left[\frac{2}{M} \left(P^\mu - \frac{P \cdot q}{q^2} q^\mu \right) \left(P^\nu - \frac{P \cdot q}{q^2} q^\nu \right) \right], \quad (2.5)$$

$$W_A^{\mu\nu}(P, S; X) = G_1 \left[iM \epsilon^{\mu\nu\alpha\beta} q^\alpha S^\beta \right] + G_2 \left[\frac{i}{M} \epsilon^{\mu\nu\alpha\beta} q^\alpha (P \cdot q S^\beta - S \cdot q P^\beta) \right]. \quad (2.6)$$

The vector S^μ defines the Lorentz covariant nucleon spin orientation. In the lab frame, $S^\mu = (0, \vec{S})$ where \vec{S} is the (3-vector) spin direction relative to the positron initial momentum \vec{k} , as shown in Figure 2-2.

The role of the hadron in scattering may be summarized by four nucleon structure functions, W_1 , W_2 , G_1 , and G_2 . These functions represent the influence of the nucleon's internal structure in the scattering. As they are Lorentz invariant scalars, they depend on the two independent Lorentz invariant scalars in the scattering: $P \cdot q$ and q^2 . The physics below motivates a more

convenient choice of variables,

$$x = \frac{Q^2}{2P \cdot Q}, \quad Q^2 = -q^2, \quad y = \frac{P \cdot q}{P \cdot k}, \quad (2.7)$$

which obey the kinematic limits,

$$0 < x < 1, \quad Q^2 > 0, \quad 0 < y < 1. \quad (2.8)$$

Only two of these variable are independent as $xy = \frac{Q^2}{2ME}$. Inclusive DIS experiments actually measure the lepton kinematic variables (E, E', θ) ; the variables (x, y, Q^2) are extracted by the laboratory frame relations given in Table 2.1.

The cross-section defined in terms of x and Q^2 may be rewritten with the help of four functions:

$$F_1(x, Q^2) = M W_1(P \cdot q, q^2), \quad F_2(x, Q^2) = \nu W_2(P \cdot q, q^2), \quad (2.9)$$

$$g_1(x, Q^2) = \frac{(P \cdot q)^2}{\nu} G_1(P \cdot q, q^2), \quad g_2(x, Q^2) = \nu(P \cdot q) G_2(P \cdot q, q^2), \quad (2.10)$$

For unpolarized scattering, one may rewrite Eq.(2.2) as [6],

$$\frac{d^2\bar{\sigma}}{dx dy} = \frac{2\pi\alpha_e}{ME x^2 y^2} \left\{ \left(1 - y - \frac{y^2}{4}\gamma^2\right) \mathbf{F}_2(x, Q^2) + (xy^2) \mathbf{F}_1(x, Q^2) \right\}. \quad (2.11)$$

where $\bar{\sigma}$ is the cross-section averaged over initial spins, and $\gamma^2 = \frac{Q^2}{\nu^2}$. With both the positron beam and the target nucleon polarized, one may also define the helicity difference cross-section for a nucleon spin oriented at angles α and $\alpha + \pi$ with respect to the electron spin [7]:

$$\begin{aligned} \frac{d^3\Delta\sigma(\alpha)}{dx dy d\phi} &= \frac{d^3\sigma(\alpha)}{dx dQ^2 d\phi} - \frac{d^3\sigma(\alpha + \pi)}{dx dQ^2 d\phi} \\ &= \frac{2\alpha_e^2}{ME xy} \left\{ \cos \alpha \left(\left[1 - \frac{y}{2} - \frac{y^2}{4}\gamma^2\right] \mathbf{g}_1(x, Q^2) + \left[\frac{y}{2}\gamma^2\right] \mathbf{g}_2(x, Q^2) \right) \right. \\ &\quad \left. - \sin \alpha \cos \phi \sqrt{\gamma^2 \left[1 - y - \frac{y^2}{4}\gamma^2\right]} \left(\frac{y}{2} \mathbf{g}_1(x, Q^2) + \mathbf{g}_2(x, Q^2) \right) \right\}. \end{aligned} \quad (2.12)$$

Equations (2.11) and (2.12) are the basic relations in the study of polarized deep-inelastic scattering. Information on nucleon structure from DIS is contained in the functions F_1 , F_2 , g_1 , and g_2 .

The unpolarized cross-section above may be rewritten to identify it with photoabsorption on a proton:

$$\frac{d^2\bar{\sigma}}{dxdy} = \Gamma(\sigma_T + \epsilon\sigma_L). \quad (2.13)$$

The factor Γ is the flux of virtual photons generated by the lepton beam. The ratio of the probability of the lepton to emit a longitudinally or transversely polarized photon, ϵ , is

$$\epsilon = \frac{1 - y - \frac{1}{4}\gamma^2 y^2}{(1 - y) + \frac{1}{4}y^2(2 + \gamma^2)}. \quad (2.14)$$

σ_L and σ_T are the longitudinal (helicity 0) and transverse (helicity ± 1) virtual photon absorption cross-sections on a nucleon. In the limit of real photon absorption ($Q^2 \rightarrow 0$), their ratio,

$$R(x, Q^2) = \frac{\sigma_L}{\sigma_T} = \frac{F_2(x, Q^2)}{2xF_1(x, Q^2)}(1 + \gamma^2) - 1. \quad (2.15)$$

approaches zero.

2.1.1.1 The Quark-Parton Model and DIS

Until now, only the general scattering formalism has been presented. The underlying physics of deep-inelastic scattering was born out of the seminal observations of the SLAC-MIT experiments in the late 1960s [8]. Unexpectedly high scattering rates were noticed in reactions with large momentum transfer Q^2 and large final state mass, W . Feynman, Bjorken, and Paschos [9, 10] developed the Quark-Parton Model (QPM) to understand these reactions.

In DIS, the structure functions F_1 and F_2 , are observed to *scale* approximately with x in the Bjorken limit where ν and Q^2 become large (approach infinity), but x remains constant. Both

structure functions become functions of only one variable x , dropping their Q^2 dependence. The Quark-Parton Model explains this behavior by suggesting that incident positrons scatter elastically on point-like centers of charge inside the proton. These centers were called “partons” but they were later identified with the “quarks” invented by Gell-Mann [1] and Zweig [2] to describe hadronic spectra. For sufficiently large energy transfers, hadrons seem composed of free, point-like quarks which do not interact with each other. In this view, “deep-inelastic” scattering on nucleons simply involves elastic scattering on the quarks.

If one considers a Lorentz frame in which the proton has infinite momentum (called the Breit or brick-wall frame), then the scaling variable x corresponds to the fraction of the proton momentum carried by the struck quark: $p_q = xP$. Bjorken scaling can be viewed as a consequence of momentum conservation in elastic scattering, which connects x and Q^2 via $Q^2 = 2(m_q)\nu = 2(xM)\nu$.

The structure functions parameterize the quark properties in this model. The function $F_1(x)$ is proportional to the number of quarks available for scattering at a given x averaged over spin, while $g_1(x)$ measures the difference in populations for parallel (\uparrow) and anti-parallel (\downarrow) to the proton spin.

$$F_1(x) = \frac{1}{2} \sum_q e_q^2 (q^\uparrow(x) + q^\downarrow(x)) = \frac{1}{2} \sum_q e_q^2 q(x), \quad (2.16)$$

$$g_1(x) = \frac{1}{2} \sum_q e_q^2 (q^\uparrow(x) - q^\downarrow(x)) = \frac{1}{2} \sum_q e_q^2 \Delta q(x), \quad (2.17)$$

where e_q is the quark electric charge and $q(x)$ is the parton distribution function (PDF) of the quark flavor q . At HERMES, q includes the lightest quarks and antiquarks: $q=u, d, s, \bar{u}, \bar{d}$, and \bar{s} .

Physically, $q(x)dx$ represents the number density of a quark q between momentum fractions x and $x + dx$. The parton densities are normalized so that they correspond to the static quark densities in the proton. Each proton has two up quarks, one down quark, no net strange quarks in its wavefunction, so that

$$\int_0^1 u(x) - \bar{u}(x) dx = 2, \quad \int_0^1 d(x) - \bar{d}(x) dx = 1, \quad \int_0^1 s(x) - \bar{s}(x) dx = 0. \quad (2.18)$$

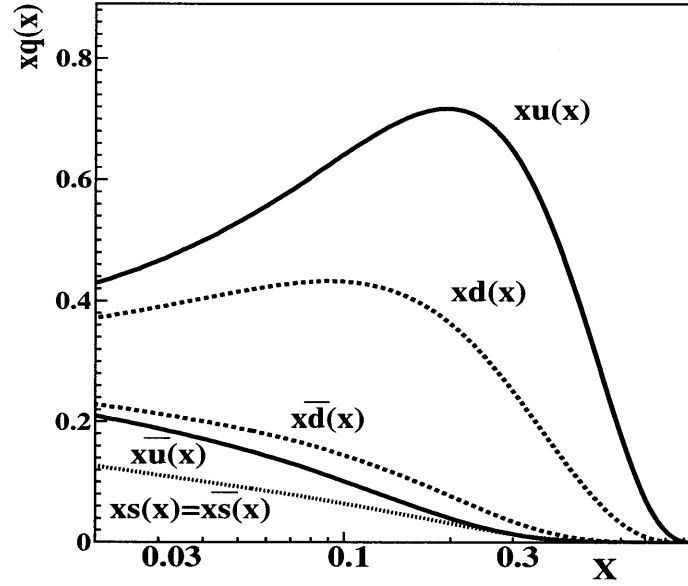


Figure 2-3: The unpolarized quark distributions in the proton versus Bjorken x , as fit by CTEQ Collaboration [11] (set “CTEQ4LQ”) to world data.

where antiquarks subtract from the flavor content of the wavefunction. While the parton distributions are defined on the proton, one may naively obtain distributions for other baryons by assuming a symmetry that connects them to the proton. The most important examples of this are the neutron parton densities, which are isospin symmetry rotations of their proton counterparts: $u^n(x) = d(x)$, $d^n(x) = u(x)$, $s^n(x) = s(x)$, and similarly for antiquarks.

An important assumption of the QPM is the *universality* of the parton description. If partons are the fundamental components of hadrons, the cross-section of any deep-inelastic probe of hadron structure should then be proportional to the parton distributions. Theorists use this fact to fit universal parton distributions to measured cross-sections in a wide variety of processes, including DIS, Drell-Yan scattering, W boson production, high- p_T jet production, and prompt photon production both in the Quark-Parton Model and NLO QCD (Section 2.1.1.2 below). Parton distribution fits by the CTEQ Collaboration [11] are shown in Figure 2-3. In the QPM, the photon cross-section ratio, $R(x, Q^2)$, tends to zero as $\frac{1}{Q^2}$ for absorption on spin $\frac{1}{2}$ particles. This behavior is seen in DIS studies at SLAC and at CERN confirming that quarks are spin $\frac{1}{2}$ objects. In the Bjorken limit, Eq. (2.15) yields the Callen-Gross [12] relation, relating

F_2 to F_1 :

$$F_2(x) = 2x F_1(x) = \sum_q x e_q^2 q(x). \quad (2.19)$$

$F_2(x)$ then corresponds to the total momentum fraction carried by quarks in the nucleon.

In defining $q(x)$, spin degrees of freedom are averaged. The polarized parton distribution, $\Delta q(x)$, is the difference of quark densities having spins oriented parallel and anti-parallel to the proton spin. The integral of $\Delta q(x)$ over the entire x range, $0 < x < 1$, yields the fraction of the proton spin carried by quarks. Hence, the structure function $g_1(x)$ is a key window into understanding proton spin structure.

The only remaining structure function to discuss, $g_2(x)$, describes binding effects, which are ignored in the Quark-Parton Model approximations. For partons that do not interact, $g_2(x)$ is zero.

2.1.1.2 Quantum Chromodynamics and DIS

While the QPM provides a simple interpretation of DIS structure functions, it does not yield any physical understanding of the forces that confine quarks in protons. Experimentally, a number of measurements suggest deficiencies in the QPM, including the observation of scaling violations $F_2^p(x)$. A summary of world data on $F_2^p(x, Q^2)$ relevant to HERMES kinematics is shown in Figure 2-4. Strong Q^2 dependence of the structure functions begins to manifest below $x \lesssim 0.18$.

A more sophisticated treatment of the behavior of partons inside a proton can be described using Quantum Chromodynamics. QCD is a non-Abelian quantum field theory describing the strong interaction of the Standard Model. Quarks possess one of three strong force charges, named for the primary colors: red, green, and blue. The formal symmetry of color charges is described by the $SU(3)_{\text{color}}$ group. Colored objects interact with each other through the exchange of a new parton, the massless, spin 1 gluon. The gluon also possesses color charge in the adjoint representation of the $SU(3)_{\text{color}}$ group [5].

In the qualitative picture suggested by QCD, color neutral, or “white”, objects form by binding quarks with the strong force, just as electrically neutral atoms form by electromagnetic

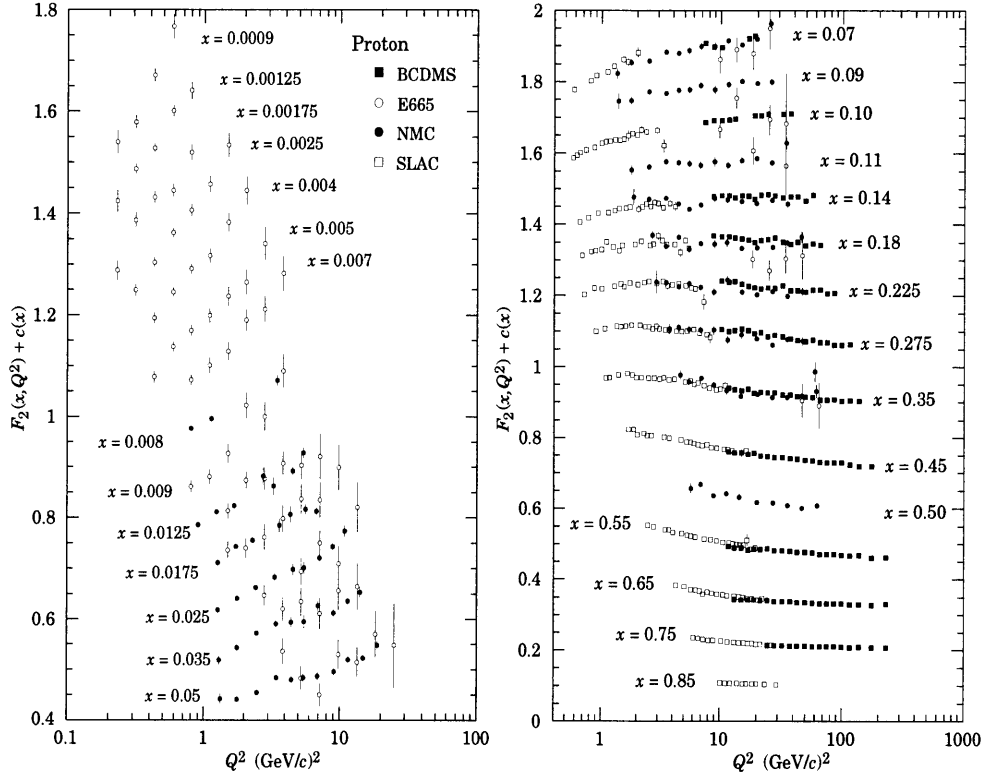


Figure 2-4: The unpolarized proton structure function $F_2(x, Q^2)$ as function of Q^2 for fixed x . The data in each x bin are offset by a constant $c(x) = 0.1i_x$ where i_x is the bin number. The plot reproduced from the Particle Data Group [13]; the data points come from BCDMS [14], E665 [15], NMC [16], and SLAC [17].

binding of electrons and protons. Baryons consist of three bound quarks while mesons have a bound quark and antiquark. Unlike photons in electromagnetism, though, the gluons may also interact with each other through their color charge.

The quark-gluon coupling constant, α_s , governs a quantitative description of the strong interaction. The coupling α_s varies with the renormalization energy scale μ of the field theory. While QCD does not directly predict the strength of strong force coupling, it does specify this variation in μ . This variation is calculated by a perturbation series in α_s itself to fourth

order [13]:

$$\begin{aligned}
\mu \frac{\partial \alpha_s}{\partial \mu} &= -\frac{\beta_0}{2\pi} \alpha_s^2 - \frac{\beta_1}{4\pi^2} \alpha_s^3 - \frac{\beta_2}{64\pi^3} \alpha_s^4 - \mathcal{O}(\alpha_s^5), \\
\beta_0 &= 11 - \frac{2}{3} n_f, \\
\beta_1 &= 51 - \frac{19}{3} n_f, \\
\beta_2 &= 2857 - \frac{5033}{9} n_f + \frac{325}{27} n_f^2,
\end{aligned} \tag{2.20}$$

where n_f is the number quarks with mass less than the energy scale μ ; at HERMES, $n_f = 3$.

In solving Eq. (2.20) for $\alpha_s(\mu)$, an integration constant appears in the theory. This is the only free parameter in QCD, and it must be determined by experiments. One may express this constant as the value of α_s at a conventionally fixed value of μ or as a logarithmic constant, $\Lambda_{QCD}^{(n_f)}$: $\mu_{\text{fixed}} \equiv M_Z = 91.187 \text{ GeV}$ or $\Lambda_{QCD}^{(5)} = 219_{-23}^{+25} \text{ MeV}$ [13]. Using Λ , the coupling constant in QCD is,

$$\begin{aligned}
\alpha_s(\mu) &= \frac{4\pi}{\beta_0 \ln(\mu^2/\Lambda^2)} \left[1 - \frac{2\beta_1}{\beta_0} \frac{\ln[\ln(\mu^2/\Lambda^2)]}{\ln(\mu^2/\Lambda^2)} \right. \\
&\quad \left. + \frac{4\beta_1^2}{\beta_0^4 \ln^2(\mu^2/\Lambda^2)} \left((\ln[\ln(\mu^2/\Lambda^2)] - \frac{1}{2})^2 + \frac{\beta_2 \beta_0}{8\beta_1^2} - \frac{5}{4} \right) + \dots \right].
\end{aligned} \tag{2.21}$$

In DIS, μ is often identified with Q , the virtual photon mass. A key insight of theory is that $\alpha_s(Q)$ scales as $\approx \frac{1}{\ln(Q^2/\Lambda^2)}$. As Q increases, α_s decreases and it approaches zero in the $Q^2 \rightarrow \infty$ limit. This important feature of the theory is known as *asymptotic freedom*; at very high energies, quarks interact with photons freely, as if they are no longer bound inside a nucleon. This key assumption in the QPM is reproduced by QCD in the Bjorken limit. All experiments are performed at finite Q^2 . Perturbative QCD corrections expanded in $\alpha_s(Q)$ are necessary to adjust parton model interpretations. Figure 2-5 displays the Feynman diagrams for such corrections. As long as $\alpha_s(Q) \ll 1$, these corrections may be small.

For studying the structure of the nucleon, one is interested in probing the low- Q^2 limit of QCD. How do quarks and gluons interact to reproduce the static properties of the nucleon? In the low energy limit of QCD $\alpha_s(Q)$ exceeds unity near $Q \sim \Lambda_{QCD}$. Predictions from perturbative QCD expansions begin to diverge; in this region, only more difficult non-perturbative calculation techniques may be applied to understand the strong interactions. As a result, though

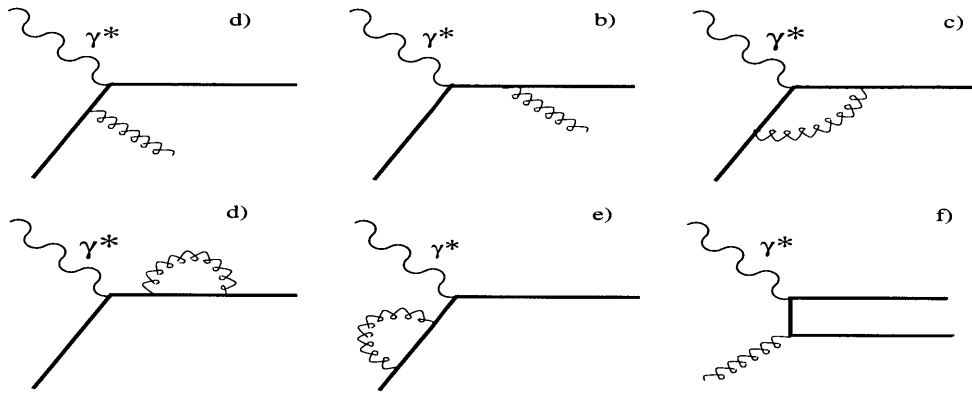


Figure 2-5: Feynman Diagrams contributing QCD corrections to deep-inelastic scattering. a) and b) represent initial and final state gluon bremsstrahlung; c), vertex corrections; d) and e), vacuum polarization corrections; and f) photon-gluon fusion.

QCD is believed to provide the exact description of the force binding quarks in nucleons, much of the detailed nucleon structure is beyond our ability to calculate. The distributions of parton momenta and spins inside a proton are examples of interesting, but incalculable, structure.

The factorization theorem provided by QCD states that the cross-sections for deep-inelastic processes may be separated into short distance, perturbative and long distance, non-perturbative pieces [18]. Perturbation theory describes the incoherent, high energy scattering on quarks. For sufficiently high energy, the scattering occurs in a short time and distance, and only one quark inside then nucleon is involved. The distribution of parton momentum before the scattering and the breakup of the nucleon after the scattering may be neatly parceled into parton distributions and fragmentation functions. The factorization theorem validates the measurement of parton distributions in deep-inelastic processes.

In the QPM, one argues that elastic scattering on free quarks yields proton structure function scaling. In QCD at finite Q^2 , the dynamics of the strong interaction interfere coherently with the electromagnetic scattering. Valence quarks may spontaneously emit gluons, which carry away a fraction of their momentum; the gluons themselves may then split into a quark-antiquark pair adding a “sea” contribution to the quark densities. The resulting Q^2 dependence

of parton distributions is described by the DGLAP equations [19, 20, 21].

$$\frac{d}{d \ln Q^2} q(x, Q^2) = \frac{\alpha_s(Q^2)}{2\pi} \int_x^1 \frac{dy}{y} \left(q(y, Q^2) P_{qq}\left(\frac{x}{y}\right) + g(y, Q^2) P_{qg}\left(\frac{x}{y}\right) \right), \quad (2.22)$$

$$\frac{d}{d \ln Q^2} g(x, Q^2) = \frac{\alpha_s(Q^2)}{2\pi} \int_x^1 \frac{dy}{y} \left(\sum_q q(y, Q^2) P_{gq}\left(\frac{x}{y}\right) + g(y, Q^2) P_{gg}\left(\frac{x}{y}\right) \right). \quad (2.23)$$

$P_{ij}(\frac{x}{y})$ are splitting functions, which represent the probability of finding a parton j with momentum fraction y inside a parton i with fraction x . In the polarized case, helicity difference splitting functions $\Delta P_{ij}(\frac{x}{y})$ may be defined, giving analogous evolution equations,

$$\frac{d}{d \ln Q^2} \Delta q(x, Q^2) = \frac{\alpha_s(Q^2)}{2\pi} \int_x^1 \frac{dy}{y} \left(\Delta q(y, Q^2) \Delta P_{qq}\left(\frac{x}{y}\right) + \Delta g(y, Q^2) \Delta P_{qg}\left(\frac{x}{y}\right) \right), \quad (2.24)$$

$$\frac{d}{d \ln Q^2} \Delta g(x, Q^2) = \frac{\alpha_s(Q^2)}{2\pi} \int_x^1 \frac{dy}{y} \left(\sum_q \Delta q(y, Q^2) \Delta P_{gq}\left(\frac{x}{y}\right) + \Delta g(y, Q^2) \Delta P_{gg}\left(\frac{x}{y}\right) \right). \quad (2.25)$$

$P_{ij}(\frac{x}{y})$ and $\Delta P_{ij}(\frac{x}{y})$ parameterize the effects of the gluon emission and gluon splitting processes, and they are calculated perturbatively. By knowing the complete nucleon parton distributions as a function x at one Q_{initial}^2 , distributions at any other Q^2 may be predicted.

The Q^2 dependence of the nucleon structure in DIS may be understood by analogy to optics. The distance probed by a photon depends on its wavelength λ , which varies inversely with the photon momentum $|\vec{q}| \approx Q$: $\lambda \propto \frac{1}{Q}$. The internal structure of a proton is resolved as the Q of the virtual photon “probe” increases beyond the proton’s charge radius, $Q \gg \frac{1}{r_P} = 0.240 \text{ GeV}^2$ [22]. Pointlike quarks have no such characteristic radius, and yield scale invariance or Q independence of the process. In QCD, soft gluon processes may screen valence quarks with sea quarks and give rise to effective Q^2 dependence as this screen is penetrated. Figure 2-6 depicts this view schematically.

2.1.1.3 OPE and DIS

The above perturbative QCD corrections model the evolution in Q^2 of a free quark interaction. Quark binding effects inside a nucleon can be included by the analysis of the operator product expansion(OPE). The current matrix element in Eq. (2.4) is expanded in terms of

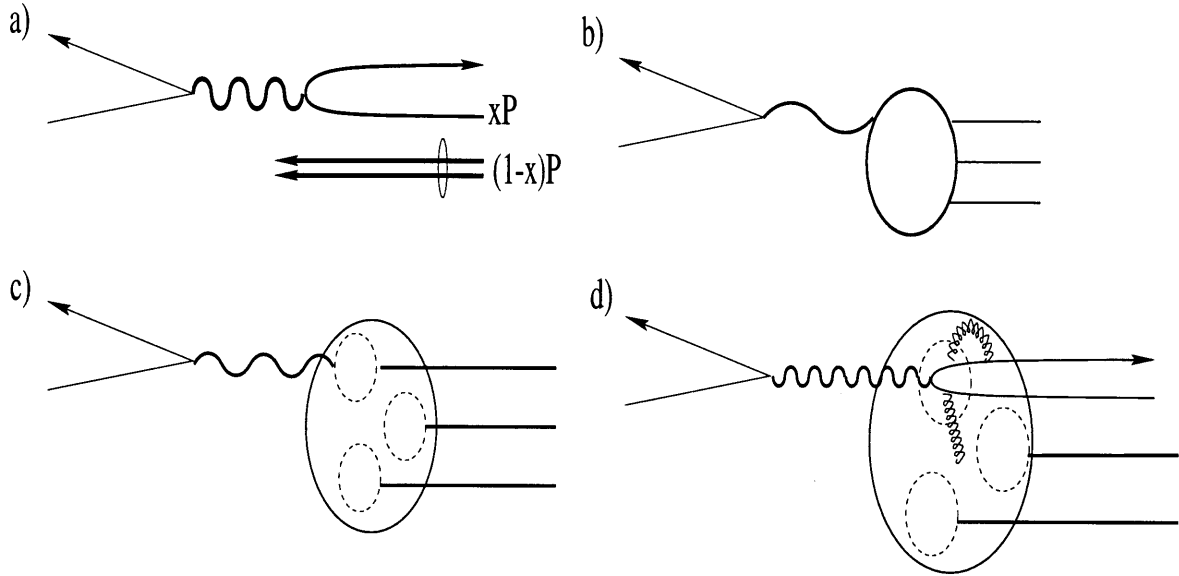


Figure 2-6: Evolution of the scattering process with Q^2 . a) The Quark-Parton Model analysis in the infinite momentum frame describes elastic scattering of free quarks. b) the proton as a whole is probed for low Q^2 , corresponding to long photon wavelengths. c) As Q^2 increases, individual quarks are resolved up to QCD corrections. d) With very high- Q^2 , the point-like nature of the quarks appears.

local operators. The result is a general expansion for $W^{\mu\nu}$ in terms of structure functions multiplied by $(\frac{\Lambda_{QCD}}{Q})^{\tau-2}$, where τ is the *twist* of the structure functions. The twist controls the power of $\frac{1}{Q}$ multiplying the structure function expansion [23]. In the Bjorken limit, only twist-2 functions contribute to the cross-section, including the familiar $F_1(x)$ and $g_1(x)$. At experimental $Q^2 \gtrsim \Lambda_{QCD}$, higher twist functions may play a role in the deep-inelastic cross-section. These effects model, for example, quark-gluon correlations and intrinsic parton k_T in the nucleon. While the structure function $g_2(x)$ has no definite parton model interpretation, it arises naturally from the OPE as a twist-3 structure function.

2.1.2 Semi-Inclusive DIS

Semi-inclusive deep-inelastic scattering is a subprocess of inclusive scattering in which the additional high-momenta hadrons are detected in coincidence with the scattered lepton:

$$l + N \rightarrow l' + h + X.$$

The hadrons h are generated in the nucleon break-up, or fragmentation, after the lepton scattering. One makes the assumption of local parton-hadron duality [24, 25]: the flow of the hadrons quantum numbers reflects the flow of parton quantum numbers in the scattering. If the hadronic fragments are correlated to the initial quarks, they provide more information on the nucleon structure.

The cuts on the variables z and x_f , defined in Table 2.1, separate hadronic debris into different classes experimentally by their momenta. These classes include current fragments, which correlate to the interacting quark and typically have $x_f > 0$ and $z > 0.2$, and target fragments, which relate the spectator remnant of the nucleon and typically have $x_f < 0$ and $z < 0.2$. Semi-inclusive studies may tag the flavor of the struck quark in the interaction, by identifying the current fragments from the collision.

The deep-inelastic cross-section to detect hadrons in coincidence with leptons, σ^h , has exactly the same structure as inclusive cross-section Eq. (2.11). By analogy, generalized structure functions F_1^h and g_1^h relevant to semi-inclusive reactions may be defined. In the Quark-Parton Model, these may be written

$$F_1^h(x) = \frac{1}{2} \sum_{q=u,d,s\dots} e_q^2 q(x) D_q^h(z), \quad (2.26)$$

$$g_1^h(x) = \frac{1}{2} \sum_{q=u,d,s\dots} e_q^2 \Delta q(x) D^h(z). \quad (2.27)$$

The fragmentation function, $D_f^h(z)$, reflects the probability for a quark of flavor f to produce a hadron of type h with momentum fraction z during hadronization. The functions are normalized to conserve total particle multiplicity, n_h , and total energy [5]:

$$\sum_h \int_0^1 D_q^h(z) dz = n_h, \quad (2.28)$$

$$\sum_h \int_0^1 z D_q^h(z) dz = 1. \quad (2.29)$$

In the QPM, the semi-inclusive differential cross-sections may be simply related to the inclusive cross-sections:

$$\frac{d^3\bar{\sigma}^h}{dx dQ^2 dz} = \frac{\sum_q e_q^2 q(x) D_q^h(z)}{\sum_q e_q^2 q(x)} \frac{d^2\bar{\sigma}}{dx dQ^2}, \quad (2.30)$$

$$\frac{d^2\Delta\sigma^h}{dx dQ^2 dz} = \frac{\sum_q e_q^2 \Delta q(x) D_q^h(z)}{\sum_q e_q^2 \Delta q(x)} \frac{d^2\Delta\sigma}{dx dQ^2}, \quad (2.31)$$

As in the parton distribution case above, QCD is unable to predict directly the detailed features of fragmentation; the fragmentation process occurs at low-energy and therefore cannot be calculated perturbatively. The fragmentation functions provide a simple parameterization of our ignorance of the fragmentation process.

QCD guides a general understanding of the features of fragmentation. The diverging strength of the strong coupling at low energies guarantees that free quarks cannot be found in the products of the nucleon breakup. In order for quarks to escape the nucleon, both the struck quark and the target remnant must form bound, color neutral systems. In addition, the factorization theorem in QCD suggests that the final state hadronization is independent of the initial state parton distribution, in the Bjorken limit. The fragmentation functions must also be universal; $D_q^h(z)$ measured in deep-inelastic scattering are equivalent to $D_q^h(z)$ measured in $e^+ - e^-$ colliders [26]. QCD also predicts scale dependence for $D_q^h(z)$. Quark fragmentation functions may mix with gluon fragmentation functions, yielding evolution equations similar to Eq. (2.23) [27, 28].

At HERMES energies, the fragmentation of six quarks and antiquarks dominantly produces six charged hadrons: $\{u, d, s, \bar{u}, \bar{d}, \bar{s}\} \rightarrow \{\pi^+, \pi^-, K^+, K^-, p \text{ and } \bar{p}\}$. Thirty-six independent fragmentation functions then describe semi-inclusive particle production. Symmetries may limit the number of fragmentation functions, in the same way as they relate proton and neutron parton densities. In the pion case, twelve fragmentation functions may be reduced to three by

charge conjugation symmetry, $D_u^{\pi^+}(z) = D_{\bar{u}}^{\pi^-}(z)$, and isospin symmetry, $D_u^{\pi^+}(z) = D_d^{\pi^-}(z)$:

$$D_1(z) = D_u^{\pi^+}(z) = D_d^{\pi^-}(z) = D_{\bar{u}}^{\pi^-}(z) = D_{\bar{d}}^{\pi^+}(z) \quad (2.32)$$

$$D_2(z) = D_u^{\pi^-}(z) = D_d^{\pi^+}(z) = D_{\bar{u}}^{\pi^+}(z) = D_{\bar{d}}^{\pi^-}(z) \quad (2.33)$$

$$D_3(z) = D_s^{\pi^+}(z) = D_{\bar{s}}^{\pi^-}(z) = D_s^{\pi^-}(z) = D_{\bar{s}}^{\pi^+}(z) \quad (2.34)$$

$D_1(z)$ is called the favored fragmentation function as the pion produced by each quark has that quark in its ground state wavefunction. This fragmentation is more probable than the unfavored and strange quark cases described by $D_2(z)$ and $D_3(z)$.

2.1.3 Fragmentation Models

As the formation of color singlet hadrons from nucleon fragments involves low energy phenomena, QCD can provide only a general guide to features of hadron production. A number of QPM and QCD inspired models exist to describe hadronization phenomenologically.

These models generally break the fragmentation into several phases [29]. Initially, a quark in the nucleon is struck by a virtual photon on a very short time scale determined by $\frac{1}{Q^2}$. Second, a cascade of quarks develops from gluon emission by the initial quark $q \rightarrow qg$ and subsequent gluon splitting $g \rightarrow q\bar{q}$. The cascade is modeled perturbatively until the parton energies drop below a cutoff scale $t_0 \gg \Lambda_{QCD}$. Finally, the quarks are assigned to hadrons by an effective model of soft hadronization. The final state consists of quarks confined in color singlet hadrons. Three models are used to describe hadron production at HERMES.

2.1.3.1 Independent Fragmentation

Field and Feynman [30] developed the independent fragmentation model, which supposes partons fragment completely independently from each other. In this simple scheme, the struck quark q_s leaving the nucleon picks up an antiquark from a $q_1\bar{q}_1$ pair created out of the vacuum. This pickup produces a “primary” meson with energy fraction z , and leaves behind another quark q_1 with energy fraction $1 - z$. q_1 is then fragmented by introducing another antiquark \bar{q}_2 from pair creation in the same way. This process of meson formation proceeds until the leftover energy fraction drops below a certain energy cutoff. The remaining low energy quark is then neglected.

The model is controlled by four parameters which may be fit to experimental data. A one parameter function $f(z)$ controls the distribution of momentum fraction between each produced meson and remnant quark. Two parameters model the relative abundance of the u , d , and s flavors in $q\bar{q}$ pair creation: 2γ is the u and d fraction (assumed equal) while γ_s is the s fraction. $\gamma_s = 0.3\gamma$ has been determined experimentally from the ratio of K to π yields in fragmentation [31, 32]. Since the total quark fractions are normalized to unity, $2\gamma + \gamma_s = 1$, this implies $\gamma = 0.435$. Each created $q\bar{q}$ pair has a relative transverse momentum assigned according to a Gaussian with $\langle p_{\perp}^2 \rangle = 0.35 \text{ (GeV}/c)^2$. The ratio of vector to pseudovector meson production is also tuned in the model [33].

The model is surprisingly successful in describing hadronization in e^+e^- collisions [34, 35, 36]. The model, however, has severe weaknesses. By ignoring the last quark in the hadronization, color and flavor quantum numbers are not explicitly conserved. Also, the assignment of energy fractions is frame dependent, and Lorentz transformation to another frame may lead to a violation of momentum conservation [33]. These weaknesses have led to the investigation of more physically motivated models.

2.1.3.2 String Model

The LUND string model [37] is based on the idea that a fragmenting quark system is connected by color flux tubes, or strings. One imagines that the self-interacting property of gluons produces a tubes of gluons between a struck quark and a remaining diquark. The tube may be approximated by a long distance linear potential with strength $\sim kr$ for a distance r , which is consistent with quarkonium spectroscopy [29]. This string stretches as the struck quark and diquark separate, building potential energy. The string may then break into two pieces by forming $q\bar{q}$ pairs along its length. Each q and \bar{q} forms the end points of two new strings which continue to hadronize in this method. The process of string stretching and breaking continues until each string-connected quark pair reaches the on-shell mass of a hadron.

The model shares many features with the independent fragmentation model. Energy is distributed in the string using a three-parameter distribution $f(z)$, including parameterization of quark-antiquark pair transverse momentum. The ratios of generated quarks to diquarks, the ratios of vector mesons to pseudoscalar meson, and the ratios of strange quarks to light quarks are also free parameters [32].

The LUND model does provides a simple, Lorentz covariant picture of the hadronization process, which explicitly conserves color and flavor. The model also differs from the independent fragmentation in its treatment of gluons. Gluons may be radiated from strings producing “kinks” in the fragmentation [38]. The resulting angular distributions are in good agreement with experimental observations.

2.1.3.3 Cluster Model

In the cluster model of hadronization, perturbative QCD is used as long as possible to describe hadron formation [39]. After the initial quark interaction and showering, the resulting partons are evolved into low-mass color neutral clusters. This cluster assignment is calculated in the QCD Leading Log Approximation, and is achieved by $q\bar{q}$ pair formation. The cut-off mass t_0 may be as low as a few times Λ_{QCD} . In a second step, these clusters decay isotropically into hadron pairs, with branching ratios dictated by the available phase space. The model is driven by QCD and has only a few adjustable parameters: Λ_{QCD} , the parton masses, and the cluster cut-off mass [33].

2.1.4 Measurements in Polarized Deep-Inelastic Scattering

2.1.4.1 Polarized Observables in the QPM

The structure function $g_1(x)$ in Eq. (2.11) provides direct access to the nucleon quark spin content in deep-inelastic scattering. To measure it, experimental physicists use cross-section asymmetries between two relative orientations of the target and the beam spin. In the parallel case, $\alpha=0$ in (2.12), and one has

$$A_{\parallel}(x, Q^2) = \frac{\frac{d^2\sigma^{\uparrow\downarrow}}{dx dQ^2} - \frac{d^2\sigma^{\uparrow\uparrow}}{dx dQ^2}}{\frac{d^2\sigma^{\uparrow\downarrow}}{dx dQ^2} + \frac{d^2\sigma^{\uparrow\uparrow}}{dx dQ^2}} \quad (2.35)$$

Acceptance and efficiency factors cancel in the cross-section ratio, greatly simplifying the analysis. A transverse polarization asymmetry can similarly be defined, in which the target proton spin is oriented at right angles to the incoming lepton spin.

$$A_{\perp}(x, Q^2) = \frac{\frac{d^2\sigma^{\uparrow\Rightarrow}}{dx dQ^2} - \frac{d^2\sigma^{\uparrow\Leftarrow}}{dx dQ^2}}{\frac{d^2\sigma^{\uparrow\Rightarrow}}{dx dQ^2} + \frac{d^2\sigma^{\uparrow\Leftarrow}}{dx dQ^2}} \quad (2.36)$$

These target and beam asymmetries may be converted to the asymmetries in virtual photoabsorption, A_1 and A_2 , by

$$A_{\parallel} = D \cdot (A_1 + \eta A_2) \quad (2.37)$$

$$A_{\perp} = d \cdot (A_2 + \xi A_1) \quad (2.38)$$

where d , D , η , and ξ are kinematic factors [6]:

$$D = \frac{1 - (1-y)\epsilon}{1 + \epsilon R} \quad (2.39)$$

$$\eta = \frac{2\gamma(1-y - \frac{1}{4}\gamma^2 y^2)}{(2-y)(1 + \frac{1}{2}\gamma^2 y)} \quad (2.40)$$

$$d = D \sqrt{\frac{2\epsilon}{1+\epsilon}} \quad (2.41)$$

$$\xi = \eta \frac{1+\epsilon}{2\epsilon} \quad (2.42)$$

This conversion removes explicit y and ϵ dependence in the asymmetries arising from helicity transfer and longitudinal cross-section effects. The depolarization factor, D , represents the suppression of the exchanged virtual photon polarization relative to the lepton polarization.

A_1 and A_2 are directly related to the desired polarized structure functions:

$$A_1 = \frac{g_1 - \gamma^2 g_2}{F_1} \quad (2.43)$$

$$A_2 = \frac{\gamma(g_1 + g_2)}{F_1}. \quad (2.44)$$

In particular, note that in the Bjorken limit, $\gamma \rightarrow 0$ and $g_1 = A_1 F_1 = \frac{A_{\parallel} F_1}{D}$. The above kinematic relations hold whether the inclusive structure function g_1 or the semi-inclusive functions g_1^h are measured.

In addition to the A_1 measurements, a number of other polarized measurements have been proposed with semi-inclusive particle detection [40, 41]. These relations use the simple Quark-Parton Model expression for the cross-section in (2.31) with the assumption of fragmentation symmetry in (2.34). One suggestion considers the longitudinal asymmetry in the difference in π^+ and π^- production cross-sections in DIS,

$$A^{\pi^+-\pi^-} = \frac{(\sigma^{\pi^+} - \sigma^{\pi^-})^{\uparrow\downarrow} - (\sigma^{\pi^+} - \sigma^{\pi^-})^{\uparrow\uparrow}}{(\sigma^{\pi^+} - \sigma^{\pi^-})^{\uparrow\downarrow} + (\sigma^{\pi^+} - \sigma^{\pi^-})^{\uparrow\uparrow}}. \quad (2.45)$$

In the QPM, sea quark distributions cancel in the differences, and fragmentation functions cancel in the ratio, leaving direct sensitivity to the valence quark polarizations. The asymmetry varies for different targets:

$$A_p^{\pi^+-\pi^-} = \frac{4\Delta u_{\text{val}}(x) - \Delta d_{\text{val}}(x)}{4u_{\text{val}}(x) - d_{\text{val}}(x)}, \quad (2.46)$$

$$A_{^3\text{He}}^{\pi^+-\pi^-} \approx \frac{4\Delta d_{\text{val}}(x) - \Delta u_{\text{val}}(x)}{7u_{\text{val}}(x) + 2d_{\text{val}}(x)}, \quad (2.47)$$

where the ^3He expression is an approximation assuming perfect neutron polarization. A detailed discussion of the “valence” as opposed to “sea” quarks is saved for Section 2.2.6. A measurement of these asymmetries on two targets allows direct extraction of the valence quark contribution to the nucleon spin.

Another idea uses the ratio of the total pion and inclusive cross-sections in each spin state [40],

$$n^{\uparrow\uparrow(\uparrow\downarrow)}(x, z) = \frac{\sigma^{\pi^++\pi^-}}{\sigma}(x, z) \quad (2.48)$$

to access the strange sea polarization, Δs :

$$\Delta s(x) - A_1(x)s(x) = \frac{9F_1(x)(1 - A_1(x))}{D_s^\pi(z) - D_u^\pi(z)}(n^{\uparrow\downarrow}(x, z) - n^{\uparrow\uparrow}(x, z)) \quad (2.49)$$

The sensitivity in this measurement comes from the difference of pion and inclusive asymmetries. Since $\frac{1}{9}s(x) \ll 2F_1$, one can show [42, 43, 44]

$$n^{\uparrow\uparrow}(x, z) - n^{\uparrow\downarrow}(x, z) \sim 2D^\pi(A_1^\pi - A_1). \quad (2.50)$$

Note that kaon production asymmetries, A_1^K , provide a complementary access to Δs as the strange sea fragmentation to kaons is favored [41]. One then expects a larger strange quark sensitivity in this asymmetry.

In Chapter 6, a more general method of accessing quark polarizations in semi-inclusive data is presented. A global fit to the double-spin asymmetries in all inclusive and semi-inclusive channels yields a complete view of the quark polarizations in the QPM. The ratios described above still provide an understanding of how measurements of semi-inclusive asymmetries access quark polarizations.

2.1.4.2 Further Access to Nucleon Spin

Several other probes of nucleon spin are discussed in the literature, but are not used in this work. They are mentioned to give a broader context of experimental nucleon spin structure studies.

Current theories of nucleon structure suggest that gluons may have significant contributions to the nucleon spin (see Section 2.2.7). Though electromagnetic scattering is not directly sensitive to the uncharged glue, a few possibilities exist to infer their properties from scattering measurements. If the polarized structure function $g_1(x, Q^2)$ is measured as function of Q^2 , then the DGLAP equations in Eq. (2.23) may be used to disentangle quark and gluon contributions. Sensitivity to gluons may be enhanced by isolating the photon-gluon fusion process shown in Figure 2-5f. The process may be isolated by searching for two hadrons emitted at large relative transverse momentum, $p_T^h \gtrsim 1.5$ GeV. The asymmetry for such events is proportional to the gluon polarization, $\frac{\Delta g}{g}(x, Q^2)$. Charmed hadrons are also a tag for this process, as there is little intrinsic charm quark content in the nucleon. Both measurements are under study at the HERMES experiment [45, 46] and in future experiments [47].

Experiments are now studying Δq and ΔG , but getting access to parton orbital angular momentum remains difficult. The process of deeply-virtual Compton scattering [48] is under study theoretically as a possible experimental tag.

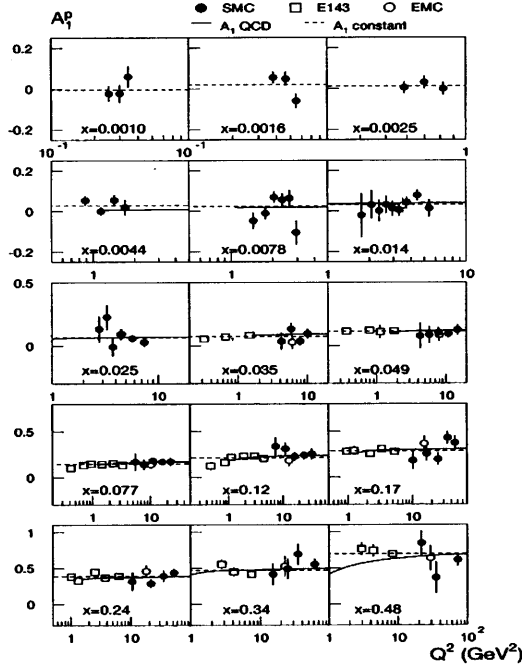


Figure 2-7: World Data on $A_1(x, Q^2)$ for the proton. The dotted line in the plot represents a constant fit to the Q^2 dependence, while the solid line is an NLO QCD fit from Reference [49]. The figure is taken from Reference [50].

2.1.4.3 Previous Experiments in Polarized DIS

Prior to HERMES, a long program of experiments at SLAC and CERN collected significant statistics on the polarized nucleon structure functions. The focus of these experiments has been the study of inclusive polarized deep-inelastic scattering.

The first polarized DIS experiments, E80 [51] and E130 [52], occurred at SLAC in the late 70s and early 80s. These experiments scattered polarized electrons from polarized butanol targets. Since then, SLAC experiments E142 [53], E143 [54], E154 [55], and E155 [56] have measured the inclusive DIS asymmetries with increasing beam energy and precision. E142 and E154 used dense ^3He targets that were polarized by optical pumping and spin exchange. The measured ^3He asymmetries were converted to neutron asymmetries by nuclear corrections. E143 and E155 measured proton and deuteron structure functions with polarized ammonia

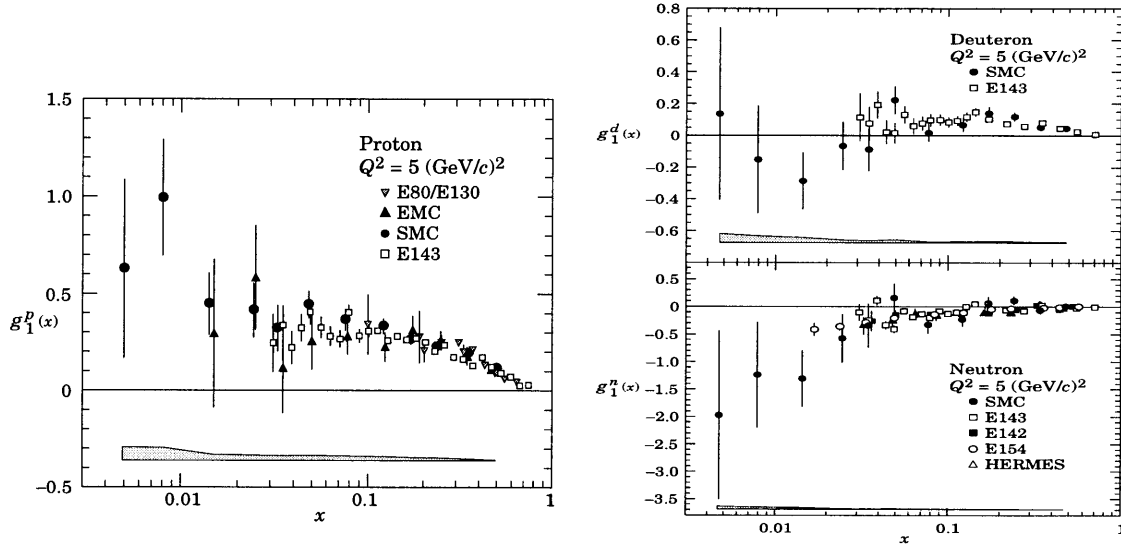


Figure 2-8: World Data on the $g_1(x)$ Structure Functions for the proton, neutron, and deuteron. The figure is taken from Reference [13].

(NH_3 , ND_3) and deuterated lithium (LiD_6) targets. Multiple single arm spectrometers provided tracking of the scattered electrons for each of the SLAC experiments.

The CERN experiments, EMC [3] and SMC [50], directed muons onto polarized fixed targets. The muon beam was extracted from high energy π and K decays, and parity violation in these decays provided high muon polarization. Compared to SLAC, much higher beam energies were available, though with more limited currents. These experiments used polarized butanol (C_4H_9OH , C_4D_9OD) and ammonia targets to measure the proton and deuteron asymmetries. Larger acceptance spectrometers allowed a broader acceptance for inclusive DIS events as well as semi-inclusive acceptance.

Table 2.2 summarizes the relevant features of these experiments. Comparisons of the measured $A_1(x)$ asymmetries is shown in Figure 2-7. The Q^2 dependence of the asymmetries is not yet well enough measured to exclude a constant dependence. Figure 2-8 compares the world data on $g_1(x)$.

Experiment	Beam	Energy [GeV]	Target	x range	Q^2 range [GeV ²]	Ref.
E80	e^-	6 - 13	H	0.1 - 0.7	1 - 10	[51]
E130	e^-	23	H	0.2 - 0.6	1 - 10	[52]
E142	e^-	19.4 - 25.5	³ He	0.029 - 0.8	1 - 10	[50]
E143	e^-	9.7 - 29.1	H, D	0.029 - 0.8	1 - 10	[54]
E154	e^-	48.35	³ He	0.014 - 0.7	1 - 17	[57]
E155	e^-	48.35	H,D	0.014 - 0.85	1 - 17	[56]
EMC	μ^+	100 - 190	H	0.005 - 0.75	1 - 200	[3]
SMC	μ^+	100 - 190	H, D	0.003 - 0.7	1 - 190	[50]
HERMES	$e^+(e^-)$	27.5	H, ³ He	0.023 - 0.6	1 - 10	[58]

Table 2.2: A Comparison of Experiments in Polarized DIS

2.2 Nucleon Spin Structure

This section motivates the use of deep-inelastic scattering in spin physics. As a proton consists of a composite sum of various constituents, a successful model of these constituents should reproduce a proton's static and dynamic properties. The studies of this thesis use the fact that the proton is a fermion with spin 1/2, and the angular momentum of all the components of the proton should add to reproduce this value. The spin sum rule, the fundamental relation of the study of nucleon spin structure, directly follows [59],

$$\langle J_p \rangle = \frac{1}{2} = \frac{1}{2}\Delta\Sigma + L_q + \Delta G + L_G. \quad (2.51)$$

The sum rule is written in the framework of QCD. $\Delta\Sigma$ is the total quark intrinsic spin contribution to the nucleon spin, while L_q adds their orbital angular momentum contribution. Gluons may also contribute intrinsic spin, ΔG , and orbital angular momentum, L_G .

2.2.1 Constituent Quark Model

The $SU(6)$ Constituent Quark Model describes hadron properties using wavefunctions of three spin $\frac{1}{2}$ quarks. In this model, hadron wavefunctions possess symmetry represented by the group $SU(6) = SU(3)_{\text{flavor}} \otimes SU(2)_{\text{spin}}$ [60]. In this model, quarks are treated non-relativistically and their masses are phenomenologically fit to observed hadron properties.

In the proton case, the flavor content is $|uud\rangle$. The requirements of wavefunction anti-symmetrization, flavor symmetry, and spin $\frac{1}{2}$ yield a total wavefunction [22]:

$$\begin{aligned}
|p \uparrow\rangle = & \frac{1}{\sqrt{18}} \{ (2|u \uparrow u \uparrow d \downarrow\rangle + |u \uparrow d \downarrow u \uparrow\rangle + |d \downarrow u \uparrow u \downarrow\rangle) \\
& - (|u \uparrow u \downarrow d \uparrow\rangle + |u \uparrow d \uparrow u \downarrow\rangle + |d \uparrow u \uparrow u \downarrow\rangle) \\
& - (|u \downarrow u \uparrow d \uparrow\rangle + |u \downarrow d \uparrow u \uparrow\rangle + |d \uparrow u \downarrow u \uparrow\rangle) \}.
\end{aligned} \tag{2.52}$$

The neutron simply represents a σ_z rotation of the proton in isospin space, the $SU(2)_{\text{flavor}}$ group consisting of the u and d quark.

Simple predictions for the quark content of the proton spin easily follow. The expectation value of the spin projection operators yields $\langle p | s_z^u | p \rangle = \Delta u = \frac{4}{3}$ and $\langle p | s_z^d | p \rangle = \Delta d = -\frac{1}{3}$. By construction, the model ignores quark dynamics and nucleon binding forces so that $L_q = L_g = \Delta G = 0$. All of the proton spin originates from the intrinsic spin of its constituent quarks, $\Delta\Sigma = 1$.

The model has been used successfully to explain the static properties of baryons. In particular, predicted magnetic moment of the baryons are in excellent agreement with the measured values [22]. In the lowest order in QED, the spin operator and the magnetic moment operator are related by

$$\vec{\mu} = g\mu_D \vec{s} = g \frac{e_q \hbar}{2m_q c} \vec{s} \tag{2.53}$$

where μ_D is the quark dipole moment, and m_q is its mass. Using fitted constituent quark masses, one can derive a prediction for the ratio of the proton and neutron moments:

$$\frac{\mu_n}{\mu_p} \approx -\frac{2}{3}. \tag{2.54}$$

This agrees well with the experimental ratio, $= -0.685$ [22]. However, the model is not completely successful: the predicted axial vector coupling in neutron β -decay, $\left| \frac{g_A}{g_V} \right| = \Delta u - \Delta d$ is $\frac{5}{3}$, which is higher than the measured value ~ 1.257 [13].

2.2.2 Relativistic Quark Model

While the Constituent Quark Model derives general properties of hadrons from SU(6) symmetry, relativistic extensions assume that massive constituent quarks may possess linear and orbital angular momentum inside the nucleon. QCD-inspired bag models [61, 62] picture a nucleon composed of three free, nearly massless quarks confined by a hard boundary. If a free quark is described by a two-component spinor χ^\dagger in its rest frame, after a boost this quark may be described by a Dirac four-component spinor [63]

$$\Psi^\dagger = \begin{bmatrix} \chi \\ \frac{\boldsymbol{\sigma} \cdot \mathbf{p}}{E+m} \cdot \chi \end{bmatrix}. \quad (2.55)$$

The bottom component of the spinor carries transverse momentum and gives rise to orbital angular momentum.

In the limit of zero mass, the theory predicts $\Delta\Sigma$ to 0.65 [59] with L_q contributing the remainder of the nucleon spin. For the bag model to correctly predict the axial vector coupling $\left| \frac{g_A}{g_V} \right|$, quark masses of a few MeV must be introduced. The $\Delta\Sigma$ prediction increases to ~ 0.75 in this case [59]. Similar results are obtained in a light-cone quantization model [64]. The flavor separation of $\Delta\Sigma$ in this model correspond to $\Delta u = 1.0$, $\Delta d = -0.25$, and $\Delta s = 0$.

2.2.3 Current Algebra

Further insight into nucleon spin can be gained from examining the covariant spin projection operators. In a relativistic treatment, one identifies the quark spin contribution, Δq , as the difference of proton wavefunction projections in left and right helicities [65]. These projections can be related to the proton axial vector current:

$$\Delta q s^\mu = \langle p | \bar{q}_R \gamma^\mu q_R - \bar{q}_L \gamma^\mu q_L | p \rangle = \langle p | \bar{q} \gamma^\mu \gamma^5 q | p \rangle. \quad (2.56)$$

In general, the currents relate to the $SU(3)_{\text{flavor}}$ operators,

$$A_i^\mu = a_i s^\mu = \langle p | \bar{q} \gamma^\mu \gamma^5 T^i q | p \rangle . \quad (2.57)$$

where T^i are the generators of the group for $i = 0, 1, \dots, 8$. The singlet current, a_0 , relates to the total quark contribution to the proton spin,

$$a_0 = \Delta\Sigma = (\Delta u + \Delta\bar{u}) + (\Delta d + \Delta\bar{d}) + (\Delta s + \Delta\bar{s}). \quad (2.58)$$

The identification is particularly interesting as a number of physical processes are sensitive to the axial vector currents. Hyperon weak β -decays are one significant example. The transition rates may be parameterized to constrain two decay parameters, F and D . Assuming strong isospin symmetry, neutron decay rates yield $\left| \frac{g_A}{g_V} \right| = F + D = 1.257 \pm 0.0028$ [13]. With $SU(3)_{\text{flavor}}$ symmetry, Λ and Σ decays further constrain $\frac{F}{D} = 0.575 \pm 0.016$ [66]. This gives

$$F = 0.459 \pm 0.008, \quad (2.59)$$

$$D = 0.798 \pm 0.008. \quad (2.60)$$

F and D directly relate to the non-singlet and octet axial vector couplings in $SU(3)$:

$$a_3 = (\Delta u + \Delta\bar{u}) - (\Delta d + \Delta\bar{d}) = F + D, \quad (2.61)$$

$$a_8 = (\Delta u + \Delta\bar{u}) + (\Delta d + \Delta\bar{d}) - (\Delta s + \Delta\bar{s}) = 3F - D. \quad (2.62)$$

Using these relations, one obtains direct constraints on the flavor decomposition of the nucleon spin. Model dependence mainly enters in the assumption of $SU(3)_{\text{flavor}}$ symmetry. To directly identify the helicities of three quark flavors, one more piece of information must be added. Ellis and Jaffe [67] made one simple assumption: the non-valence s quarks make no contribution to the proton spin. With $\Delta s + \Delta\bar{s} \equiv 0$, Eq. (2.62) gives

$$\Delta u + \Delta\bar{u} = 0.92, \quad (2.63)$$

$$\Delta d + \Delta\bar{d} = -0.34, \quad (2.64)$$

$$\Delta\Sigma = 0.58. \quad (2.65)$$

Here, the $\Delta\Sigma$ is lower than but generally consistent with the relativistic quark models above.

The strange quark assumption may be avoided by investigating other processes sensitive to axial vector currents. Polarized DIS provides one example. Inclusive polarized DIS measures the structure function $g_1(x)$, which corresponds in the Quark-Parton Model to the charge weighted sum of parton distributions:

$$\begin{aligned}\Gamma_1^p &= \int_0^1 g_1^p(x) dx = \frac{1}{2} \left[\frac{4}{9}(\Delta u + \Delta \bar{u}) + \frac{1}{9}(\Delta d + \Delta \bar{d}) + \frac{1}{9}(\Delta s + \Delta \bar{s}) \right], \\ &= \frac{1}{12} \left[+a_3 + \frac{1}{3}a_8 \right] + \frac{1}{9}[a_0]\end{aligned}\tag{2.66}$$

$$\begin{aligned}\Gamma_1^n &= \int_0^1 g_1^n(x) dx = \frac{1}{2} \left[\frac{4}{9}(\Delta d + \Delta \bar{d}) + \frac{1}{9}(\Delta u + \Delta \bar{u}) + \frac{1}{9}(\Delta s + \Delta \bar{s}) \right] \\ &= \frac{1}{12} \left[-a_3 + \frac{1}{3}a_8 \right] + \frac{1}{9}[a_0]\end{aligned}\tag{2.67}$$

Note that antiquark spin fractions are suppressed in this expression. When comparing QCD and parton model expressions with low energy decay and constituent quark model results, one generally wishes to sum quark and antiquark spins of the same flavor. Hence, q and \bar{q} are summed to q for the current algebra analysis.

By simple manipulation of the above expressions, the hyperon beta decay analysis yields structure function predictions that may be checked in DIS. The Bjorken Sum Rule [68] predicts the difference of the proton and neutron Γ_1 integrals:

$$\Gamma_1^p - \Gamma_1^n = \frac{1}{6} [(\Delta u + \Delta \bar{u}) - (\Delta d + \Delta \bar{d})] = \frac{1}{6} \left| \frac{g_A}{g_V} \right|\tag{2.68}$$

This prediction is powerful and fundamental in that it relates polarized DIS structure functions to the precisely measured neutron lifetime with little model dependence. The chief assumption behind the result is strong isospin symmetry; the sum rule has also been shown to be a rigorous consequence of QCD [69].

Assuming $\Delta s = 0$, one may derive the Ellis-Jaffe Sum Rules [67] for the proton and neutron integrals separately,

$$\Gamma_1^p = 0.186 \quad (2.69)$$

$$\Gamma_1^n = -0.019 \quad (2.70)$$

These predictions are close to the values that may be derived from relativistic quark models, $\Gamma_1^p = 0.208$ and $\Gamma_1^n = 0$. In order to compare DIS measurements at finite Q^2 with operator relations, perturbative QCD corrections must be included.

2.2.4 Perturbative QCD

While QCD is expected to be an exact description of quark and gluon interactions, perturbative calculations of nucleon spin structure are beyond our current ability. But as discussed in Section 2.1.1.2, QCD does tell us how to relate the results of DIS experiments to the understanding of spin structure from other sources. The DGLAP equations in (2.23) may be integrated over x to yield the Q^2 evolution of the total helicity densities probed by DIS [70]:

$$\frac{d}{d \ln Q^2} \begin{pmatrix} \Delta \Sigma(Q^2) \\ \Delta G(Q^2) \end{pmatrix} = \frac{\alpha_s(Q^2)}{2\pi} \begin{bmatrix} \Delta P_{qq}^0 & 2f \Delta P_{qG} \\ \Delta P_{Gq} & \Delta P_{GG} \end{bmatrix} \begin{pmatrix} \Delta \Sigma(Q^2) \\ \Delta G(Q^2) \end{pmatrix} \quad (2.71)$$

In the language of QCD, $\Delta \Sigma$ is a *singlet* density that involves the sum of the individual quark helicity densities. If one takes the difference of two quark distributions, gluon terms may cancel, and this *non-singlet* density evolves without gluon mixing,

$$\frac{d}{d \ln Q^2} \Delta q^{NS}(Q^2) = \frac{d}{d \ln Q^2} (\Delta q^i - \Delta q^j)(Q^2), \quad i \neq j; \quad (2.72)$$

$$= \frac{\alpha_s(Q^2)}{2\pi} \Delta P^{NS} \Delta q^{NS}(Q^2). \quad (2.73)$$

The difference of u and d helicity populations in Eq. (2.68) is an important example of a non-singlet density.

As Q^2 becomes large, $\alpha_s(Q)$ approaches zero and the structure functions asymptotically approach fixed values. The simple QPM analyses of Eqs. (2.67), (2.68), and (2.70) apply in this limit. To understand DIS data at finite Q^2 , perturbative QCD corrections to the Γ_1 identities must be applied:

$$\Gamma_1^{p(n)} = \frac{1}{12} \left[+ (-)a_3 + \frac{1}{3}a_8 \right] C_{NS} + \frac{1}{9} [a_0] C_S,$$

where C_S and C_{NS} are the singlet and non-singlet QCD corrections. They are calculated in the modified minimal subtraction scheme to be [71, 72]

$$C_S = 1 - \left(\frac{\alpha_s(Q^2)}{\pi} \right) - 0.5496 \left(\frac{\alpha_s(Q^2)}{\pi} \right)^2 - 4.4473 \left(\frac{\alpha_s(Q^2)}{\pi} \right)^3 + \mathcal{O}(\alpha_s^4), \quad (2.74)$$

$$C_{NS} = 1 - \left(\frac{\alpha_s(Q^2)}{\pi} \right) - 3.5833 \left(\frac{\alpha_s(Q^2)}{\pi} \right)^2 - 20.2153 \left(\frac{\alpha_s(Q^2)}{\pi} \right)^3 + \mathcal{O}(\alpha_s^4). \quad (2.75)$$

The Ellis-Jaffe Sum Rule and the Bjorken Sum Rule predictions are modified by C_{NS} and C_S . The corrections above may be used either to evolve experimental Γ_1 measurements to infinite Q^2 or to express the predictions for the integrals at $\langle Q^2 \rangle$ of a DIS experiment.

2.2.5 Impact of Inclusive DIS Measurements

The measured Γ_1 integrals from past DIS experiments are displayed in Table 2.3. The early SLAC experiments originally measured [52]

$$\Gamma_1^p(\langle Q^2 \rangle \sim 4GeV^2) = 0.17 \pm 0.05,$$

which is consistent with both the Ellis-Jaffe prediction in Eq. (2.70) and with the relativistic quark model prediction. These experiments measured only at $x > 0.1$ and a large uncertainty was assigned to the low x extrapolation. When EMC [3] returned to the Γ_1^p measurement in the late 80s, the asymmetry at low x was significantly smaller than expected, resulting in a total integral of

$$\Gamma_1^p(\langle Q^2 \rangle = 10.7GeV^2) = 0.123 \pm 0.013 \pm 0.019.$$

Experiment	$\Gamma_1 \pm \delta_{\text{stat}} \pm \delta_{\text{sys}}$	Q^2 (GeV ²)	Reference
E80,E130	$\Gamma_1^p = 0.17 \pm 0.05(\text{total})$	4	[51, 52]
EMC	$\Gamma_p^1 = 0.123 \pm 0.013 \pm 0.019$	10.7	[3]
SMC	$\Gamma_p^1 = 0.120 \pm 0.005 \pm 0.015$	10	[50]
E143	$\Gamma_p^1 = 0.133 \pm 0.003 \pm 0.009$	3	[54]
SMC	$\Gamma_d^1 = 0.019 \pm 0.006 \pm 0.013$	10	[50]
E143	$\Gamma_d^1 = 0.047 \pm 0.003 \pm 0.006$	3	[54]
E142	$\Gamma_n^1 = -0.031 \pm 0.006 \pm 0.009$	2	[53]
E154	$\Gamma_n^1 = -0.041 \pm 0.004 \pm 0.006$	5	[57]

Table 2.3: Measured integrals of the proton, neutron and deuteron g_1 structure functions by inclusive DIS experiments.

This result is significantly lower than the Ellis-Jaffe expectation. The surprise result launched numerous theoretical papers discussing its significance and earned such colorful labels as the “spin crisis” [73] and the “Helen of Spin” [65]. The result was the first indication of a serious problem in the view of the nucleon spin structure.

The EMC result also inspired several more experiments to confirm its validity, as listed in Section 2.1.4.3. Violations of the Ellis-Jaffe Sum Rules have now been confirmed on both the proton and neutron. To summarize all world polarized data taken at different Q^2 , a perturbative QCD analysis is required. A recent analysis was performed by SMC [49]. They conclude that

$$\begin{aligned}
 \Gamma_1^p(Q^2 = 5\text{GeV}^2, \text{NLO Fit}) &= 0.121 \pm 0.003(\text{stat}) \pm 0.005(\text{sys}) \pm 0.017(\text{theory}), \\
 \Gamma_1^n(Q^2 = 5\text{GeV}^2, \text{NLO Fit}) &= -0.075 \pm 0.007(\text{stat}) \pm 0.005(\text{sys}) \pm 0.019(\text{theory}),
 \end{aligned}
 \tag{2.76}$$

and for the Bjorken Sum Rule

$$(\Gamma_1^p - \Gamma_1^n)(Q^2 = 5\text{GeV}^2, \text{NLO Fit}) = 0.174 \pm 0.005(\text{stat})_{-0.009}^{+0.011}(\text{sys})_{-0.006}^{+0.021}(\text{theory}).
 \tag{2.77}$$

In the analysis the Bjorken Sum Rule was assumed valid in the separate fits of Γ_1^p and Γ_1^n ; this constraint was removed in fitting the $\Gamma_1^p - \Gamma_1^n$ difference. These can be compared to the QCD corrected Sum Rules at the same Q^2 ,

$$\Gamma_1^p(Q^2 = 5\text{GeV}^2) = 0.1602 \pm 0.004 \quad (\text{Ellis - Jaffe S.R.}) \quad (2.78)$$

$$\Gamma_1^n(Q^2 = 5\text{GeV}^2) = -0.0179 \pm 0.004 \quad (2.79)$$

$$(\Gamma_1^p - \Gamma_1^n)(Q^2 = 5\text{GeV}^2) = 0.178 \pm 0.005 \quad (\text{Bjorken S.R.}) \quad (2.80)$$

One sees that the Ellis-Jaffe Sum Rules on the proton and neutron are violated by over two sigma, while the fundamental Bjorken Sum Rule appears to be confirmed at the present precision of world data.

The breakdown of the Ellis-Jaffe Sum Rule suggests weaknesses in the simple picture of nucleon spin structure assumed by it. Three major trends of the discussion of this subject are summarized below.

2.2.6 Sea Polarization

Implications of the Ellis-Jaffe Sum Rule violation become clearer when the spin fractions are directly evaluated from the polarized DIS data. Using Eqs. (2.62) and (2.2.4), one may derive the quark polarizations implied by the Γ_1 measurements in DIS. Following Ellis and Karliner [65], one gets the following picture of nucleon spin structure:

$$\Delta\Sigma = 0.27 \pm 0.04 \quad (2.81)$$

$$\Delta u + \Delta\bar{u} = 0.82 \pm 0.03 \quad (2.82)$$

$$\Delta d + \Delta\bar{d} = -0.44 \pm 0.03 \quad (2.83)$$

$$\Delta s + \Delta\bar{s} = -0.11 \pm 0.03 \quad (2.84)$$

The deep-inelastic scattering data suggest a surprisingly small fraction of the nucleon spin comes from its quarks: $\Delta\Sigma$ is less than half the expectation in a relativistic quark model. Also, strange quarks are required to have a significantly negative contribution to the nucleon spin,

in contrast to the original $\Delta s + \Delta \bar{s} = 0$ assumption in the Ellis-Jaffe Sum Rule derivation. As nucleons do not have valence strange quarks, this polarization must be dynamically generated in the sea.

An ambiguity in this analysis involves the comparison of quark properties measured in DIS at $Q^2 \rightarrow \infty$ with quarks in low energy effective models. The constituent quarks in Section 2.2.1 have masses of ~ 300 MeV, where current quarks in the QCD Lagrangian have masses ~ 5 MeV. DIS also probes the quark charge squared distribution inside the nucleon, while the hyperon magnetic moments in Eq. (2.53) are proportional to e_q . The observables then have opposite properties under charge conjugation. If one assumes there exists a sea quark contribution to the u and d quark populations in the proton that are charge symmetric with \bar{u} and \bar{d} , $\Delta u_{\text{sea}} = \Delta \bar{u}$ and $\Delta d_{\text{sea}} = \Delta \bar{d}$, then one may define “valence” quarks by subtracting this contribution:

$$\Delta u_{\text{val}} = \Delta u - \Delta \bar{u}, \quad (2.85)$$

$$\Delta d_{\text{val}} = \Delta d - \Delta \bar{d}. \quad (2.86)$$

Constituent quark models then fit valence quark properties under this ansatz. If one further assumes that sea quark contributions are $SU(3)_{\text{flavor}}$ symmetric, $\Delta \bar{u} = \Delta \bar{d} = \Delta s = \Delta \bar{s}$, then the valence quark helicity contributions extracted from (2.84) are

$$\Delta \Sigma_{\text{valence}} = 0.60, \quad (2.87)$$

$$\Delta u_{\text{val}} = 0.93, \quad (2.88)$$

$$\Delta d_{\text{val}} = -0.33. \quad (2.89)$$

which agree well with low energy models. The interpretation is surprising as it suggests strange quarks have a large contribution to the nucleon spin, though they are not included in the naive nucleon wavefunction.

2.2.7 Gluon Polarization

A further complication arises from the QCD axial anomaly [74, 75]. The anomaly allows an effective point-like interaction between a virtual photon and a gluon that survives even as

$Q^2 \rightarrow \infty$. As a result, the total spin of quarks in a nucleon is not actually an *observable* in polarized DIS.

The process is sensitive to a mixture of quark and gluon contributions even at infinite momentum scale [76, 77, 78]. The exact contribution of the gluon interaction to Γ_1 is factorization scheme-dependent. In chiral-invariant schemes, such as the Adler-Bardeen scheme [79], the gluon contribution subtracts directly from the singlet moment,

$$a_0^{AB}(Q^2) = \Delta\Sigma_{\text{inv}} - \frac{3\alpha_s(Q^2)}{2\pi} \Delta G(Q^2). \quad (2.90)$$

This scheme has the advantage that $\Delta\Sigma_{\text{inv}}$ is invariant under evolution, and hence its interpretation as the spin fraction of quarks is independent of momentum scale in DIS.

In gauge-invariant schemes, such as the modified minimal subtraction ($\overline{\text{MS}}$) scheme [80], soft gluon interactions are absorbed into the definition of $\Delta\Sigma$:

$$a_0^{\overline{\text{MS}}}(Q^2) = \Delta\Sigma(Q^2). \quad (2.91)$$

This is the only scheme in which the perturbative QCD corrections beyond NLO have been calculated. In (2.75), the coefficients are valid for the $\overline{\text{MS}}$ scheme and for an evolution invariant singlet axial vector matrix element, $a_0 = a_0(Q^2 = \infty)$.

Results may be converted between the schemes [81] by

$$\Delta q^{MS} = \Delta q^{AB} - \frac{\alpha_s(Q^2)}{2\pi} \Delta G(Q^2). \quad (2.92)$$

In first order perturbative QCD calculations, one can show that $\alpha_s(Q^2)\Delta G(Q^2)$ is a constant and does not evolve in Q^2 . $\alpha_s(Q^2)$ in (2.21) decreases as $\frac{1}{\ln Q^2}$ For increasing Q^2 , implying $\Delta G(Q^2)$ actually grows as $\ln Q^2$ [73]. In order to balance a diverging gluon spin in the proton spin sum, one must assume the parton orbital angular momentum grows with nearly equal magnitude and opposite sign [82].

From Eq. (2.92), the observed violation of the Ellis-Jaffe Sum Rule may originate in a large positive gluon polarization. In this view, the sea polarization of -0.11 in Eq. (2.84) actually corresponds to gluon polarization of $\Delta G(Q^2 = 1\text{GeV}^2) \sim 1.6$ [83].

Note that the valence quarks defined in Eq. (2.86) are also non-singlet observables, and hence they do not receive contributions from the anomaly. The observation that the valence structure of the nucleon is preserved remains valid with gluon polarization.

2.2.8 $SU(3)_{\text{flavor}}$ Symmetry Breaking

Much discussion of the Ellis-Jaffe Sum Rule violation has focused on the $SU(3)_{\text{flavor}}$ symmetry assumption. Corrections for mass differences among hyperons and for recoil effects in the decay are typically not included in the extraction of $\frac{F}{D}$. A reduction of $\frac{F}{D}$ by 20% would reduce the strange sea polarization to zero in the analysis above [84], though the $SU(3)$ corrections are expected to be less than 10% effects [85].

Several models probe the ways $SU(3)$ symmetry might be broken in sea polarization. The basic observation is that this symmetry is not explicitly preserved in QCD. Gluon splitting into sea quarks is a flavor-blind process in perturbative QCD; however, parton distributions develop non-perturbatively in the nucleon. One simple toy model [86, 87, 88] suggests that the polarized strange quark distributions are suppressed relative to the light quark distributions, in the same manner as in the unpolarized case: if $\bar{d}(x) = (1 + \epsilon)\bar{s}(x)$, then $\Delta\bar{d}(x) = (1 + \epsilon)\Delta\bar{s}(x)$. The quark polarizations are $SU(3)$ symmetric in this model, $\frac{\Delta\bar{d}}{d} = \frac{\Delta\bar{u}}{u} = \frac{\Delta\bar{s}}{s} = \frac{\Delta s}{s}$, even though distributions are not symmetric. Assuming valence quarks do obey $SU(3)$ symmetry, the model reproduces both the successes of the constituent quark model and the analysis in the previous sections, except that the strange quarks are no longer required to be strongly polarized.

Other variations of $SU(3)$ breaking abound. Experiments [89, 90, 91] have confirmed an flavor asymmetry in the unpolarized sea $\bar{d} > \bar{u}$. A leading interpretation of this effect involves fluctuations of the nucleon into pion-baryon states that survive over long enough time scales to be observed in deep inelastic processes. Nucleon emission of pseudoscalar mesons (pions and kaons) involves a spin-flip to conserve parity; the models then predict a substantial reduction of the effective valence quark polarization [92, 93]. Groups studying chiral quark models [94] and meson-baryon fluctuation models [95] also predict differences in sea quark and sea antiquark helicity distributions. A study of ρ meson clouds around the nucleon [96] suggests that $\Delta\bar{u}$ may be significantly different from $\Delta\bar{d}$.

2.2.9 Lattice Gauge Theory

While perturbative QCD only predicts the scale evolution of nucleon structure, lattice gauge theory offer a promising avenue to calculating this structure directly. Lattice QCD calculations allow limited but direct determination of the axial vector matrix elements in the non-perturbative regime. The procedure evaluates QCD functional integrals on a lattice of discretely spaced points [97]. While an exact solution may be found on this lattice, the procedure remains computationally intensive, and systematics uncertainties, including the extrapolation to continuous spacetime, must be understood.

	Dong <i>et al.</i> [98]	Fukugita <i>et al.</i> [99]		Göckeler <i>et al.</i> [100]
$\Delta\Sigma$	0.25 ± 0.12	0.18 ± 0.10	Δu_{val}	0.841 ± 0.052
$\Delta u + \Delta \bar{u}$	0.79 ± 0.11	0.638 ± 0.054	Δd_{val}	-0.245 ± 0.015
$\Delta d + \Delta \bar{d}$	-0.42 ± 0.11	0.347 ± 0.046	$x\Delta u_{\text{val}}$	0.198 ± 0.008
$\Delta s + \Delta \bar{s}$	-0.12 ± 0.01	0.109 ± 0.030	$x\Delta d_{\text{val}}$	-0.048 ± 0.003

Table 2.4: Recent calculations in lattice gauge theory of the quark contributions to the nucleon spin. The results of Reference [100] are quoted at a scale $Q^2 \sim 5\text{GeV}^2$.

Several groups have made predictions for the quark spin contributions to the nucleon spin [98, 99, 100] as shown in Table 2.4. These calculations are made in the quenched approximation in which internal quark loops are neglected, and their ability to predict sea effects has been questioned [100]. A direct lattice calculation of ΔG is not yet feasible, but this may become possible in the near future [70].

2.3 Summary

Polarized deep-inelastic lepton scattering provides a window into nucleon spin structure. Previous results from DIS experiments suggest that the simple quark models of the nucleon require significant modification. Valence quark intrinsic spin seems to provide less than half of the nucleon spin while sea quark, gluon, and orbital contributions could be large. This interpretation, however, relies heavily on the combination of DIS data with hyperon β decay constants.

A more direct access of the nucleon spin structure is available in semi-inclusive deep-inelastic scattering. By performing a global analysis of all detected final states in deep-inelastic scattering, one may hope to constrain the different contributions to the nucleon spin with DIS alone. This approach to understanding the “spin puzzle” has been pursued by the HERMES experiment and is the subject of the analysis in this thesis.

Chapter 3

The HERMES Experiment

The HERMES experiment was designed to study the process of deep-inelastic lepton scattering with pure targets. The experiment design was motivated by the important requirements of polarized semi-inclusive DIS studies:

- To maximize the deep-inelastic scattering rate, a DIS experiment needs high beam currents, I , and nucleon target densities, n .
- In polarized physics, one further needs large beam and target polarizations, P_B and P_T , to maximize sensitivity to spin observables. To minimize systematic uncertainties, the relative target and beam spin orientations should alternate frequently, and each polarization should be measured precisely.
- The fraction of unpolarized background material in the beam-target interaction region needs to be minimized. The dilution factor f , which is the ratio of polarized to total nucleons in the target, characterizes this background.
- For inclusive studies, the scattering kinematics should be determined with high precision. Separation of the scattered lepton from background particles is also essential.
- For semi-inclusive studies, the spectrometer should be large enough to accept a variety of multi-particle final states. Identification of the different hadron types in the final states opens further physics possibilities.

The statistical precision of an experiment may be characterized by a relative figure of merit (FOM). In the field of polarized DIS, this figure of merit may be written

$$\text{FOM} = n I t (P_B P_T f)^2 \quad (3.1)$$

where t is the running time of the experiment. Relative statistical uncertainties may scale as $\frac{1}{\sqrt{\text{FOM}}}$; maximizing the figure of merit is then a goal of the experimental design. In addition, reducing systematic uncertainties has equal concern in the experimental process.

This chapter discusses how HERMES is designed to provide precise polarized DIS measurements. The HERMES experiment consists of an internal gas target assembly in place along the East Hall interaction point (IP) of the HERA positron storage ring. Extending 8.5 meters behind the target, a forward acceptance spectrometer captures the high energy particles produced in the gas-positron interaction. This unique design deviates from previous polarized DIS experiments in two notable respects. By using an internal target, the experiment enjoys the advantages of high atomic purity in gas ($f \sim 1$) and of high beam currents available in a storage ring. Previous experiments used fixed solid and liquid targets which are limited by small dilution factors from unpolarized material in and around the target. Difficulties in determining these dilution factors contribute significant systematic uncertainties to results. HERMES is also the first experiment designed to probe semi-inclusive final states in polarized scattering. Previous “first generation” polarized DIS experiments are lacking either the acceptance, the statistics, or the particle identification that is available for these studies with HERMES.

3.1 The HERA Accelerator

HERMES is located in the East Hall of the Deutsches Elektronen Synchrotron (DESY) laboratory in Hamburg, Germany. The lepton beam for the experiment is provided by the Hadronen Elektronen Ring Anlage (HERA) facility. HERA consists of two rings with a stored, counter rotating 820+ GeV protons and 27.5 GeV positrons or electrons. Two beam lines share the same 6.3 kilometer circumference underground tunnel. As schematically depicted in Figure 3-1, experiments study these beams in four halls along the tunnel:

- The *ZEUS* experiment in the South Hall.

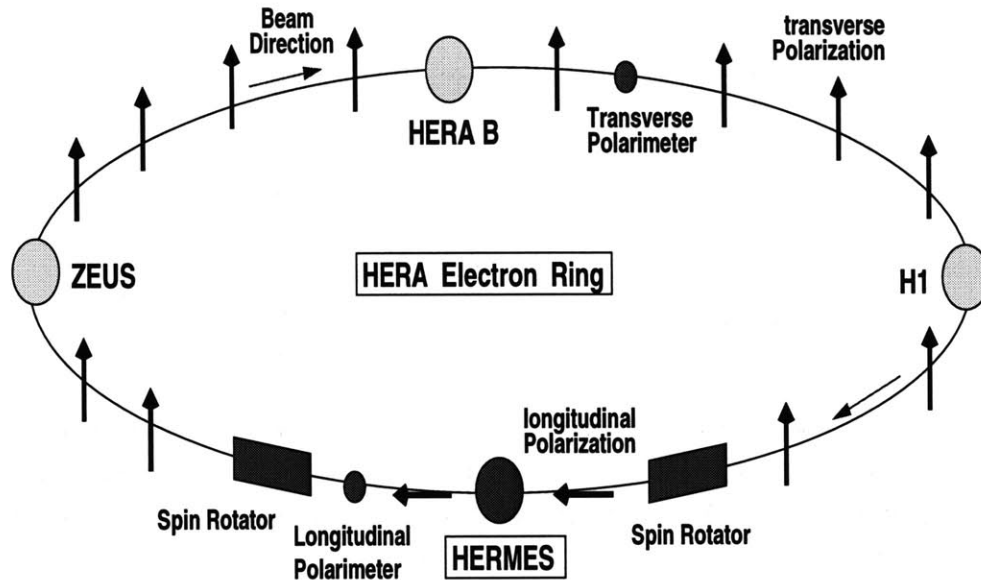


Figure 3-1: A schematic top view of the HERA positron storage ring at DESY. The experiments ZEUS, H1, HERA-B, and HERMES sit in four directions in the ring. The arrows depict the positron beam polarization, which is rotated from the vertical to the longitudinal direction by spin rotators surrounding HERMES. A longitudinal and transverse beam polarimeters measure the polarization on opposite sides of the ring.

- the *H1* experiment in the North Hall surrounds a crossing of the lepton-proton beam with large acceptance. Both experiments study high energy deep-inelastic scattering and photoproduction processes in this configuration.
- *HERA-B* in the West Hall scrapes the halo of the proton beam with target wires. A forward angle spectrometer allows studies of the production and decay characteristics of *B* mesons.
- *HERMES* is located in the East Hall.

Essential characteristics of the HERA beams are listed in Table 3.1. The HERMES experiment is designed to study deep-inelastic scattering with fixed nuclear targets, and is primarily concerned with the lepton beam. The HERA proton beam is not used, and it glides through the experimental area essentially undisturbed. The storage of the HERA lepton beam in the ring allows it to accumulate high currents of over 30 mA, which is large by DIS experiment standards. The ring may store either positrons or electrons, though the positron beam has significantly longer lifetimes than the electron beam. As the negatively charged electron beam

	Positron	Proton
Energy	27.5 GeV	820 GeV
Average Initial Current	36 mA	77 mA
Typical Lifetime	10 h	>100 h
Number of Bunches	189	180
Average Polarization	55 %	-
Polarization Rise Time	22 min	-
Bunch Length	11 mm (37 ps)	
Bunch Spacing	29 m (96 ns)	
Ring Circumference	6336 m	
Duration of Fills	10 h	

Table 3.1: Relevant Parameters of the HERA beams. Typical values of the 1997 running are listed.

tends to attract positively-charged ionized dust into its path, bremsstrahlung losses severely limit the electron beam lifetime. A HERA vacuum upgrade improved the electron beam running recently, but for the running period studied in this thesis, only positrons were used in the ring. The physics processes at HERMES are dominated by single photon exchange, which occurs independently of the sign of the beam charge; corrections from weak effects are tiny. The discussion here will treat positrons though the main physics is identical for the more recent electron running at HERA.

3.1.1 Positron Beam Polarization at HERA

HERA enjoys natural high positron beam polarization transverse to the plane of the ring. An asymmetry in the emission of synchrotron radiation generates the polarization. This effect was first described by Loskutov, Korovina, Sokolov and Ternov [101, 102]. For positrons moving in a plane perpendicular to uniform magnetic field, there exists a small asymmetry in the rate of synchrotron emission between the cases where the positron spin is oriented parallel or anti-parallel to field. The spin-flip to parallel orientation proceeds more rapidly than the spin-flip to the anti-parallel case [103]. Over time, a difference in the two spin populations, N^\uparrow and N^\downarrow , develops, as measured by the polarization:

$$P = \frac{N^\uparrow - N^\downarrow}{N^\uparrow + N^\downarrow} \quad (3.2)$$

Radiation with a spin flip is suppressed by ten orders of magnitude compared to radiation without a spin-flip, causing changes in spin populations that are very slow compared to other processes in the ring.

The resulting spin polarization in the positron beam changes as an exponential.

$$P_B(t) = P_{\max} \cdot (1 - e^{-\frac{t}{\tau_P}}) \quad (3.3)$$

P_{\max} is the equilibrium polarization and τ_P is the rise time constant; the initial polarization $P_B(t=0)$ is assumed to be zero. In an ideal ring with only vertical magnetic fields and without any depolarizing effects, both constants reach their theoretical maximum values, P_{ST} and τ_{ST} :

$$P_{ST} = \frac{8}{5\sqrt{3}} = 92.38\%, \quad (3.4)$$

$$\tau_{ST} = \frac{8}{5\sqrt{3}} \frac{m_e^2 c^2 \rho^3}{e^2 \hbar \gamma^5} = 37 \text{ min.} \quad (3.5)$$

This value of τ_{ST} is calculated for 27.5 GeV/c positrons with the Lorentz factor $\gamma = \frac{E}{m_e c^2} = 53800$ and for an average HERA bending radius $\rho = 707$ m [104].

The dynamics of the spin orientation in the ring can be understood by the Thomas-Bargmann-Michel-Telegdi (Thomas-BMT) equation [105, 106],

$$\frac{d\vec{P}}{ds} = \frac{e\vec{P}}{m_e c \gamma} \times [(1 + a\gamma)\vec{B}_{\perp} + (1 + a)\vec{B}_{\parallel}], \quad (3.6)$$

where \vec{B}_{\perp} and \vec{B}_{\parallel} are the magnetic fields perpendicular and parallel to the positron trajectory, s is the distance along the trajectory, and $a = \frac{g-2}{2}$ is the positron anomalous magnetic moment. The equation may be solved for a periodic, closed orbit solution for the positron polarization direction in the ring. The positron spins precess around this solution, and the number of precessions per orbital revolution is called the spin tune ν .

$$\nu = a\gamma = \frac{E(\text{GeV})}{0.440625}.$$

With 27.5 GeV positrons, ν is 62.5, meaning that the positron spins precess 62.5 times in one revolution around the ring.

The natural rise of the positron beam polarization competes with the depolarizing effects in any real ring facility. The chief source of these effects is again synchrotron radiation emission; radiation emission stochastically produces kicks in the positrons' orbital motions. Magnet imperfections and misalignments also generate slight horizontal and even longitudinal magnetic fields in the ring. When combined with synchrotron emission, a random precession of the positron spins may occur, reducing the polarized fraction.

If the depolarization rate is parameterized by a time constant τ_{depol} , the effective P_{max} and τ_P are modified from the theoretical maximum by the ratio of the Sokolov-Ternov time constant and the depolarization time constant,

$$P_{\text{max}} = P_{ST} \frac{\tau_{\text{depol}}}{\tau_{ST} + \tau_{\text{depol}}}, \quad (3.7)$$

$$\tau_P = \tau_{ST} \frac{\tau_{\text{depol}}}{\tau_{ST} + \tau_{\text{depol}}}. \quad (3.8)$$

Depolarizing effects have been modeled in the SITROS Monte Carlo [107, 108], which tracks an ensemble of classical spin vectors through the storage ring with all synchrotron emission effects. This can yield only approximate understanding of the ring polarization though, as not all imperfections can be precisely known. Empirical optimization of the positron orbit is employed to reduce depolarizing influences. The most important of these techniques is the harmonic bump correction, in which eight closed orbit bumps counteract the influence of perturbing magnetic fields [109]. The magnitude of these orbit corrections must be determined experimentally.

While transverse polarization occurs naturally in the ring, high energy spin physics studies require the lepton beam to be longitudinally polarized. At HERA, a pair spin rotators placed in the ring arcs surrounding the HERMES experiment provide this longitudinal polarization [110]. The rotators are matched such that the rotator before the HERMES IP turns the positron spin into the axis of the beam momentum, and the one behind the IP turns the spin back to the transverse direction for travel around the remainder of ring. Each rotator consists of a collection of six interleaved horizontal and vertical dipole magnets, extending over 56 m.

The effect of these dipoles is depicted in Figure 3-2. From the Thomas-BMT equation in (3.6), the influence on the spin orientation of magnetic fields generating small orbital kicks will be enhanced by $(1 + a\gamma) = 63.5$. Since rotations in space do not commute, a pattern of rotations

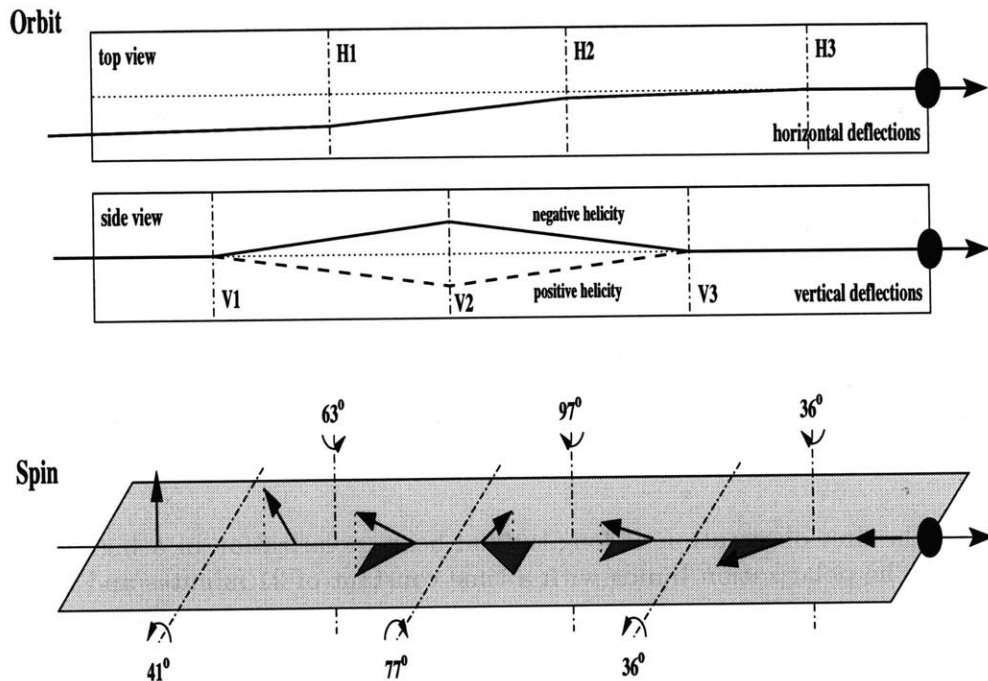


Figure 3-2: A schematic diagram showing the operation principle of one spin rotator. A sequence of vertical and horizontal magnetic fields move the beam orbit (top) and rotate the positron polarization direction (bottom). The sequence is chosen such that the vertical position of the orbit is unchanged by the rotator, but the spin receives a net rotation to the longitudinal direction.

and orbit kicks may be selected that rotates the beam polarization direction while preserving the beam trajectory. Both helicities of the positron beam at the HERMES are possible in this system by changing the sign of the vertical deflections; this involves a physical repositioning of the magnets. HERA is the first high energy positron (or electron) storage ring to achieve longitudinal polarization [111].

Figure 3-3 shows a measured rise of the HERA positron polarization. A 55% maximum polarization and a 20 minute rise constant are typical of the HERA running conditions.

Two laser Compton backscattering polarimeters provide precise measurements of the HERA positron polarization. The details of polarimetry at HERA are discussed in Chapter 4.

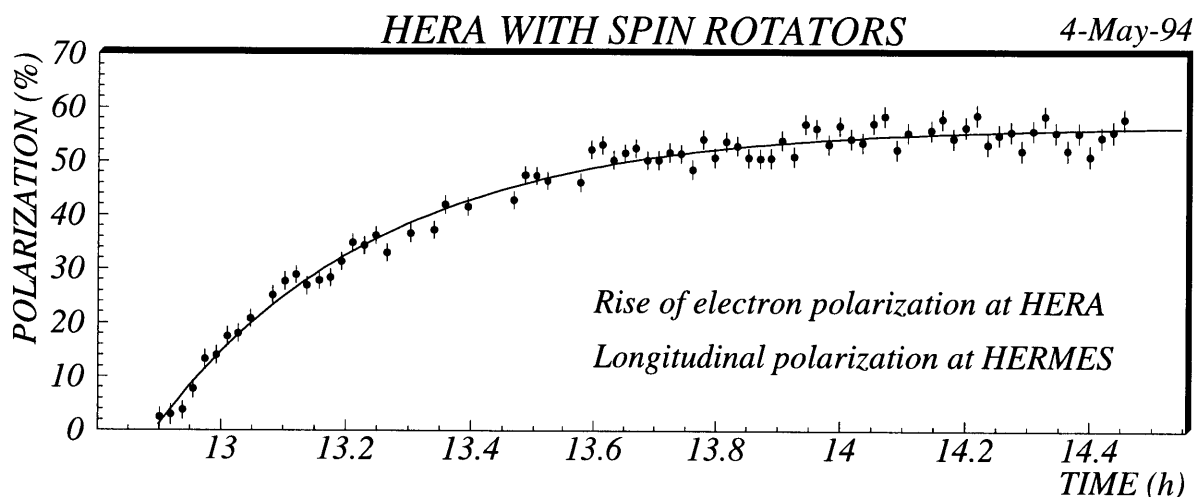


Figure 3-3: The first observation of longitudinal beam polarization in a high energy electron storage ring. The polarization builds with a time constant of 21 minutes and reaches 57%, as shown by the exponential fit.

3.2 The Internal Target

The HERMES target consists of an atomic gas flowing through a cylindrical storage cell contained in the HERA positron beam line. Figure 3-4 shows a diagram of the target region.

The positron beam travels coaxially through the center of the storage cell, interacting with the contained gas. A gas target without windows is clearly required in a storage ring as a beam would not survive a solid or liquid in its path. The ends of the storage cell are open and a differential vacuum pumping system removes the gas on either side. With the five turbomolecular pumps, the ring vacuum of 5×10^{-9} mbar is preserved even though pressures in the target region reach 10^{-6} .

The target storage cell confines the gas atoms near the positron beam; the resulting average density is two orders of magnitude greater than one would get with a free gas jet crossing the beam [112]. A gas target has the added advantage that a single atomic species may be injected into the target without dilution from windows and background material. Target gas atoms are injected into the cell near the center of the active volume. The equilibrium of the injection gases in the center of the cell and the diffusion of the gases near the ends generates a triangular density profile along the beam direction, as shown in Figure 3-5.

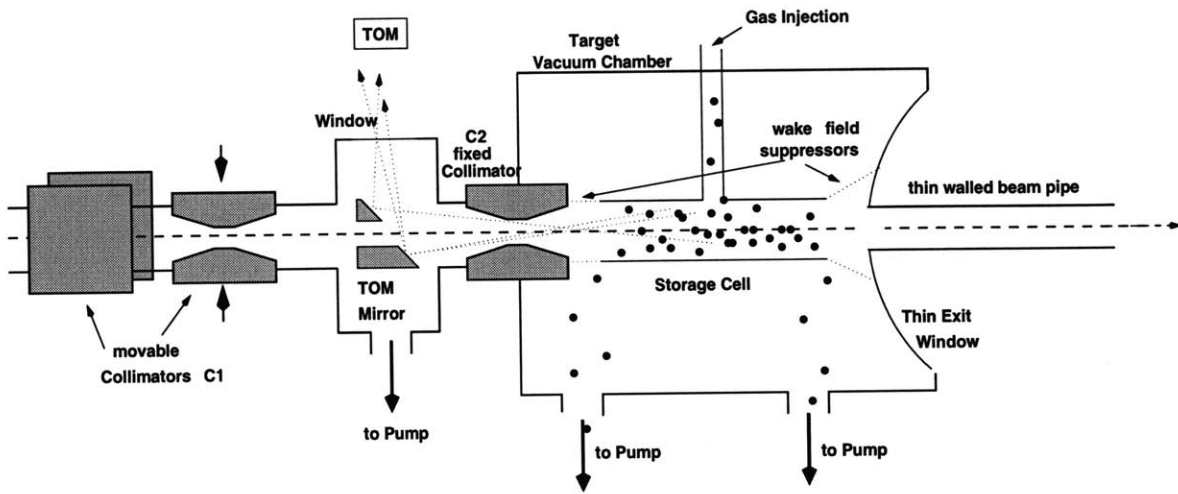


Figure 3-4: A schematic diagram of the HERMES target region

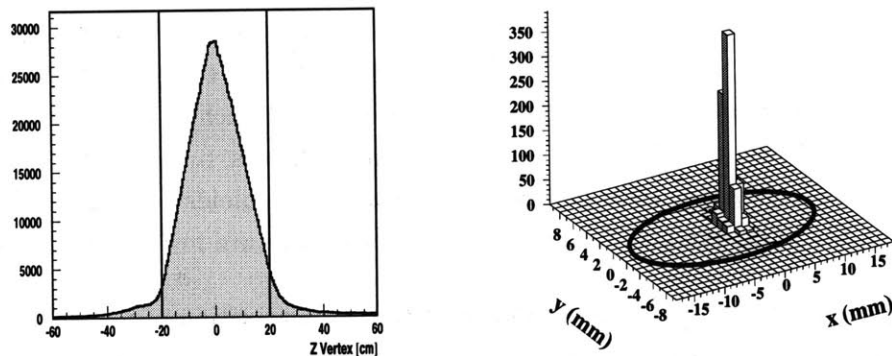


Figure 3-5: Event Distribution in the Target Cell. On the left, the triangular distribution of events along the positron beam direction, z , is shown. The event distribution transverse to the beam direction is shown on the right. The dark ellipse indicates the boundaries of the storage cell.

The target cell is a 550 mm long cylinder with a 29×9.8 mm elliptical cross-section. The cell is fabricated from sheets of about $100 \mu\text{m}$ thick, 99.999% pure aluminum [112] and is cryogenically cooled to the 15-100K range by cold helium gas flowing through the supports. This cooling increases the target gas density by slowing the thermal diffusion of the gases towards the ends of the cell. Surrounding the cell is an aluminum vacuum chamber. Scattered particles from the target enter the spectrometer through a thin (0.3 mm) stainless steel exit window. Thin-walled metal meshes known as wakefield suppressors connect the target cell to the positron beam pipe and ensure the continuity of electromagnetic fields. The target cell, the

	${}^3\text{He}$	${}^1\text{H}$
Ave. Polarization	46%	88% (1997)
Relative Error, $\frac{\Delta P}{P}$	$\pm 5\%$	$\pm 4\%$ (1997)
Thickness, n	10^{15} nucleons/cm ²	$7.6 \cdot 10^{13}$ nucleons/cm ²
Atomic Fraction, α	1.0	0.93 ± 0.04 (1997)
Source intensity	$1 \cdot 10^{17}$ atoms/s	$6 \cdot 10^{16}$ atoms/s
Switching Time	10 min	45 s
Cell temperature	25 K	100 K
Holding field	3.2 mT	335 mT
Cell coating	None	Dri-film, Ice

Table 3.2: A Comparison of parameters of the ${}^3\vec{\text{He}}$ and ${}^1\vec{\text{H}}$ Targets.

wakefield suppressors, and the exit window are all required to be as thin as possible to limit the straggling of particles that pass through them to reach the spectrometer.

Intense synchrotron radiation from the beam may damage the HERMES target cell coatings and may also increase the detector background. A system of two collimators is employed to minimize this background. Collimator (C1) blocks direct synchrotron light from its position 2m upstream of the target. C1 actually consists of two pieces, one horizontally and vertically movable. A fixed collimator (C2) sits next to the cell and shields it from secondary scattered particles from C1. The fixed collimator is the smallest aperture in HERA [113].

Two different technologies create and monitor the polarization of nuclei in the target. The ${}^3\text{He}$ target was originally installed in the 1995 run, and the H-D target has replaced it since 1996. Table 3.2 gives a comparison of the features of these targets.

3.2.1 The ${}^3\text{He}$ Target

The ${}^3\text{He}$ nucleus is interesting as a polarized neutron target; it may be viewed approximately as a spin-polarized neutron with two spin-paired protons providing unpolarized dilution. The ${}^3\text{He}$ target consists of a cubic quartz ‘‘pumping’’ cell illuminated by infrared laser light through which ${}^3\text{He}$ becomes polarized and flows into the storage cell. A schematic diagram of this setup is shown in Figure 3-6. Polarization is achieved through direct optical pumping of the electron energy levels. A weak radio frequency discharge excites a small fraction of the ${}^3\text{He}$ in the pumping cell to the $2{}^3\text{S}_1$ metastable state. Circularly polarized laser light at 1083 nm then induces transitions between the ${}^3\text{S}_1$ and ${}^3\text{P}_0$ energy levels. The excited ${}^3\text{P}_0$ state decays

back to the 3S_1 by the isotropic emission of unpolarized light; the net angular momentum of the laser light remains with the meta-stable atom. Hyperfine interactions may mix the electron and nuclear spins, producing a net polarization in the ^3He nuclei. At this point, if the meta-stable atoms de-excite, the nuclear polarization may not be preserved. But the ^3He atoms may reach a stable ground state through metastability exchange collisions. In collisions between ^3He atoms, the electron clouds of the two atoms may be exchanged. In this way, the small population of metastable atoms may collide and exchange their electrons clouds with the larger population of stable atoms. Stable, polarized ^3He nuclei remain and flow into the storage cell. The quantization axis of the nuclear spin is determined by a slight magnetic field surrounding the target area [114].

The target polarization is flipped by reversing the sign of the circular light polarization. The reversal takes nearly one minute, and one is typically made every ten minutes.

The final target polarization of the ^3He is measured with two techniques. Both techniques measure the circular polarization of light emitted in de-excitation of electronic states. One polarimeter monitors light from the pumping cell polarimeter. This light is detected by a photomultiplier tube after passing through a rotation quarter-wave plate and a linear polarizer. Circularly polarized light creates a sinusoidal signal in the optical system, and its amplitude is proportional to the nuclear polarization. Since the relaxation of nuclear polarization of ^3He is very slow, a measurement in the pumping cell is sufficient to characterize the storage cell polarization.

A Target Optical Monitor (shown in Figure 3-4) directly monitors nuclear polarization in the target cell. Coulomb interactions between the target atoms and the HERA positron beam may excite electronic states. As in the pumping cell, the de-excitation of these states emits circular polarized light tagging the nuclear polarization. A mirror located upstream of the target cell directs this light through a vacuum winder and focusing lens and into a quarter-wave plate/polarizer/phototube assembly analogous to the pumping cell polarimeter [112].

Typical polarizations of the HERMES target reach 50%. The areal target density at HERMES with ^3He is limited to 1×10^{15} nucleons/cm², as in order to minimize the influence of target gas bremsstrahlung on the positron lifetime. Details of the HERMES ^3He Target can be found in Reference [112].

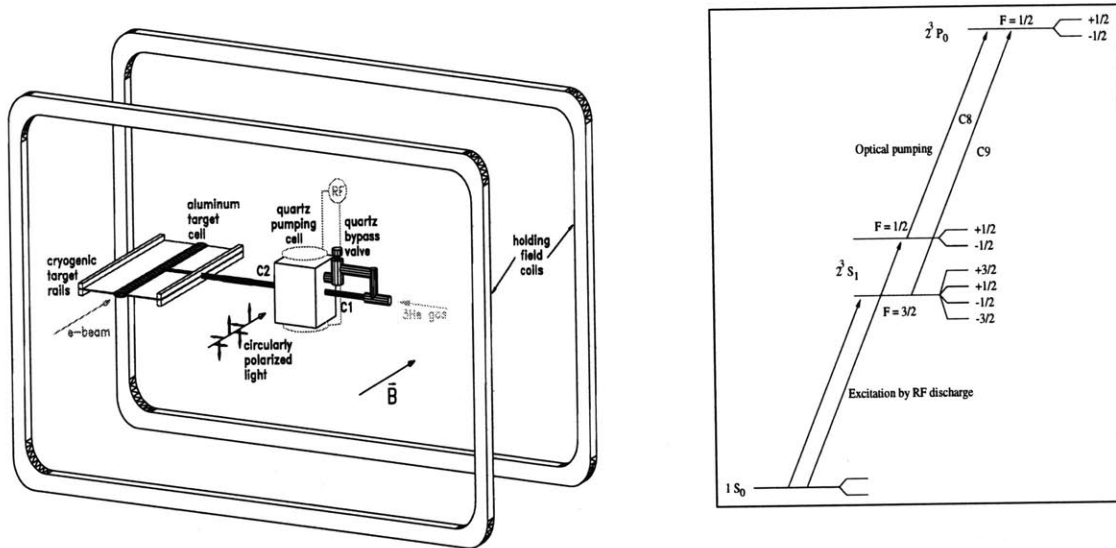


Figure 3-6: Operation of the ^3He Target. On the left is a schematic diagram of the setup. ^3He atoms flow right to left through a polarizing quartz cell and into the target storage cell. The right diagram depicts the electron energy level structure in ^3He . A weak RF radio frequency discharge populates the metastable state 2^3S_1 . Circularly polarized light induces the C8 and C9 transitions between different hyperfine levels and the 2^3P_0 state.

3.2.2 The H-D Target

Since 1996, polarized protons have been injected into the storage cell by an Atomic Beam Source (ABS). Figure 3-7 shows the setup of the ABS and its polarimeter, Breit-Rabi Polarimeter (BRP). In the ABS dissociator, a strong 13.56 MHz radio frequency field separates H_2 molecules into atomic hydrogen. Collimators then form a beam of atomic hydrogen directed toward the target cell. Five sextupole magnets spin polarizes the electrons in the beam atoms, by a Stern-Gerlach separation of electron spin states. High frequency magnetic fields induce adiabatic hyperfine transitions which exchange electron spin polarization for nuclear polarization of either sign. The final set of sextupole magnets focuses the polarized atomic beam into an entrance tube to the storage cell [113]. The target polarization may be reversed as often as every second in this setup. At HERMES, the polarization is flipped more slowly on the minute time scale in order to limit time synchronization problems in the data acquisition.

For the H-D target, a superconducting magnet surrounding the storage cell generates a 0.335 T solenoid field. This field provides a quantization axis for the nuclear spins and also prevents loss of nuclear polarization through further hyperfine interactions. The target cell is also coated

with Drifilm and water. The coatings minimize molecular recombination and randomization of nuclear spins from interactions between atoms and the cell walls. The cell temperature is chosen to be near 100K which maximizes target density while limiting polarization degradation from wall interactions.

To measure the resulting polarization in the cell, the entire polarization procedure reverses in the BRP. A small sample of gas flows from the storage cell into an extraction tube located across the beam axis from the ABS injection tube. The gas sample is spin separated by sextupoles. A beam chopper and quadrupole mass spectrometer measure the resulting atomic signal. Hyperfine transitions before the sextupole may be used to alter the spin state of the beam yielding a different beam flux. Four independent flux measurements may be achieved in this way; from them, the four possible occupations of electron and proton spin states may be determined.

A portion of the extracted gas from the target is also directed to the Target Gas Analyzer (TGA). The TGA uses a mass spectrometer to measure the relative flux of atomic and molecular hydrogen [115].

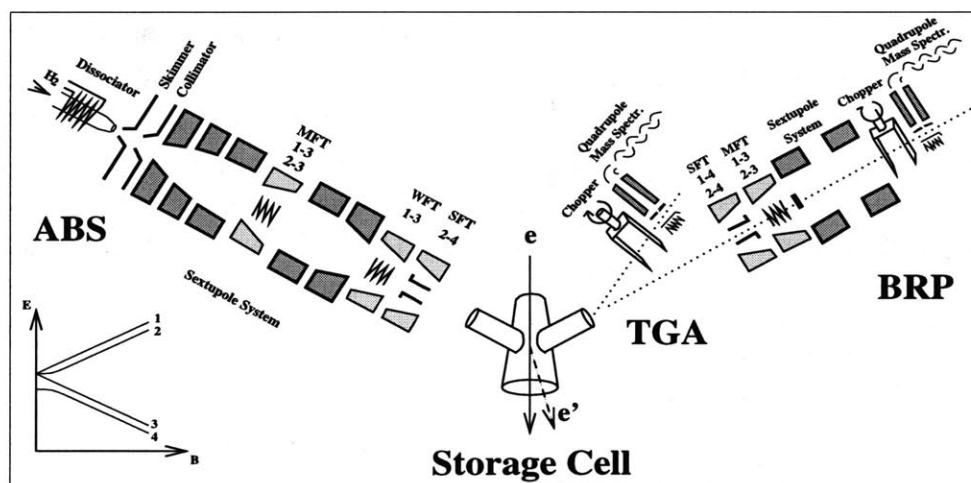


Figure 3-7: A schematic diagram of the H-D target. The Atomic Beam Source (left) dissociates and polarizes ^1H and ^2H atoms. The atoms flow through an injection tube into the storage cell (center). A sampling tube across the cell extracts atoms for study in the BRP polarimeter and TGA mass spectrometer (right).

The polarization of the target is calculated from the expression

$$P_T = \alpha_0(\alpha_r + (1 - \alpha_r)\beta)P_T^{\text{atom}} \quad (3.9)$$

α_0 is the initial fraction of hydrogen atoms leaving the ABS, which approaches 0.99 ± 0.01 . The fraction of undissociated hydrogen entering the target is very small. α_r represents the fraction of atoms that do not recombine to molecules in the storage cell, and β is the nuclear polarization of the recombined molecules relative to the nuclear polarization of the atoms, P_T^{atom} . This molecular polarization is generally unknown, and a significant portion of the target systematic uncertainty is attributed to it.

The TGA and BRP only measure α_r and P_T^{atom} at one sampled position in the cell. These Measurements of the TGA and BRP are combined with extensive Monte Carlo simulations of diffusion and spin relaxation in order to determine the target parameters over the entire cell. In particular, Monte Carlo determined sampling corrections, c_α and c_P relate the BRP and TGA measurements to the cell average values:

$$\alpha_r = c_\alpha \alpha_r^{\text{TGA}} \quad (3.10)$$

$$P_T^{\text{atom}} = c_P P_{\text{BRP}} \quad (3.11)$$

The simulations may be cross checked, by measuring how the HERMES luminosity and physics asymmetries vary with the measured α_r^{TGA} . A constraint for the molecular polarization $0.2 \leq \beta \leq 1.0$ has been obtained in this way [116]. By injecting electron polarized atoms, a large Bhabba scattering asymmetry may be measured in the luminosity monitor (Section 3.3.2.6). The electron polarization is particularly sensitive to dynamic effects in the target cell, and this asymmetry further constrains the simulations [117]. The average areal target density of hydrogen is extracted from the models to be 7.6×10^{13} nucleons/cm². This density is mainly limited by the dissociation flux in the ABS [118]. For 1997, α_r is 0.93 ± 0.04 and P_T^{atom} is typically 0.92 ± 0.03 , leading to an average target polarization of 0.88 ± 0.04 .

In 1998, the ABS switched from polarized hydrogen to polarized deuterium running; however, the principles of operation remain the same.

3.2.3 The Unpolarized Gas Feed System

In addition to polarized gases, HERMES has the option of flowing unpolarized gases into the storage cell with a direct gas feed. Scattering from unpolarized H₂, D₂, ³He, and N₂ molecules has been investigated with this system. While data with these targets are not studied here,

unpolarized data taking does allow detailed study of unpolarized model assumptions used in the polarized analysis. Unpolarized observables are not suppressed in the cross-section by the polarization factors (e.g. beam, target, and virtual photon) limiting polarized investigations. For hydrogen and deuterium, dense gases of the order 10^{15} nucleons/cm² may be achieved with the gas feed.

3.3 The Spectrometer

The large angular acceptance of the HERMES spectrometer was designed for a precision measurement of deep-inelastic scattering products over a large kinematic range. The spectrometer consists of two main systems of detectors. In the tracking system, drift and microstrip gas chambers are positioned before and after a spectrometer magnet. The chambers identify the scattering angles and trajectories of charged particles, and the bending of the tracks in the magnetic field constrains their momenta. The particle identification system consists of detectors employing a variety of technologies to separate electron and positron tracks from charged hadrons. Pion identification is provided by a Čerenkov counter. Details of these detectors can be found in Reference [58].

The electron and proton beam lines pass through the center of the spectrometer, separated horizontally by 72 cm. For this reason, most of the spectrometer components are implemented in two pieces, one above and one below the beam plane. A side view of the detector is shown in Figure 3-8.

The entire experiment including the target is supported by a movable platform. By moving the apparatus out of the beam line, HERMES may receive major repairs or upgrades without disturbing the collider operation, and HERA service vehicles may cross the tunnel in the East Hall.

3.3.1 The Tracking System

Tracking at HERMES may be divided into the front region, the magnet region, and back region. In the front region, a series of detectors extends from the thin target exit window to the spectrometer magnet. These chambers include the Vertex Chambers, the Drift Vertex

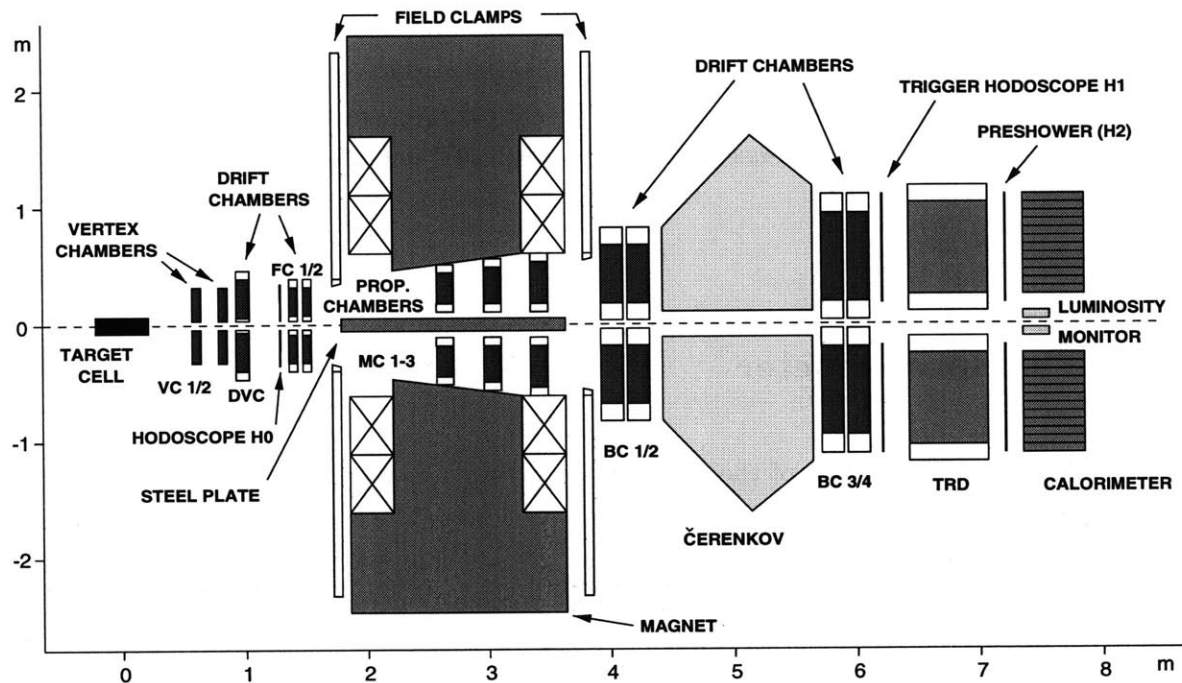


Figure 3-8: Diagram of the HERMES Spectrometer.

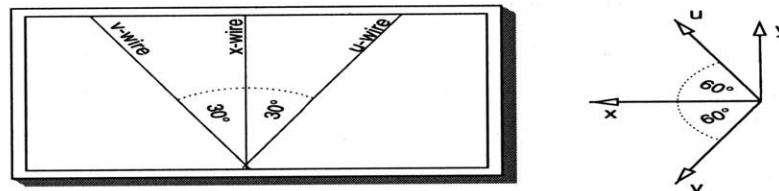


Figure 3-9: The orientation of the U, V, and X planes in the tracking system.

Chambers, and the Front Chambers. The front tracking detectors combine to measure the kinematic scattering angles of charged tracks leaving the target. They are also important for identifying whether a track originates in the target gas or background material surrounding the target. A spectrometer magnet sits behind these front chambers centered 2.75 m from the target. This magnet bends the charged tracks in the horizontal plane. Inside the magnet are placed Magnet Chambers, which help to constrain this bending directly. Behind the magnet, the Back Chambers measure the deflected trajectories. This rear tracking not only determines the track momenta, but it also localizes each trajectory inside the particle identification detectors.

For ease in reconstruction, three axes of wires were defined for all chambers. Vertical wires measure the X position, while wires rotated 30° clockwise or counter-clockwise define U and V

	Vertex		Drift Vertex	Front		Magnet			Back	
Detector	VC1	VC2	DVC	FC1	FC2	MC1	MC2	MC3	BC1/2	BC3/4
Design	micro-strip gas		horizontal-drift	horizontal-drift		proportional			horizontal-drift	
Distance (mm) from Target	731	965	1100	1530	1650	2725	3047	3369	4055	5800
Chamber gas	DME/Ne		Ar/CO ₂ /CF ₄	Ar/CO ₂ /CF ₄		Ar/CO ₂ /CF ₄			Ar/CO ₂ /CF ₄	
Gas Composition (%)	60:40		90:5:5	90:5:5		65:5:30			90:5:5	
Num. of modules (In each half)	1	1	1	1	1	1	1	1	2	2
Rad. length/module	0.8%		0.25%	0.075%		0.29%			0.26%	
Module Config.	VUX	XVU	XX'UU'VV'	UU'XX'VV'		UVX			UU'XX'VV'	
Wires per X Plane	1674	2046	80	96	96	496	608	720	128	192
Wires per U,V Plane	2170	2170	96	96	96	512	608	720	128	192
Active Area										
Horizontal (mm)	323	393	474	680	680	996	1210	1424	1888	2890
Vertical (mm)	137	137	290	180	180	263	306	347	520	710
Resolution/plane	65 μm		220 μm	225 μm		700 μm			275 μm	300 μm

Table 3.3: A listing of relevant parameters of the tracking chambers.

planes, as shown in Figure 3-9. This configuration has maximum tracking redundancy in the X plane, in which the magnet deflects the charged particles.

The relative positioning of the chambers in the spectrometer is determined by optical measurements. Taking data with the spectrometer magnet field off allows fine tuning of this positioning by requiring the hits to reproduce straight particle trajectories. A laser alignment system monitors the chamber positions precisely and online, by recording a changes in the diffraction pattern of laser light from a perforated target attached to each detector frame.

The entire system accepts scattered particles in an angular range of $40 \leq \theta_y \leq 140$ mrad and $-170 \leq \theta_x \leq 170$ mrad. A summary of the tracking detector properties is given in Table 3.3.

3.3.1.1 The Vertex Chambers

The first chambers encountered by a track leaving the target are the Vertex Chambers (VC). These detectors must precisely determine the scattering angles of particles in the target under the duress of large backgrounds and tight spatial constraints. For this task, they employ microstrip gas chamber technology. Each VC plane consists of planar cathode foil separated

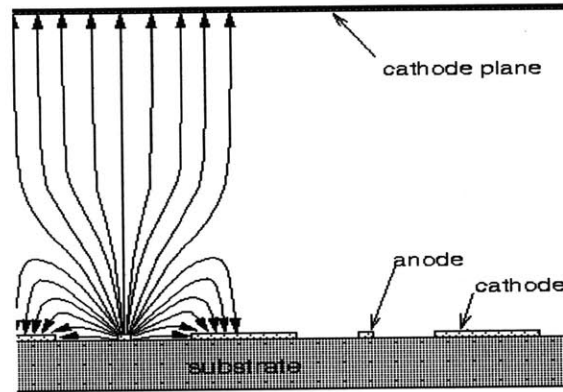


Figure 3-10: A diagram of a drift cell in the Microstrip Gas Counter, showing electric field lines [119].

by 3mm from a thick glass substrate. Etched on the substrate are alternating aluminum $7\ \mu\text{m}$ anode lines and $85\ \mu\text{m}$ cathode strips, as shown in Figure 3-10. The cathode plane and strips are maintained at 1800 and 580 V. The chamber is filled with a DiMethylEther (DME)/Ne gas mixture to achieve high gas gain. About $65\ \mu\text{m}$ spatial resolutions are obtained with this technique. The VC planes on each half of the detector are group into two modules (VC1 and VC2) of three planes each.

In 1995, the chambers suffered low efficiencies due to problems in the electronics readout, and only one half of the detector operated throughout 1996. Hence, the VCs have only been used for the track reconstruction since the 1997 running.

3.3.1.2 The Drift Vertex and Front Chambers

Two Front Chambers (FC1 and FC2) back up to the spectrometer magnet, while the Drift Vertex Chambers lie in between the VCs and FCs. Both sets of conventional horizontal drift chambers improve tracking resolution before the magnet. Each drift chamber consists of six planes of interlaced anode and cathode wires separated by cathode planes. The drift cell size is 7 mm in the FCs, 6mm in the DVCs. The orientations of the planes are paired (UU', XX', and VV'), and the second plane of each pair is offset by 3.5 mm from the first to resolve position ambiguities.

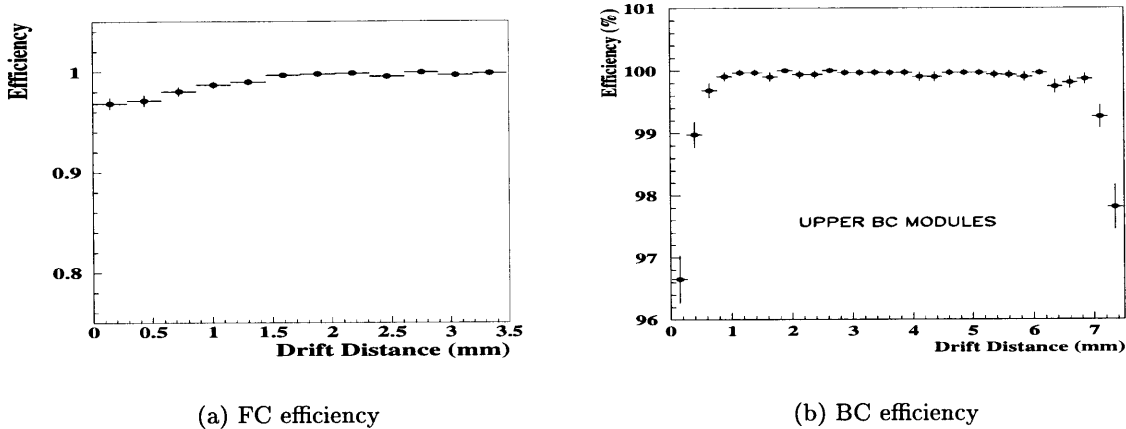


Figure 3-11: Efficiencies for planes in the front and back chambers as a function of drift distance.

With difficulties in the VCs, the experiment relied on the FCs alone throughout most of 1995 and 1996. The DVCs were proposed in 1995 and commissioned in 1997 to provide redundancy in front chamber tracking [120].

3.3.1.3 The Spectrometer Magnet

The HERMES dipole magnet produces an integrated field of 1.3 T·m in the center of the spectrometer. The variation in this deflecting power is under 10% within the acceptance. An iron plate and a correction coil prevent this field from influencing the positron and proton beam lines passing through the spectrometer. A gap in the magnet between the poles provides an entrance for charged particles to the rear of the spectrometer, effectively defining the angular acceptance of the spectrometer. Field clamps in front and in back of the magnet keep the fringe fields in the adjacent drift chambers below 0.1 T.

3.3.1.4 The Magnet Chambers

Three multiwire proportional chambers (MC1, MC2, and MC3) sit in the gap of the spectrometer magnet on either side of the iron plate. These chambers were originally designed to simplify the comparison of front and back region chamber information by pinning particle trajectories

inside the magnet. In practice, the reconstruction of high energies proceeds well without the magnet chambers. They remain useful, though, for detecting very low energy tracks that deflect out of the HERMES acceptance before passing through the back region.

Each chamber consists of three planes in the U, X, and V orientations. Anode wires 2 mm apart and at ground potential are layered with two cathode planes in each module. Resolutions of 577 μm are achieved in this setup.

3.3.1.5 The Back Chambers

The final tracking chambers, the Back Chambers (BC1/2 and BC3/4), constrain the path of charged particles behind the magnetic field. These horizontal drift chambers employ a design nearly identical to the FCs, except that a larger drift cell of 15mm is used. The chambers cover an area significantly larger than the FCs, and care in the BC design is placed on a prestressed frame which maintains the stability of the wires and foils. Each Back Chamber consists of two modules each containing six planes. A total of 24 BC planes in either half of the detector are active. Two sets of modules are separated by the Čerenkov, giving a better lever arm on particle trajectories. The Back Chambers are documented in detail in Reference [121].

3.3.1.6 Performance of the Tracking System

A description of the interpolation of particle trajectories from chamber hits is given in Section 5.1.3. Overall this tracking design yields a momentum resolution near 1% over the HERMES kinematic range. The scattering angle resolution remains below 0.6 mrad. In terms of DIS kinematics, the x and Q^2 of events may be determined from the scattered positron with accuracies of 4-8% and 2% respectively.

3.3.2 The Particle Identification Detectors

The study of deep-inelastic scattering requires the identification of scattered leptons and coincident charged hadrons. Four particle identification (PID) detectors accomplish this at HERMES: a Čerenkov counter, a transition radiation detector, a preshower detector consisting of a lead

curtain and a plastic scintillator hodoscope, and an electromagnetic calorimeter. Each detector responds to positrons and hadrons differently, allowing a distinction to be made. The detectors are located in the back region of the spectrometer, and they have poorer spatial resolution than the tracking detectors. Trajectories determined from Back Chamber information help assign detector responses to tracks. Details of the PID system are discussed in Reference [122].

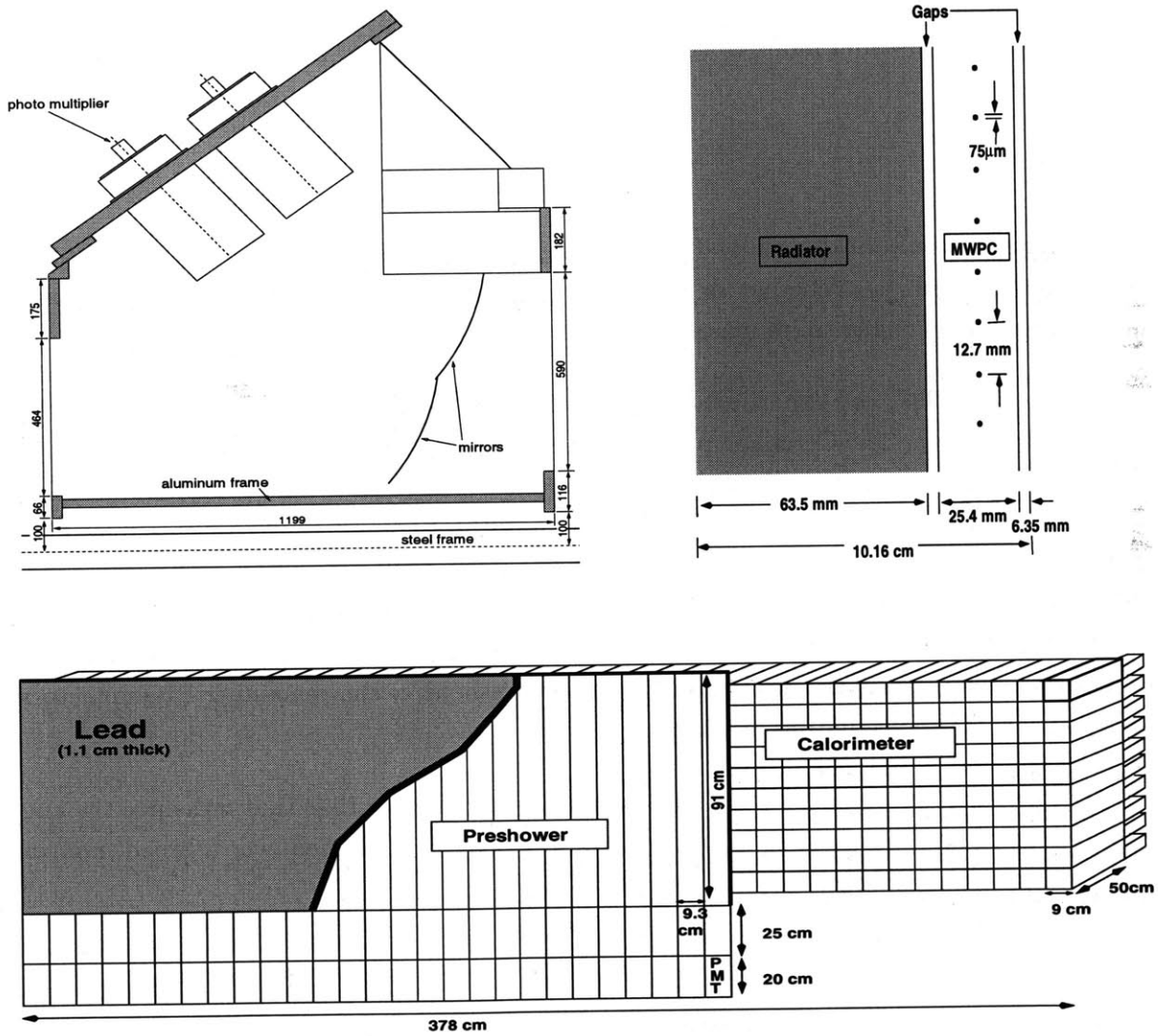


Figure 3-12: Schematics of the four particle identification detectors. Shown are the Čerenkov (top left), the Transition Radiation Detector (top right), and the Preshower and Calorimeter (bottom).

3.3.2.1 The Čerenkov Counter

The HERMES Threshold Čerenkov Counter relied on difference in the Čerenkov radiation to identify charge particles. When a particle traverses a medium with a velocity, faster than the phase velocity of light in that medium, the particle will radiate light. The radiation is an electromagnetic analogy of shock waves formed by “breaking” the speed of sound. For a particle velocity β and a medium index of refraction n , the threshold for radiation occurs when

$$\beta > \frac{1}{n}.$$

For a given momentum determined by tracking, lighter mass particles have larger velocities, which may exceed $\frac{1}{n}$. Whether or not a charge particle radiates in a Čerenkov at a given momentum yields a clue to its mass and identity.

From 1995-1997, the experiment incorporated a threshold Čerenkov counter operating on the above principle. The Čerenkov placed a 1.17 m deep volume of mixed nitrogen and C_4F_{10} in the path of charged particles. A system of 20 spherical mirrors at the back of the volume focused Čerenkov light on 20 matching phototubes, as shown in Figure 3-12. In 1995, a pure nitrogen gas radiator yielded π , K , and p momentum thresholds 5.6, 19.8, and 37.6 GeV respectively. In 1996 with 70:30 $N_2:C_4F_{10}$, these were lowered to 3.8, 13.6 and 25.8 GeV. The detector cleanly identified electrons and positrons for momenta up to the pion threshold. Pions may be cleanly identified between their threshold and the kaon threshold, if the remaining PID detectors are used to separate the radiating positrons.

A Ring-Imaging Čerenkov (RICH) detector was installed in 1998 that measures the angular correlations of the light. Pions, kaons, and protons may be identified over a broad momentum range using this technique.

3.3.2.2 The Transition Radiation Detector

Transition radiation forms when a relativistic charged particle crosses a boundary between mediums of different dielectric constants ϵ . The mean energy of the emitted radiation scales with $\gamma = \sqrt{\frac{1}{1-\beta^2}}$. A 5 GeV positron has a γ of 10^4 and may radiate X-rays in the keV range;

a 5 GeV pion has a γ of only 36. Hence, the detection of high energy X-rays from transition radiation provides a clean identification of positrons among charged particles.

The HERMES Transition Radiation Detector (TRD) consists of six modules above and below the beam plane. Each module places a radiator in front of a multi-wire proportional chamber (MWPC), as shown in Figure 3-12. The radiator is formed from layers of loosely packed array of polyethylene/polypropylene fibres. Each fiber is 17-20 μm thick, and total radiator thickness is 6.35 cm. To a charged particle crossing the radiator, the fibers appear to be a random array of many dielectric transitions between air and fiber; copious transition radiation results.

The MWPC has conventional design of a plane 256 vertical anode wires 1.27 cm apart between two cathode foil sheets. The chamber volume is filled with 90% Xe and 10% CH_4 gas; this mixture exploits the efficient X-ray absorption of Xenon. Xenon avalanches under high fields may emit photons that cause secondary avalanches. The quench gas CH_4 serves to absorb these secondary photons by exciting vibrational or rotational energy levels.

All charged particles deposit energy in the TRD modules by gas ionization. The key to identifying positrons is to detect the additional transition radiation signal.

3.3.2.3 The Hodoscopes

Two hodoscopes (H1 and H2) are installed in the HERMES back region in each half of the detector to assist in triggering and particle identification. The hodoscopes each have 42 9.3 cm wide, vertical plastic scintillator paddles. The paddles are staggered and overlap each other by 1.5 mm in order to avoid acceptance gaps. In H2, each paddle is aligned with a corresponding column of lead-glass blocks in the calorimeter, as shown in Figure 3-12. Both hodoscopes form a critical part of the HERMES trigger, and they may also be used to identify the mass of low-energy particles by time-of-flight techniques.

H2 also serves as a preshower detector for high energy particle identification. The hodoscope sits behind 11 mm of lead surrounded by 1.3 mm steel sheets. Positrons passing through the lead radiator may initiate electromagnetic showers that deposit energy in the scintillator while hadrons produce only a minimum ionizing signal in the scintillator. Positrons are then separated from hadrons by their energy deposition.

A front region trigger hodoscope (H0) was installed in 1996 before the Front Chambers in both halves of the detector. Each consists of a 3.2 mm thick single sheet of plastic scintillator.

3.3.2.4 The Calorimeter

The electromagnetic calorimeter in the rear of the spectrometer is a key component both in the trigger and in the particle identification. The calorimeter consists of a 42×10 array of $9 \times 9 \times 50$ cm blocks in each half of the detector. The blocks use F101 lead-glass, which is selected for its radiation resistance, and they are polished and wrapped by foil to provide light insulation. Each block is coupled to photomultiplier tube by silicone glue. During injection of the HERA, harsh radiation near the beam may damage the lead-glass. The both halves of the calorimeter are therefore mounted on a movable frame, which can retract the walls 50cm vertically until stable beam is available.

Charged particle identification in the calorimeter relies on a difference in energy deposition between positrons and heavier particles. The 50cm depth of the lead-glass corresponds to about 18 radiation lengths. Hence, a positron striking the lead-glass blocks deposits nearly all of its energy inside. Hadronic energy loss is dominated by the nuclear interaction length, which is significantly longer than the radiation length. Less of a hadron's total energy is lost inside the 50 cm block. Tracks from the Back Chambers may be extrapolated to match energy clusters in the calorimeter. For charged tracks, one may compare the total deposited energy (in both the calorimeter and preshower), E , to the track momentum, p . One expects $\frac{E}{p} \sim 1$ for positrons but $\frac{E}{p} \ll 1$ for hadrons.

The calorimeter is also useful for photon and π^0 decay identification; one may assume that clusters without an associated track originate in neutrals. Details of the calorimeter performance are given in Reference [123].

3.3.2.5 Performance of the PID system

The analysis of the PID detector responses is discussed in Section 5.3.1. Overall, the combination of the four detectors allows identification of leading positrons with hadron contamination less than 1% over the HERMES kinematic range.

3.3.2.6 The Luminosity Monitor

The luminosity monitor at HERMES consists of two calorimeters flanking the beam pipe in the horizontal plane, 7.2 m downstream of the target cell. The calorimeters are particularly sensitive to Bhabba scattering ($e^+e^- \rightarrow e^+e^-$) and annihilation interactions ($e^+e^- \rightarrow \gamma\gamma$) between beam positrons and target electrons. The rates of both processes are known precisely in Quantum Electrodynamics. They may be used to monitor the relative luminosity at the experiment and to normalize the rates of all other detected events. The calorimeters consist of 3×4 array of $22 \times 22 \times 200$ mm³ NaBi(WO₄)₂ Čerenkov crystals, each connected to a photomultiplier. Bhabba and annihilation events may be separated from beam background by requiring coincident high energy clusters in each calorimeter. As in the case of the electromagnetic calorimeter wall, the lumi monitors are moved 20 cm horizontally away from the beam pipe during injection.

3.3.3 The Gain Monitoring System

The gain stability of photomultiplier in the experiment is checked online with a standard source of light. The light of a dye laser at 500 nm is split into glass fibers leading to each PMT and to a reference photodiode. The PMT responses to different light intensities are monitored to determine relative gain differences over time.

3.3.4 The Trigger

The trigger system of HERMES makes a fast decision of which signals in the detector are interesting for physics analysis. These events are selected from the background with high efficiency and are recorded by the data acquisition. A first-level trigger is implemented in readout electronics and in programmable logic units(PLU). Higher-level triggers using digital signal processors have been studied in detail, but have not yet been necessary for reducing online data-taking rates.

Different triggers are used for the different physics studied at HERMES. DIS event candidates are selected by the following criteria:

- A high energy cluster must be found in the calorimeter. Large energy depositions likely come from scattered positrons. The calorimeter energy threshold was set to 3.5 GeV in 1995, which corresponds to $y < 0.85$ for DIS events. In 1996, the threshold was lowered to 1.4 GeV in order to accept higher y events.
- A preshower (H2) signal above the minimum ionizing level must be detected. This further suppresses hadron tracks.
- H0, H1 and H2 signals must be present in the event. This condition suppresses showers from photons, which may still produce large signals in preshower and calorimeter.
- The signals in the hodoscopes must be time-ordered. The relative timing of hodoscope signals should correspond to a relativistic positron traveling from target to calorimeter and striking each hodoscope in sequence. This timing is also compared to the HERA beam clock, which identifies the time windows in which the positron bunches pass through the target. These conditions suppress proton beam background, which typically traverses the detector in a direction opposite the positron signal, calorimeter to target. The H0 detector was installed in 1996 in the front region in order to provide a larger timing separation of protons than is available in H1 and H2 alone.

Another important trigger also selects photoproduction events, in which a positron scatters almost directly forward into the beam pipe. In this case, two track events are efficiently identified by requiring hits in the top and bottom detector hodoscopes and back chambers.

The trigger electronics determine if an event is usable within 400 ns of the positron bunch passing. A data acquisition (DAQ) consisting of Fastbus crates connected to a DEC Alpha workstation cluster collects TDC (Time to Digital Converters) and ADC (Analog to Digital Converters) from each detector. The system collected triggered events at a rate of 150 Hz to 300 Hz, increasing as the workstations were upgraded.

Chapter 4

Polarimetry at HERA

The Transverse and Longitudinal Polarimeters at HERA provide accurate measurements of the positron beam polarization. The requirements of a polarimetry at HERA are challenging. Any study of the ring should be non-invasive and proceed without any noticeable effect on the stored positrons. The equipment of the polarimeter should be compact, so that it fits into the HERA tunnel. The device needs to be insensitive to the frequent changes in the positron orbit, or at least it should adjust to such changes quickly. As the beam polarization may rise or fall with time constants of minutes, a measurement of the polarization with an accuracy of a few percent should be possible on this time scale. Finally, the systematic uncertainty of polarized experiments is typically limited by polarimetry. HERMES is no exception: beam polarimetry uncertainties produce the second largest systematic uncertainty in the experiment.

This chapter reviews the techniques of polarimetry at HERA with particular emphasis on the Transverse Polarimeter (TPOL). The Transverse Polarimeter was first operated in 1991. Over the next few years, the device firmly established the presence of high positron polarization in HERA, which was an important precondition for HERMES. It was subsequently used to study maximization of the HERA polarization. In 1995, HERMES began data taking on polarized targets, and constant, reliable measurement of the beam polarization was required. However, the TPOL measurement was limited by instabilities causing a low data taking efficiency and by a large normalization uncertainty of over 9%. To solve these problems, a Longitudinal Polarimeter was commissioned in 1996 to provide a complementary measurement. In addition, manpower was assigned to solve problems in the Transverse Polarimeter operation. The author was chiefly involved in the second phase of this project. This chapter reviews the polarimeter principles and design and discusses its operation as a precise instrument.

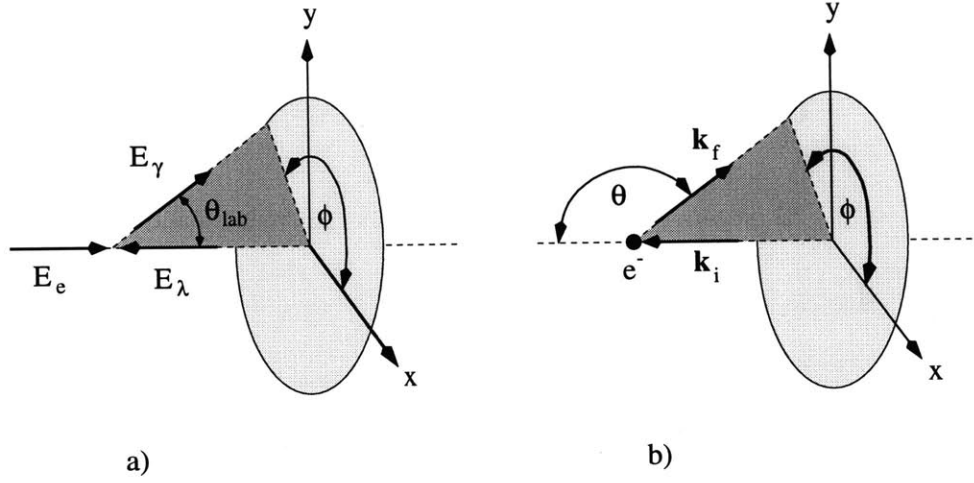


Figure 4-1: A diagram of the kinematic relationships in Compton scattering for a) the laboratory frame and b) the positron rest frame.

4.1 Polarized Compton Scattering

In contrast to nucleon studies in which the cross-section depends on structure functions that are nearly incalculable in QCD, Compton scattering is one of the best understood processes in the Standard Model. By investigating the dependence of the cross-section on polarization in detail, the positron polarization may be extracted from this interaction. The leading order differential Compton cross-section may be evaluated in the rest frame of the positron as [124]

$$\frac{d\sigma_c}{d\Omega}(\vec{S}, \vec{P}) = \Sigma_0 + \Sigma_1(S_1) + \Sigma_2(S_3, \vec{P}), \quad (4.1)$$

where the terms are

$$\begin{aligned} \Sigma_0 &= \frac{e^2 k_f^2}{2m_e k_i^2} [(1 + \cos^2 \theta) + (k_i - k_f)(1 - \cos \theta)], \\ \Sigma_1(S_1) &= \frac{e^2 k_f^2}{2m_e k_i^2} S_1(\phi) \sin^2 \theta, \\ \Sigma_2(S_3, \vec{P}) &= -\frac{e^2 k_f^2}{2m_e k_i^2} S_3(1 - \cos \theta)(\vec{k}_i \cos \theta + \vec{k}_f) \cdot \vec{P}. \end{aligned} \quad (4.2)$$

The terms Σ_0 , Σ_1 , and Σ_2 represent cross-section contributions from unpolarized, linearly polarized, and circularly polarized light, respectively. Figure 4-1 shows the kinematics of Compton scattering for this discussion. k_i and k_f are the wavenumbers of the incoming and outgoing photons:

$$k_i = \frac{2\gamma E_\lambda}{m_e}, \quad (4.3)$$

$$k_f = \frac{1}{1 - \cos \theta + \frac{1}{k_i}}, \quad (4.4)$$

where E_λ is the laboratory frame photon energy and $c=1$.

The polarization vector of the positrons is $\vec{\mathbf{P}} = (P_X, P_Y, P_Z)$. Here, the beam momentum points along the +z axis, the +x axis points into the center of the ring, and the +y axis is normal to the HERA ring in the direction of the positron beam dipole fields. It is the P_Y component, which develops naturally in an ideal ring (see Section 3.1.1), that one seeks to measure.

The polarization of the photons is represented by a Stokes vector, $\vec{\mathbf{S}} = (S_0, S_1, S_2, S_3)$. The components relate to the orthogonal components of the electric fields, E_1 and E_2 with a phase difference δ between them. One may fix a normalization of $\vec{\mathbf{S}}$ by $S_0 = 1$. The linear polarization of the photons has a magnitude $S_{\text{lin}} = \sqrt{S_1^2 + S_2^2}$, and the circular polarization has a magnitude $|S_3|$. The sign of S_3 indicates the photon helicity: by convention, right handed photons have $S_3 < 0$ and left handed photons have $S_3 > 0$. The linear and circular polarization are part of the total polarization of the light:

$$P_\gamma = \sqrt{S_{\text{lin}}^2 + S_3^2}. \quad (4.5)$$

For laser sources, $P_\gamma = 1$ typically. $S_1(\phi)$ projects the linear polarization of the light onto the rest frame scattering plane defined by $\vec{\mathbf{k}}_i$ and $\vec{\mathbf{k}}_f$. If ϕ is the azimuthal scattering angle and ϕ_{lin} is the angle between the photon polarization and the positron polarization (y-axis), then

$$S_1(\phi) = S_{\text{lin}} \cos 2(\phi_{\text{lin}} - \phi). \quad (4.6)$$

A few calculations of the Compton scattering relations demonstrate their use at HERA. With the Transverse Polarimeter, circularly polarized green laser light ($E_\gamma = 2.41$ eV) shines on the positron beam with a crossing angle of only 3.1 mrad. In the rest frame of the $E_e = 27.5$ GeV positrons with $\gamma = 54000$, the initial photons have a boosted energy of 260 keV, corresponding to $k_i=0.5$. The photons scatter in all directions in the rest frame; but when boosted back to the laboratory frame they appear highly collimated into a cone around the original positron momentum. A photon scattering at $\theta = \frac{\pi}{2}$ will have an angle $\theta_{\text{lab}} = \gamma^{-1} = 19\mu\text{rad}$ and energy $E_\gamma=9.3$ GeV. The lab frame scattered photon energy, E_γ , may be derived from Eq. (4.4):

$$E_\gamma = E_e \frac{1 - \cos \theta}{1 - \cos \theta + \frac{1}{k_i}} \quad (4.7)$$

The maximum photon energy allowed is 13.85 GeV, and this corresponds to backwards scattering, $\theta = \pi$.

The Transverse Polarimeter studies Compton scattering in the “single-photon method,” which simply means that the scattered photon rates are low enough that only one photon is detected at a time; multiple photon interactions occur rarely. Measuring the energy and angular dependence of Eq. (4.2) each scattered photon allows access to the polarization. At HERA, the positron beam profile in the x - y plane is elliptical; the bunch width at the interaction point is many times larger in the x direction than in the y direction. As the beam width and divergence smears the angular distributions, the Compton cross-sections are projected onto the y coordinate for study; the x dependence is integrated. If a scattered photon travels D millimeters away from the interaction vertex in the lab frame, then its transverse displacement y can be determined from (θ, ϕ) by

$$y(\theta, \phi) = \frac{D \sin \phi}{\gamma \tan \frac{\theta}{2}} \quad (4.8)$$

For vertical coordinate studies, equation (4.1) may then be simplified to

$$\frac{d\sigma_c}{dydE_\gamma} = \Sigma_0 + S_1(0)\Sigma'_1 + S_3 \left[P_Y \Sigma_{2Y} + P_Z \Sigma_{2Z} \right], \quad (4.9)$$

The energy distribution for unpolarized positrons, integrated over y is shown in Figure 4-2. The figure also shows the differential cross-section in y integrated over the energy range where

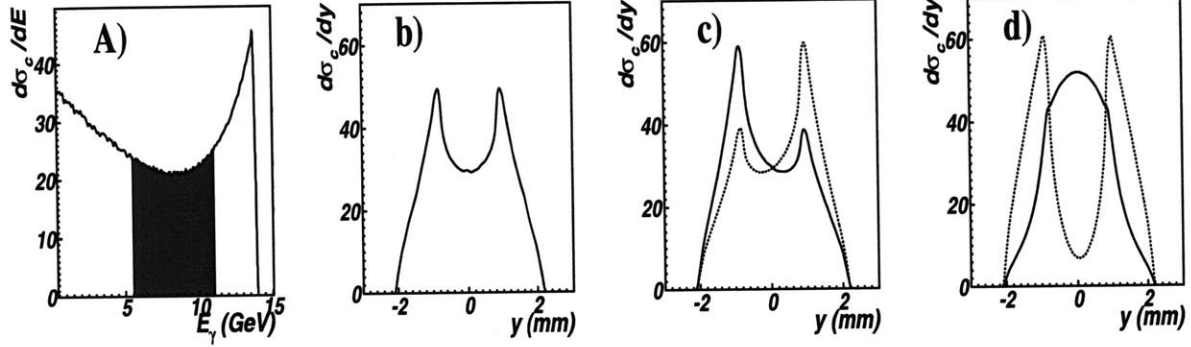


Figure 4-2: The energy and y distributions of backscattered photons. a) The cross-section as a function of energy. The largest transverse beam polarization effects occur in the shaded region, $5.54 < E_\gamma < 11.08$ GeV. The next three figures show cross-section averaged over this energy range and projected onto the vertical coordinate at the TPOL position, y . The figures show the response to photon and positron polarizations: b) unpolarized positrons and photons; c) vertically polarized positrons, $P_Y = 1$, and left (solid) and right (dotted) circularly polarized light; d) unpolarized positrons and linearly polarized light, $S_{\text{lin}} = 1$, and $\phi_{\text{lin}} = 0^\circ$ (solid) and 90° (dotted).

beam polarization terms are largest, 5.54 to 11.08 GeV. The term Σ_{2Y} is antisymmetric in the vertical coordinate, while Σ'_1 is completely symmetric, as can be seen in the figure.

4.1.1 Extracting Beam Polarization Observables

Beam polarization may be extracted from Eq. (4.9) by using the symmetry properties of the cross-section around the HERA beam plane, $y = 0$. Assuming negligible longitudinal polarization, two cross-section manipulations yield transverse polarization sensitivity. First, if one considers the cross-section difference for two laser helicities (L, R) for a fixed energy E_γ , the resulting asymmetry is

$$A(y) \Big|_{E_\gamma} = \frac{\frac{d\sigma}{dydE_\gamma} \Big|_{\text{L}} - \frac{d\sigma}{dydE_\gamma} \Big|_{\text{R}}}{\frac{d\sigma}{dydE_\gamma} \Big|_{\text{L}} + \frac{d\sigma}{dydE_\gamma} \Big|_{\text{R}}} \quad (4.10)$$

$$= \Delta S_1 \frac{\Sigma'_1}{\Sigma_0} + P_Y \Delta S_3 \frac{\Sigma_{2Y}}{\Sigma_0} \quad (4.11)$$

ΔS_3 and ΔS_1 are the differences of the circular and linear polarizations in each helicity: $\Delta S_3 = \frac{1}{2}(S_{3|L} - S_{3|R}) = \frac{1}{2}(|S_{3L}| + |S_{3R}|)$. The light polarizations are assumed to have equal magnitudes and opposite signs in each helicity, and the linear light polarization is assumed changes sign with the helicity. In this case, $\langle S_1 \rangle$ and $\langle S_3 \rangle$ are negligible. To extract ΔS_1 and $\Delta S_3 P_Y$, one fits the y dependence of the cross-section with Eq. (4.11). The two extracted parameters are uncorrelated, since the cross-section terms involved are orthogonal to each other.

A simpler approach directly uses the y symmetry of the cross-section. Σ_{2Y} is the term in the cross-section odd in y . If one calculates the average vertical coordinate of backscattered photons for a given energy and light helicity, this is

$$\langle y \rangle \Big|_{E_\gamma} = \frac{\int_{-\infty}^{\infty} y(S_3 P_Y \Sigma_{2Y}) dy}{\int_{-\infty}^{\infty} \Sigma_0 dy} \quad (4.12)$$

$$= S_3 P_Y \Pi(E_\gamma) \quad (4.13)$$

Often, systematic uncertainties may be reduced by considering the difference in the $\langle y \rangle$ for opposite light helicities:

$$\Delta y(E_\gamma) = \Delta S_3 P_Y \Pi(E_\gamma) \quad (4.14)$$

In this formula, linear light polarization disappears as the cross-section term Σ'_1 has a $\cos 2\phi$ dependence. $\Pi(E_\gamma)$ is the analyzing power for this technique, known as the shift of the means method.

The energy dependence of the Compton cross-section yields sensitivity to longitudinal beam polarization, P_Z . For example, when integrating the y dependence of the cross-section and considering the helicity asymmetry, one gets

$$A(E_\gamma) = \frac{\frac{d\sigma}{dE_\gamma} \Big|_L - \frac{d\sigma}{dE_\gamma} \Big|_R}{\frac{d\sigma}{dE_\gamma} \Big|_L + \frac{d\sigma}{dE_\gamma} \Big|_R} \quad (4.15)$$

$$= \Delta S_3 P_Z \frac{\Sigma_{2Z}}{\Sigma_0} \quad (4.16)$$

4.2 The Transverse Polarimeter

4.2.1 The Polarimeter Setup

The Transverse Polarimeter is located in the West Hall of the HERA ring opposite the HERMES experiment (see Figure 3-1). The TPOL optics and electronics laboratory sits in the ninth floor of the Hall. A series of optics propagate intense, circularly polarized laser light to the positron beam in the HERA tunnel. A calorimeter downstream of the positron-laser IP then detects the backscattered photons. By its segmentation in the vertical coordinate, this calorimeter may measure the vertical position of the photons as well as their total energy. An overview of the polarimeter setup is shown in Figure 4-3.

4.2.1.1 The Optical System

The polarimeter optics laboratory in the HERA West Hall centers around a 25W Argon ion laser by Coherent. The laser produces a continuous green laser beam at 514.5 nm with up to 10W of power. The exiting light is linearly polarized to greater than 99%.

Elements on an optics table at the laser aperture condition the light beam before its transport to the positrons. A Pockels Cell converts the natural linear polarization of the light to circular polarization. The voltages of the Pockels Cell are selected to maximize circular polarization at the positron-laser interaction point; phase shifts of the light in the remainder of the optical transport are empirically compensated on the laser table. For polarization measurement, polarization helicity is flipped at 83.3 Hz by changing the sign of the voltages on the cell. Helicity correlated displacements of the light as it propagates through the cell have been studied and have been found to be negligible. Also on the laser table is a Galilean system of two lenses, which increase the size of the beam by an order of magnitude but reduce its divergence. This facilitates the transfer of the beam over the long distance to the HERA tunnel. Finally, a remotely controlled “chopper” may block the laser path for frequent background measurements without the laser light.

From the laser table, the beam is transported to the interaction point of the HERA positron beam. The technical challenge of this transport is contained in the distances involved: the ninth floor laboratory in HERA’s West Hall is 25 meters above and over 130 meters away from the

interaction point. A system of four mirrors (named M1a, M1b, M2, M3, and M4) steer the laser through a pipe leading to the tunnel IP. Each mirror is mounted on a remotely controlled Aerotech stepper motor; a camera and screen behind each mirror facilitate their adjustment. A majority of the laser transport path (from the optics laboratory to the mirror M3 three meters above the IP) is evacuated to less than 10 mbar. This reduces sensitivity of the beam path and beam intensity to air density fluctuations. Before the mirror M3, another double-lens system focus the light beam so that its width at the positron IP is near 0.6mm. The light enters the HERA vacuum through a window after M4; at this point, it approaches the positron beam from above with a vertical angle of 3.1 mrad.

Nearly all of the light passes through the IP and enters an polarization analyzing box. A mirror (M5) directs the beam through a rotating Glan-Thompson prism and onto a photosensitive diode. The intensity of the light is measured as a function of the ϕ angle of the polarizer by

$$I(\phi) = I_0 + J \cos 2(\phi - \phi_{\text{lin}}). \quad (4.17)$$

The linear polarization of the light is $S_{\text{lin}} = \frac{J}{I_0}$, and S_3 may be calculated from Eq. (4.5).

4.2.1.2 The HERA Beam

Compton scattering interactions between the laser light and the positrons generates multi-GeV photons in a tight cone around the positron beam direction. The natural width and divergence of each positron bunch smears the backscattered photon distributions from the point-like interaction limit. The smearing is significant as the angular correlation of the photon distribution to polarization and energy may be diluted by this effect. The optics of HERA were optimized to ensure minimize beam smearing in the vertical direction at the TPOL IP. Assuming approximately the positron bunches are distributed as Gaussian distributions, the Twiss parameters of the beam at the interaction point determine the projection of the positron beam profile downstream at the calorimeter location [126]:

$$\sigma(D) = \sqrt{\epsilon(\beta - 2\alpha D + \frac{1 + \alpha^2}{\beta^2} D^2)} \quad (4.18)$$

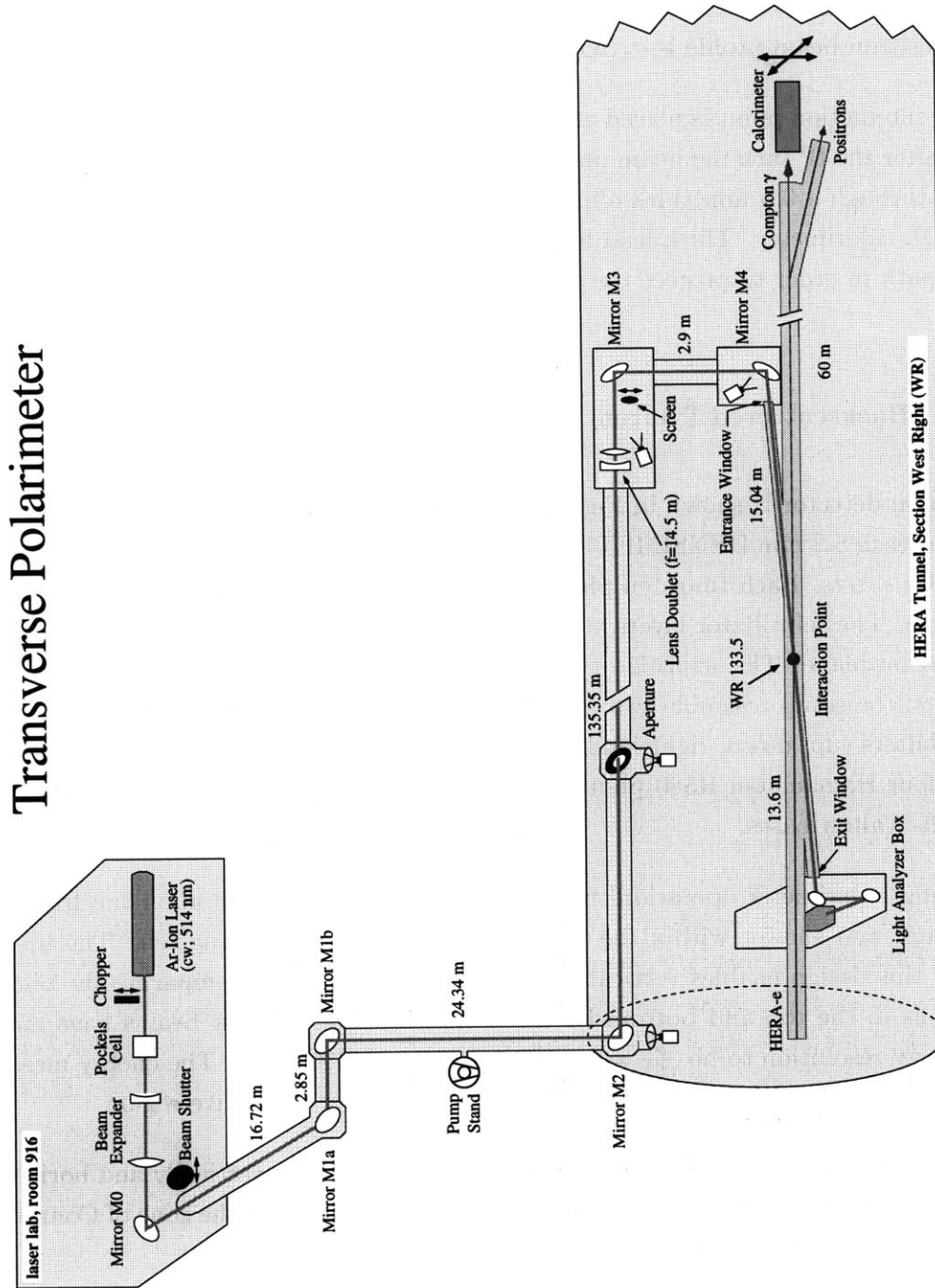


Figure 4-3: A schematic of the TPOL layout [125].

At the IP, $(\alpha_y, \beta_y, \epsilon_y) = (0.649, 43.2 \text{ m}, 2.2 \times 10^{-6})$ and $(\alpha_x, \beta_x, \epsilon_x) = (0.129, 12.2 \text{ m}, 3.4 \times 10^{-5})$ [127]. D is distance of the detector from the interaction point; at the calorimeter, the projected spread of the positron beam profile is $\sigma_x(65 \text{ m}) = 3.4 \text{ mm}$ and $\sigma_y(65 \text{ m}) = 0.46 \text{ mm}$.

The interaction point is placed at the end of the West area straight section in HERA. Weak dipoles after the IP turn the beam positrons away from the photons. The photons exit the beam vacuum through a 0.5 mm thick aluminum window, and they travel 65 meters from the IP to the TPOL calorimeter. Thick lead horizontal and vertical collimators may be moved into this photon path in order to protect the detector during periods of beam instability.

4.2.1.3 Backscattered Photon Detection

The photon detector is shown in Figure 4-4. This sampling calorimeter consists of 12 layers of tungsten (each 6.2 mm DENSIMET17, for 1.6 radiation lengths) and 2.6 mm plastic scintillator (SCSN-38) sheets. Each tungsten plate is $60 \times 55 \text{ mm}^2$ and is supported by a $120 \times 100 \text{ mm}^2$ lead frame. The scintillator layers are split into top and bottom pieces, symmetric around the HERA beam plane. The scintillators are wrapped in foil to prevent light transfer between the two layers; the setup resemble two independent calorimeters on top of each other. Four wave-length shifters (up, down, right, and left) surround the calorimeter and direct the scintillation light to four Hamamatsu R580 photomultiplier tubes. PMT voltages are generated locally by Cockcroft-Walton bases.

During polarimeter operation, backscattered photons impinge upon the front face of the calorimeter, and shower within the 19 radiation lengths of the tungsten. The up-down symmetry of this design enables vertical position measurements, by comparing the photon energy depositions in the top and bottom halves of the calorimeter. Test beams have measured the total energy resolution to be $\frac{\sigma}{\langle E \rangle} = \frac{22.7 \pm 0.5\%}{\sqrt{E}} + (3.4 \pm 0.2)\%$ [128]. The energy measurement is uniform at the 1.5% level and linear at the 0.5% level over the active region.

The entire calorimeter is place on a table which may move vertically and horizontally with a step size of $0.2 \mu\text{m}$. The table is remotely controlled and centers the cone of Compton photons to within $50 \mu\text{m}$ [126].

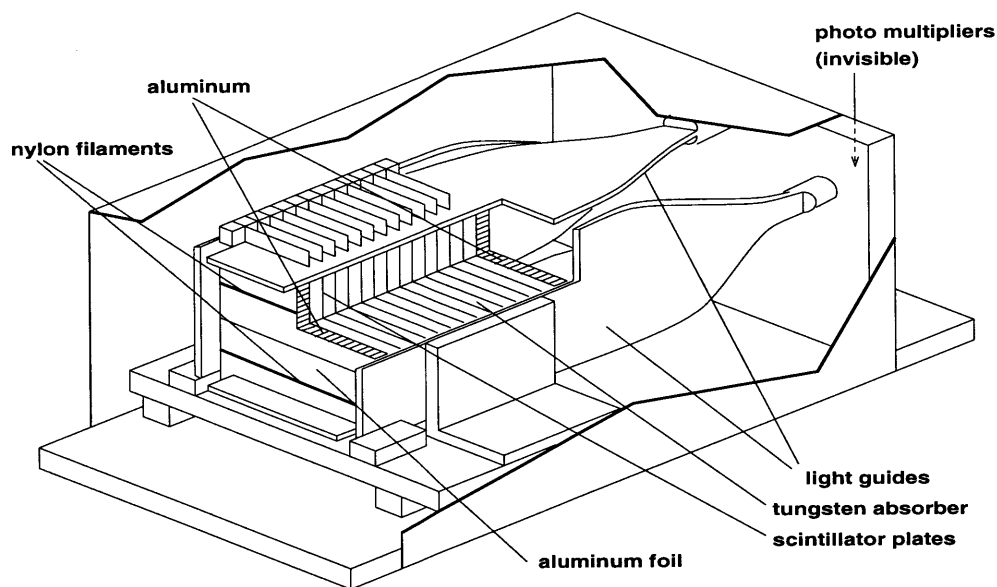


Figure 4-4: A cutaway drawing of the calorimeter at the Transverse Polarimeter.

4.2.1.4 The Data Acquisition and Control Systems

Allcoax cables carry PMT signals nearly 300 meters from the HERA tunnel to the electronics laboratory on the ninth floor of West Hall. The attenuation in each cable is measured to be 0.003 dB/m. At the electronics laboratory, linear fan-outs divide the signals, sending them to both the trigger logic and to the ADCs. The trigger is formed by adding the left and right PMT signals, and requiring this to be over a discrimination threshold corresponding to 3 GeV photons. This threshold suppresses low energy photons from synchrotron radiation and rest gas bremsstrahlung. The trigger produces a 100 ns gates in an integrator, which produces a voltage signal proportional to the charge collected inside the each. The integrator voltage of each PMT signal is fed into a Zeus (NEVIS) Digital Card, along with a laser helicity from the Pockels Cell. The card contains four ADCs sampling the integrator voltage; a DSP on the Card bins the ADC spectra in pre-programmed histograms, sorted by laser helicity. FASTBUS scalers also monitor the trigger rates, allowing a DAQ dead time determination.

For the operating currents of HERA, typical trigger rates are 50 kHz with the laser on, 20 kHz laser off, though these numbers vary widely depending on background conditions and beam tune. The practical limit of the data acquisition is 100 kHz; non-linearities in calibration spectra and significant dead times become issues above this limit. For this reason, the trigger is pre-scaled by a factor of two when the trigger rates exceed 100 kHz.

The data acquisition cycle consists of 40 seconds of Compton scattering measurements and 20 seconds of background measurements with the laser light path blocked by the chopper. Independent polarization measurements occur nearly every minute, which is fast enough to track polarization changes in HERA.

Until 1996, all the systems described above were controlled by a μ VAX-III. The μ VAX also reads the histograms from the DSP. In 1998, these functions were moved to a DEC alpha workstation.

4.2.2 The Transverse Polarization Measurement

The polarization measurement of the TPOL is based simply on a collection of two PMT signals from the calorimeter. For each triggering event, the up and down signals, E_U and E_D , are placed in histograms by the DAQ binned in the variables η and E .

$$E = E_U + E_D, \quad (4.19)$$

$$\eta = \frac{E_U - E_D}{E_U + E_D}. \quad (4.20)$$

(η, E) relate to the physical cross-section variables (y, E_γ) , discussed in Section 4.1. E is the total energy deposition in the calorimeter for each photon, in arbitrary units of ADC binning. A scale constant relates E and the photon energy E_γ , which is calibrated by examining the Compton edge in the ADC spectra (Section 4.2.4.1).

η measures the asymmetry in energy deposition in the calorimeter. As the TPOL calorimeter is separated into two pieces at positron beam plane, a backscattered photon with $y > 0$ will deposit more energy in the top half than the bottom half. The inverse holds for photons with $y < 0$. η and y then have a one-to-one mapping; but this mapping depends on the details of the calorimeter geometry and shower development. So far, information on $\eta(y)$ have primarily come from test beam measurements [129, 130, 128] and EGS4 [131] Monte Carlo simulations [132]. The $\eta(y)$ function beam is parameterized with the functional form

$$\eta(y) = \frac{|y|}{y} \left[1 - \exp -b_2|y| + 2 \frac{a_1}{b_1} (\exp -b_2|y| - \exp^{-b_1|y|}) \right] \quad (4.21)$$

Parameter	Mean	High	Low
a_1 (cm^{-1})	0.480 ± 0.015	0.533	0.327
b_1 (cm^{-1})	1.66 ± 0.03	1.75	1.38
b_2 (cm^{-1})	8.52 ± 0.27	9.11	6.70

Table 4.1: The best fit parameters for the parameterized Transverse Polarimeter response function $\eta_V(y)$ in (4.21). The first uncertainty represents a nominal fit and its statistical uncertainty. The second and third columns represent the high and low values of the fit parameters when the maximum range of the y coordinate used in the fit is varied[128].

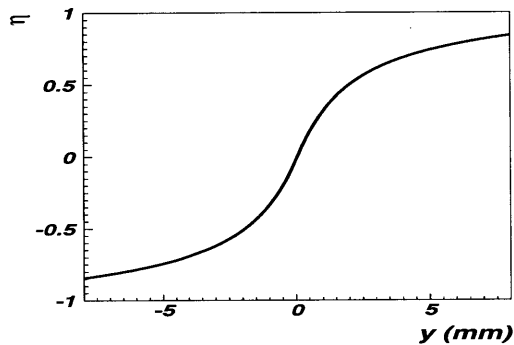


Figure 4-5: The relationship between the physical y coordinate of backscattered photons and measured energy asymmetry η in the calorimeter.

The best fit values for a_1 , b_1 , and b_2 from the most recent test beam measurements [128] are listed in Table 4.1. The resulting parameterization is shown in Figure 4-5.

The data acquisition histograms in 128 bins in η and 64 bins in E . Absolute gain calibration places the Compton edge in bin 29 in the ADC spectra. An example of such a two-dimensional histogram is shown in Figure 4-6.

These histograms map out a differential cross-section, $\frac{d\sigma}{d\eta dE}$. The relations between (η, E) and (y, E_γ) allow a polarization determination, similar to the approach in Section 4.1.1. In the

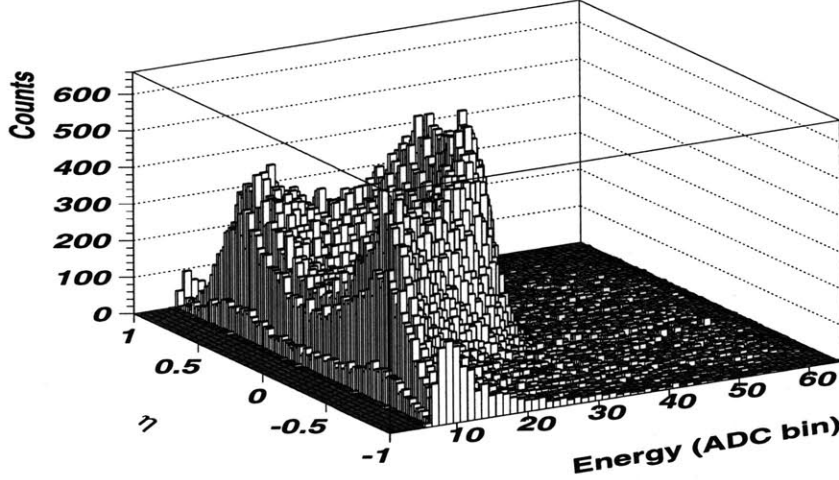


Figure 4-6: A two-dimensional histogram of Compton photon spectra for one minute of data taking, binned in relative energy, E , and energy asymmetry, η .

shift of the means approach, one can form the $\langle \eta \rangle$ in each laser helicity:

$$\langle \eta \rangle \Big|_{L,R} = \frac{\sum_{i=E_{\text{low}}}^{E_{\text{high}}} \sum_{j=\eta_{\text{low}}}^{\eta_{\text{high}}} (N_{ij}^{L,R} - \tau N_{ij}^{\text{OFF}}) \cdot \eta_j}{\sum_{i=E_{\text{low}}}^{E_{\text{high}}} \sum_{j=\eta_{\text{low}}}^{\eta_{\text{high}}} (N_{ij}^{L,R} - \tau N_{ij}^{\text{OFF}})}. \quad (4.22)$$

Here, background counts with laser off, N^{OFF} are subtracted from left and right laser helicity counts, $N^{L,R}$ in each (η, E) bin (i, j) . τ is the laser on/off DAQ livetime ratio for each laser helicity. Taking the $\langle \eta \rangle$ difference in each helicity state, one can relate the mean to beam

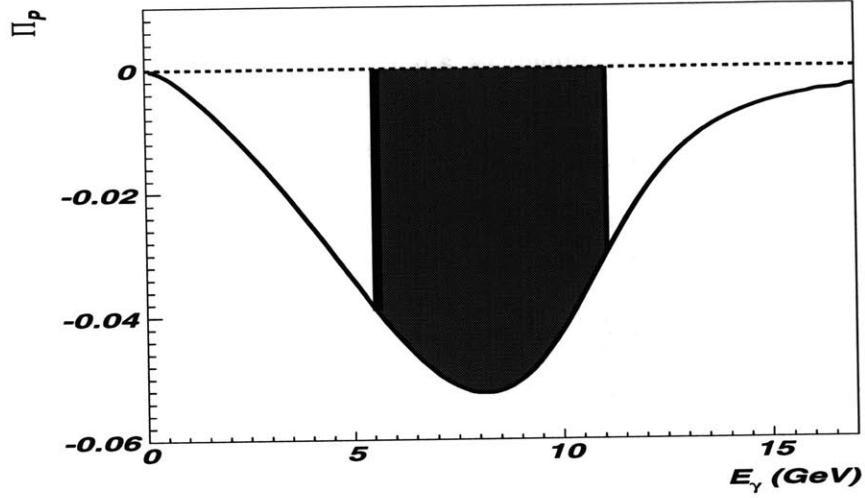


Figure 4-7: The shift of the means analyzing power as a function of energy, $\Pi_P(E_\gamma)$. The shaded area delimits the region of the maximum asymmetry used for polarization analysis, $5.54 < E_\gamma < 11.08$ GeV.

polarization:

$$\langle \Delta\eta \rangle = \frac{1}{2} \left[\langle \eta \rangle|_L - \langle \eta \rangle|_R \right], \quad (4.23)$$

$$= \frac{\int_{E_{\text{low}}}^{E_{\text{high}}} \int_{\eta_{\text{low}}}^{\eta_{\text{high}}} \Delta S_3 P_Y \Sigma_{2Y}(\eta, E) \eta d\eta dE}{\int_{E_{\text{low}}}^{E_{\text{high}}} \int_{\eta_{\text{low}}}^{\eta_{\text{high}}} \Delta S_3 P_Y \Sigma_0(\eta, E) d\eta dE}, \quad (4.24)$$

$$= \Delta S_3 P_Y \Pi_P. \quad (4.25)$$

where the same cross-section symmetry in y is also manifest in η . Π_P is the TPOL analyzing power and is the most important number in this measurement. The function $\Pi_P(E_\gamma)$ is shown in Figure 4-7. In practice, Compton events are integrated between ADC E bins $(E_{\text{low}}, E_{\text{high}}) = (12, 24)$; for a Compton edge in bin 30, this corresponds to an E_γ range of (5.54 GeV, 11.08 GeV). The polarization correlated position asymmetry of the backscattered photons is largest in this region. The shift of the means technique is the main method for polarization analysis.

4.2.2.1 Other Measured Parameters

In addition to the polarization asymmetries, a number of diagnostic quantities may be extracted from the Compton distributions. A few that are relevant to the discussion below are the Compton edge, the focus, the y offset, and the linear light polarization.

The Compton edge position in the ADC spectra is useful for gain calibration and may be determined from the maximum in the energy derivative of the Compton spectra. The focus measures the width or second moment of the helicity-averaged η distributions near the Compton edge, $25 \leq E \leq 29$ or $11.08 < E_\gamma < 13.38$ GeV. The energy interval is chosen for its insensitivity to the polarization asymmetry. The width has contributions from both the natural angular divergence of the backscattered photons and from smearing effects in the beam divergence ($\sigma_y(65\text{m})$) and calorimeter response. y_{center} measures the deviation of the backscattered photon center from the symmetry plane of the calorimeter. It is monitored online by calculating the helicity-averaged $\langle \eta \rangle$ in the same energy interval as the focus is measured.

Finally, the projected linear light polarization, ΔS_1 , is monitored online by its influence on the differential cross-section near y (or η)=0. In the same energy range, the laser helicity asymmetry of the photon rate near the center of the calorimeter, $-0.2 < \eta < 0.2$, is proportional to ΔS_1 :

$$A_{\text{lin}} = \frac{\sum_{i=E_{\text{low}}}^{E_{\text{high}}} \sum_{j=-0.2}^{0.2} (N_{ij}^L - N_{ij}^R)}{\sum_{i=E_{\text{low}}}^{E_{\text{high}}} \sum_{j=-0.2}^{0.2} (N_{ij}^L + N_{ij}^R)} \quad (4.26)$$

$$= \Delta S_1 \Gamma_\eta \quad (4.27)$$

Γ_η is an analyzing power determined by detector simulations.

4.2.3 A Polarimeter Monte Carlo

Detailed simulation of the Transverse Polarimeter has proven critical to understanding its measurement. A large number of physical effects may modify the analyzing power of the detector.

By modeling these effects, the overall systematic uncertainty of the measurement may be reduced.

A polarimeter Monte Carlo, “POLMC,” was developed for this purpose. The simulation generates a photon distribution according to the Compton cross-section and then model the distortion of the distribution by the beam. The photons are propagated to the TPOL calorimeter position. The calorimeter response is approximated by acceptance and resolution functions; this approach allows fast, high statistics study of the system. Background effects are not modeled; the Monte Carlo describes the detected spectra after background subtraction. The essential parameters of the simulation have already been described in Section 4.2.2.

4.2.4 The Transverse Polarimeter Operation

4.2.4.1 Gain Calibration

The voltages of the photomultipliers are set using the Compton spectra itself. The photomultipliers on the left and right side should receive identical amounts of light from showers in the calorimeter, since there is no scintillator separation in the x coordinate. The voltages on these PMTs are adjusted to give identical signals to each shower in the calorimeter. The distribution of the horizontal energy asymmetry,

$$\eta_H = \frac{E_L - E_R}{E_L + E_R}, \quad (4.28)$$

should then be centered on zero. Figure 4-8 shows a well calibrated η_H distribution.

The up and down PMT voltages are relatively calibrated so that their response to showers is symmetric in the vertical coordinate: $E_U(\eta) = E_D(-\eta)$. An absolute voltage scale for both PMTs may be set in two ways. First, one may require that the total energy from the vertical PMTs, $E_U + E_D$, is the same as that from the horizontal PMTs, $E_L + E_R$. The last two conditions are equivalent to requiring that the distribution,

$$R(\eta) = \frac{E_U + E_D}{E_L + E_R}(\eta) \quad (4.29)$$

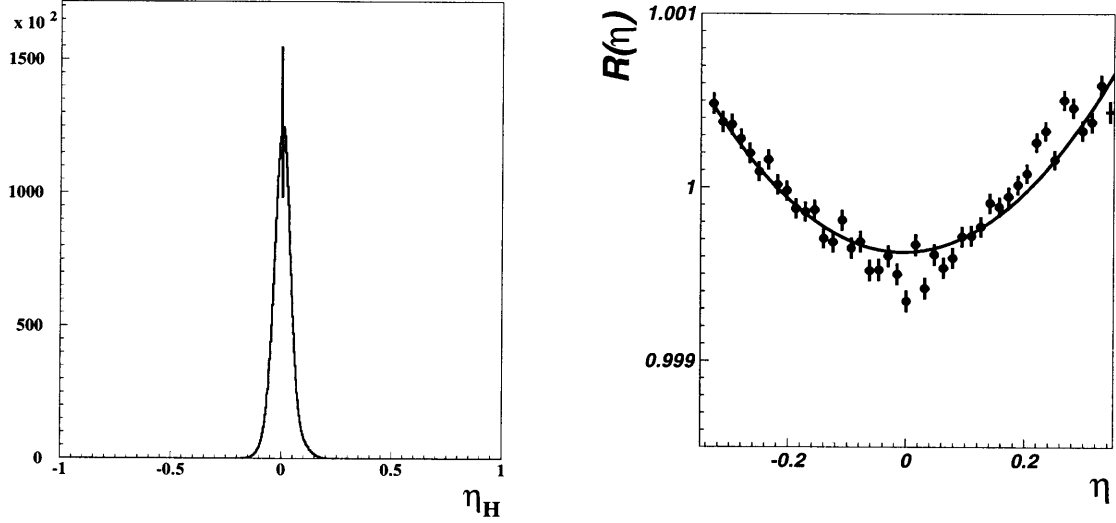


Figure 4-8: The relative gain calibration spectra for the PMTs. The left plot shows the balancing of the signal in the Right and Left PMTs. At the right, the Energy ratio, $R(\eta) = \frac{E_U + E_D}{E_L + E_R}$, is used to set the Up and Down PMT voltages. The line represents the best fit parabola, $R(\eta) = 0.997 + 0.00175 \eta + 0.0137 \eta^2$.

is a symmetric parabola with $R(\eta = 0) = 1$. A calibrated $R(\eta)$ spectrum is shown in Figure 4-8.

Alternatively, one may set the up and down PMT voltages such that the characteristic Compton edge of the backscattered photons is placed in defined ADC channel. As mentioned, energy bin 30 of the two-dimensional histograms is chosen. Note that background from bremsstrahlung has its own kinematic cutoff at the beam energy 27.5 GeV. This edge should then fall in bin 60, assuming detector linearity. Both absolute calibrations are equivalent, though the second approach is more useful for offline gain studies and corrections.

Offline corrections eliminate the measurement dependence on the gain calibration. A strong dependence on the absolute gain calibration is seen both in dedicated studies and in Monte Carlo. The agreement between the two estimations is quite good, as shown in Figure 4-9. In this plot, the uncorrected polarization is plotted versus the position of the Compton edge in the ADC spectra. The data points are fit by a polynomial curve. Overlaid on the plot is also a Monte Carlo prediction for this measurement. The Monte Carlo curve determines the absolute calibration correction, C_{Edge} , which normalizes the analyzing power to the value in the center ADC bin 30. The difference between the fit and the MC prediction is taken as a systematic

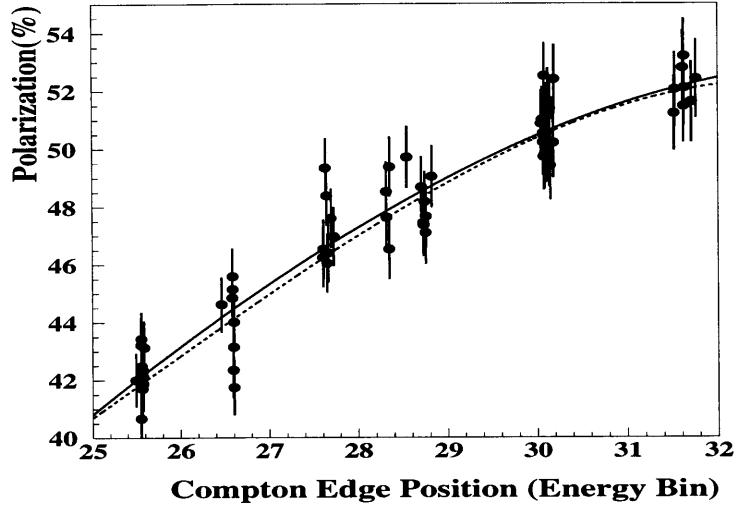


Figure 4-9: Measurement dependence on the absolute gain calibration, as measured by the position of the Compton Edge in the ADC spectra. The data points come measurements in 1996. The solid line is a polynomial fit to the data, and the dotted line is a Monte Carlo simulation of the effect.

uncertainty $\frac{\delta P}{P}|_{\text{Gain}}$. No dependence of the measurement on the relative up and down PMT calibration has been seen within the normal operating range of the device.

4.2.4.2 Position Calibration

The measurement procedure in Section 4.2.2 implicitly assumes that the polarimeter's vertical separation is coplanar with the vertical symmetry axis of the Compton photons. Table motors adjust the calorimeter during operation to track the photons' center, which may move during HERA positron orbit corrections. Since the parameter y_{center} monitors the photon offset online, a correction, $C_{\text{Table}}(y_{\text{center}})$, may eliminate measurement dependence on this centering. According to Monte Carlo simulations, the polarization and linear light asymmetries in

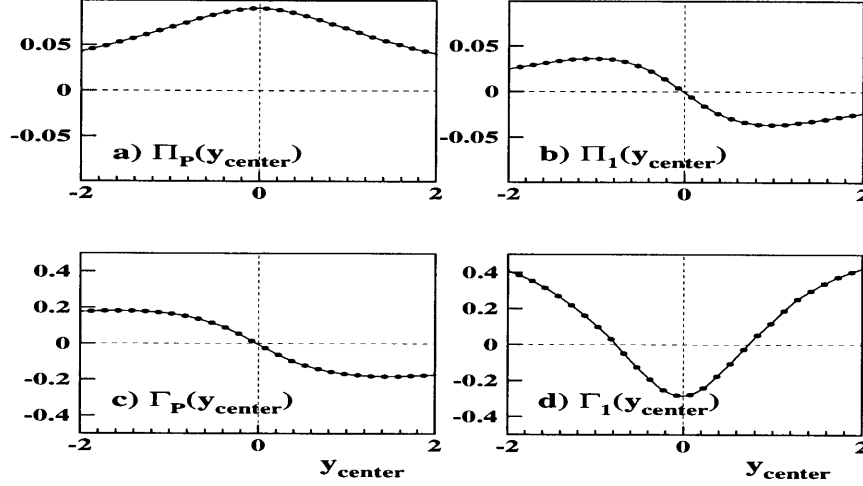


Figure 4-10: The beam and linear light polarization response functions as a function of the vertical centering of the Compton photons on the calorimeter. The functions were determined by Monte Carlo simulation.

Equations (4.25) and (4.27) become coupled when $y_{\text{off}} \neq 0$:

$$\langle \Delta\eta \rangle(y_{\text{center}}) = \Delta S_3 P_Y \Pi_P(y_{\text{center}}) + \Delta S_1 \Pi_1(y_{\text{center}}) \quad (4.30)$$

$$A_{\text{lin}}(y_{\text{center}}) = \Delta S_3 P_Y \Gamma_P(y_{\text{center}}) + \Delta S_1 \Gamma_1(y_{\text{center}}) \quad (4.31)$$

The purely even functions $\Pi_P(y_{\text{center}})$ and $\Gamma_1(y_{\text{center}})$ and the purely odd functions $\Gamma_P(y_{\text{center}})$, and $\Pi_1(y_{\text{center}})$ are shown in Figure 4-10. The relations predict that there should be false asymmetry due to linear light polarization anti-symmetric about $y_{\text{center}} = 0$ (or $\eta = 0$) in the beam polarization measurement.

The polarization dependence on y_{center} has been measured seven times between 1995 and 1997. An example of one such measurement is shown in Figure 4-11, and a list of fit parameters to the dependence is in Table 4.2. The above formalism is indirectly supported by the data. For example, the polarization dependence in Figure 4-11 is asymmetric about $y_{\text{center}} = 0$, and size of the asymmetry agrees well with the Monte Carlo prediction. The false asymmetry due to linear light polarization is the only known effect that can make the dependence asymmetric.

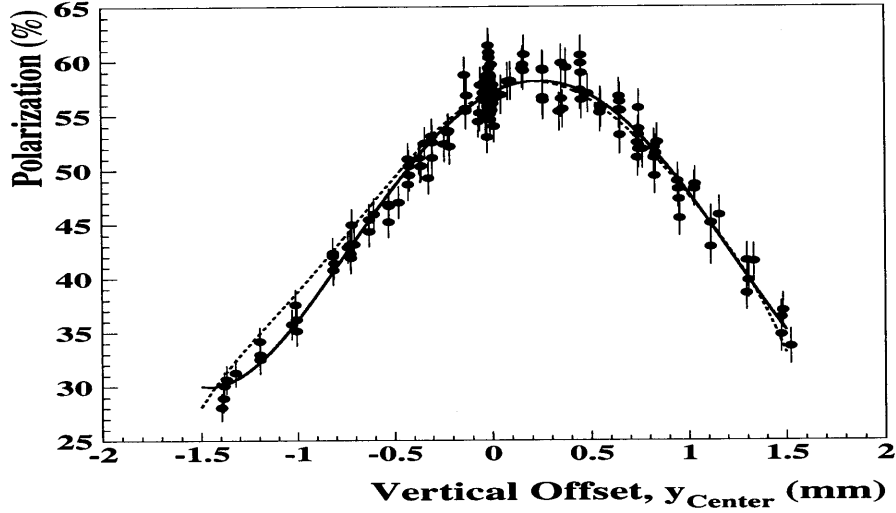


Figure 4-11: A study of measurement dependence on the backscattered photon position from 1996. The solid line shows the best fit to the data. The dotted line represents Monte Carlo simulation of this measurement, assuming $\Delta S_3 P_Y = 57\%$ beam polarization and $\Delta S_1 = -12\%$.

However, the linear light false asymmetry has not yet been directly observed; one would like to measure Π_1 with zero beam polarization, P_Y . Hence, the current y_{center} corrections, C_{Table} , apply a conservative systematic uncertainty, $\frac{\delta P}{P}|_{\text{Center}}$, for the possible variation from Π_1 . The statistical uncertainty of the determination of the fit in Figure 4-11 is also included.

4.2.4.3 Scale Calibration and Monitoring

Assuming the polarimeter operation is optimized, the systematic uncertainty of the polarization measurement is dominated by knowledge of the shift of the means analyzing power, Π_P . The Sokolov-Ternov effect described in Section 3.1.1 provides a convenient determination of this number. By examining Eq. (3.8), one can see that the ratio of the maximum polarization to the rise time constant, $\frac{P_{\text{max}}}{\tau_P}$, is a constant in a flat ring, independent of depolarizing influences. A measurement of the polarization build-up time constant, yields a polarimeter determination of the HERA equilibrium polarization:

$$P_{\text{max}} = \frac{P_{ST}}{\tau_{ST}} \tau_P. \quad (4.32)$$

Coefficient	1996 (Data)	$\frac{1}{P_{Y\Pi_P(0)}} P_{Y\Pi_P}(Y_{\text{Center}})$	$\frac{1}{P_{Y\Pi_P(0)}} \Delta S_1 \Pi_1(Y_{\text{Center}})$
A_0	1.000	1.000	0.0
A_1	0.162 ± 0.007	0.0	0.157
A_2	-0.323 ± 0.011	-0.330	0.0
A_3	-0.059 ± 0.005	0.0	-0.092
A_4	0.059 ± 0.006	0.113	0.0

Table 4.2: A Comparison of measured parameters of the polarization measurement dependence on Compton photon centering, with the Monte Carlo predictions for linear and circularly polarized light. The data in Figure 4-11 were fit with a four parameter polynomial, $P_{\text{Measured}} = A_0 + A_1 y_{\text{center}} + A_2 y_{\text{center}}^2 + A_3 y_{\text{center}}^3 + A_4 y_{\text{center}}^4$. The data and Monte Carlo are normalized to unity at $Y_{\text{center}} = 0$. The linear light polarization of the measurement, ΔS_1 , equals -12% .

By comparing fitted P_{max} in a polarization rise with the TPOL measured value, one may determine the detector calibration k .

$$P_{\text{measured}} = k P_{\text{max}}. \quad (4.33)$$

In practice, these measurements are difficult to obtain. In order to determine k precisely, rise times measurements must be taken in a flat ring, without the longitudinal spin rotators. A quantum mechanical treatment of the Sokolov-Ternov effect was provided by Derbenev and Kondratenko [133]. From their treatment, horizontal magnetic fields, introduce a correction $(1+\delta)$ to above relations:

$$P_{\text{max}} = \frac{P_{ST}}{\tau_{ST}} \tau_P (1 + \delta) \quad (4.34)$$

δ is difficult to calculate, but it is expected to be on the order of a few percent in HERA with spin rotators [111]. It provides a limiting systematic uncertainty for rise times in the normal operating condition of HERA.

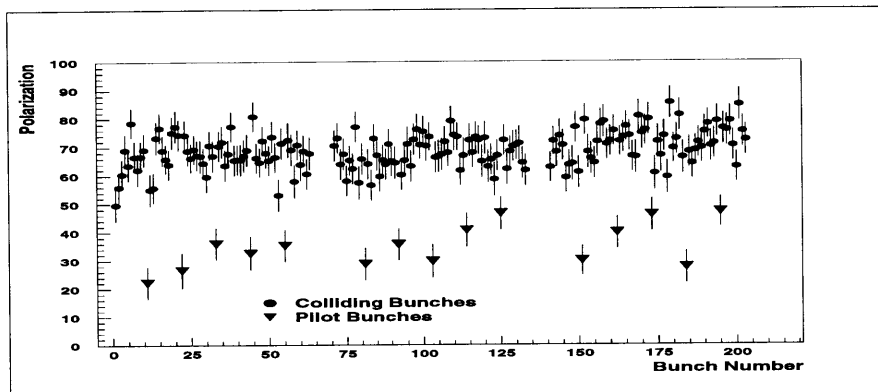


Figure 4-12: The bunch dependence of HERA positron polarization measured by the Longitudinal Polarimeter.

Also, rise times can only be taken when both the polarimeter and HERA positron machine is perfectly stable over a period of hours so that neither the measured nor the true equilibrium polarization is drifting. Almost no orbit corrections to HERA are tolerable during the measurement. Due to strong beam-beam effects, HERA bunches which interact with the proton beam may have significantly different average polarizations than the non-interacting, “pilot” bunches. An example of the bunch dependence of the polarization, determined by the Longitudinal Polarimeter, is shown in Figure 4-12 [134]. In such a situation, a measured polarization rise time will be an incoherent superposition of exponentials rising with different time constants. The average polarization will no longer simply depend on the effective polarization rise time. A systematic deviation of the determined analyzing calibration up to 5% may develop if (4.32) is naively applied [134]. It is difficult then for either HERMES or the HERA collider experiments to take data in parallel with the rise time determination. Dedicated running is required for these calibrations.

Though they may not be used for scale calibration, rise times with the HERA spin rotators operating are still important. Frequent rise time determinations check that the polarization scale is constant, independent of radiation damage, hardware changes, or other imaginable time dependences.

Fourteen flat machine measurements of the polarimeter calibration by the rise time technique were conducted in 1994. Of these, eight had HERA and polarimeter conditions stable enough for analysis. Together, they calibrate the Π_P to -0.04804 ± 0.00156 [135]. The relative scale uncertainty, $\frac{\delta P}{P}|_{\text{Scale}}$, equals 3.26%. The statistical uncertainty of this calibration was under 1%, but a large systematic uncertainty was applied to account for large, unexplained

fluctuations among the eight rise time measurements. The last year HERA ran without spin rotators was 1994. Between 1995 and 1997, thirty-six more measurements with spin rotators on were conducted. These measurements show that the analyzing power remained stable at the 1% level over this period [136]

4.2.4.4 Beam Size Effects

Monte Carlo simulations indicate that the polarization analyzing power depends strongly on the smearing effects of the positron beam profile. The photon focus discussed in Section 4.2.2.1 is partly sensitive to this beam smearing. Four measurements of the polarization dependence on the measured focus have been attempted, as shown in Figure 4-13. Unfortunately, the measurements are not all consistent with each other. Two (4-13a and d) agree well with Monte Carlo predictions while two others (4-13b and c) suggest very different dependences. The difficulty in these measurements is that the width of the high energy photon distribution is not a direct indicator of the beam smearing. Linear light polarization and the photon position offset on the calorimeter will also vary this measured width. No correction for the focus, C_{FOCUS} , has been applied to date. Within the normal range of HERA and TPOL operation, the analyzing power variation due to focus changes is less than 1.9%. A preliminary investigation into beam smearing was made in conjunction with the 1994 rise time analysis [137]. That work concluded that such variation may be the largest contribution to the rise time measurement instability. It is then assumed that the scale systematic uncertainty covers focus variation, and no additional systematic uncertainty is applied.

4.2.4.5 Other Dependences

Early in 1996, high beam currents in HERA combined caused the detector trigger rate to exceed the budgeted 100 kHz. A prescaling of the trigger subsequently cured the problem. Nonlinearities in gain calibration spectra were seen for rates over 87 kHz, and a systematic uncertainty of $\left. \frac{\delta P}{P} \right|_{\text{Rate}} = 2.7\%$ was assigned to polarization measurements taken with trigger rates over this threshold.

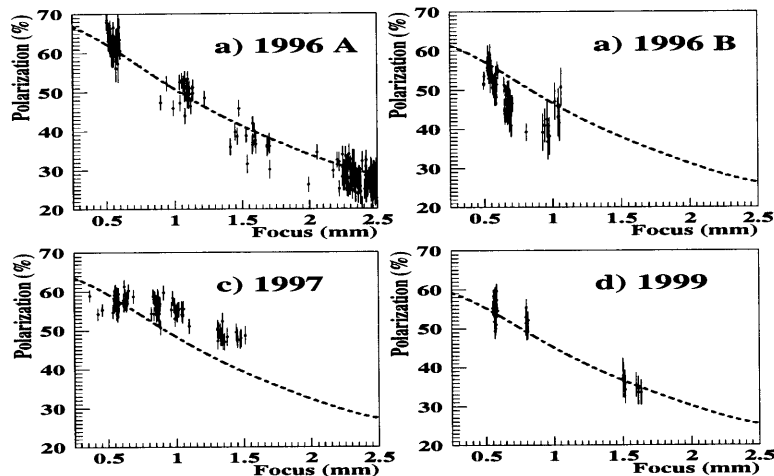


Figure 4-13: The dependence of the polarization measurement on the photon distribution width, or focus, near the Compton edge. The focus is sensitive to smearing effects from the positron beam. Four different studies are compared to Monte Carlo predictions in the dotted line.

4.2.4.6 Calibration Without Beam

A number of polarimeter studies occur between HERA fills. Pedestal and LED runs provide a relative monitor and history of the electronics performance and of the PMT gain. Dedicated light polarization runs check the S_3 and S_1 at the interaction point at least every 24 hours. The polarization measurement may be corrected with the measured ΔS_3 , though it is determined to be 1.0 in practice. A relative systematic uncertainty, $\frac{\delta P}{P}|_{\text{Light}} = 0.5\%$, is assigned to this light polarization measurement and propagates to the beam polarization measurement.

4.2.4.7 Online Monitoring and Slow Control

One solution to the polarimeter operation difficulties in 1995 was implemented in a major upgrade of TPOL slow control. The automated software was upgraded to perform the following tasks:

- **Provide automatic identification of and response to HERA beam conditions.**
Responses include opening and closing the collimators in front of the calorimeter, adjusting

the light path mirrors to maximize luminosity, and adjusting the calorimeter table position to remain centered on the backscattered photons.

- **Maintain constant gain calibration of the PMTs.** With the beam, the PMT voltages may be adjusted every 30 minutes using the calibration techniques in Section 4.2.4.1.
- **Perform frequent calibrations without the beam.** These include pedestal, LED, and the light polarization measurements.
- **Provide simple diagnostics of the polarimeter performance for the HERMES crew.** The performance of the TPOL is displayed in a standard user-friendly computer window, as shown in Figure 4-14.
- **Identify problems in the TPOL operation.** Both the hardware readbacks and the photon spectra are constantly monitored to ensure they fall within their normal range. A window changes color and displays a simple error message when deviations are found.

A large number of motors and voltages must be constantly adjusted during polarization data-taking. Yet the TPOL “autopilot” may track the positron beam, self-calibrate, and collect polarization data for weeks without human interference.

4.2.5 Asymmetry Fitting

While the shift of the mean technique offers a simple measurement, a more detailed fit of the asymmetry in the photon spectra may yield a better understanding of the polarization. Explorative studies of these fits have been made. In analogy to Eq. (4.11), an η asymmetry may be defined as

$$A(\eta_j) = \frac{\sum_{i=E_{\text{low}}}^{E_{\text{high}}} (N_{ij}^L \tau^R - N_{ij}^R \tau^L)}{\sum_{i=E_{\text{low}}}^{E_{\text{high}}} (N_{ij}^L \tau^R + N_{ij}^R \tau^L - 2 \frac{\tau^L \tau^R}{\tau^{\text{OFF}}} N_{ij}^{\text{OFF}})}, \quad (4.35)$$

$$= \frac{\Sigma'_1}{\Sigma_o}(\eta) + P_Y \Delta S_3 \frac{\Sigma_{2\eta}}{\Sigma_0}(\eta). \quad (4.36)$$

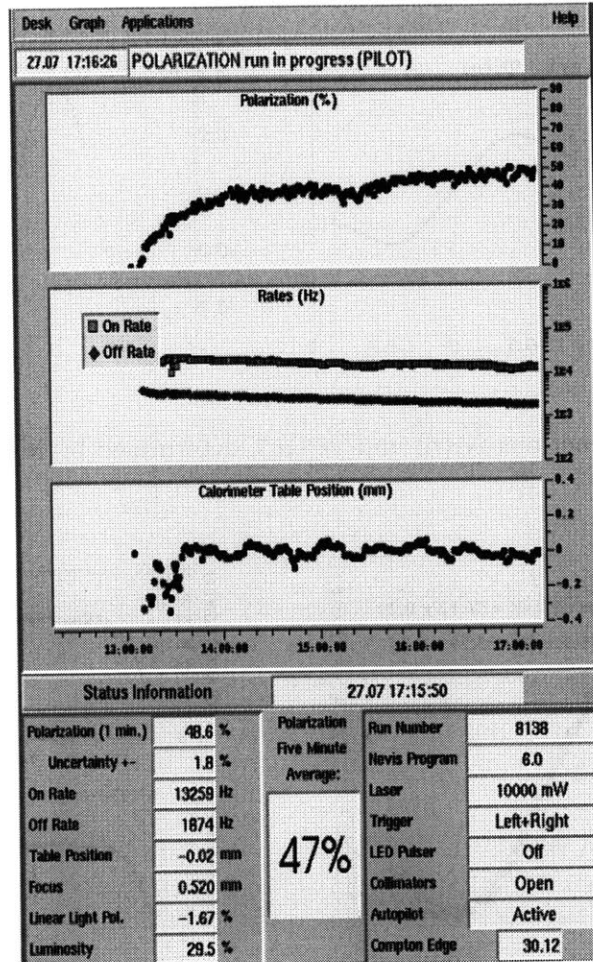


Figure 4-14: The online display of the Transverse Polarimeter information for the HERMES shift crew.

where the Monte Carlo generated functions $\frac{\Sigma_1}{\Sigma_0}(\eta)$ and $\frac{\Sigma_{2Y}}{\Sigma_0}(\eta)$ for the usual energy binning, $5.54 < E_\gamma < 11.08$ GeV, are shown in Figure 4-15. The fits not only yield $\Delta S_3 P_\gamma$ but they also monitor the projected linear light polarization ΔS_1 . The quality of this procedure may be monitored by the fit χ^2 . An example of an asymmetry fit is shown in Figure 4-16.

Asymmetry fits generally reproduce the same polarization values as the shift of the means technique, which is an important validation of the latter method. A comparison of two methods for one fill is also shown in Figure 4-16.

As an independent determination of the polarization, the fits suffer from a lack of a clear calibration criteria. A simple normalization calibration, for example by rise times, is insuf-

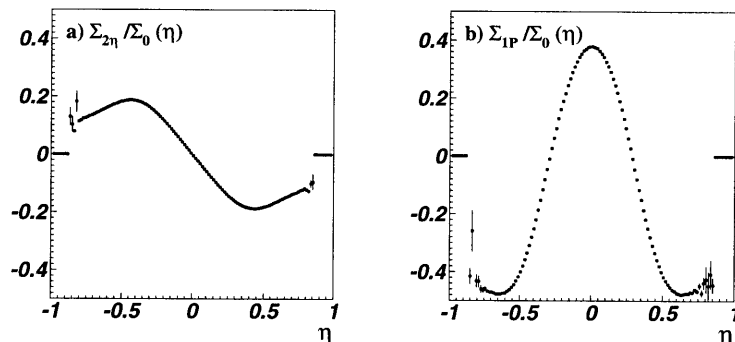


Figure 4-15: The functions $\frac{\Sigma'_1}{\Sigma_0}(\eta)$ and $\frac{\Sigma_{2Y}}{\Sigma_0}(\eta)$, determined by Monte Carlo simulations.

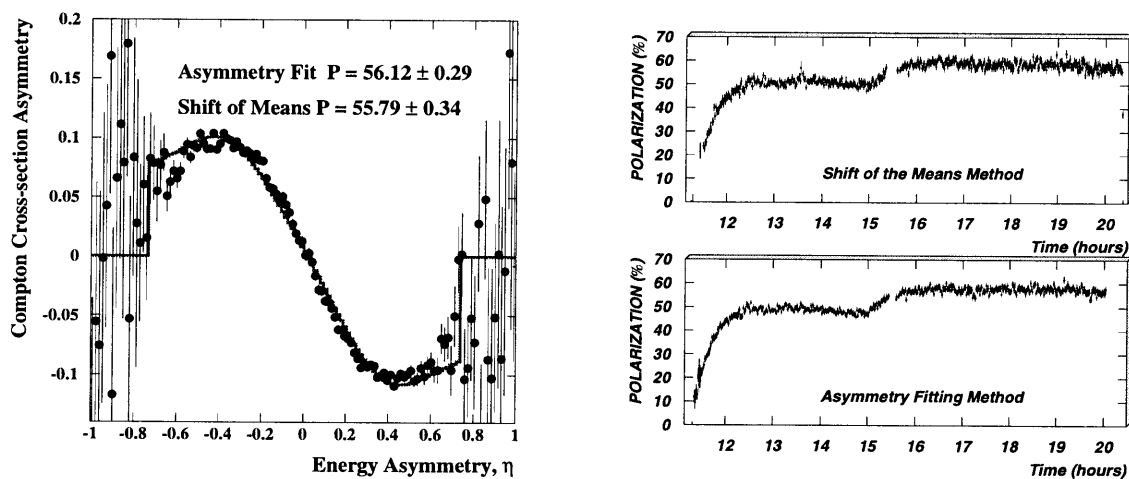


Figure 4-16: Asymmetry Fitting. The left plot shows a fit to thirty-five minutes of data with a stable asymptotic polarization of 55.79 as determined by the shift of the means method. Assuming near perfect circular light, the beam polarization is fit to be 56.12 ± 0.29 %. The fit of the projected linear light polarization, ΔS_1 , yields 1.14 ± 0.14 %. The fit χ^2 is 3.0. The right plot compares the asymmetry fitting and shift of the means techniques for one fill.

efficient to specify the $\Sigma(\eta)$ distributions in detail. The $\chi^2/\text{d.o.f}$ for the fit in Figure 4-16 is disappointingly large at 3.0; this suggests the parameters of the Monte Carlo are not yet tuned well enough for the physical detector. Investigations into the resulting systematic uncertainty are still needed. A more general fitting technique is discussed in Section 4.2.7.2.

	1995	1996	1997
$\langle P_B \rangle$ at HERMES	55%	54 %	53 %
Typical $\delta P_B _{\text{Statistics}}$ (per one minute)	2.5 %	1.5%	1.7%
Relative Systematic Uncertainties (%) :			
Gain Calibration, $\frac{\delta P}{P} _{\text{Gain}}$	1.8	0.075	0.046
Table Centering, $\frac{\delta P}{P} _{\text{Center}}$	1.1	0.55	0.47
Rate Dependence, $\frac{\delta P}{P} _{\text{Rate}}$		0.1	0.01
Light Polarization, $\frac{\delta P}{P} _{\text{Light}}$	0.5	0.5	0.5
Scale Calibration, $\frac{\delta P}{P} _{\text{Scale}}$	3.26	3.26	3.26
Total Uncertainty, $\frac{\delta P}{P} _{\text{Total}}$	4.0	3.34	3.33

Table 4.3: A summary of transverse polarimeter performance from 1995-1997.

4.2.6 TPOL Performance 1995-97

A comparison of HERA of the polarization measurements from 1995 to 1997 are shown in Table 4.3. The statistical uncertainty of the measurement is generally neglected, as the polarization measurements may be fitted with a cubic spline assuming only smooth changes in the values occur. The resulting uncertainty of the fit is much smaller than the systematic uncertainty [138]. The overall systematic uncertainty of the detector is calculated by adding the individual contributions described above in quadrature. This uncertainty is often subdivided into time dependent or “point-to-point” instabilities, described by the first four entries in Table 4.3, and the overall scale uncertainty. An improvement in the measurement uncertainty from 1995 to 1996 may be attributed to diligent calibration and monitoring by the automatic software described in Section 4.2.4.7. The measurement uncertainty remains dominated by the normalization uncertainty of the rise time measurements in 1994.

4.2.7 Improving the TPOL Performance

After the year 2000 running, the ZEUS and H1 experiments will use longitudinal beam polarization to make precision tests of electroweak theory. For this physics, a total systematic polarization uncertainty below 2% is required. HERMES also would benefit greatly from polarization measurement improvements. A number of hardware and software changes have been proposed to improve the stability of Transverse Polarimeter operation for this purpose [139]. Two suggestions for improving the data analysis are discussed below in order to help reach this precision.

4.2.7.1 The Vertical Rate Asymmetry

A complementary polarization asymmetry to the “shift of the mean” is the vertical rate asymmetry. If one considers the total counting rate in each calorimeter half for an energy range,

$$N_{\text{top}} = \sum_{i=E_{\text{Min}}}^{E_{\text{Max}}} \sum_{j=0}^{\eta_{\text{high}}} N_{ij}, \quad (4.37)$$

$$N_{\text{bot}} = \sum_{i=E_{\text{Min}}}^{E_{\text{Max}}} \sum_{j=\eta_{\text{low}}}^0 N_{ij}, \quad (4.38)$$

then a top-bottom asymmetry may be defined for each light helicity:

$$A_V \Big|_{L,R} = \frac{N_{\text{top}} - N_{\text{bot}}}{N_{\text{top}} + N_{\text{bot}}} \Big|_{L,R}. \quad (4.39)$$

The asymmetry in each laser helicity may be averaged to cancel systematic effects. The average asymmetry is proportional to polarization in the following way:

$$\Delta A_V = \frac{1}{2} \left[A_V|_L - A_V|_R \right] \quad (4.40)$$

$$= \frac{\int_{E_{min}}^{E_{max}} \int_{\eta_{min}}^{\eta_{max}} \Delta S_3 P_Y \Sigma_{2\eta}(\eta, E) \left(2\Theta(\eta) - 1 \right) d\eta dE}{\int_{E_{min}}^{E_{max}} \int_{\eta_{min}}^{\eta_{max}} \Sigma_0(\eta, E) d\eta dE}, \quad (4.41)$$

$$= \Delta S_3 P_Y R_P. \quad (4.42)$$

where $\Theta(x)$ is the step function and R_P is the analyzing power for this process.

The Monte Carlo predicts this asymmetry is completely independent of knowledge of the $\eta(y)$ transform in the calorimeter. The total backscattering photon rate in each half of the calorimeter is independent of any position measurement; one only needs to align the calorimeter plane with the photon symmetry axis. This independence is significant as all work towards a precision estimation of the Shift-of-the Means analyzing power has focused on determining $\eta(y)$. However, R_P is sensitive to effects that smear events across the vertical separation plane, such finite calorimeter position resolution. A comparison of the systematic uncertainty in the polarization scale from these two effects is shown in Table 4.4.

The Shift of the Means and the Vertical Rate Asymmetry are simple, complementary determinations of beam polarization. A detailed study of both asymmetries simultaneously may resolve ambiguities in the estimation of the polarization scale. Note, though, that the asymmetries are correlated as they study different moments of the same photon distributions. Figure 4-17 compares both techniques for one fill in 1997.

4.2.7.2 Unpolarized Cross-section Fits

Determinations of the polarimeter analyzing power from first principles generally need an independent criteria to check whether the calibration is correct. The rise time measurement provides one independent check. Test beam calibrations, on the other hand, have only limited success in

Parameter	Polarization Scale Uncertainty (%)		
	$\delta\Pi_P$ [126]	$\delta\Pi_P$	δR_P
$\eta(y)$ Transform:	7.9	1.9	$\sim (10^{-4})$
Position Resolution:	0	$\sim (10^{-3})$	2.5
Energy Resolution:	0	0.2	0.5

Table 4.4: Estimates of the systematic uncertainties in the polarization analyzing powers from the uncertainty in the calorimeter response functions. The shift of the means uncertainty, $\delta\Pi_P$, is compared with a previous determination in Reference [126]. Also shown in the vertical rate asymmetry uncertainty, δR_P .

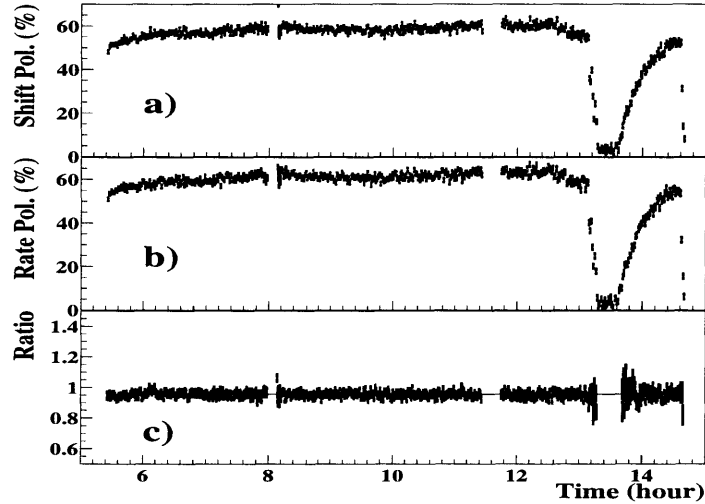


Figure 4-17: A comparison of polarization determinations with a) the shift of the means and b) the vertical rate asymmetry for one fill in 1997. A rise time calibration measurement was started at the end of the fill. The ratio (c) of the two methods is fit with a constant, 0.954 ± 0.001 .

reproducing the complexity of the HERA beam conditions. Another possibility proposed here is to use the Monte Carlo to reproduce the measured unpolarized Compton cross-section.

Polarized experiments generally measure only cross-section asymmetries, as measurements of the absolute cross-sections suffer from acceptance and stability systematics. The Transverse Polarimeter has several features that make such a determination feasible:

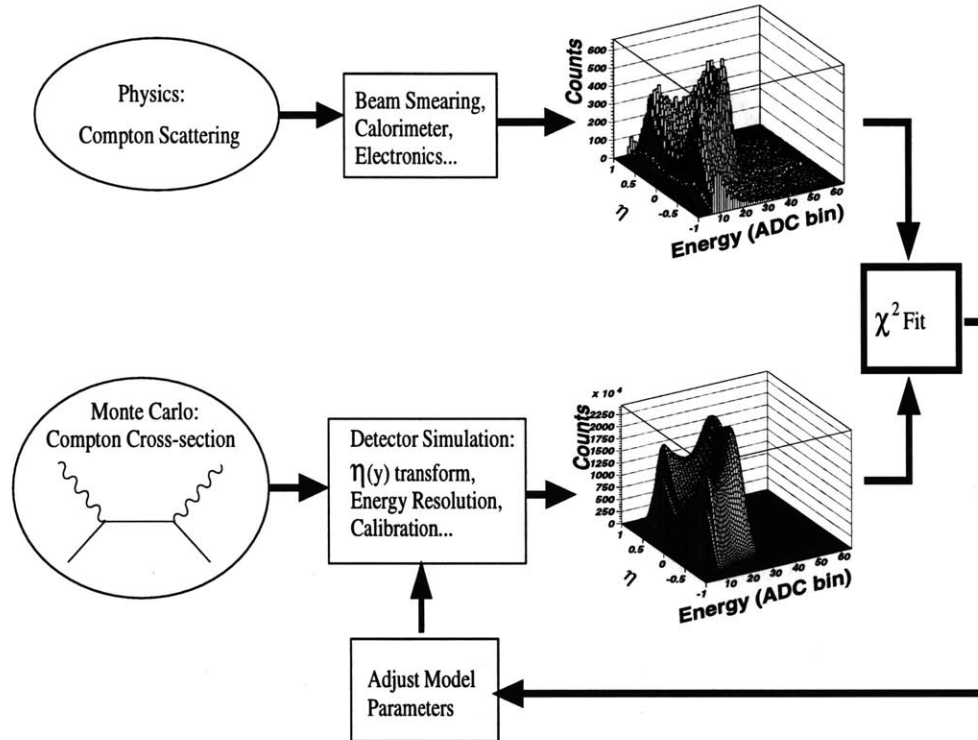


Figure 4-18: A schematic diagram of a Compton cross-section fit procedure.

- The unpolarized Compton cross-section provides a precise standard as it is calculated in QED.
- For energies above a few GeV, the entire backscattered cross-section is contained in the TPOL calorimeter, limiting acceptance systematics.
- In one year of running, the device collects an enormous amount of data, $\approx 10^{11}$ photons.
- The energy and vertical position of each detected photon is measured, precisely mapping $\frac{d\sigma_c}{dE d\eta}$ in short time periods.

To determine the polarization analyzing power, the properties of the detector and of the positron beam must be known in detail. These properties may be parameterized into response functions. The functions are then fixed by comparing Monte Carlo and data cross-sections and minimizing χ^2 , as illustrated in Figure 4-18. The enormous statistics of the measurement, combined with the constraint that the detector response is nearly time-independent, should allow

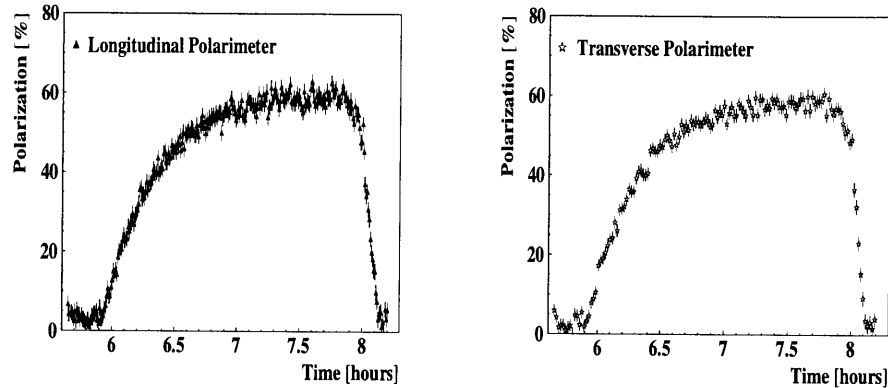


Figure 4-19: A Comparison of Longitudinal and Transverse Polarimeter Measurements.

a very precision determination of the relevant parameters of the polarimeter. If the unpolarized cross-section can be reproduced with high confidence, the uncertainty in the asymmetry analyzing power should be small.

This calibration approach is mainly computational challenge. The Monte Carlo described in 4.2.3 generates statistics comparable to the data in five minutes on a Pentium II 200 MHz. If ten parameters may describe the polarimeter response to high energy photons, a 3 point grid search with ten iterations will take $5 \text{ minutes} \times 3^{10} \text{ simulations} \times 10 \text{ iterations} \sim 6 \text{ years}$, assuming the time for calculating of χ^2 is negligible. With Monte Carlo techniques optimized for speed, more efficient χ^2 minimization procedures, faster computers, and parallel computation, this time may be significantly reduced, perhaps to a few weeks.

4.3 The Longitudinal Polarimeter

The Longitudinal Polarimeter at HERA provides a companion measurement to the Transverse Polarimeter. The device was commissioned in 1996, and began producing useful polarization data in 1997. The polarimeter uses the energy asymmetry in Equation (4.16) to measure the longitudinal polarization in the east section of HERA. A frequency-doubled, pulsed YAG laser produces circular polarized photons at 532 nm (2.3 eV). An optical system, similar to the one at the TPOL, directs the light to the positron beam IP downstream of the HERMES experiment. Backscattered photons are detected in a calorimeter 54 m from the IP, consisting of four NaBi(WO₄) Čerenkov crystals. In this configuration, bremsstrahlung from the HERMES gas target contributes significant detector background. For this reason, the LPOL measures in

the “multi-photon” method in which each laser pulse at 0.1-100 Hz and 1-250 mJ may generate over a thousand backscattered photons. The calorimeter signal is then integrated in energy, and a photon helicity asymmetry determines longitudinal polarization:

$$A(\int E_\gamma) = \Delta S_3 P_Z \Sigma_Z. \quad (4.43)$$

where

$$\Sigma_Z = \frac{\int_{E_{\min}}^{E_{\max}} \left. \frac{d\sigma_c}{dE} \right|_L - \left. \frac{d\sigma_c}{dE} \right|_R \cdot E dE}{\int_{E_{\min}}^{E_{\max}} \left. \frac{d\sigma_c}{dE} \right|_L + \left. \frac{d\sigma_c}{dE} \right|_R \cdot E dE} \quad (4.44)$$

The predicted analyzing power, Σ_Z , is 0.184. Statistical uncertainties of this polarimeter are comparable to the Transverse polarimeter: a few percent polarization measurement is achievable per minute. Systematic uncertainties are driven by the analyzing power uncertainty. Equation (4.44) is modified in practice by the detector acceptance, and this function is not yet estimated well enough to precisely calibrate the device. The rise time calibration technique used for the TPOL is not directly applicable at the LPOL. The calibration technique is only well understood in a flat machine without longitudinal polarization. In practice, the Longitudinal Polarimeter normalization is fixed to match the Transverse Polarimeter measurement. The LPOL does provide valuable redundancy in the polarization determination at HERA. It has different capabilities than the Transverse Polarimeter, including the ability to measure single bunches as shown in Figure 4-12. A comparison of the measurements of the two polarimeters is shown in Figure 4-19 [136].

Chapter 5

The Data Analysis

The HERMES experiment records several terabytes of raw data each year, consisting of detailed characterization of detector states during widely varying time periods. This chapter discusses how one reduces and interprets this vast collection of information to produce a small number of interesting plots representing physics. This process consists of several steps. Decoding and reconstruction software transforms raw spectrometer signals, such as time stamps and pulse heights, into more physically intuitive measurement quantities, such as luminosities, polarizations, and particle tracks. One then examines the derived quantities to select periods of data with quality suitable for analysis. The primary consideration in the data quality selection is the minimization of systematic uncertainties in the experiment while maximizing statistical precision. In effect, one removes data in which detector instabilities reduce the confidence in any extracted physics.

The selected data generate the fundamental experimental result, the double-spin asymmetries on ^1H and ^3He targets. The sections below further detail the calculation of the measured asymmetries at HERMES.

5.1 Data Processing

5.1.1 The Organization of the Data

This section elucidates the basic organizational concepts to understand the analysis below. When discussing HERMES data, several time scales determine fundamental divisions of data. The basic division is one *event*, consisting of all the detector signals associated with one trigger of the data acquisition. The signals correspond to an interaction of a HERA positron bunch in the HERMES target; and they may reconstruct to represent an interesting physical process.

The data acquisition bundles events online into ten second *bursts*. Polarization *records* delimit different target polarization states within each burst. When the target state is constant over a burst, the two concepts are identical; but during an ABS target spin flip, some bursts may contain two or three polarization records. Each record or burst also tags scaler values, such as luminosity and polarizations, corresponding to its event collection period.

Approximately ten minutes of bursts form a *run*, which is the basic unit of online data storage. HERMES continually saves these runs during HERA beam *fills* which typically last eight hours. Finally, the fills are separated by the *year* they were taken. Each year coincides with unique target and detector configurations for the experiment, as hardware maintenance periods at HERA are often scheduled in December and January.

The raw data are formatted using the Experimental Physics Input Output(EPIO) [140] package online. Offline, the HERMES software reframes the data into tabular structures using the ADAMO package [141], which is a scientific programming system for manipulating and validating data. ADAMO provides a basic portable structure for accessing experimental information.

Two further software packages were developed at HERMES to assist the data collection and analysis. The Distributed ADAMO Database(DAD) [142] extends ADAMO by dividing data streams among various different processes using a client-server model. DAD allows central maintenance and efficient transfer of critical HERMES information. PinK [143] is another custom HERMES software contribution. PinK incorporates ADAMO into the TCL/Tk language [144]. Using Tk extensions, colorful, user-friendly window interfaces display and control the HERMES data stream for the physicist user. Figure 4-14 is one example of a PinK display.

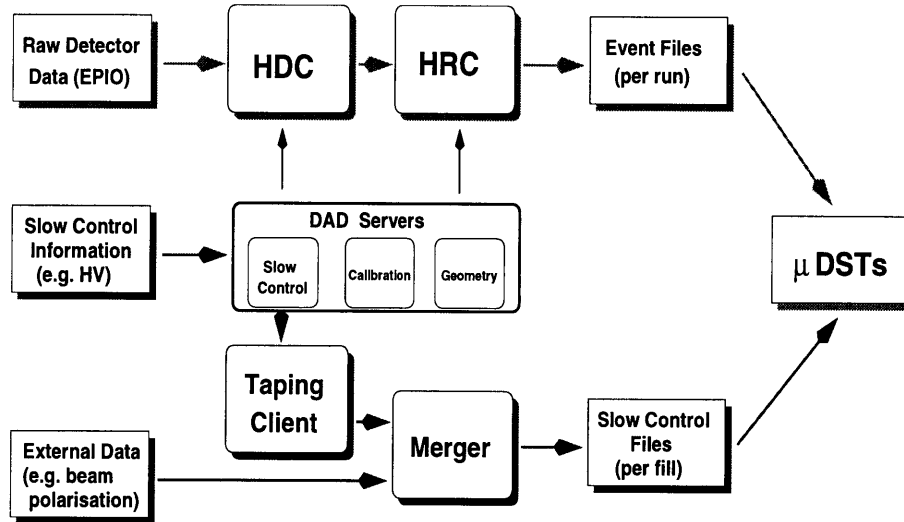


Figure 5-1: A schematic representation of the HERMES data chain.

5.1.2 The Data Production and Analysis

The HERMES data “production” consists of a team of software packages designed to work sequentially to reduce the large run files into smaller, more manageable summary files. Raw signals, such as ADC and TDC values, are interpreted to make a more physically intuitive data representation involving positions and angles, energies and momenta. Critical to the design of the system is both the ability to maintain information in a logical, stable manner and the flexibility to accommodate unforeseen changes and upgrades.

Figure 5-1 depicts the software production scheme. The production consists of several stages. Before any processing occurs, DAD servers are filled with a variety of expert information, including calibrations of various detector responses and the geometries and alignments of detector components. The HERMES decoder (HDC) draws on alignment and calibration information to translate raw ADC and TDC signals into hit positions on chamber wires and energy depositions in various detectors. In the process, the decoder converts EPIO run data to ADAMO format. The HERMES Reconstruction Code (HRC) [145] lays out particle trajectories in the chamber hit patterns in each event. Momenta and scattering angles of each track are determined, and they are correlated to responses in the particle identification detectors. The output of HRC still contains a large body of raw calibration and reconstruction performance information. The program ACE (“Alignment, Calibration, and Efficiency”)[146]

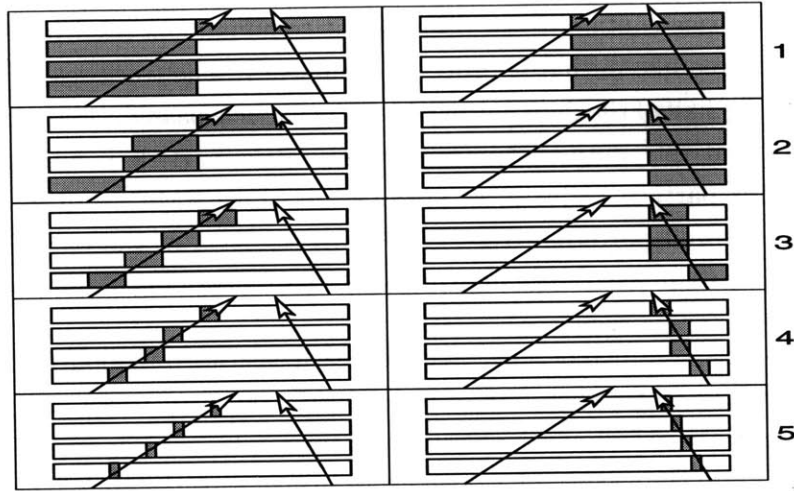


Figure 5-2: The tree-search method for finding particle trajectories. Tracks are localized in the detectors iteratively, with the resolution doubling in each step.

determines chamber calibration and tracking efficiency from the HRC files. The main production filters the essential data for a physics analysis, including track properties and scaler burst information, into a small Data Summary Tape (μ DST) for each run. The data quality studies and physics analyses principally use the μ DST information. A new set of μ DSTs is produced when better detector understanding leads to new calibrations. In this thesis, the production versions 95e5, 96c1, and 97b2 are used, which are used in the HERMES final results in References [147, 148, 149]. A custom, general HERMES analysis package, DK (“The Dark Knight of HERMES Analysis”) was developed in C and FORTRAN to implement the studies discussed below.

5.1.3 The Reconstruction of Tracks

The most critical step in the analysis chain above is the reconstruction of particle trajectories from chamber hits. Rapid analysis of the large amount of data collected by HERMES requires a fast, efficient algorithm for track finding; this algorithm should still guarantee high precision in the determined track parameters. The reconstruction algorithm is briefly reviewed in this section and is discussed in detail in Reference [145].

HRC uses a tree-search algorithm to identify trajectories as shown in Figure 5-2. In this algorithm, the hits in the detector chambers are digitized into a bit pattern. This pattern is

compared to a database containing all possible hit combinations resulting from real particles. The comparison is tree-like in that it proceeds recursively. The track search begins coarsely by determining only the half of the detector in which the particle passed. The precision of the search is then doubled iteratively until the path, or road, of the particle is well localized. Over 100 million patterns for particle trajectories are possible at HERMES, but symmetry arguments reduce number of stored patterns to 31,000. Once the road of the particle is determined, a straight line track is fit to each hit along the road by least squares minimization.

The treearch is conducted separately for each spatial direction of HERMES tracking chambers (u, v, or x) and for each half of the detector (front or back). HRC combines spatial projections to form a three-dimensional straight trajectory in each half. Next the front and back partial tracks are connected, or bridged, in the center of the HERMES magnet to form a full trajectory.

Two major strategies exist for this bridging. The standard method extends partial tracks into the center of the magnet. The distance between the front and back partial tracks is required to be less than 1.0 cm in order to have a full track. This method has been used in the 1997 analysis with the Vertex Chambers. In 1995 and 1996, the VC efficiency and operation was too poor to be used in tracking, and only Front Chamber information was available to specify forward tracks precisely. The reconstruction efficiency in these years is limited by the track resolution of the FCs. The situation is improved by iteratively refitting the track assuming back partial track is fixed precisely and allowing deviations in the front track position. The technique is called forced bridging or “NOVC” reconstruction, and it significantly improves full track resolution in these years.

Once HRC determines a full particle trajectory, the particle’s momentum can be determined. HRC converts the particle’s bending in the magnet into a momentum by consulting a lookup table and a map of the spectrometer magnetic field.

The final step of reconstruction extends the determined trajectories through each particle identification detector and through the HERMES target. The PID detector responses which correlate in space to the extrapolated track positions are assigned to that track. The closest approaches of the extended trajectories in the target to the positron beam are assigned as the most probable production point of the particle.

5.2 Data Quality Selection

Due to unanticipated difficulties in an experiment, not all of the data collected are suited for physics study. A critical step in the analysis involves the evaluation of the quality of each data subset. This step proceeds after data processing. The data quality evaluation occurs on the run, burst, and event time scales of the experiment. One wishes to cut the data set to eliminate instabilities that may cause a systematic bias in the result. At the same time, the cuts are used carefully and loosely, to maintain a high statistics sample.

5.2.1 Fill and Run Quality

The analysis of data begins by considering fills of HERA positrons. Whenever HERMES is collecting data in a fill, the experiment typically runs undisturbed. Between fills, software and hardware changes to the experiment may occur, allowing a wide variation in the experimental conditions from one fill to the next. Fills with polarized target running are selected for analysis.

Coarse data quality criteria may be applied on the run level. Experts working on the target, on the beam polarimeters, and on spectrometer components identify lists of runs in which the respective equipment did not deliver data usable for the HERMES analysis. The failure is severe enough in each case to render analysis of entire runs impossible. For example, if the HERMES beam or target polarimeters failed to measure for a period, then an analysis of spin dependent cross-sections is impossible. Scans of the HERMES shift crew logbook during data-taking yielded lists of runs which are unusable due to hardware problems.

5.2.2 Burst and Record Quality

The burst is the smallest division of data which still contains a complete snapshot of the experimental status. Hence, most studies of data quality focus on this division. Records and bursts will be used interchangeably in this section; the two concepts are identical except when the target changes polarization state.

The following paragraphs detail the selection of bursts suitable for polarized cross-section analysis. In this explanation, note that the experiment evolved considerably from 1995 to 1997 as more running experience was gained and hardware components were replaced or upgraded. The criteria necessary to ensure quality also evolved.

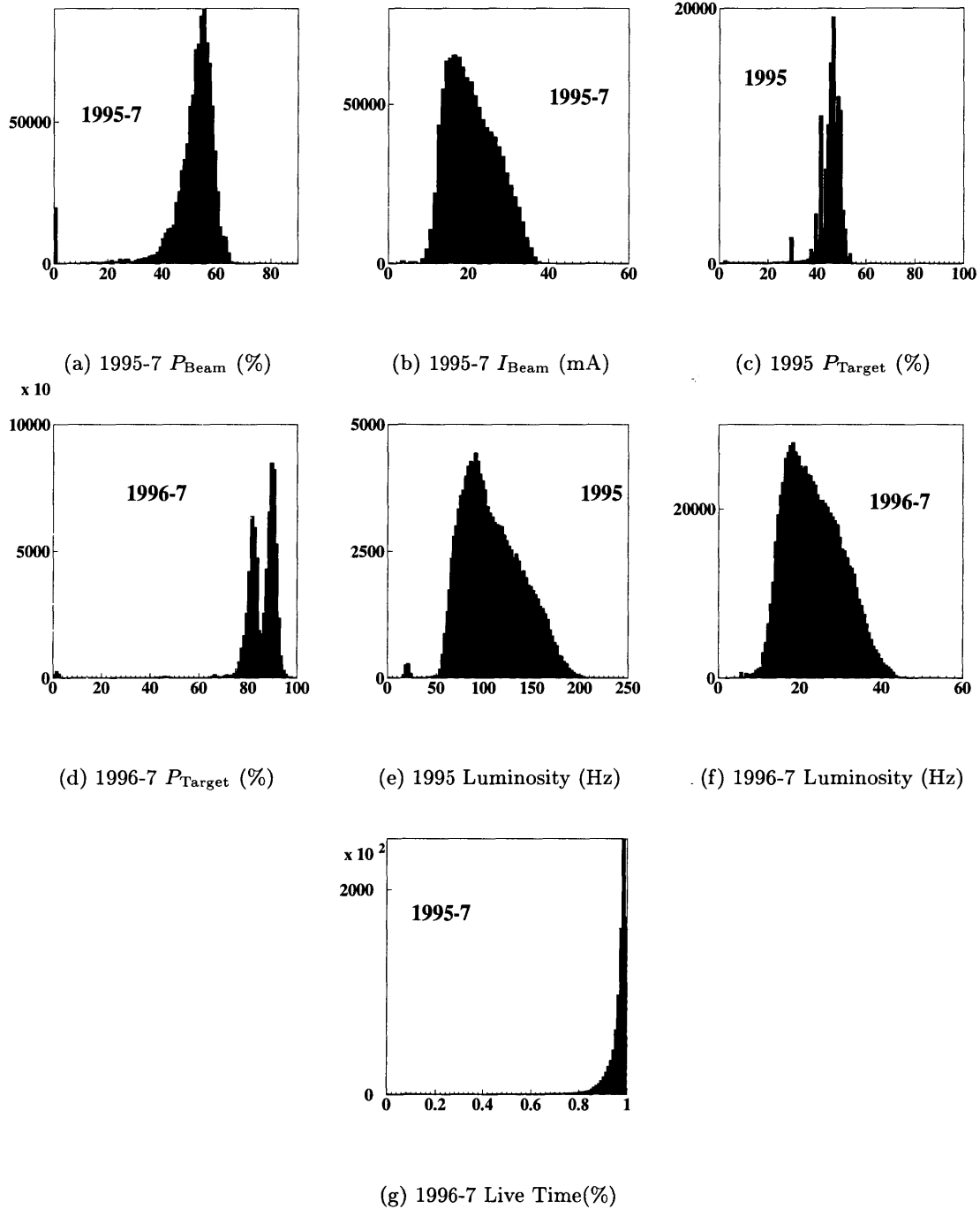


Figure 5-3: Distributions of the basic burst information at HERMES: a) the HERA beam polarization 1995-7, b) the HERA beam current 1995-7, c) The ^3He target polarization in 1995, d) the proton target polarization in 1996-7, e) the luminosity monitor rate in 1995, f) the luminosity monitor rate in 1996-7, and g) The DAQ live time.

5.2.2.1 Beam Conditions

A high precision DIS experiment require intense, stable beam currents. Experiment studying spin polarization additionally require large, stable, well-measured beam polarizations. Cuts were placed on the HERMES data records to ensure both conditions. The beam current and polarization were forced to remain in the reasonable operating range of HERA for each running year. For the polarization, the measured points each minute were smoothed by a cubic spline, and small gaps in the measurement were interpolated. Large gaps were removed from analysis. In addition, expert data quality cuts required at least one beam polarimeter to be fully operational and delivering precise polarization measurements. The exact cuts are listed in Table 5.1. These are motivated by beam current and polarization distributions shown in Figure 5-3.

5.2.2.2 Target Conditions

As with the beam, high intensity (or density), high polarization, and strong stability comprise the ideal conditions for precision measurement. The target is required to have a well-defined nuclear polarization state, either parallel or anti-parallel to the beam polarization direction. With the ABS, periods with only nuclear polarization states were selected, as multi-state rotations may cause luminosity asymmetries from higher residual electron polarization.

The target polarization and density are also required to remain in a reasonable operating range. With ^3He , the target polarization was primarily determined from Pumping Cell Polarimeter measurements. When the PCP failed, fill-averaged Target Optical Monitor values substitute. Target Expert Data Quality lists separate the polarized target running from unpolarized and remove periods of target hardware failure. The exact cuts are listed in Table 5.1.

5.2.2.3 Luminosity

The HERMES luminosity monitor provides a relative normalization to DIS cross-section measurements by detecting coincident Bhabba scattering of beam positrons off the target electrons. The rate of coincident scatters is a sensitive test of HERA positron beam stability. For each target, this rate is required to remain in a nominal operating range. For the proton target,

Beam Condition Data Selection	
1995: Good Polarization Good Current Gaps Well Constrained Expert Data Quality	$40\% < P_{e^+} < 70\%$ $8 \text{ mA} < I_{e^+} < 32 \text{ mA}$ Gap Time < 30 minutes. Select good TPOL Run List
1996-7: Good Polarization Good Current Gaps Well Constrained Expert Data Quality	$30\% < P_{e^+} < 80\%$ $8 \text{ mA} \leq I \leq 50 \text{ mA}$ Gap Time < 5 minutes. Select good TPOL/LPOL Burst List
Target Condition Data Selection	
1995: Good Spin Bit Good Density (nucleons/cm ²) Good Polarization Expert Data Quality	Bit= 0x3 ($\uparrow\downarrow$), 0x5 ($\uparrow\uparrow$) $0.85 \cdot 10^{15} < \rho_{^3\text{He}} < 1.5 \cdot 10^{15}$ $30\% < P_{^3\text{He}} < 60\%$ Select Good Target Run List
1996-7: Good Spin Bit Good Polarization in the BRP Well-defined Atomic Fraction Expert Data Quality (<i>Cal carry over?</i>)	Bit= 0x4 ($\uparrow\downarrow$), 0x8 ($\uparrow\uparrow$) $70\% < P_p < 99\%$ $\alpha_0 > 0$ and $\alpha_R > 0$ Select Good Target Record List
Luminosity Condition Data Selection	
1995: Good Lumi Monitor Rate Luminosity Ratio (Lumi Rate)/(density · current)	$40 \text{ Hz} < R_{\text{Bhabba}} < 210 \text{ Hz}$ $5 \cdot 10^{-15} < \frac{R_{\text{Bhabba}}}{\rho_{^3\text{He}} \cdot I_{e^+}} < 7.2 \cdot 10^{-15}$
1996-7: Good Lumi Monitor Rate Good GMS	$5 \text{ Hz} \leq R_{\text{Bhabba}} \leq 60 \text{ Hz}$ No Dead Blocks

Table 5.1: Beam and Target Conditions Data Quality Selection.

residual electron polarization in the hydrogen atom sample may produce spin-correlated asymmetries in the luminosity rate of a few percent. This bias is removed by smoothing the Bhabba rates in order to average them across target spin states.

Another independent determination of luminosity comes from beam current times target density values. For the 1995 data, the ratio of these luminosity determinations is required to be nearly constant. There is no direct measurement of target density with the ABS, so this requirement was not applicable in 1996-7.

Finally, the Gain Monitoring System continually monitors the response of the Luminosity Monitor calorimeter since 1996. The system compares the response of each calorimeter block to a reference laser beam with expected values. All blocks of the calorimeter are required to function optimally. The exact cuts are listed in Table 5.1.

5.2.2.4 Data Acquisition

The HERMES DAQ controls the online collection of data. Critical failures in this system can compromise the quality of the collected data; several cuts are placed to ensure the system works optimally.

The record length measures the total data taking time represented by a record in seconds. The “live time” of the DAQ measures fraction of this time that the DAQ is not busy and is able to collect new data. The live time is defined as the ratio of accepted triggers to generated triggers,

$$\text{Live Fraction} = \frac{T_{\text{Acc}}}{T_{\text{Gen}}} \quad (5.1)$$

Both the record length and the live time multiply the luminosity to normalize the experimental count rate. Cuts requiring nominal data acquisition efficiency and stability are listed in Table 5.2.

During the start and end of each run, the DAQ performs a variety of initialization and cleanup tasks, which are CPU hungry. The live time in these periods is typically very low, and occasional mistimings occurs in the event collection. For this reason, the initial and final records of each run are excluded.

Data Acquisition Related Cuts	
1995:	
Good Live Time	50% < Live Fraction < 100%
Good Record Length	$9s \leq t_{\text{record}} \leq 11s$
Remove Initialization	Exclude first 3 bursts and last burst
1996-7:	
Good Live Time	50% < Live Fraction < 100%
Good Record Length	$0s < t_{\text{record}} \leq 11s$
Remove Initialization	Exclude first and last burst
Require Synchronization	Exclude any records with errors.

Table 5.2: Data Acquisition Quality Selection

Finally, synchronization mistakes in the data acquisition may occur, in which events are associated with the wrong polarization state. The event record includes a large amount of redundant timing information, allowing one to identify and exclude records where a polarization assignment discrepancy may have occurred. These problems are mainly contained in the proton data, in which the rapid polarization reversal of the target exacerbates the synchronization difficulty.

5.2.2.5 Tracking

Confidence in the detection and determination of particle trajectories requires the proper functioning of the tracking system in the spectrometer. In 1995, failures, or trips, in the chamber high voltages were detected by examining the efficiency tracking in the front and back regions of the spectrometer. In 1996, detailed records of chamber HV readbacks began to be stored, allowing one to cut on FC and BC HV trips directly. In 1997, the Vertex Chambers were included in the tracking algorithm, and VC experts examined the detector performance to reject hardware failures. These cuts are summarized in Table 5.3.

Since the spectrometer was constructed top/bottom symmetric most components, it is possible for a failure to occur in one half of the detector and not the other. A multi-track coincidence is necessary in the detector for semi-inclusive physics, requiring the full detector acceptance to be available. Both detector halves are required to be operation for semi-inclusive event analysis.

5.2.2.6 Particle Identification Conditions

DIS studies at HERMES require separation of leptons and hadrons through the stable operation of the PID detectors. These detectors are also key in the trigger at HERMES. A variety of techniques are used to determine the performance of these detectors.

The GMS continually checks the response of the calorimeter and preshower PMTs. For the H1 hodoscope, scaler counters connected to each hodoscope channel indicate whether the channel has high voltage on and is taking data. To understand the Čerenkov performance, a lepton identification efficiency was calculated, which is simply the efficiency of leptons identified in the Čerenkov. Finally, the Čerenkov and TRD groups identify bursts where the hardware of these detectors experienced problems. The specifics of these cuts are listed in Table 5.3.

5.2.2.7 Overall Data Collection Efficiency

Studies of the 1995 data indicated that the data stability was not satisfactory even after the above cuts. To further improve data quality, running periods where portions of the detector intermittently failed were identified and removed. For example, areas where the detector tripped frequently are suspected of having conditions too poor for precision analysis. All indicators of detector stability in later years showed marked improvement, and these cuts were dropped. They are summarized in Table 5.3.

5.2.2.8 Record Quality Summary

Table 5.4 summarizes the number of analyzed records remaining in each year after the above cuts.

5.3 Event Selection

Once a collection of analyzable bursts is determined, several criteria select the recorded events representing inclusive and semi-inclusive DIS reactions. A particle identification algorithm

Tracking Condition Cuts	
1995: Good Forward Efficiency Good Backward Efficiency Previous Burst	$80 \% < \epsilon_{\text{front}} < 100 \%$ $94 \% < \epsilon_{\text{back}} < 100 \%$ Reject one burst before detected trips
1996-7: High Voltage Trips	Reject FC and BC HV trips.
1997: Vertex Chamber Expert Data Quality	Select VC Expert Run List
PID Condition Cuts	
1995-7: Gain Monitoring System $N_i^b \leq 4$ Scaler Counters TRD Expert DQ Čerenkov Expert DQ	Reject intermittent bad channels in the calorimeter and preshower. Reject bad hodoscope channels Select Good Run List Select Good Run List
Overall Efficiency Cuts	
1995: Maximum Fraction of Gaps in a Run Minimum Fraction of Good Bursts in a Run Minimum Good Bursts in a Fill (top and bottom separately):	$\frac{n_{\text{gaps}}}{n_{\text{bursts}}} < 0.10$ $\frac{n_{\text{good bursts}}}{n_{\text{bursts}}} > .40$ $n_{\text{good bursts}}^+ \geq 100$ $n_{\text{good bursts}}^- \geq 100$

Table 5.3: Data quality cuts on the tracking and particle identification detectors, as well as cuts on overall running efficiency.

	1995	1996	1997
$\langle P_{\text{Beam}} \rangle$	55.1%	52.4 %	53.0%
$\langle P_{\text{Target}} \rangle$	45.8 %	81.9 %	89.3%
Good Runs	2178	3308	7284
Good μ DST records, spins $\uparrow\downarrow$	29913	82442	187158
Good μ DST records, spins $\uparrow\uparrow$	29590	82436	186843

Table 5.4: A Summary of the Final Burst Selection.

Track Selection Criterion	
Geometry Requirements: Require origin inside target: (1995) (1996-7) (1995-7) Impose angular acceptance: Require direct hit in calorimeter :	$-30 < z_{\text{vertex}} < 30 \text{ cm}$ $-18 < z_{\text{vertex}} < 18 \text{ cm}$ $r_{\text{vertex}} < 0.75 \text{ cm}$ $40 < \theta_y < 140 \text{ mrad}$ $-170 < \theta_x < 170 \text{ mrad}$ $ x_{\text{Calo}} < 175 \text{ cm}$ $ y_{\text{Calo}} > 30 \text{ cm}$
Kinematic Cuts: Isolate scaling region Remove resonance region (inclusive) Ensure factorization (semi-inclusive) Reduce radiative corrections	$Q^2 > 1 \text{ GeV}^2$ $W^2 > 4 \text{ GeV}^2$ $W^2 > 10 \text{ GeV}^2$ $y < 0.85$
PID Criteria: Identify leptons cleanly: Identify hadrons cleanly: (1995, 4 detectors) (1996-7)	$\text{PID}_{95} > 2$ $\text{PID}_{95} < -1$ $\text{PID}_3 + \text{PID}_5 < 0$
Semi-Incl. Hadron Criterion: Increase parton-hadron correlation:	$z_h > 0.2$ $x_F > 0.1$
Pion Identification: Require Čerenkov ID: (1995) (1996-7) Reduce p/K misidentification:	Average number of photoelectrons > 0.25 $9.5 < P_h < 21 \text{ GeV}/c$ $4.9 < P_h < 13.5 \text{ GeV}/c$ $ x^{e/\pi} - x^h _{\check{C}er} < 52 \text{ cm}$

Table 5.5: Cuts selecting inclusive and semi-inclusive deep-inelastic events.

separates scattered positrons from hadronic background. Kinematic cuts on this positron and any coincident hadrons then define our DIS samples. Table 5.5 summarizes the selection criteria. These criteria are motivated in the sections below.

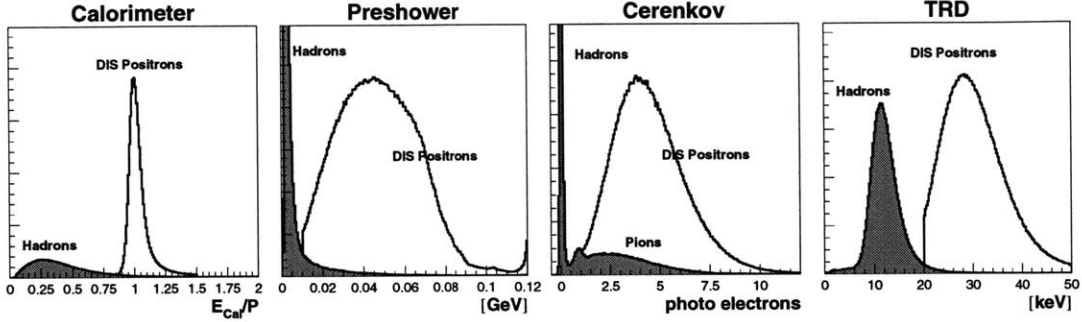


Figure 5-4: Responses of the particle identification detectors to positrons passing deep-inelastic scattering kinematic cuts (white) and hadrons (shaded).

5.3.1 Particle Identification

5.3.1.1 Electron and Hadron Separation

Each of the four HERMES particle identification detectors responds differently to the passage of electrons and hadrons, as discussed in 3.3.2. Figure 5-4 shows sample response distributions for each of the four PID detectors. For the data analysis, a convenient algorithm establishes a reliable method to use these responses for electron and hadron separation.

The response of each PID detector to both hadrons and electrons has been pre-determined either by test beam data or Monte Carlo simulations [122]. These determinations yield a response function for each detector D , $P^D(i|R)$, which represents the conditional probability that particle i generated response R . $P^D(i|R)$ is normalized to one. In practice, the detector responses for a give particle are momentum and angle dependent, and this information is provided by the track reconstruction procedure in section 5.1.3. Bayes theorem tells us for a response R , the probability it was generated by particle i is given by

$$P(i) = \frac{\phi^i P(i|R)}{\sum_j \phi^j P(j|R)}. \quad (5.2)$$

ϕ^i is the average flux of particle type i for a given kinematics.

In the simplest case, only electrons and hadrons require separation. Hence Eq. (5.2) becomes,

$$P(e) = \frac{P(e|R)}{\Phi P(h|R) + P(e|R)}, \quad (5.3)$$

$$P(h) = \frac{P(h|R)}{\Phi P(h|R) + P(e|R)}. \quad (5.4)$$

where Φ is the hadron/electron flux ratio, ϕ^h/ϕ^e .

For the analysis, it is convenient to define a logarithmic likelihood particle identification parameter, "PID," by taking the ratio of the electron and hadron probabilities above,

$$\text{PID} = \log_{10} \left(\frac{P^e}{P^h} \right) = \log_{10} \left(\frac{P(e|R)}{\Phi P(h|R)} \right) = \log_{10} \left(\frac{P(e|R)}{P(h|R)} \right) - \log_{10} \Phi. \quad (5.5)$$

A PID parameter may be defined for each detector. Composite likelihoods are then formed by adding the PID parameter for several detectors, which is equivalent to multiply the probability ratios in Equation (5.5). For example,

$$\text{PID3} = \text{PID}^{\check{\text{Cerenkov}}} + \text{PID}^{\text{Calorimeter}} + \text{PID}^{\text{Preshower}}, \quad (5.6)$$

and

$$\text{PID5} = \text{PID}^{\text{TRD}}. \quad (5.7)$$

In a first order analysis, one ignores the flux factor, which provides a constant offset to the coordinate axis of the distributions. These variables, then, possess a simple interpretation. Particles with positive PID are likely to be electrons, and particles with negative PID, hadrons. The PID3+PID5 distribution for all tracks in the 1997 data is shown in Figure 5-5.

In 1996-7, PID3+PID5 provides the cut variable to separate electrons and hadrons. The first attempt at this analysis in 1995, though, involved two further complications. In this analysis, parent distributions for the TRD were not yet considered. Instead, a hard cut was

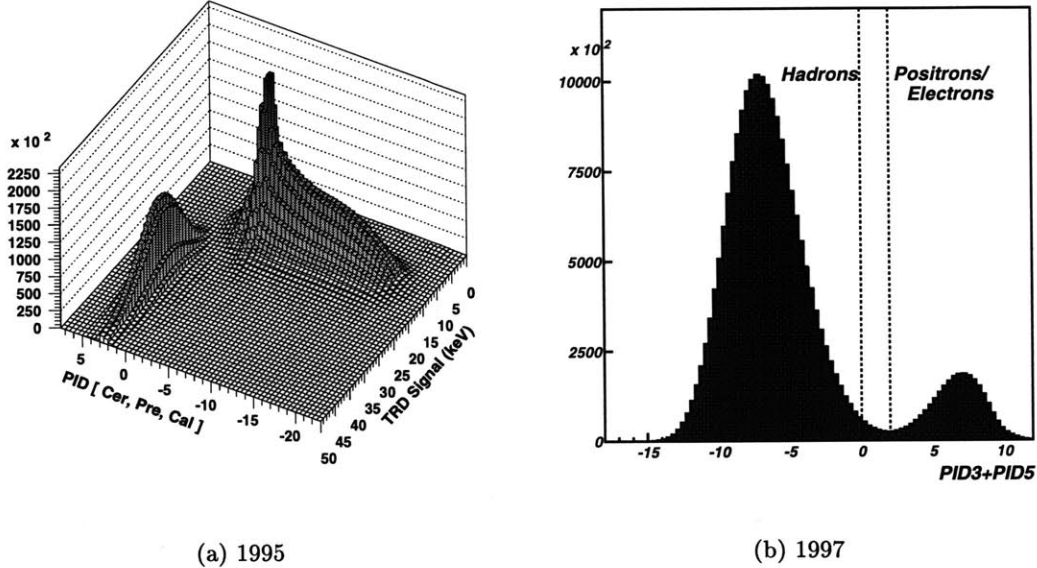


Figure 5-5: The distribution of PID variables for detected tracks in (a) 1995 and (b) 1997. In 1995, the PID3 versus TRD mean response plane is shown. In 1997, the distribution of PID3+PID5 is plotted for all tracks with momentum greater than 3.5 GeV/c. The dotted lines show the regions of identified hadrons and leptons.

placed on a truncated mean response of the TRD modules and the PID3:

$$PID_{95} = PID3 + 0.31 (\text{TRD}_{\text{Mean}}) - 5.48. \quad (5.8)$$

In addition, instabilities led to more frequent trips of the PID detectors. When the TRD in particular failed, the particle identification relied only on the other three detectors.

$$PID_{95} = PID3. \quad (\text{No TRD}) \quad (5.9)$$

The positron and hadron separation in 1995 is also shown in Figure 5-5. For the cuts chosen, the contamination of misidentified hadrons in the deep-inelastic scattered positron sample is estimated to be less than 1% [122]. The contamination of positrons and electrons in the semi-inclusive hadron sample is also negligible. A more detailed discussion of HERMES particle identification can be found in Reference [122].

5.3.1.2 Pion Separation

A unique feature of HERMES is the identification of pions among hadrons using the threshold Čerenkov detector, as described in Section 3.3.2.1. By requiring identified hadrons with momenta between 3.8 and 13.8 GeV/c in 1996-7 to produce photoelectrons in the Čerenkov, a clean sample of pions may be established. In 1995, this window is between 5.6 and 19.8 GeV/c.

In practice, however, the efficiency for pion detection is a strong function of momentum below 4.9 GeV/c in 1996-7 and 9 GeV/c in 1995. This threshold behavior is not well enough understood to minimize pion acceptance systematic uncertainties [150]. A conservative window is motivated by the need to simulate the Čerenkov accurately (see Section 6.2.3), which requires restriction to the high efficiency momentum region.

One other concern affects pion identification. The coarse resolution of the Čerenkov mirrors may allow two tracks whose trajectories through the Čerenkov detector nearly overlap to be assigned to the identical Čerenkov response in the reconstruction. Hence, low momenta kaons and protons may seem to fire the Čerenkov if they are coincident with a high momentum pion or electron [151]. This is a source of background on the otherwise clean pion sample, and it is rejected by requiring that a pion candidate does not approach any other positron or pion candidate by less than 52 cm in the Čerenkov.

5.3.2 Selection of DIS Events

Once leptons have been identified in the detector, their kinematics completely specify the x , Q^2 , W^2 of the event. Electrons are considered here in addition to the positrons, as they measure charge-symmetric background in the positron sample. Kinematic cuts on the lepton delimit the phase space associated with deep-inelastic scattering.

For each event, the highest momentum lepton is selected for calculation of the event properties. Cuts on the lepton longitudinal and radial vertex position, z_{vertex} and r_{vertex} , ensure this track originated inside the HERMES gas target. Angular cuts in θ_x and θ_y require the track to pass directly through the HERMES acceptance. A further requirement that the track struck inside the calorimeter spatial limits is used to ensure the calorimeter PID is properly determined.

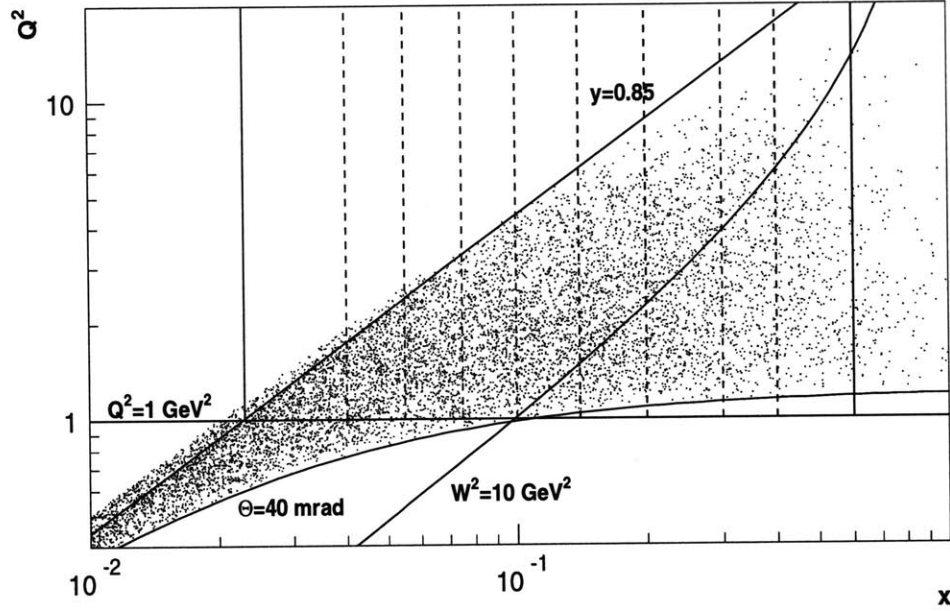


Figure 5-6: The distribution of DIS events in the HERMES in the x and Q^2 kinematic plane. The solid lines show the applied cuts in the semi-inclusive analysis [152].

For quality lepton tracks, physics cuts are placed. An upper limit on kinematic y suppresses radiative corrections to the cross-section. The cut, $W^2 > 4 \text{ GeV}^2$, selects events in the deep-inelastic region, where the nucleon breaks apart incoherently. The requirement, $Q^2 > 1 \text{ GeV}^2$, allows one to model the events with perturbative QCD concepts, and it also suppresses higher twist effects. These cuts establish a base sample of inclusive DIS, distributed as shown in Figure 5-6.

In semi-inclusive DIS, one or more hadrons are coincident with each DIS positron in the event. Hence, these events form subsamples of the inclusive sample. Hadron fragmentation is analyzed assuming factorization; Monte Carlo studies suggest that a cut of $W^2 > 10 \text{ GeV}^2$ is the best choice for ensuring the validity of this assumption at HERMES [153].

Each hadron track is required to originate in the target and propagate directly through the detector as in the lepton case. Further cuts, $z_h > 0.2$ and $x_F > 0.1$ maximize the correlation of the particles to the struck quark in the event. These cuts are also necessary to achieve good agreement between HERMES data and Monte Carlo; this is discussed further in Section 6.2.2.

	1995	1996	1997
e^+	2143301	719959	1551177
e^-	21784	10164	23468
h^+	269958	95107	207575
h^-	169666	54762	118691
π^+	15657	23085	72490
π^-	10848	22490	48885

Table 5.6: Particle Multiplicities for Each Year.

During each year of running, a summation of the inclusive e^+ and e^- , and for semi-inclusive h^+, h^-, π^+ , and π^- passing the above cuts is formed. The semi-inclusive samples consists of the total yield of particular hadrons that passes all cuts, allowing events with multiple detected hadrons to be counted several times. The summary of these total particle yields is listed in Table 5.6.

5.4 Formation of the Asymmetries

With event samples established, the procedure to form the DIS double-spin asymmetry on a nuclear target becomes straightforward. The total yield of events of type h per spin state, $N_{\uparrow\downarrow(\uparrow\uparrow)}^h$, may be related to the positron-target double-spin asymmetry, A_{\parallel}^h by

$$N_{\uparrow\downarrow(\uparrow\uparrow)}^h(x, Q^2, z) = \int \mathcal{A}(t, x, Q^2, z) \bar{\sigma}(x, Q^2, z) \mathcal{L}(t) \left(1 + (-) A_{\parallel}^h(x, Q^2, z) p_B(t) p_T(t) \right) dt, \quad (5.10)$$

where $\bar{\sigma}(x, Q^2, z)$ is the unpolarized DIS cross-section in Equation (2.11). $\mathcal{L}(t)$ represents the effective luminosity at the experiment in each spin state; and $\mathcal{A}^h(t, x, Q^2, z)$ contains the acceptance and efficiency factors for HERMES events of type h . Here, h may represent any of the inclusive or semi-inclusive event channels considered on either the proton or ^3He targets. Note the inclusive cross-sections have x and Q^2 dependence only, while semi-inclusive cross-sections have additional z_h dependence. One wishes to study the primary dependence of the asymmetry

on the quark momentum fraction x_{Bjorken} . Equation (5.10) is further integrated over the Q^2 and z_h dependences.

The acceptance and efficiency of the experiment are assumed to be constant on the time-scale of the target spin-flip, so that a time-averaged $\langle \mathcal{A}(x, Q^2, z) \rangle$ can be factored out of the integral. The luminosities and polarizations are then the only time-dependent quantities in the integral. This time integral is effectively a sum over all collected bursts in the experiment: if one rewrites the luminosity integrals as,

$$L = \int \mathcal{L}(t) dt, \quad (5.11)$$

$$L_P = \int \mathcal{L}(t) |P_B(t) P_T(t)| dt, \quad (5.12)$$

then the raw counting rate asymmetry, $A_{||}^h(x)$ is,

$$A_{||}^h(x) = \frac{N^{\uparrow\downarrow} L^{\uparrow\uparrow} - N^{\uparrow\uparrow} L^{\uparrow\downarrow}}{N^{\uparrow\downarrow} L_P^{\uparrow\uparrow} + N^{\uparrow\uparrow} L_P^{\uparrow\downarrow}}. \quad (5.13)$$

In this asymmetry, the average acceptance and efficiency factors cancel between the numerator and denominator. In 1995, the efficiencies were considered stable during fills but were suspected to be unstable between fills [114, 154]. Hence, the asymmetries $A_{||}$ are calculated for each HERA fill independently, and are then averaged together. In 1996 and 1997, the counts were integrated over the entire year.

The beam and target double-spin asymmetry, $A_{||}^h$, relates to the virtual photoabsorption asymmetry, by

$$A_1^h = \frac{g_1^h}{F_1^h}(x) = \frac{1}{(1 + \gamma\eta)} \frac{A_{||}^h}{D}(x) \quad (5.14)$$

$$= \frac{1}{(1 + \gamma\eta)} \frac{N^{\uparrow\downarrow} L^{\uparrow\uparrow} - N^{\uparrow\uparrow} L^{\uparrow\downarrow}}{N^{\uparrow\downarrow} L_P^{\uparrow\uparrow} D^{\uparrow\uparrow} + N^{\uparrow\uparrow} L_P^{\uparrow\downarrow} D^{\uparrow\downarrow}}(x). \quad (5.15)$$

$$(5.16)$$

Bin	x range	$\langle x \rangle$
1	0.023-0.040	0.033
2	0.040-0.055	0.047
3	0.055-0.075	0.065
4	0.075-0.100	0.087
5	0.100-0.140	0.119
6	0.140-0.200	0.168
7	0.200-0.300	0.245
8	0.300-0.400	0.342
9	0.400-0.600	0.465

Table 5.7: Definition of the bins in x . The $\langle x \rangle$ of deep-inelastic scattering events in each bin is also listed.

This essentially is a rearrangement of Equation (2.38), and the analysis assumes $g_2^h=0$. With this assumption, the virtual photon asymmetry, A_1^h is identical to the structure function ratio $\frac{g_1^h}{F_1^h}$. The kinematic factors, D , η , and γ , are defined in Section 2.1.4.1. The depolarization factor, D , may vary slightly between the spin states due to binning effects, and it is evaluated for each target spin. For this analysis, the HERMES events have been sorted into nine bins in x . Table 5.7 lists the range of x defining these bins, and Table A.1 shows the average values of D , γ , and η in this binning scheme.

5.5 Corrections to the Raw Asymmetries

A number of subtle corrections to the above procedure are necessary to reproduce the true asymmetries in nature for each event type. Listed here are the four corrections necessary to modify the extracted in the above formalism in order to reproduce the true physics asymmetry in nature.

5.5.1 Background Corrections

Positrons from photoproduced e^+e^- pairs may also contribute to the sample defined by the cuts in Table 5.5. This is the dominant background in the otherwise clean DIS sample. This process

$\langle x \rangle$	$K_{\text{smear}}(1996)$			$K_{\text{smear}}(1997)$		
	e^+	h^+	h^-	e^+	h^+	h^-
0.033	0.946±0.009	0.916±0.007	0.984±0.019	0.946±0.009	0.914±0.007	0.984±0.019
0.047	0.975±0.009	0.934±0.007	0.965±0.017	0.975±0.009	0.935±0.007	0.970±0.017
0.065	0.967±0.009	0.934±0.007	0.947±0.015	0.967±0.009	0.934±0.007	0.947±0.015
0.087	0.955±0.009	0.930±0.006	0.932±0.011	0.955±0.009	0.931±0.006	0.932±0.011
0.119	0.937±0.009	0.937±0.005	0.934±0.007	0.937±0.009	0.932±0.004	0.930±0.007
0.168	0.931±0.008	0.957±0.004	0.956±0.005	0.931±0.008	0.952±0.004	0.950±0.005
0.245	0.934±0.007	0.977±0.003	0.978±0.004	0.934±0.007	0.977±0.003	0.978±0.004
0.342	0.966±0.008	0.993±0.003	0.992±0.004	0.966±0.008	0.994±0.003	0.994±0.003
0.465	0.989±0.005	0.999±0.004	0.995±0.004	0.989±0.005	1.001±0.003	0.998±0.004

Table 5.8: Smearing corrections for the proton asymmetries. The two years are distinguished by the different reconstruction methods used: “NO VC” in 1996 and “Standard” in 1997[156].

is also the major source of detected electrons. Hence, detected electrons may be considered a tag on the charge-symmetric lepton production, and they allow a convenient background subtraction. The data analysis treats positrons and electrons identically, but each electron is given a negative weight in the inclusive DIS sample. When hadrons are coincident with the electron, they are also subtracted from the appropriate semi-inclusive sample.

Diffractive processes also contribute backgrounds to DIS. In this case, ρ production and decay can generate pion background uncorrelated to the nucleon spin structure. Direct estimation of this contribution, however, has indicated it is small enough to be neglected [155].

5.5.2 Smearing Corrections

In any detector, the measured kinematic quantities do not reproduce the true kinematics of Nature perfectly. The effect of such systematic deviations on the physics result must be estimated. At HERMES, the measured kinematics deviate by two effects. First, charged particles propagating through the detector can straggle and produce photons, altering kinematics as they are measured. Second, biases from imperfect detector alignment and track reconstruction contribute. Both effects can be estimated by the HERMES Monte Carlo [157]. To do this, one generates a large sample of polarized DIS events inside a perfect representation of the HERMES detector. These events are then propagated through a realistic GEANT [158] model of the spectrometer and reconstructed with HRC. Physics asymmetries are formed from both the perfect

and realistic acceptance samples. They are divided to determine the smearing correction.

$$K_{\text{smear}} = \frac{A_{\text{MC,perfect}}^h}{A_{\text{MC,real}}^h} \cdot A_{\text{corrected}}^h = A_{\text{raw}}^h K_{\text{smear}}. \quad (5.17)$$

In this procedure, the calculated correction depends on the input asymmetry in the Monte Carlo, and a few iterations in the procedure are required.

Smearing corrections have been calculated for all three years of HERMES running. The corrections for the ^3He asymmetries are small enough to be neglected [159]. The proton corrections are listed in Table 5.8. Smearing corrections for semi-inclusive π^+ and π^- events have not been calculated, and they are assumed to be identical to the hadron corrections.

5.5.3 Radiative Corrections

The discussion thus far has assumed that the scattering process can be accurately modeled using the tree diagram in QED as in Figure 2-1. Higher order radiative processes also contribute to the measured cross-section and must be corrected in the final asymmetries. The Feynman diagrams for the relevant first order QED processes are shown in Figure 5-7. Radiative tails in elastic and quasielastic positron scattering also contribute significantly to the event sample. Electroweak corrections are negligible as the HERMES Q^2 is much smaller than the mass of the Z^0 .

To model radiative effects, the ^1H and ^3He asymmetries have been input into the code POLRAD [160, 154], which calculates the correction Δ_{RC} needed to reproduce the Born cross-section.

$$A_{\text{corrected}}^h = A_{\text{measured}}^h - \Delta_{\text{RC}}, \quad (5.18)$$

where

$$\Delta_{\text{RC}} = A_{\text{total}}^h - A_{\text{Born}}^h. \quad (5.19)$$

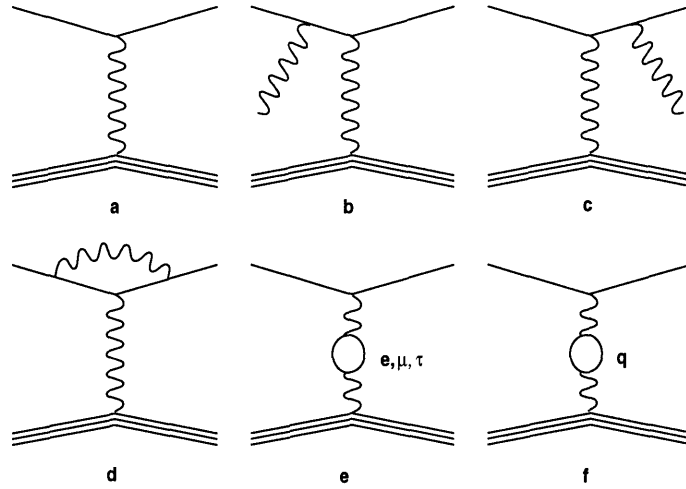


Figure 5-7: Feynman diagrams for radiative corrections. The one photon exchange term (Born) term is shown in (a). The other plots show the diagrams for (b) initial state bremsstrahlung correction, (c) the final state bremsstrahlung correction, (d) the vertex correction, and (e),(f) the vacuum polarisation correction.

$\langle x \rangle$	Δ_{RC}		
	${}^3\text{He}$	${}^1\text{H}$ (1996)	${}^1\text{H}$ (1997)
0.033	0.0571 ± 0.00292	0.00121 ± 0.00006	0.00121 ± 0.00006
0.047	0.0494 ± 0.00134	0.00119 ± 0.00004	0.00119 ± 0.00004
0.065	0.0474 ± 0.00064	0.00117 ± 0.00003	0.00117 ± 0.00003
0.087	0.0439 ± 0.00023	0.00097 ± 0.00004	0.00097 ± 0.00004
0.119	0.0423 ± 0.00062	0.00049 ± 0.00003	0.00049 ± 0.00003
0.168	0.0404 ± 0.00100	-0.00037 ± 0.00002	-0.00037 ± 0.00002
0.245	0.0389 ± 0.00138	-0.00131 ± 0.00010	-0.00123 ± 0.00010
0.342	0.0399 ± 0.00181	-0.00205 ± 0.00006	-0.00201 ± 0.00006
0.465	0.0384 ± 0.00196	-0.00223 ± 0.00013	-0.00210 ± 0.00013

Table 5.9: Radiative corrections to the inclusive asymmetries [160, 154].

The resulting corrections to the measured inclusive asymmetries are listed in Table 5.9. The ${}^3\text{He}$ corrections tend to be much larger than the proton corrections, as significant tails in elastic electron scattering on ${}^3\text{He}$ nuclei are produced. Corrections for semi-inclusive events have been determined to be small enough to be negligible [161].

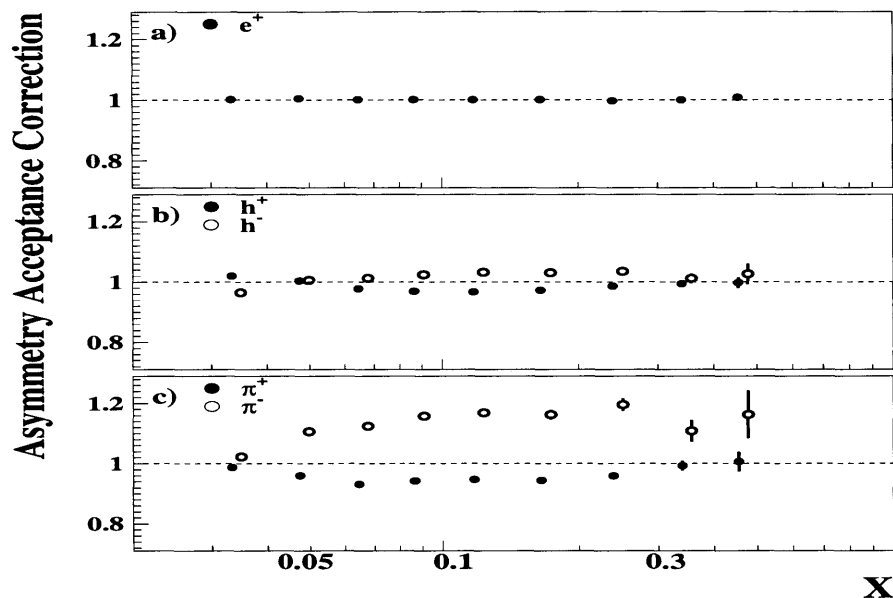


Figure 5-8: The correction to relate the HERMES measured asymmetry on the proton to an asymmetry in 4π , according to HMC. The plots show the corrections for a) the inclusive asymmetry, b) the semi-inclusive h^+ and h^- asymmetries, c) the semi-inclusive π^+ and π^- asymmetries.

5.5.4 Comment on Acceptance Corrections

As the HERMES acceptance covers only a small range in angles in space, asymmetries are measured in one corner of the phase space. For the kinematic cuts given in section 5.3.2, approximately 50% of generated DIS positrons reach the detector; only $\sim 25\%$ of semi-inclusive DIS events are accepted. Asymmetries in all space, in 4π solid angle, are needed to allow clear comparison of the data with theory and other experiments.

Figure 5-8 shows a Monte Carlo investigation of the acceptance correction in the HERMES asymmetries on the proton. Section 5.4 argued that the acceptance function $\mathcal{A}(t, x, Q^2, z)$ cancelled in the asymmetry. For the inclusive asymmetry, $A_1^{e^+}$, the acceptance correction is nearly unity as expected. The semi-inclusive asymmetries, however, have 20% corrections. The theory of section 2.1.2 indicates the shapes of semi-inclusive asymmetries are controlled by the events' correlations to quark degrees of freedom, and z_{hadron} is one measure of this correlation. The forward acceptance and high magnetic field of the HERMES spectrometer

$\langle x \rangle$	K_{accept}			
	h^+	h^-	π^+	π^-
0.033	1.02±0.00	0.96±0.01	0.99±0.01	1.02±0.01
0.047	1.00±0.00	1.01±0.01	0.96±0.00	1.11±0.01
0.065	0.98±0.00	1.01±0.01	0.93±0.00	1.12±0.01
0.087	0.97±0.00	1.02±0.01	0.94±0.00	1.16±0.01
0.119	0.97±0.00	1.03±0.01	0.95±0.00	1.17±0.01
0.168	0.97±0.00	1.03±0.01	0.94±0.01	1.16±0.02
0.245	0.99±0.00	1.04±0.01	0.96±0.01	1.20±0.02
0.342	0.99±0.01	1.01±0.02	0.99±0.02	1.11±0.04
0.465	1.00±0.02	1.03±0.03	1.01±0.03	1.16±0.08

Table 5.10: Estimated acceptance corrections to the asymmetries, $A_{4\pi}^h/A_{\text{accepted}}^h$. The corrections are calculated using the PEPSI Monte Carlo with the GRSV[162] input parametrization. The corrections are listed for completeness, but are not used in the analysis; see Section 6.2.3 for details.

tend to select hadron tracks with high momentum. As a result, the distributions of HERMES accepted hadrons are skewed to higher z values than the distributions of the generated hadrons in 4π . The correlations of the asymmetries to the underlying quark distributions change in the acceptance, making a non-trivial effect on their shape.

Despite this, no acceptance correction is implemented in this analysis. Such a correction depends on the underlying quark polarizations in the proton, and a consistent procedure to implement a large correction would require significant iteration with the Monte Carlo. Instead, a better approach to extract the polarizations from the uncorrected asymmetries is presented in Chapter 6. Table 5.10 lists an approximation to the proton acceptance corrections using the Monte Carlo described in Section 6.2.3 and using the GRSV [163] parton distributions.

5.6 Statistical Uncertainties on the Asymmetries

The calculation of the statistical uncertainty of A_1 is straightforward. The luminosities and polarizations in the experiment are determined to high statistical precision. Thus, only the counting rate contributes, and it is Poisson distributed giving, $(\delta N)^2 = N$.

The counting rates for various event classes are weighted in the analysis. Hence, given a weight w_i for the i event, the uncertainty in the corrected counting rate is

$$\delta N^{\text{cor}} = \sqrt{\sum_i w_i^2}. \quad (5.20)$$

In the inclusive analysis, $w_i = +(-)1$ for leading positrons (electrons). The hadron charge multiplicity is included as an additional weight in the semi-inclusive cases, $w_i^{\text{semi}} = w_i^{\text{incl}} n_h$, where n_h is the average number of hadrons of type h per inclusive DIS event. Note that these corrections are very small: the average semi-inclusive weight is 1.02.

If one defines,

$$T = N^{\uparrow\downarrow} L^{\uparrow\uparrow} - N^{\uparrow\uparrow} L^{\uparrow\downarrow} \quad (5.21)$$

$$B = N^{\uparrow\downarrow} L_P^{\uparrow\uparrow} D^{\uparrow\uparrow} + N^{\uparrow\uparrow} L_P^{\uparrow\downarrow} D^{\uparrow\downarrow} \quad (5.22)$$

$$\frac{\partial(A_{\parallel}/D)}{\partial N^{\uparrow\downarrow}} = \frac{L^{\uparrow\uparrow}}{B} - \frac{TL_P^{\uparrow\uparrow} D^{\uparrow\uparrow}}{B^2} \quad (5.23)$$

$$\frac{\partial(A_{\parallel}/D)}{\partial N^{\uparrow\uparrow}} = \frac{L^{\uparrow\downarrow}}{B} - \frac{TL_P^{\uparrow\downarrow} D^{\uparrow\downarrow}}{B^2}, \quad (5.24)$$

then the statistical uncertainty is

$$\delta A_1 = \left(\frac{1}{1 + \gamma\eta} \right)^2 \left\{ \left(\frac{\partial A_{\parallel}/D}{\partial N^{\uparrow\downarrow}} \right)^2 (\delta N^{\uparrow\downarrow})^2 + \left(\frac{\partial A_{\parallel}/D}{\partial N^{\uparrow\uparrow}} \right)^2 (\delta N^{\uparrow\uparrow})^2 \right\}. \quad (5.25)$$

5.6.1 The Statistical Correlation

HERMES measures a family of asymmetries, A_1^h , for a variety of event classes h . The discussion of the analysis in Chapter 6 will benefit from a look at how these asymmetries are *correlated* to each other statistically. Semi-inclusive asymmetries are subsamples of inclusive asymmetries. One then expects a significant positive correlation between the semi-inclusive and inclusive measurements. One may analytically derive [152] that the asymmetry correlations are

proportional to the particle multiplicity, n^h , for each event type:

$$\rho_{ij} = Cor(A_1^{h_i}, A_1^{h_j}) = \frac{\langle n^{h_i} n^{h_j} \rangle}{\sqrt{\langle (n^{h_i})^2 \rangle \langle (n^{h_j})^2 \rangle}}. \quad (5.26)$$

Note that $n^{e^+} = 1$ by definition and that the correlation between asymmetries measured in two different years is zero. In general, the above expression is valid when $A_{||}$ does not approach ± 1 ; at HERMES, the parallel asymmetries are less than 0.15 in an x bin. With these correlations, a statistical covariance matrix C_A^{stat} may be defined, relating all the asymmetries.

$$C_A^{\text{stat},ij} = \rho^{ij} \delta A_1^{h_i} \delta A_1^{h_j}. \quad (5.27)$$

Each running year is considered separately in this analysis, as the experimental issues in each year do vary considerably. For the analysis of inclusive, h^+ , and h^- asymmetries, C_A^{stat} is a 9×9 matrix. When π^+ and π^- asymmetries in 1996 and 1997 are added to the analysis, C_A^{stat} becomes 13×13 .

The full matrix C_A^{stat} will be used in the analysis of Chapter 6. The diagonal elements of C_A^{stat} provide the systematic variance on each asymmetry,

$$\delta_{\text{stat}} A^i = \sqrt{C_A^{\text{stat},ii}}. \quad (5.28)$$

5.7 Systematic Uncertainties in the Asymmetries

Several experimental biases and theoretical ambiguities contribute uncertainty in the measured asymmetries. When discussing them, it will also be useful to consider the correlation of these uncertainties among all of the asymmetries. Hence one defines C_A^{sys} as the asymmetry systematic covariance matrix,

$$C_A^{\text{sys},ij} = Cov(A^i, A^j). \quad (5.29)$$

5.7.1 Beam Polarization Uncertainty

The beam polarization was continuously monitored by the Transverse Polarimeter except during one month when the Longitudinal Polarimeter alone was employed. The detailed systematics of this measurement are discussed in Chapter 4. The beam polarization measurement sets the scale of the y-axis in any presentation of an asymmetry. As this scale was determined only once in 1994 to a relative precision of $\frac{\delta P_{\text{scale}}}{P} = 3.26\%$, the uncertainty in this scale is 100% correlated among all HERMES asymmetry measurements. Point-to-point instabilities of $\frac{\delta P_{\text{point}}}{P} = (2.2\%, 0.9\%, 0.9\%)$ in (95, 96, 97) have been estimated independently for each year: they are 100% correlated among asymmetries within one year but are not correlated between years. Hence, the beam polarization covariance is

$$C_A^{\text{PB},ij} = A^i A^j \left[\left(\frac{\delta P_{\text{scale}}}{P} \right)^2 + \rho_{\text{point}} \left(\frac{\delta P_{\text{point}}}{P} \right)^2 \right], \quad (5.30)$$

where ρ_{point} is one within each year, but zero between years.

5.7.2 Target Polarization Uncertainty

The scale of the asymmetries is further determined by the target polarization measurement. In 1995, the ^3He target possessed a relative polarization uncertainty of $\frac{\delta P_{^3\text{He}}}{P} = 5\%$. Hence,

$$C_{A_{^3\text{He}}}^{\text{PT},ij} = A_{^3\text{He}}^i A_{^3\text{He}}^j \left(\frac{\delta P_{^3\text{He}}}{P} \right)^2. \quad (5.31)$$

The ABS requires more complicated treatment. In 1997, the relative target polarization uncertainty was determined to 4.5 %. In 1996, the target was first commissioned, and not yet well understood. Molecular recombination inside the target cell was much larger in this year, leading to an directly estimated polarization uncertainty over 12 % [164].

As this normalization uncertainty is too large for a precision analysis, the target polarization in 1996 was determined differently. The inclusive A_{\parallel} of both 1996 and 1997 were formed using the best target polarization calculations in each year. As both years measure the same physics, the resulting asymmetries should be identical within statistics. The 1996 target polarization is then determined by renormalizing the 96 inclusive asymmetry to match the 97 asymmetry.

The statistical error of this fitting constant, k , yields a polarization scale uncertainty of 4%, correlated among all 1996 asymmetries. The 96 normalization is fixed to the 97 values, so that 97 target polarization uncertainty of 4.5% correlates among both years.

$$C_{A_p}^{\text{PT},ij} = A_p^i A_p^j \left(\left(\frac{\delta P_{97}}{P} \right)^2 + \rho_{96} \left(\frac{\delta k}{k} \right)^2 \right). \quad (5.32)$$

The total target polarization uncertainty for the 1996 asymmetries becomes 6 % with this procedure.

5.7.3 Yield Fluctuations

The normalized yield of positrons during the running of the experiment should be a constant for constant acceptance and efficiency. Instabilities in the detector efficiencies can alter these yields in time-dependent manner; if the time constant of these instabilities is comparable to the target spin-flip time, then the asymmetries may be noticeably affected.

To test for instability, bits representing the target spin orientation are replaced by a random spin sequences. For each sequence i , a new asymmetry, $A_i^h(x)$, is calculated, for the entire x range. These random spin asymmetries should average to the true target spin asymmetry, and their variance should match the statistical uncertainty of physics asymmetry. A difference in the spread of the random asymmetry distribution from the expected sigma signals the presence of additional systematic effects.

The 1996 and 1997 inclusive and semi-inclusive asymmetries behave statistically and pass this test[165]. In 1995, however, the inclusive and semi-inclusive asymmetry variances are larger than expected [154, 166]. The likely cause of this extra uncertainty is fluctuations in particle yields on the time scale of spin flip. The difference between the expected and actual variance is included as a systematic uncertainty for each asymmetry on ${}^3\text{He}$,

$$(\sigma_{\text{Yield}}^h)^2 = (\sigma_{\text{observed}}^h)^2 - (\sigma_{\text{expected}}^h)^2. \quad (5.33)$$

This random spin uncertainty has been obtained using asymmetries averaged over all kinematics in the experiment. To apply this systematic uncertainty in each x bin, one further assume that any bias in the measured asymmetry produced by a yield fluctuation affects each bin coherently.

Asymmetry Type	σ_{Yield}
e^+	0.00256
h^+	0.00575
h^-	0.00547

Table 5.11: The inclusive and semi-inclusive asymmetry systematic uncertainties due to yield fluctuations in 1995[154, 166].

The calculated systematic uncertainties are listed in Table 5.11. Note that the pion uncertainty has not been directly calculated and it is assumed identical to the hadron uncertainty. One then applies the systematic error σ_{Yield}^h to the covariance matrix of every x bin. This gives the yield fluctuation covariance,

$$C_{A_{3\text{He}}}^{\text{Yield},ij} = \sigma_{\text{Yield}}^i \sigma_{\text{Yield}}^j. \quad (5.34)$$

5.7.4 Smearing and Radiative Corrections

Systematic uncertainties have been estimated for both the smearing and radiative corrections during the calculations described in 5.5.2 and 5.5.3. The smearing contributions are assumed completely correlated among asymmetries in each year, and they only apply to the proton asymmetries. Radiative corrections and systematic uncertainties are only needed for the inclusive asymmetries.

$$C_A^{\text{Smear./Rad.},ij} = A^i A^j \left(\frac{\delta k_{\text{smear}}}{k} \right)^2 + \rho_{\text{inclusive}} (\delta \Delta_{\text{RC}})^2. \quad (5.35)$$

5.7.5 Model for g_2

The derivation of Equation (5.14) assumes the structure function $g_2(x)$ is zero. In general, for a non-zero g_2 , A_1 and $\frac{g_1}{F_1}$ are not equivalent. This equation becomes,

$$\frac{g_1^h}{F_1^h}(x) = \frac{A_{||}^h(x)}{D(x)(1 + \gamma\eta)} + \frac{\gamma^2 - \eta\gamma}{1 + \gamma\eta} \frac{g_2^h}{F_1^h}, \quad (5.36)$$

$$A_1(x) = \frac{A_{||}^h(x)}{D(x)(1 + \gamma\eta)} + \frac{\eta\gamma(1 + \gamma^2)}{1 + \gamma\eta} \frac{g_2^h}{F_1^h}. \quad (5.37)$$

The function $g_2(x)$ has been measured directly at SLAC and CERN with inclusive DIS, and all these measurements are consistent with zero within the relevant x range of HERMES [167]. To estimate the systematic bias for the $g_2(x)$ assumption, the measurements of SLAC E154 [168] and E155 [169] have been fit to a second order polynomial.

The semi-inclusive asymmetries are assumed to have the same systematic uncertainty as the measured uncertainty in the inclusive case. Also, the effects of g_2 on the ^3He asymmetry extraction is estimated from g_2^n and g_2^p using nuclear corrections (see Section 6.4). The g_2 contributions are completely correlated for each target, but not between targets. Hence, the contributions become,

$$C_A^{g_2,ij} = \rho_{\text{target}} \frac{\gamma^2 - \eta\gamma}{1 + \gamma\eta} \left(\frac{\delta g_2}{F_1} \right)^2. \quad (5.38)$$

5.7.6 The uncertainty in R

The ratio of longitudinal to transverse cross-sections, R , enters the asymmetry calculation through the depolarization factor in Equation (2.42). The uncertainty of the world-averaged R measurement [17] contributes, as

$$\delta_R = \frac{\epsilon}{1 + \epsilon R} \delta R, \quad (5.39)$$

$\langle x \rangle$	R	δA_1
0.033	0.339 ± 0.087	0.040
0.047	0.333 ± 0.077	0.044
0.065	0.324 ± 0.067	0.043
0.087	0.311 ± 0.059	0.040
0.119	0.293 ± 0.042	0.030
0.168	0.268 ± 0.046	0.035
0.245	0.238 ± 0.039	0.031
0.342	0.188 ± 0.035	0.029
0.465	0.131 ± 0.036	0.031

Table 5.12: The value of R and its systematic uncertainty. Also shown is the corresponding uncertainty in A_1 .

and

$$C_A^{R,ij} = (\delta_R)^2 A^i A^j. \quad (5.40)$$

Table 5.12 lists the values of R and its uncertainty in the HERMES kinematic region.

5.8 The Final Asymmetries

The extracted asymmetries for the HERMES 1995, 1996 and 1997 data are presented in this Section. For all the figures, the values plotted represent the structure function ratio $\frac{g_1}{F_1}$, which is identical to the photon asymmetry A_1 except for the systematic uncertainty due to g_2 . The discussion will then use both the asymmetry and structure function ratio interchangeably. For the presentation of the final asymmetries, the proton asymmetries measured in 1996 and 1997 are combined to form the total HERMES asymmetries on the proton. Figure 5-9 compares the inclusive and semi-inclusive asymmetries in each year. Statistical agreement is observed between the two years; Table 5.13 lists the χ^2 compatibility of the two data sets.

The systematic uncertainty for each asymmetry is formed from the square root of a diagonal element of the matrix,

$$C_A^{\text{Sys}} = C_A^{\text{P}_B} + C_A^{\text{P}_T} + C_A^{\text{Smear./Rad.}} + C_A^{g_2} + C_A^R + C_A^{\text{Yield}}. \quad (5.41)$$

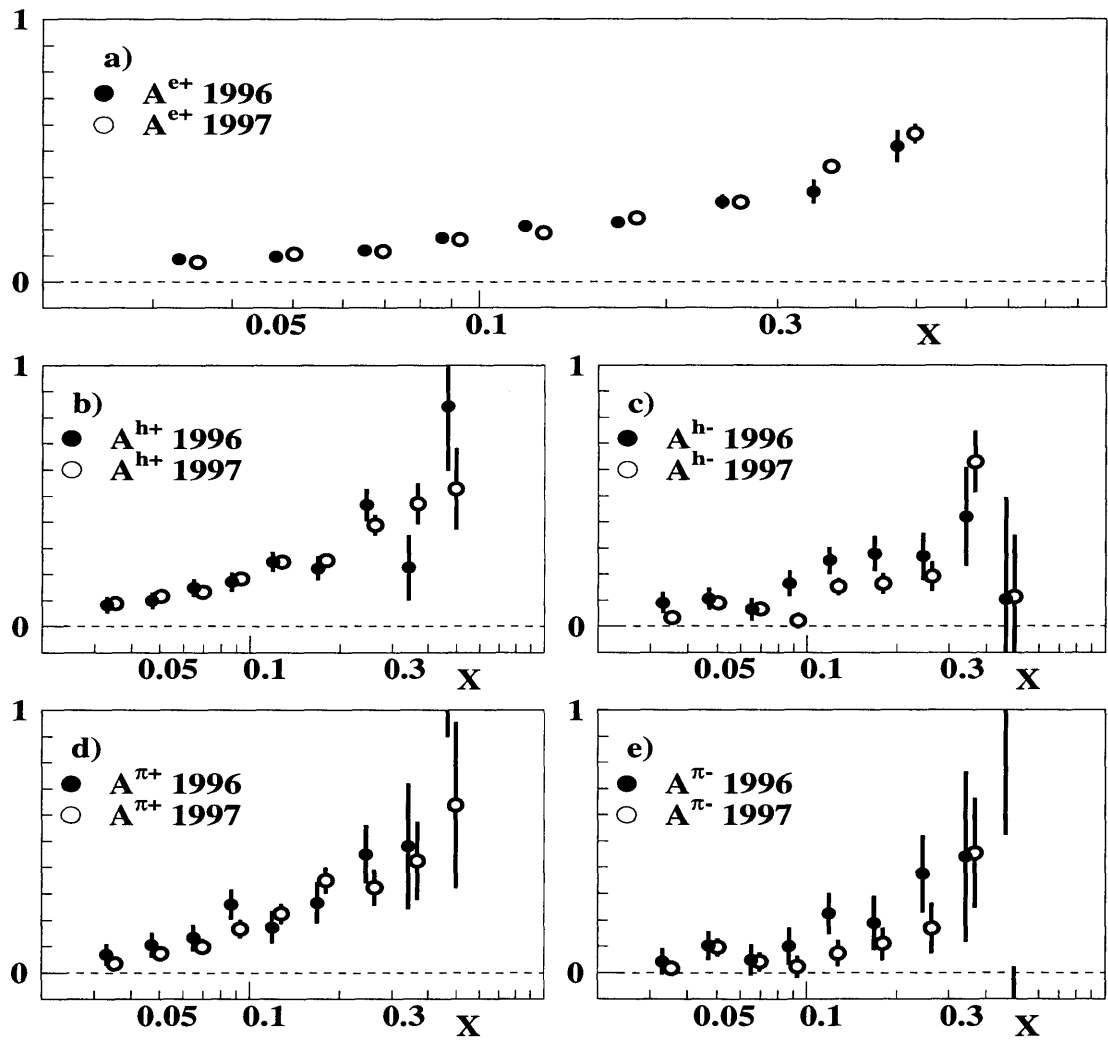


Figure 5-9: A comparison of 1996 and 1997 proton asymmetries. Only statistical uncertainties are shown.

Asymmetry	$\chi^2/\text{d.o.f.}$
$A_1^{\epsilon^+}$	0.690
$A_1^{h^+}$	0.611
$A_1^{h^-}$	1.39
$A_1^{\pi^+}$	0.77
$A_1^{\pi^-}$	1.06

Table 5.13: The $\chi^2/\text{d.o.f.}$ for a fit of the 96 and 97 asymmetries to each other. The calculation includes both statistical and (correlated) systematic uncertainties.

To combine the two proton data sets, one fits the value of each asymmetry in each x bin with a constant, using the above statistical and systematic covariance matrices.

The final asymmetries from the HERMES 1995-7 running are then presented in Figures 5-10, 5-11, and 5-12. Figure 5-10 compares the inclusive DIS results to the best measurements at SLAC [57, 54], which have high statistical precision and similar kinematical range to HERMES. The inclusive measurements of SLAC and HERMES are consistent. The HERMES and E143 proton precisions are comparable, while E154 has greater inclusive DIS statistics on ^3He .

Semi-inclusive hadron asymmetries in DIS have been investigated at CERN by SMC [167]. Figure 5-12 compares the SMC proton asymmetries to the HERMES measurements. The values of the asymmetries are compatible, though HERMES has greater the precision in its kinematic range. In the comparison, note that the accepted semi-inclusive asymmetries in each experiment are compared, and acceptance corrections would be needed to compare the measurements in all space.

The ability of HERMES to identify pions in the semi-inclusive hadron flux is unique among DIS experiments. Total hadron asymmetries on ^3He and identified pion asymmetries are measured for the first time at HERMES. The values of the HERMES asymmetry measurements are summarized in Table A.3.

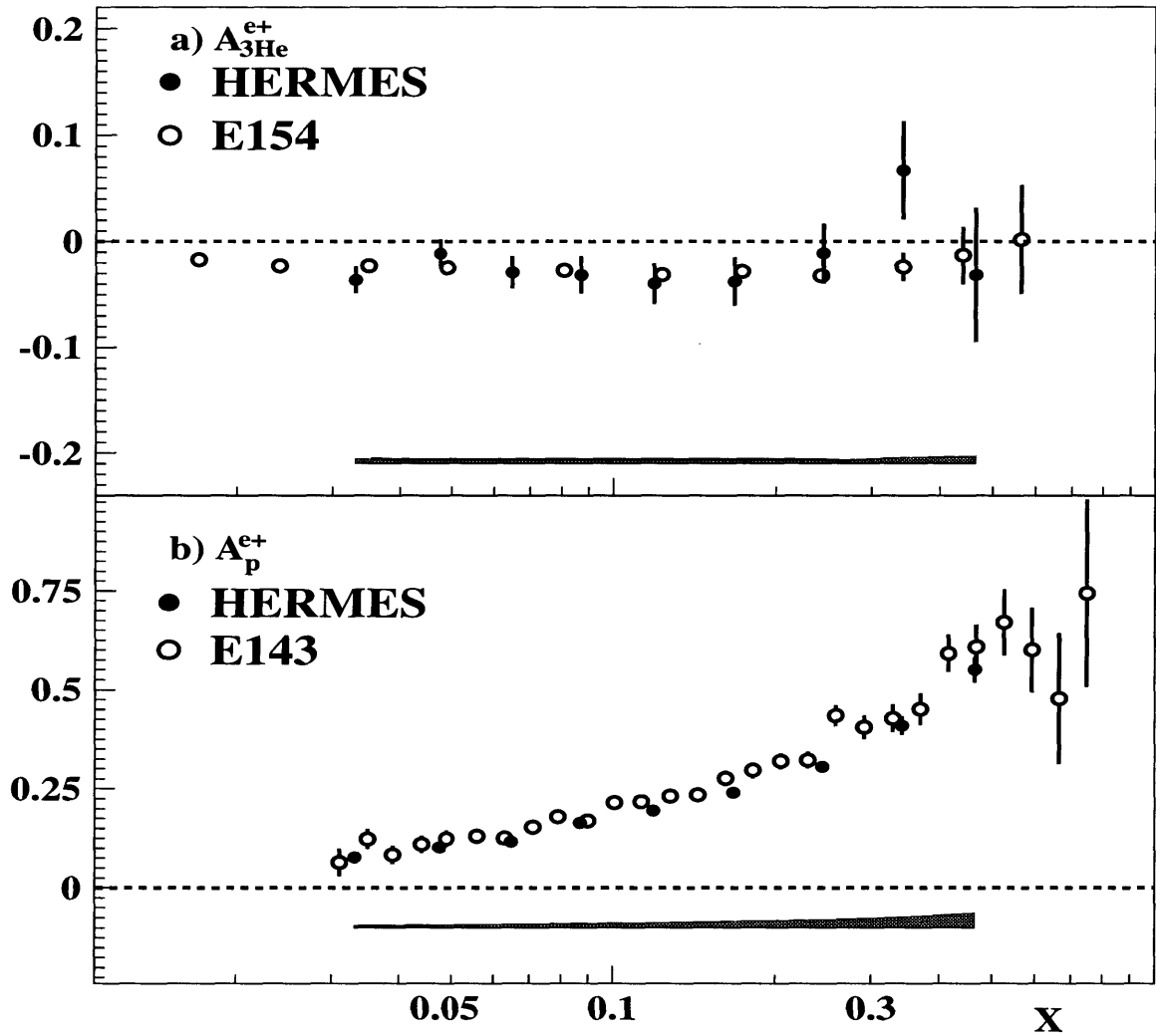


Figure 5-10: The final inclusive DIS structure function ratios from HERMES: (a) $\frac{g_1^{e+}}{F_1^{e+}}$ on ^3He , (b) $\frac{g_1^{e+}}{F_1^{e+}}$ on ^1H . The dark band shows the HERMES systematic uncertainties. Statistical uncertainties only are plotted for the SLAC data.

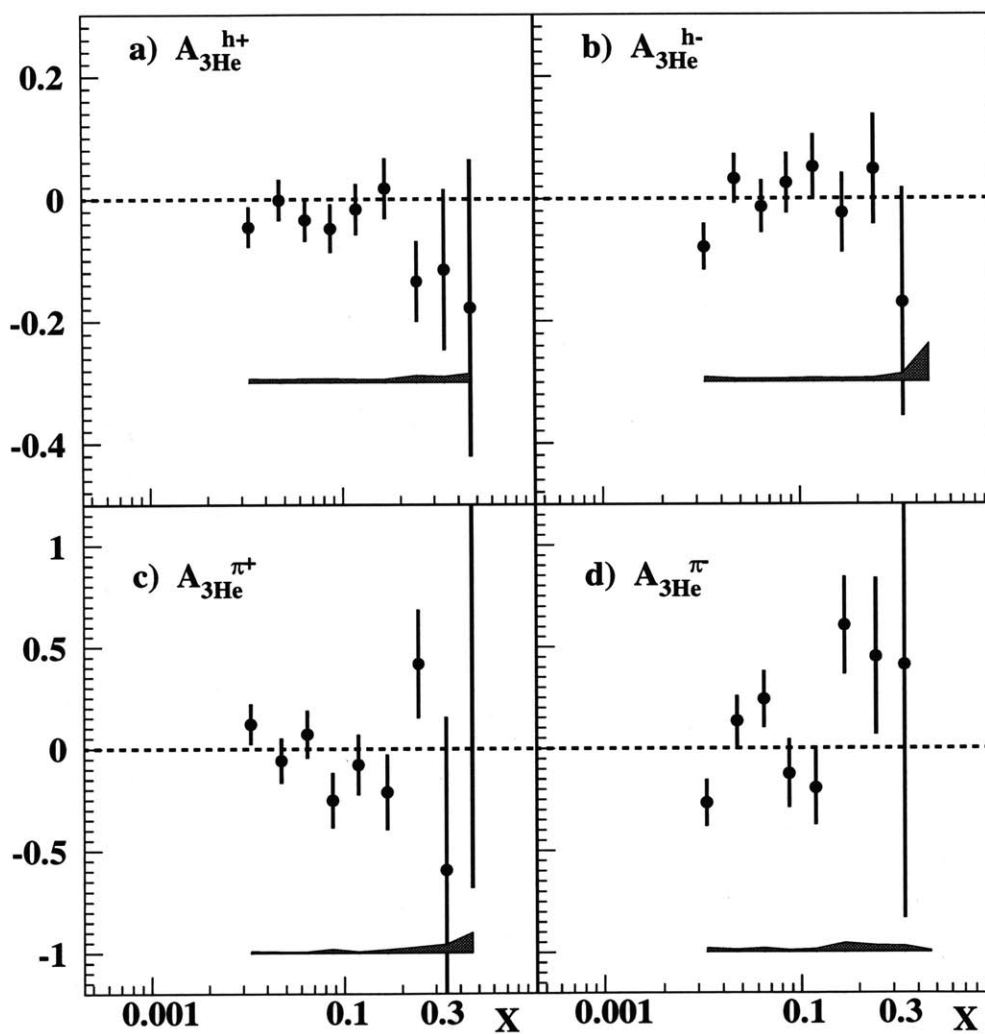


Figure 5-11: The final semi-inclusive DIS ^3He structure function ratios, $\frac{g_1^h}{F_1^h}$. The dark band shows the HERMES systematic uncertainties.

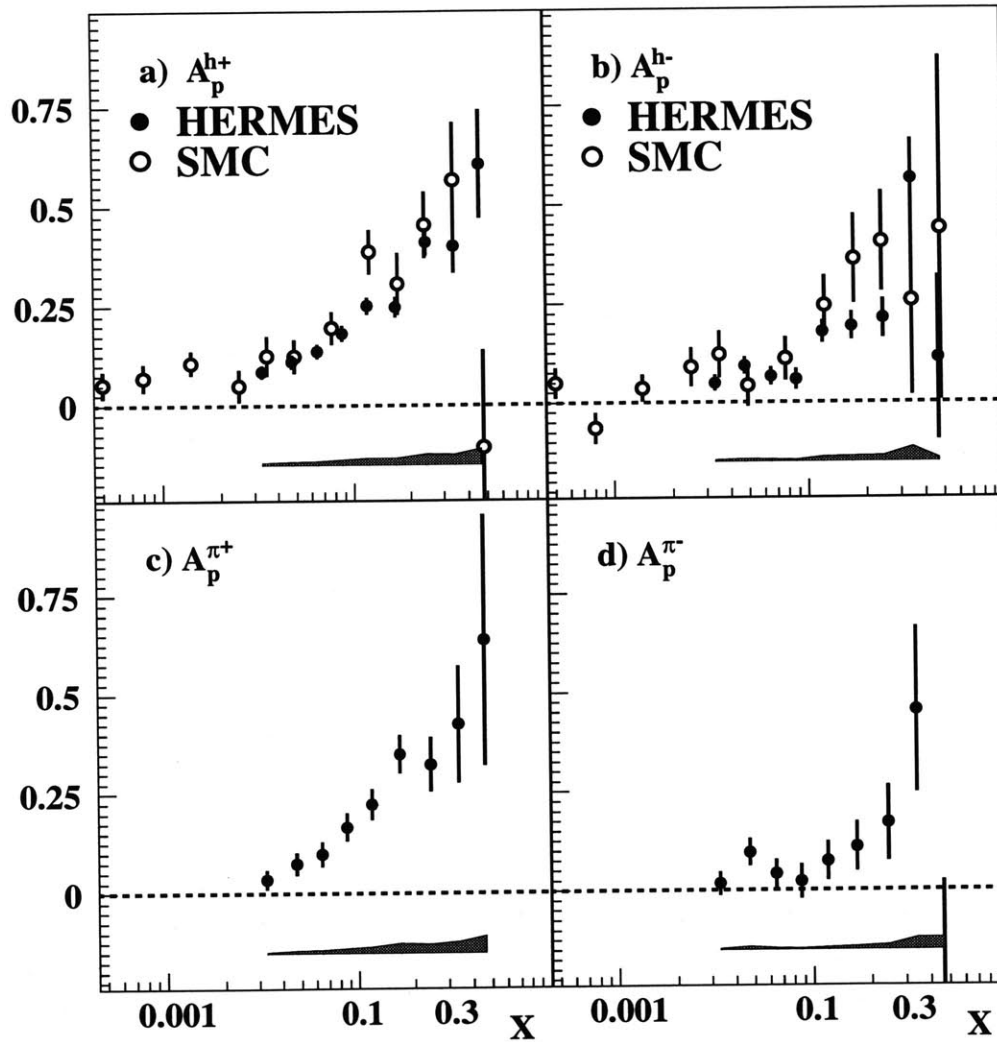


Figure 5-12: The final semi-inclusive DIS proton structure function ratios, $\frac{g_1^h}{F_1^h}$, compared to SMC. The dark band shows the HERMES systematic uncertainties. Statistical uncertainties only are plotted for the SMC data.

5.9 Summary

The double-spin asymmetries in deep-inelastic scattering are the basic experimental results of HERMES. However, they alone give little insight into the structure of the nucleon. The next chapter will use the guidance of theory and unpolarized data to extract the quark polarizations in the nucleon from these asymmetries.

Chapter 6

The Extraction of Polarized Parton Distributions

Chapter 2 discussed the interpretation of the deep-inelastic cross-section as proportional to a sum of quark distributions inside the nucleon. The Quark-Parton Model provides a framework for relating each deep-inelastic event detected at HERMES to an underlying parton distribution function. This chapter studies the HERMES DIS asymmetries in this model. From these asymmetries, the spin fractions of quarks are extracted, and fundamental questions about the nucleon spin are addressed.

6.1 The Purity Model

To extract polarized parton distributions from asymmetry measurements, this work uses a convenient formalism known as the *purity* method. The formalism is based on the Quark-Parton Model and assumes factorization. To understand this approach, consider the DIS cross-section presented in Section 2.1.2. For each DIS event type h , the polarized cross-section may be related to a sum of quark distributions, $q(x)$, and fragmentation functions, $D_q^h(z)$:

$$d\sigma^{h,\uparrow\downarrow(\uparrow\uparrow)}(x,z) \sim \sum_q e_q^2 q^{\uparrow\downarrow(\uparrow\uparrow)}(x) D_q^h(z). \quad q = \{u, d, s, \bar{u}, \bar{d}, \bar{s}\} \quad (6.1)$$

The quark flavor, q , is generalized to include the three light quark and anti-quark flavors. The double-spin asymmetries measured at HERMES are the difference of the spin-dependent

photoabsorption cross-sections divided by their sum. In this model, they then relate to the polarized parton distribution functions as,

$$A_1^h(x, z) = \frac{\sum_q e_q^2 \Delta q(x) D_q^h(z)}{\sum_{q'} e_{q'}^2 q(x) D_{q'}^h(z)}. \quad (6.2)$$

With any detector, these equations are complicated by the acceptance effects. The detected yield is formed from a convolution of an acceptance function, $\mathcal{A}^h(x, Q^2, z)$, and the cross-section in all space. Also, parton distributions primarily depend on x_{BJ} , and one integrates over the z and Q^2 variables in the cross-section. Define $D_q^{\text{eff},h}(x)$ as the effective multiplicity of event type h inside the HERMES acceptance coming from a quark flavor q . Then,

$$d\sigma_{\text{accept}}^{h,\uparrow\downarrow(\uparrow\uparrow)}(x) \sim \sum_q e_q^2 q^{\uparrow\downarrow(\uparrow\uparrow)}(x) \int_{0.2}^{1.0} dz \int_{1.0}^{\infty} dQ^2 D_q^h(z) \mathcal{A}^h(x, Q^2, z), \quad (6.3)$$

$$\sim \sum_q e_q^2 q^{\uparrow\downarrow(\uparrow\uparrow)}(x) D_q^{\text{eff},h}(z). \quad (6.4)$$

Using $D_q^{\text{eff},h}(x)$, the asymmetry relation becomes,

$$A^h(x) = \frac{\sum_q e_q^2 \Delta q(x) D_q^{\text{eff},h}(x)}{\sum_{q'} e_{q'}^2 q(x) D_{q'}^{\text{eff},h}(x)}. \quad (6.5)$$

The key of this approach is contained in the definition of the *purity* of quark flavor q in an event h :

$$P_q^h(x) = \frac{q(x) D_q^{\text{eff},h}(x)}{\sum_{q'} e_{q'}^2 q(x) D_{q'}^{\text{eff},h}(x)}. \quad (6.6)$$

This purity may be physically interpreted as the probability that each event of type h originated in scattering from a quark flavor q in the nucleon. Upon rearrangement of Equations (6.5) and

(6.6) with extra factors of $q(x)$ introduced, one arrives at the master equation for the purity analysis,

$$A^h(x) = \sum_q P_q^h(x) \frac{\Delta q}{q}. \quad (6.7)$$

The goal of this analysis is to use Equation (6.7) to access the polarized quark distributions, $\Delta q(x)$. As shown in the last chapter, HERMES measures the A^h for a variety of processes h . Equation (6.7) is really a system of equations, which may be recast in matrix form. For each bin in x , column vectors of N_A asymmetries and N_q quark polarizations may be defined, and the purities then form a $N_A \times N_q$ rectangular matrix:

$$\vec{\mathbf{A}}(x) = \begin{pmatrix} A^{h_1}(x) \\ \vdots \\ A^{h_{N_A}}(x) \end{pmatrix}, \quad \vec{\mathbf{Q}}(x) = \begin{pmatrix} \frac{\Delta q_1(x)}{q_1(x)} \\ \vdots \\ \frac{\Delta q_{N_q}(x)}{q_{N_q}(x)} \end{pmatrix}, \quad \mathbf{P}(x) = \begin{bmatrix} P_{q_1}^{h_1}(x) & \cdots & P_{q_1}^{h_{N_A}}(x) \\ \vdots & \ddots & \vdots \\ P_{q_{N_q}}^{h_1}(x) & \cdots & P_{q_{N_q}}^{h_{N_A}}(x) \end{bmatrix} \quad (6.8)$$

Equation (6.7) becomes,

$$\vec{\mathbf{A}} = \mathbf{P}\vec{\mathbf{Q}}. \quad (6.9)$$

Matrix algebra provides the solution $\vec{\mathbf{Q}}$ [170]. As the number of measured asymmetries, N_A , is typically larger than the number of independent quark polarizations, N_q , the system of equations is overconstrained. Using the asymmetry covariance matrix discussed in the last chapter, a least squares fit is performed; one finds that the quark polarization covariance, $\mathcal{C}_{\mathbf{Q}}$, is simply

$$\mathcal{C}_{\mathbf{Q}} = (\mathbf{P}^T \mathcal{C}_{\mathbf{A}}^{-1} \mathbf{P})^{-1}. \quad (6.10)$$

The solution to the purity equation is then

$$\vec{\mathbf{Q}} = \mathcal{C}_{\mathbf{Q}}^{-1} \mathbf{P}^T \mathcal{C}_{\mathbf{A}}^{-1} \vec{\mathbf{A}}. \quad (6.11)$$

This solution vector, \vec{Q} , is the vector which minimizes

$$\chi^2 = \left(\vec{A} - \mathbf{P} \cdot \vec{Q} \right)^T c_A^{-1} \left(\vec{A} - \mathbf{P} \cdot \vec{Q} \right). \quad (6.12)$$

These equations summarize the formal procedure of the extraction of polarized parton distributions by the purity method. Detailed reviews of the procedure can be found in Reference [152, 171]. More sophisticated methods have been investigated, including a matrix approach based on the Singular Value Decomposition [152], and an iterative Monte Carlo fit procedure [166], and a direct cross-section fit using the MINUIT package [172]. All methods have been demonstrated to be equivalent to the above simple approach.

The usefulness of this formalism derives from isolating the fit quantity $\frac{\Delta q}{q}$ from all other physics in the expression. All unpolarized contributions to the measured asymmetry compact into one set of numbers, the event purities, P_q^h . The procedure assumes that the purities are understood at higher precision than the quark polarizations under investigation. This is typically true as unpolarized physics is studied with much higher statistics than polarized physics. Whenever the calculation of the purities becomes questionable, it may be useful to pursue alternative analysis methods, such as counting rate difference asymmetries, e.g. Equations (2.45) and (2.48). Propagating uncertainties from purities is more difficult than propagating uncertainties from asymmetries into the final extracted Δq values.

6.2 Generating the Purities

The most critical aspect of this analysis is the generation of the quark purities. From Eqs. (6.4) and (6.6), the purity represents three distinct processes:

- The unpolarized parton distribution, $q(x)$, reflects the probability of scattering from a quark of flavor q at the detected x inside the nucleon.
- The fragmentation function, $D_q^h(z)$, describes the probability that an event class h with hadron energy fraction z is produced in the hadronization of the struck quark in the nucleon.

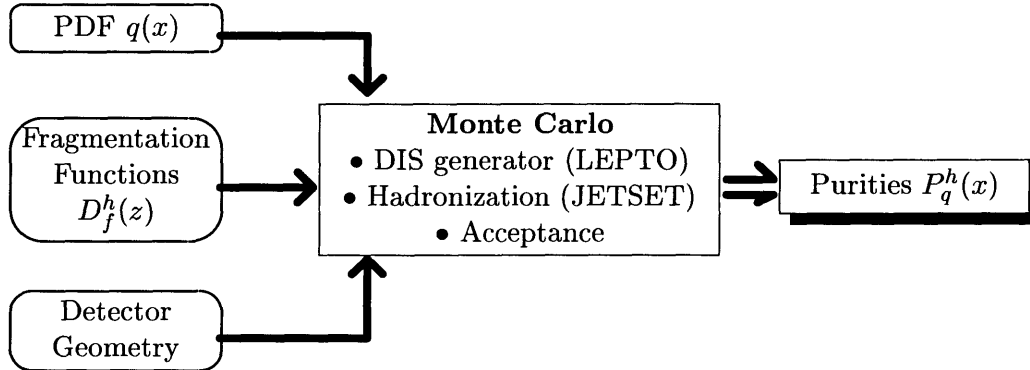


Figure 6-1: A schematic diagram of the purity generation.

- The acceptance function, $\mathcal{A}^h(x, Q^2, z)$, models the probability that this event h is detected with the HERMES spectrometer, after each track is propagated out of the target.

Much of the world's knowledge of fragmentation and parton distributions comes from other experiments measuring unpolarized cross-sections, in for example $e-p$ and e^+e^- colliders. A significant feature of the HERMES experiment is its ability to do both polarized and unpolarized physics; this allows many of the physics models assumed in the purity analysis to be tested with unpolarized target running.

In this work, the understanding of the above three points are combined into a code based on the PEPSI Monte Carlo [173], which is a polarized extension of LEPTO [174] deep-inelastic scattering Monte Carlo. Figure 6.2 illustrates the role of the MC in the purity analysis. The sections below discuss the different aspects of generating purities.

6.2.1 Unpolarized Parton Distributions

The CTEQ [11], GRV [162], and MRS [175] collaborations have fitted parton distribution functions to the results of a variety experiments. The extrapolation of these fits into the

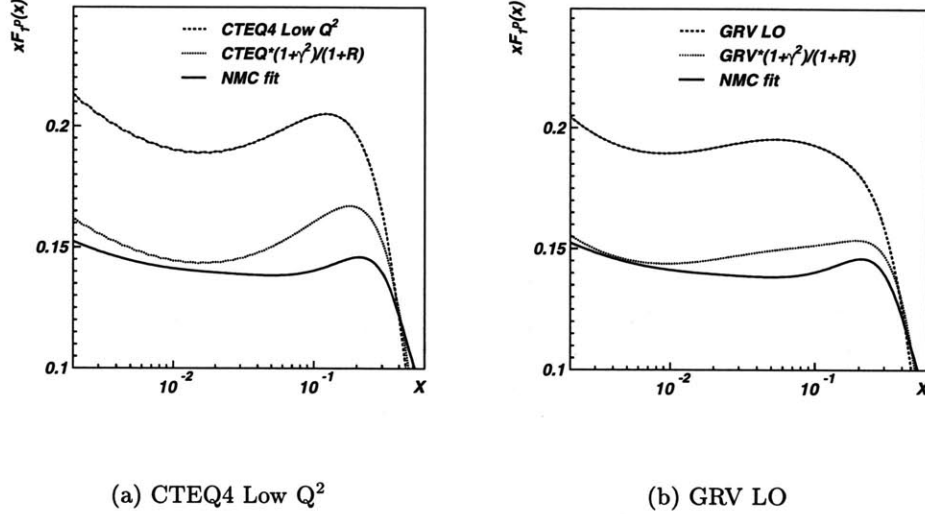


Figure 6-2: A comparison of distributions of $F_1(x)$ at $Q^2 = 2.5\text{GeV}^2$, constructed from parton distributions fit by the CTEQ [11] and GRV [162] groups. The dashed line shows the construction according to Eq. (6.13), and dotted shows the construction corrected by $\frac{1+\gamma^2}{1+R}$. The NMC fitted $F_1(x)$ [16] is shown for comparison in the solid line. All lines are evaluated at $Q^2 = 2.5\text{GeV}^2$

HERMES kinematic range provides a precise description of the unpolarized parton distributions in the nucleon. While HERMES alone does not determine DIS cross-sections well enough to constrain unpolarized parton distributions internally, the world parameterizations have been checked at HERMES directly with $\frac{F_2^n}{F_2^p}$ and $\bar{u} - \bar{d}$ measurements [91, 176, 177]. For this analysis, the CTEQ Low Q^2 PDF set is the main parameterization used. The set is plotted in Figure 2-3. The unpolarized PDF sets are input into the PEPSI Monte Carlo.

A subtle aspect of using these fitted parton distributions concerns the treatment of the longitudinal scattering cross-section. Leading order QCD fits derive the PDFs from measured F_2 data assuming that the longitudinal/transverse cross-section ratio, $R(x, Q^2)$ is zero. Assuming the Callen-Gross relation in Eq. (2.19) holds, the measured F_2 are identified as the sum of the true parton distributions, $q(x)$, as

$$F_2(x) = 2x F_1(x) = \sum_q x e_q^2 q(x). \quad (6.13)$$

However, world data indicate R varies from 10 to 30% in HERMES kinematics [17], as shown in Table 5.12.

For non-zero R , F_2 is related to F_1 through Equation (2.15). In order to use parton distributions defined on F_2 consistently, a correction for non-zero R must be included in the purity formalism:

$$A^h(x) = \frac{g_1^h}{F_1^h} = \frac{g_1^h (1+R)}{F_2^h (1+\gamma^2)} \quad (6.14)$$

$$= \left[\sum_q P_q^h(x) \frac{\Delta q}{q} \right] \frac{(1+R)}{1+\gamma^2} \quad (6.15)$$

The R_{1990} parameterization from Whitlow *et al.* [17] is used for this correction. Note that no such ambiguity exists in the polarized case, for $g_1(x)$. The longitudinal cross-section is assumed spin-independent and therefore cancels in helicity differences.

6.2.2 Fragmentation Models

The properties of hadronization are directly measured at HERMES. By comparing inclusive and semi-inclusive yields on unpolarized targets, HERMES may extract the fragmentation functions in our kinematic region; the ratio of the pion fragmentation functions $D^+ (= D_1)$ and $D^- (= D_1)$ extracted from 1996 data [32] is shown in Figure 6-3.

In principle, one may take the HERMES measured functions, integrate over z , and directly evaluate the purities in Equation (6.6). This is the approach adopted by the SMC experiment, in their polarized parton distribution analysis [167].

This analysis adopts a different tactic. The LUND string model described in Section 2.1.3.2 is implemented in the JETSET [179] package and may reproduce the hadronization process inside a Monte Carlo simulation of DIS. By embedding the fragmentation process in a larger Monte Carlo, one may easily take into account kinematic correlations between the parton distributions, the fragmentation and the acceptance function. Also, the fragmentation symmetries of Equations (2.34) are no longer explicitly required to hold. The LUND string model has been used successfully to describe world data at higher energies on fragmentation [180]. At these higher energies, the model incorporates higher order QCD processes to simulate jet production

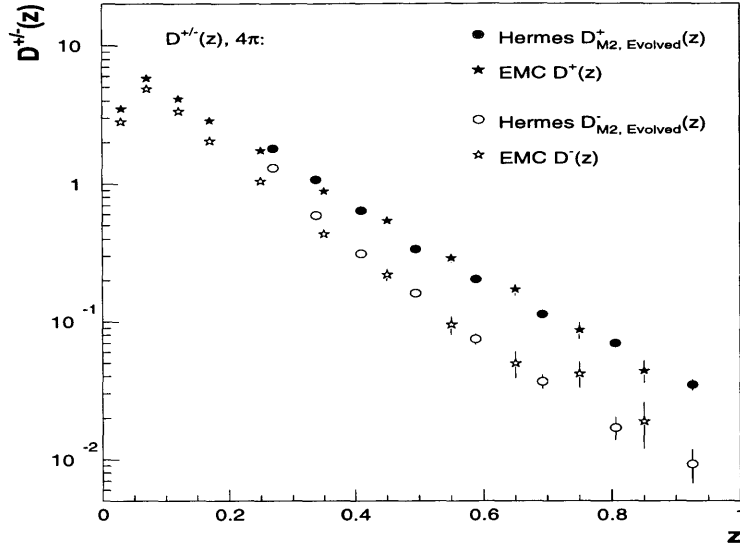


Figure 6-3: A comparison of HERMES favored and unfavored fragmentation functions in 4π with the results of the EMC [178] experiment from Reference [32]. The results from HERMES are evolved to the average Q^2 of the EMC experiment.

effects. As HERMES does not have the energy to produce jets, the default LUND string model does not seem to reproduce low energy hadron yields at HERMES well. Therefore, the HERMES data has been simulated using first order matrix elements, and the free parameters of the LUND model have been adjusted to fit measured semi-inclusive yields at HERMES [166]. Using the notation of JETSET, these parameters are the longitudinal string breaking probability “PARJ(41)”, the tunneling probability “PARJ(42)”, and the average transverse momentum “PARJ(21)” [32]. These parameters have been fit to both the charged hadron z and p_T distributions [166] and to the Čerenkov-identified pion distributions [181]. The diquark production “PARJ(1)” and s-quark suppression “PARJ(2)” have both been adjusted to reproduce HERMES K_s^0 and Λ^0 yields. Figure 6-4 compares the HERMES hadron multiplicity with the LUND MC distributions. The fitted Monte Carlo reproduces HERMES hadronization properties above $z > 0.2$. Since the work relies heavily on the Monte Carlo description, this z cut has been chosen throughout the analysis.

Similar fits have been performed using the independent fragmentation and cluster fragmentation models. The cluster model is not successful in describing HERMES yields [32], so that only results from the independent model fit are compared in the extraction. The default and fitted model parameters are listed in Table 6.1.

Fragmentation Model	PARJ(1)	PARJ(2)	PARJ(21)	PARJ(41)	PARJ(42)
Default String Model	0.1	0.3	0.36	0.3	0.58
String Model Fitted to Hadrons	0.025	0.16	0.34	0.82	0.24
String Model Fitted to Pions	0.01	0.3	0.4	0.15	0.35
Independent Fragmentation Fitted to Hadrons	0.025	0.16	0.31	1.38	1.16

Table 6.1: The JETSET parameters for four models fragmentation models[166, 32]. The parameters and models are described in the text.

Both the LUND string and the independent fragmentation models are included the JETSET [179] package, which is a part in the HERMES Monte Carlo.

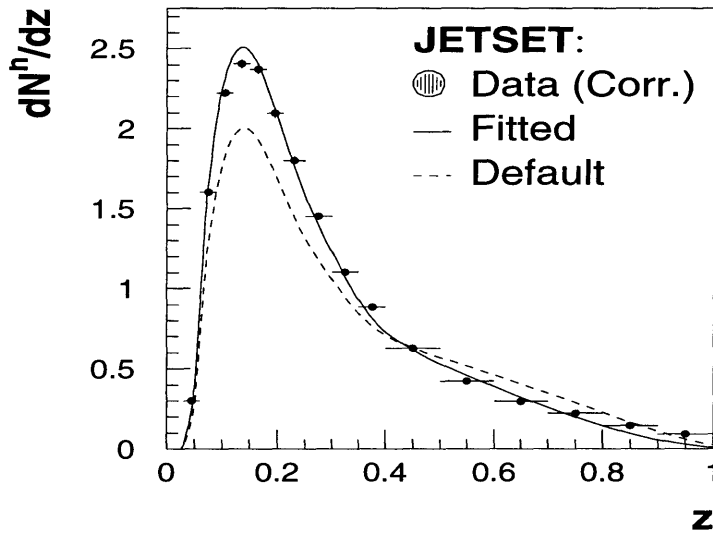


Figure 6-4: A comparison of two parameterization of the LUND string model with HERMES data. The “Default” scenario was fitted to higher energy data, including the EMC experiment. In the “Fitted” scenario, the LUND string model was fitted to HERMES positive and negative hadrons yields [32].

6.2.3 Acceptance

For detailed study of the HERMES spectrometer effects, a GEANT-based HERMES Monte Carlo is available to simulate the response of each component of the spectrometer. While it is the best acceptance description available, the GEANT code is far too slow for high statistics generation of purities. A simpler approach combines on the geometric box shape of the spectrometer with a map of the HERMES magnetic field. The HRC momentum lookup table determines the magnetic bending of the tracks in each Monte Carlo event. The bent trajectories are extrapolated through the detector, and required to pass inside the HERMES calorimeter, according to the simple geometric cuts in Table 5.5.

The procedure assumes that the response of HERMES spectrometer is ideal. This is reasonable, since all real detector effects are removed from the measured asymmetries by the corrections of Section 5.5. The asymmetry discussion also noted that the acceptance corrections to the semi-inclusive asymmetries are large and non-trivial. By including the HERMES acceptance in the purity calculation, these acceptance effects are automatically compensated; the quark polarization extraction is then independent of the HERMES acceptance.

When separating pions from hadrons, one must also model the efficiency of the HERMES Čerenkov. One technique for estimating this efficiency involves identifying semi-inclusive positive and negative hadron pairs which reconstruct to the neutral rho invariant mass [181]. These hadrons must be pions, and they may be used to estimate the Čerenkov pion identification efficiency. A parameterization of the Čerenkov response to rho-produced pions is shown in Figure 6-5. To be conservative, the analysis here compares this fitted response with an ideal “step” threshold response at 4.9 GeV/c.

6.2.4 Purity Results

Inclusive DIS purities, which involve no fragmentation functions and no acceptance corrections, may be directly estimated from Eq. (6.6). For all semi-inclusive events, high statistics Monte Carlo simulations generate purities using the CTEQ Low Q^2 PDFs, Fitted LUND string fragmentation, and HERMES acceptance with a fitted Čerenkov threshold. In Monte Carlo, one may know exactly which quark was struck for each scattered event. If all accepted Monte Carlo

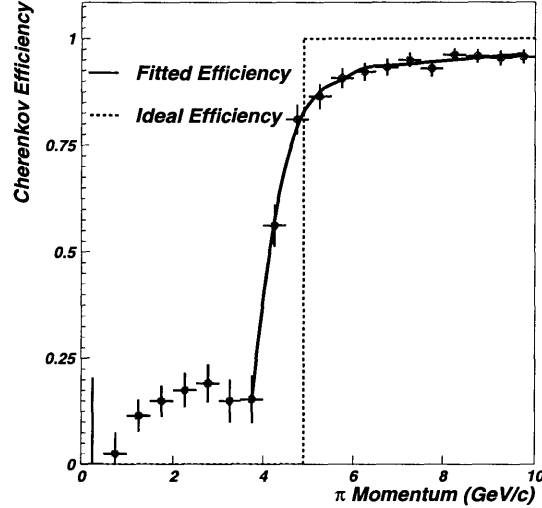


Figure 6-5: The average response of the HERMES Čerenkov to identified pions from neutral rho decays versus the pion momentum [181]. The solid line represents an empirical fit to the response above 4 GeV/c. The dotted line represents the threshold behavior for an ideal Čerenkov which becomes sensitive above 4.9 GeV/c.

events of type h coming from flavor q , N_q^h , are counted, then the purity for this process is simply

$$P_q^h(x) = \frac{N_q^h(x)}{\sum_{q'} N_{q'}^h(x)}. \quad (6.16)$$

Semi-inclusive purities were then calculated from the Monte Carlo using Equation (6.16).

Figure 6-6 displays the purities for a proton target. Most of the features of the calculated purities come from the parton distribution and charge factors in Equation (6.6). In the proton, u -quarks dominate the deep-inelastic scattering, with less than 10% of the inclusive events originating from other quark species. For each quark, the fragmentation functions either enhance or suppress the semi-inclusive purity when compared to the inclusive purity.

Figure 6-7 adds semi-inclusive pion purities for the up quark and strange quark. The u -quark pion purities display the same features as the total hadron purities; this is also the

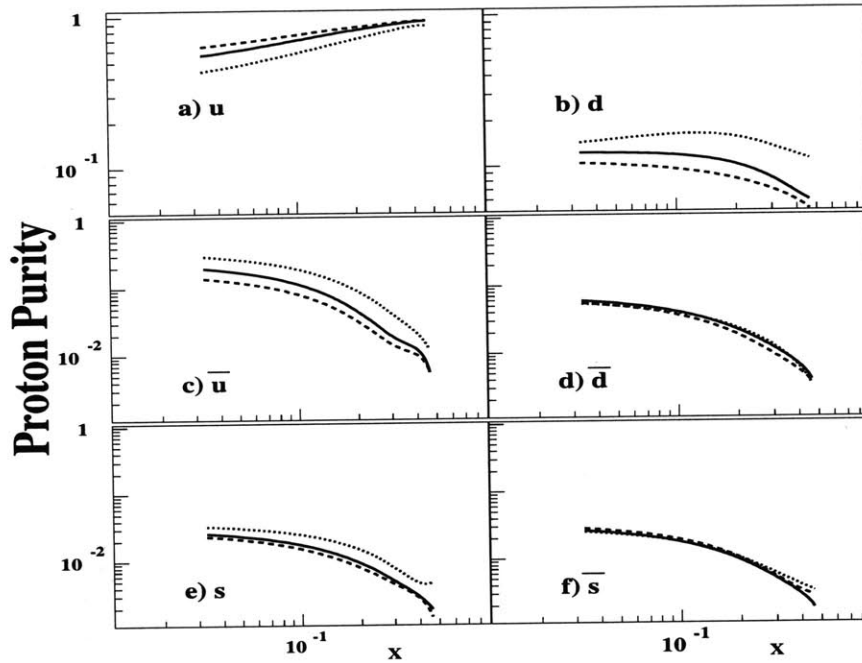


Figure 6-6: Inclusive positron (solid line) and semi-inclusive h^- (dashed line) and h^- (dotted line) proton purities compared for six quark flavors.

case for the other light quarks. In the strange sea case, though, the pion purities are heavily suppressed relative to the hadron purities. This is a consequence of pions having no strange content in their wavefunction; pion production from s -quarks is unfavored. This suppression makes the combination of inclusive and semi-inclusive pion data particularly sensitive to strange sea influences.

6.3 Models of Quark Polarization

Important to the practical use of the purity approach is the choice of the form of the fitted vector \vec{Q} . One wishes to fit all quark polarizations which may contribute significantly to the spin structure of the nucleon. The c , b , and t quarks are immediately ignored as their large

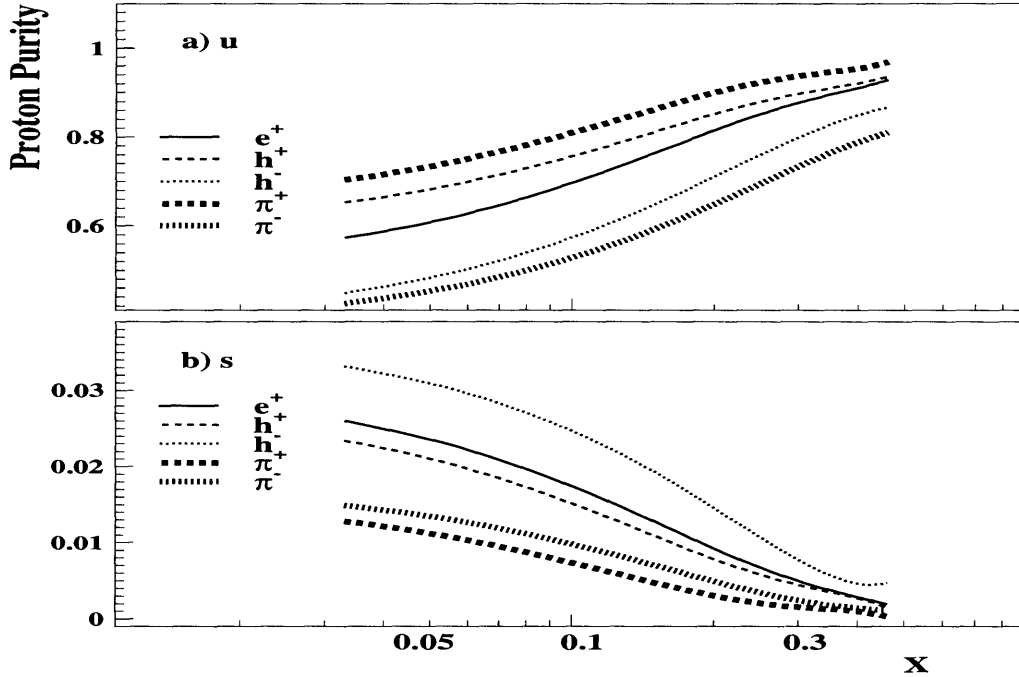


Figure 6-7: Semi inclusive π^+ (thick dashed line) and π^- (thick dotted line) purities are compared to the corresponding inclusive and semi-inclusive hadron proton purities for a) the up quark and b) the strange quark.

mass prohibits a significant intrinsic sea density in the nucleon. This leaves u , d , and s quarks and their charge-conjugates for a total of six independent quark species.

The number of fitted polarizations in the purity equation is limited by the number of physically distinct asymmetries: as this analysis studies at least six distinct asymmetries, a complete fit of six quark polarizations is possible. However, section 6.2.4 noted that the u quarks dominate the purity in the proton; d quarks are nonetheless significant in effective neutron targets; but sea quark purities are relatively tiny. For the most general understanding of nucleon spin structure, one wishes to fit all quark species separately in the polarization vector. In practice, the small sensitivity of the asymmetries to sea quarks make a full separation difficult.

To get a handle on the helicity distribution of the nucleon sea, one instead imposes a phenomenologically motivated model on sea quark polarizations. The HERMES asymmetries have a larger sensitivity to one parameter reflecting the average sea properties, than to each sea flavor polarization individually. Four important choices of such models are listed here:

- **Sea Model I: Unpolarized Sea:** In this simple model, sea quark spins are assumed to make no contribution to the nucleon spin: $\Delta\bar{u} = \Delta\bar{d} = \Delta\bar{s} = \Delta s = 0$. HERMES asymmetry distributions are proportional to two quark helicity densities, Δu and Δd . While this model allows the most precise determination of up and down quark polarizations, the discussion in Section 2.2.6 emphasized that polarized sea quark distributions may have a special role in resolving the nucleon spin puzzle. They cannot be assumed to be zero for studying nucleon spin structure.
- **Sea Model II: SU(3) Distribution Symmetric Fit:** If one assumes sea quarks may be polarized, then the next simplest assumption is that their parton distributions are identical. In QCD, most sea quarks originate from the splitting of gluons, which is nearly a flavor independent process. One then assumes that the mechanism generating polarization in the sea may also be flavor independent. For the purity fit, one defines an “average helicity distribution of the sea”:

$$\Delta q_{\text{sea}} \equiv \Delta\bar{u} = \Delta\bar{d} = \Delta\bar{s} = \Delta s \neq 0. \quad (6.17)$$

The purity of the average sea is then defined by

$$P_{q_{\text{sea}}} \frac{\Delta q_{\text{sea}}}{q_{\text{sea}}} = \left(P_{\bar{u}} \frac{1}{\bar{u}} + P_{\bar{d}} \frac{1}{\bar{d}} + P_{\bar{s}} \frac{1}{\bar{s}} + P_s \frac{1}{s} \right) \Delta q_{\text{sea}} \quad (6.18)$$

In this model, the unpolarized distribution, q_{sea} , is arbitrary, as one multiplies and divides by it in defining the purity. Three parameters are fit: $\frac{\Delta u}{u}$, $\frac{\Delta d}{d}$, and $\frac{\Delta q_{\text{sea}}}{q_{\text{sea}}}$.

From Figure 6-6, one sees that \bar{u} purities are typically much greater than other sea purities, due to the charge factor. Hence, the average sea quark purity is dominated by \bar{u} contributions. If the polarized sea distributions are not equal in Nature, the average polarized sea distribution in this model will be dominated by $\Delta\bar{u}$.

- **Sea Model III: SU(3) Polarization Symmetric Fit:** This is a slight variation on the above in that one assumes the sea quark *polarization* not the sea quark helicity *distribution* is symmetric:

$$\frac{\Delta q_{\text{sea}}}{q_{\text{sea}}} \equiv \frac{\Delta\bar{u}}{\bar{u}} = \frac{\Delta\bar{d}}{\bar{d}} = \frac{\Delta\bar{s}}{\bar{s}} = \frac{\Delta s}{s}. \quad (6.19)$$

The purity of the average sea is defined by

$$P_{q_{\text{sea}}} \frac{\Delta q_{\text{sea}}}{q_{\text{sea}}} = (P_{\bar{u}} + P_{\bar{d}} + P_{\bar{s}} + P_s) \frac{\Delta q_{\text{sea}}}{q_{\text{sea}}} \quad (6.20)$$

The difference between the symmetric distribution and symmetric polarization cases can be found in two places. First, NA51 [90], E866 [89], and HERMES [91] data indicate that $\bar{d}(x) \sim 2\bar{u}(x)$. The best fit to E866 data indicates that the difference in these PDFs arises from interactions with pion clouds surrounding nucleons [92]. It is unclear in the literature whether these models suggest $\Delta\bar{u} \neq \Delta\bar{d}$ in the proton. Second, the SU(3) distribution assumes that the helicity difference of strange quarks is as large as the light quark helicity difference. Polarized quark distributions cannot exceed their corresponding unpolarized distributions, and this is smaller for s than for \bar{d} . If the sea polarization is large enough to exceed s -quark positivity, Model II becomes unfeasible. There is no indication of such a large contribution currently. Symmetric sea polarizations is also a natural consequence of the toy model discussed in Section 2.2.8.

- **Sea Model IV: Strange Quark Fit:** Fits to inclusive DIS and hyperon decay data indicate that strange quark polarization may be significantly different from light quarks in the sea. A direct separation of strange quark polarizations from the light sea polarizations tests this indication. In this approach, one expands the fit polarizations to constrain the strange sea polarization independently: one fits $\frac{\Delta u}{u}$, $\frac{\Delta d}{d}$, $\frac{\Delta l q_{\text{sea}}}{l q_{\text{sea}}}$, and $\frac{\Delta s}{s}$. The average polarization of the sea is assumed symmetric in light quark flavor as in model III; *i.e.* $\frac{\Delta l q_{\text{sea}}}{l q_{\text{sea}}}$ equal for all light sea flavors. One still assumes s and \bar{s} quarks have the same polarization, $\frac{\Delta s}{s}$.

In addition to the sea models, several different treatments for the valence quarks, u and d , are available. As gluon splitting is a charge symmetric process, one postulates that there must exist a “sea” contribution, as defined in Equation (2.86) Three types of u and d quark polarization extractions are motivated by this separation:

- **The Valence Fit:** Fit $\frac{\Delta u_{\text{val}}}{u_{\text{val}}}$, $\frac{\Delta d_{\text{val}}}{d_{\text{val}}}$, and sea polarizations.
- **The Simple Fit:** Fit $\frac{\Delta u}{u}$, $\frac{\Delta d}{d}$, and sea polarizations.
- **The Flavor Symmetric Fit:** Fit $\frac{\Delta u + \Delta \bar{u}}{u + \bar{u}}$, $\frac{\Delta d + \Delta \bar{d}}{d + \bar{d}}$, and sea polarizations.

The three fits differ only by how sea and valence polarizations are separated. The results of any one fit can be used to derive the others using the definitions of $u_{\text{sea}}(d_{\text{sea}})$ and $u_{\text{valence}}(d_{\text{valence}})$ above.

The different types of fits will be interesting when comparing to theory. The hyperon decay analysis in Section 2.2.3 groups quarks and anti-quarks by flavor, while recent lattice gauge theory calculates valence quark properties.

6.4 Corrections for Nuclei

All parton distributions are defined on the proton, and the Monte Carlo techniques above allow straightforward calculation of proton purities. When considering neutron purities, they may be derived from the proton case by isospin rotation. One switches $u \leftrightarrow d$ and $\bar{u} \leftrightarrow \bar{d}$ in both the MC parton distribution inputs and in the polarization vector \vec{Q} .¹ Experimentally, effective neutron targets are nuclei with proton and neutron mixtures. Nuclear corrections are required to relate purities and quark polarizations of the measured asymmetries on these targets.

The foundation for nuclear corrections originates from the assumption that nuclear structure functions are incoherent superpositions of proton and neutron structure functions. In this model, non-linear nuclear medium effects are negligible: shadowing and the EMC effect in inclusive structure functions, and the hadronization attenuation in semi-inclusive yields must both be small. For a nucleus of A nucleons, with Z protons and N neutrons, one has

$$F_1^{A,h}(x) = \frac{Z}{A} F_1^{p,h}(x) + \frac{N}{A} F_1^{n,h}(x), \quad (6.21)$$

$$g_1^{A,h}(x) = P_A^p \frac{Z}{A} g_1^{p,h}(x) + P_A^n \frac{N}{A} g_1^{n,h}(x), \quad (6.22)$$

where P_A^p and P_A^n are the effective polarizations of protons and neutrons inside the nucleus.

Two nuclear targets are interesting at HERMES. The data analyzed here come from ${}^3\text{He}$ which has effective nucleon polarizations, $P_{{}^3\text{He}}^n$ and $P_{{}^3\text{He}}^p$, of 0.865 and -0.027 respectively [182, 183]. The discussion also applies to the deuterium target used in future HERMES running.

¹Note that fragmentation functions are defined such that they do not isospin rotate going from a proton to a neutron.

Suppose that for an asymmetry of event class h measured on a nuclear target, the asymmetry in the same class has also been measured on the proton. In this case, one may manipulate Eq. (6.22) to subtract the proton contribution to the nuclear asymmetry. This isolates the neutron contribution as

$$A_1^{n,h}(x) = \frac{g_1^{n,h}}{F_1^{n,h}}(x) = \frac{1}{P_A^n(1-f_p^h)}(A_1^{A,h} - P_A^p f_p^h A_1^{p,h}). \quad (6.23)$$

The dilution factor, f_p^h , is defined as the ratio of yields of h on the proton and on the nucleus.

$$\begin{aligned} f_p^h &= \frac{\sigma_p^h}{\sigma_A^h} = \frac{F_2^{p,h}}{F_2^{A,h}} \\ &= \frac{n_h^p}{n_h^A} \frac{F_2^p}{F_2^A} \end{aligned} \quad (6.24)$$

The second line of Equation (6.24) follows from multiplying and dividing the inclusive DIS cross-section: n_h is the DIS-normalized hadron multiplicity used in Section 5.6. This allows a direct measurement of the semi-inclusive dilution factor from HERMES unpolarized data, in a manner that cancels acceptance and normalization systematic uncertainties. Note that $f_p^h + f_n^h$ is unity.

To use Equation (6.23), one generates proton and neutron purities in Monte Carlo and separates the proton and nuclear asymmetries in the matrix purity equation. There exists a matrix \mathcal{N} such that,

$$\begin{pmatrix} \vec{\mathbf{A}}^p \\ \vec{\mathbf{A}}^A \end{pmatrix} = \mathcal{N} \cdot \begin{pmatrix} \mathbf{P}^p \\ \mathbf{P}^n \end{pmatrix} \vec{\mathbf{Q}} \quad (6.25)$$

If $\vec{\mathbf{A}}^p$ and $\vec{\mathbf{A}}^A$ are arranged so that the asymmetry types h appear in the same order, then from (6.23) it is clear that

$$\mathcal{N} = \begin{pmatrix} 1 & & & & & \\ & \ddots & & & & \\ & & 1 & & & 0 \\ a_{h_1} & & & b_{h_1} & & \\ & \ddots & & & \ddots & \\ & & a_{h_m} & & & b_{h_m} \end{pmatrix},$$

where

$$a_h \equiv f_p^h P_A^p, \quad (6.26)$$

$$b_h \equiv (1 - f_p^h) P_A^n. \quad (6.27)$$

This is the technique used for the analysis in this thesis. For a more detailed review, see Reference [152]. The only limitation in this method comes from the requirement that the corresponding proton asymmetry must be known for all nuclear asymmetries measured. This condition was satisfied in the ^3He measurements in 1995, but it will not be the case with future HERMES deuterium running with RICH particle identification. A more general approach is described in Appendix B

6.5 Monte Carlo Studies of the Extraction Procedure

The PEPSI Monte Carlo models polarized contributions to the deep-inelastic cross-sections in addition to the unpolarized contributions. Monte Carlo asymmetries may test of the implementation of the above formalism: choose an initial parameterization of polarized parton distributions, generate MC asymmetries and purities, and verify that the correct parton distributions are extracted by the purity analysis.

Figure 6-8 shows such a Monte Carlo inversion; GRSV 95 [163] provides the polarized parton distribution set. In general, this is a check of software implementation since the same physics assumptions in the analysis are also in the Monte Carlo.

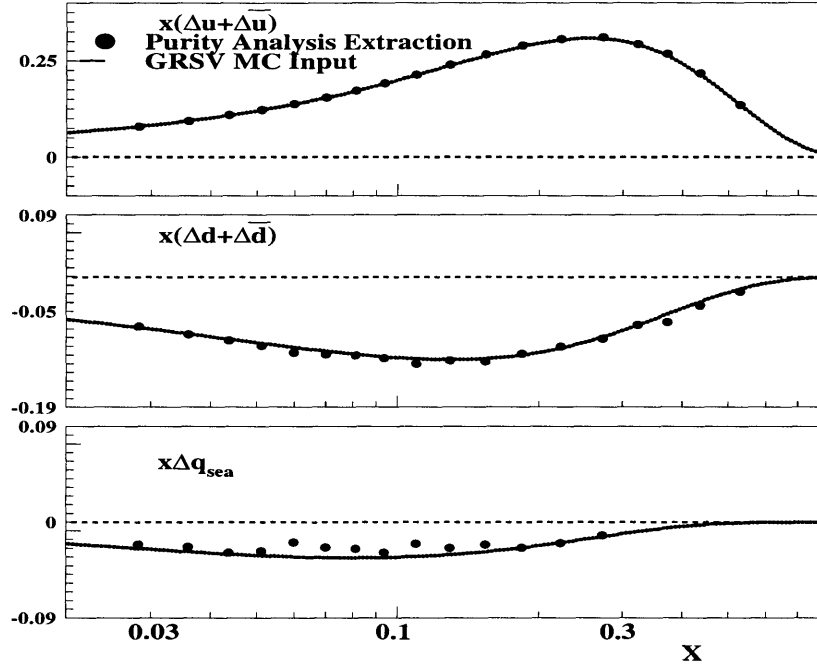


Figure 6-8: The Monte Carlo inversion with purities. The solid line represents the polarized parton distributions in the GRSV parameterization. The points are the extracted parton distributions from the Monte Carlo, using the purity analysis.

The test also investigates a more interesting concern, whether finite binning effects influence the extracted result. In calculating asymmetries, purities, and corrections, many physical distributions are evaluated in x bins, including $D(x)$, $R(x)$, $F_2(x)$, and $q(x)$. If the bin averaging of the distributions is not treated carefully, systematic deviation in the extracted values can result. Reference [184] provides a detailed explanation of this pitfall. Subtle bin size effects can be estimated from the ratio of the Monte Carlo extracted quark distributions to the input parameterization. The ratio is then used as a “bin size” correction on the experimental distributions. From Figure 6-8, one sees that these bin size effects are negligible in the polarized parton distribution extraction, and they are neglected in the analysis.

6.6 Uncertainties on the Extracted Polarizations

6.6.1 Propagation of Asymmetry Uncertainties

The statistical and systematic uncertainties of the extracted quark polarizations can be derived from the asymmetric uncertainties, using Equation (6.10) and the asymmetry covariances of the last chapter. The covariance C_Q is calculated twice: once using the statistical asymmetry covariance matrix only and once using the total (systematic and statistical) covariance matrix. The systematic covariance matrix is then the difference:

$$C_Q^{\text{sys}} = C_Q^{\text{total}} - C_Q^{\text{stat}}, \quad (6.28)$$

where

$$\delta \frac{\Delta q_i}{q_i} = \sqrt{C_Q^{\text{sys},ii}}. \quad (6.29)$$

A few more contributions to the systematic uncertainty require special treatment. Section 6.2.1 introduced a $1+R$ correction factor to the analysis, which itself has an uncertainty. This correction is equivalent to dividing all asymmetries by $\frac{1+\gamma^2}{1+R}$. For the purpose of fitting quark polarizations, one may modify the R contribution to the systematic asymmetry covariance, in order to include both the uncertainty in this correction and the uncertainty in the virtual photon depolarization. Following section 5.7.6, the new uncertainty is,

$$\delta_R = \frac{1 - \epsilon}{(1 + R)(1 + \epsilon R)} \delta R, \quad (6.30)$$

$$C_A^{\text{R},ij} = (\delta_R)^2 A^i A^j. \quad (6.31)$$

For the extraction, the g_2 systematic uncertainty on $\frac{g_1^h}{F_1^h}$, not A_1^h , is desired.

6.6.2 The Purity Systematic Uncertainty

The uncertainty in the purities are estimated by taking the differences of competing models of the unpolarized physics involved. For each model, one calculates a set of purities and extracts \vec{Q}_{model} . The spread in the resulting polarizations contributes an uncorrelated model uncertainty.

The difference of the CTEQ Low Q^2 and GRV Low Q^2 PDF sets is taken for the unpolarized parton distributions. The fragmentation models uncertainty is the difference between the three models fitted to HERMES yields, as explained in Section 6.2.2. The systematic uncertainty in the spectrometer acceptance function is assumed negligible. When pion asymmetries are used, the difference between the fitted Čerenkov threshold and an ideal threshold is considered a conservative uncertainty in the pion identification efficiency. A subtle point in the analysis involves the fact that this treatment dependent upon the valence extraction procedure: the systematic uncertainties must be separately estimated for the valence, simple, and flavor symmetric extractions.

6.6.3 The Unpolarized Sea Model Uncertainty

When applying the Unpolarized Sea Model, one may assign a systematic uncertainty for the maximum possible variation the sea polarization from zero. From positivity, the polarized parton distribution cannot exceed the unpolarized distribution. Note that when applying this limit, one wishes the true parton distributions defined on F_1 . With the R correction discussed in Section 6.2.1, the positivity limit with respect to PDFs defined on F_2 becomes $\frac{\Delta q_{\text{sea}}}{q_{\text{sea}}} = \pm \frac{1+\gamma^2}{1+R}$. The unpolarized sea model uncertainty is estimated by refitting the asymmetries, using each positivity limit. The asymmetries for each event class are corrected for the maximum sea polarization,

$$(A^h)' = A^h - P_{q_{\text{sea}}}^h \left(\pm \frac{1+\gamma^2}{1+R} \right), \quad (6.32)$$

and the difference of the extracted \vec{Q} s is taken as an uncorrelated uncertainty.

6.7 Results as a function of x

Using the formalism in the preceding sections, a fit to HERMES 1995, 96, and 97 asymmetries determines the polarization of the quarks in the nucleon in the Quark-Parton Model.

The results focus on the SU(3) symmetric sea polarization model, Model III of Section 6.3. As a direct measurement of the sea polarization is uniquely possible with HERMES semi-inclusive measurements, it is unreasonable to assume the sea is zero as in the Unpolarized Sea model. The two light flavor densities, $\Delta u + \Delta \bar{u}$ and $\Delta d + \Delta \bar{d}$, can be constrained uniquely and precisely with inclusive DIS data on proton and neutron targets; but inclusive DIS measurements alone can not resolve the spin puzzle, as the discussion in Section 2 indicates.

In all fits presented, however, an unpolarized sea is assumed above x of 0.3. From the unpolarized parton distributions shown in Figure 2-3, one sees that sea quark density decreases rapidly as a function of x ; the number density of sea quarks carrying a large fraction of the nucleon momentum is small. The positivity limit then provides a strong constraint on possible sea contributions in this region to the nucleon spin. By assuming the sea polarization is zero, one increases the statistical precision the up and down quark extraction from a two parameter fit, at the cost of the small systematic uncertainty described in Section 6.6.3. A comparison of the purity extraction with three sea models will be presented in Section 6.7.3.

The principal results in this thesis use only inclusive and semi-inclusive hadron asymmetries, as shown in Figures 5-10, 5-11a-b, and 5-12a-b, for a total of nine asymmetries. Asymmetries in 1996 and 1997 are formally separated in the analysis for ease in systematic uncertainty treatment, though the asymmetries in both years represent the same underlying physics. When studying the SU(3) symmetric sea assumption, pion asymmetries are not explicitly used. As the up-quark purities in Figure 6-7a suggest, pion identification allows essentially no better access to light quark polarizations in the nucleon than unidentified charged hadrons do. Including pion asymmetries in the purity extraction results in slightly smaller statistical uncertainties with the cost of an additional Čerenkov acceptance systematic uncertainty. Pions do provide, however, a unique constraint to the strange quark polarization, that is unavailable in unidentified hadrons (*cf.* Figure 6-7b). Pion asymmetries on the proton are fit in conjunction with a direct fit of strange quark properties. The ^3He pion asymmetries are neglected as they have poorer statistical precision.

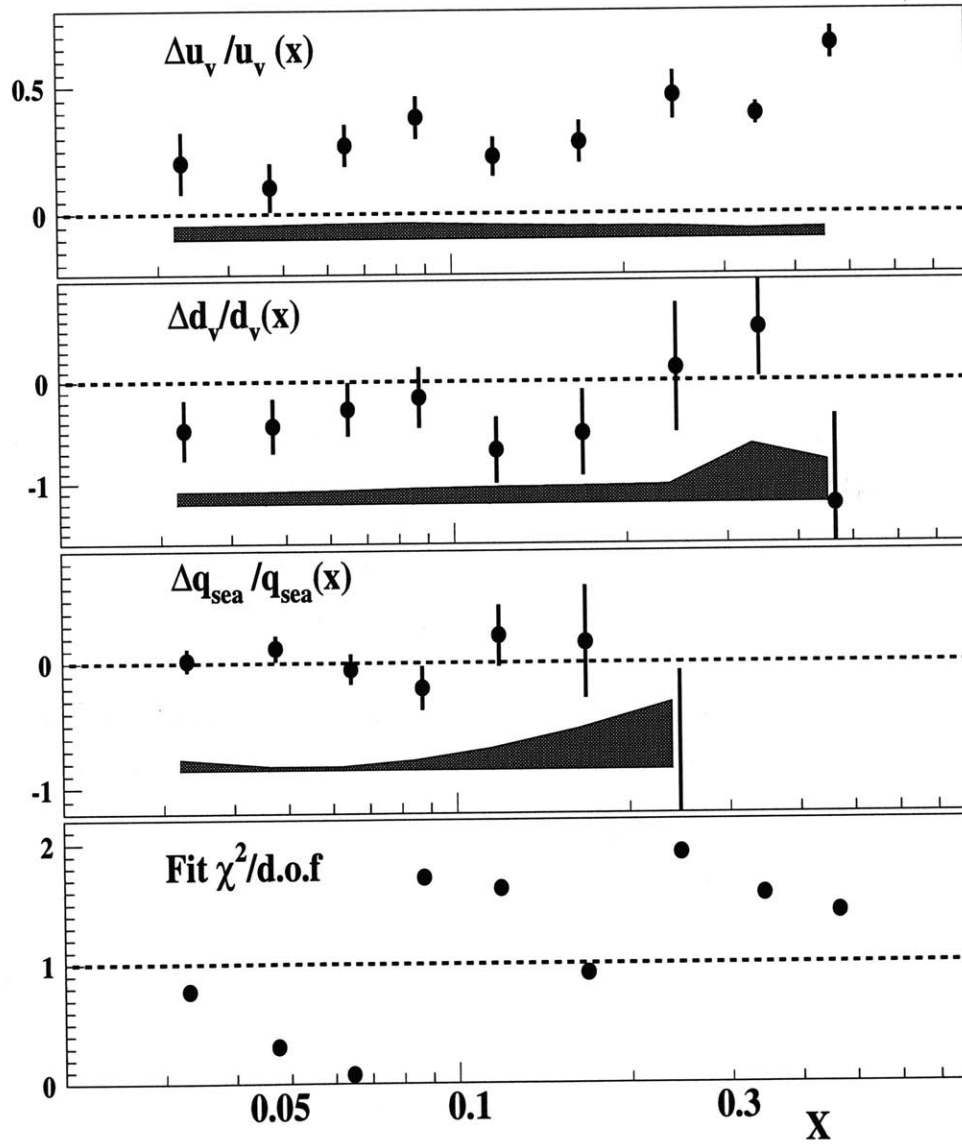


Figure 6-9: Quark polarizations in the Valence Fit and SU(3) symmetric sea polarization model constrained to nine HERMES inclusive and semi-inclusive hadron asymmetries. For $x > 0.3$, the sea polarization is assumed zero, and the two parameter unpolarized sea model is fit. The points are plotted at the measured x and Q^2 .

6.7.1 The Quark Polarization Extraction

Figure 6-9 shows the HERMES extracted polarizations in the valence parameterization, using the SU(3) symmetric sea polarization model. One observes that the up quark polarization in the proton is positive and increases with x , while the down quark polarization maintains a small negative value. The sea polarization is consistent with zero in the measured x range.

6.7.2 The Parton Distribution Extraction

Deriving parton distributions from polarizations is straightforward: The polarizations are multiplied by unpolarized parton distributions evaluated at the $\langle x \rangle$ of each bin. This procedure may also evolve the polarized parton distributions to $Q^2 = 2.5 \text{ GeV}^2$, in order to correct for the slight Q^2 dependence of the parton distributions. The quark polarizations are assumed to be Q^2 independent, which is motivated by the lack of any significant Q^2 dependence in the inclusive asymmetry measurements, as shown in Figure 2-7. The unpolarized parton distribution is then evaluated at $Q^2 = 2.5 \text{ GeV}^2$.

$$\Delta q(\langle x \rangle)_{Q^2=2.5} = \left(\frac{\Delta q}{q} \right)_{\text{extracted}} \cdot q(\langle x \rangle)_{Q^2=2.5}. \quad (6.33)$$

For ease of presentation, x_{Bj} is also multiplied in the following figures. The resulting parton distributions are shown in Figure 6-10. The final extraction from SMC is also shown for comparison. In general, the distributions from the two experiments are compatible in value. The precision in the up and sea quark distributions is greater in this work, as HERMES has taken more statistics on the proton.

The different contributions to the systematic uncertainty in the extraction are listed in Table A.9. The dominant contributions to the systematic uncertainty are plotted in Figure 6-11. For the valence extraction, one sees that uncertainties in the fragmentation model in the Monte Carlo are dominant. Beam and target polarization uncertainties also play a strong role in the u -quark systematic uncertainty. The total systematic uncertainty is nevertheless much smaller than the statistical uncertainties in the valence extraction.

Figure 6-12 compares the measured parton distributions with three parameterization of previous world data on polarized DIS: GRSV 95 Leading Order Standard Scenario [163],

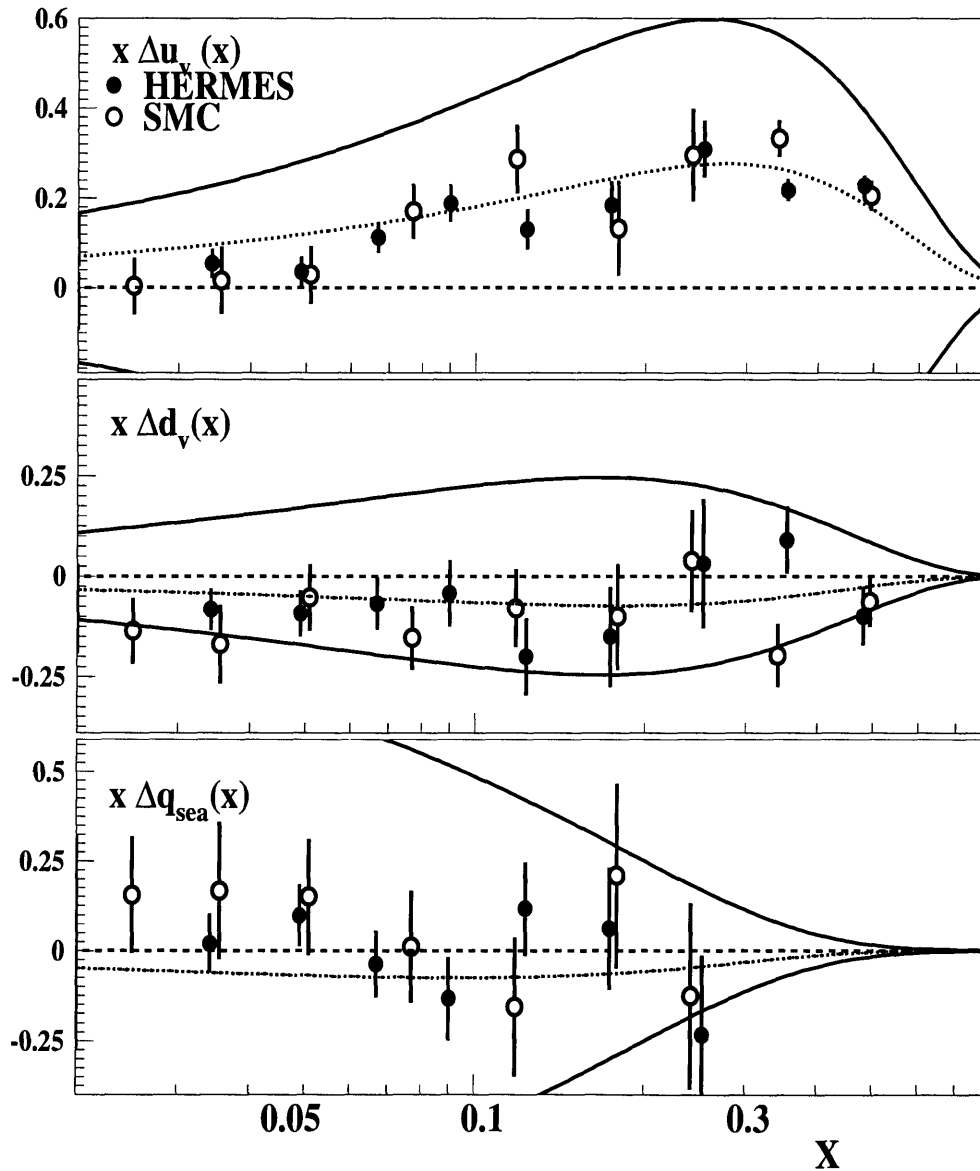


Figure 6-10: Extracted valence and sea quark helicity densities at $Q^2=2.5 \text{ GeV}^2$ compared to results of the SMC [167] experiment. The solid line represents the positivity limit from the unpolarized parton distributions. The dotted line shows the GRSV prediction (Standard, LO) for these distributions. Statistical uncertainties only are shown.

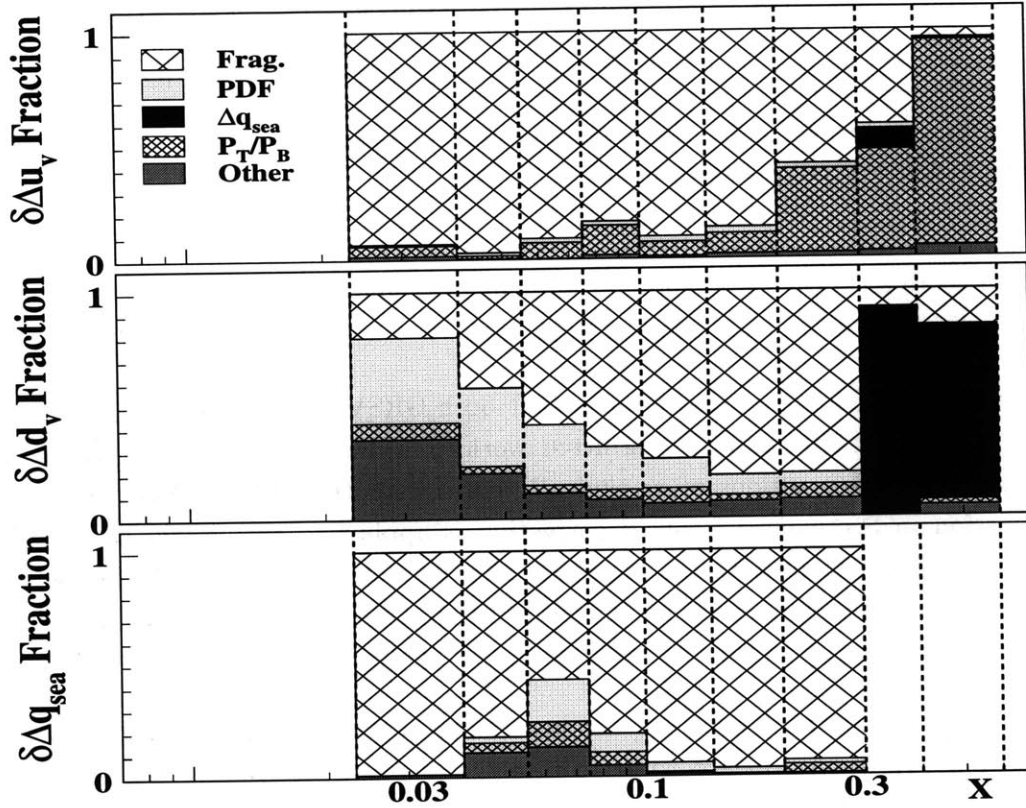


Figure 6-11: A plot of the different contributions to the systematic uncertainty in the extracted parton distributions in the valence parameterization. Each contribution is plotted as a fraction of the total systematic uncertainty. The four dominant effects are fragmentation (Frag), unpolarized parton distribution (PDF), the unpolarized sea assumption at high x (Δq_{sea}), and beam and target polarization (P_B/P_T).

Gehrmann-Stirling Leading Order Gluon Set A [185], and De Florian *et al.* Leading Order Set B [186]. In this comparison, a flavor symmetric combination of the extracted polarized quark densities is formed, for better comparison with inclusive data.

The GRSV and Gehrmann-Stirling groups have extracted leading order Δu , Δd , and Δq_{sea} distributions from world polarized data up to 1995, including results from E142, E143, and SMC. Both parameterizations assume SU(3) symmetry and the results of the hyperon decay analysis in Section 2; sea distributions are constrained to yield a negative Δs . De Florian *et al.*

Quark Distribution	N_q	α_q	β_q	$\chi^2/d.o.f$
$\Delta u + \Delta \bar{u}$	0.871 ± 0.091	0.645 ± 0.049	-	0.78/7
$\Delta d + \Delta \bar{d}$	-0.438 ± 0.22	0.392 ± 0.19	-	0.83/7
$\Delta s + \Delta \bar{s}$	1.4180 ± 5.4	0.571 ± 0.91	43 ± 51	0.94/4

Table 6.2: Parameters for a fit of x dependence of the extracted polarized parton distributions in the symmetric sea polarization model.

have fitted more recent data, including the inclusive asymmetry measurements from E154 [57] and the semi-inclusive measurements of SMC [167].

A key difference among extractions is that both GRSV and De Florian *et al.* fitted world data on A_1 , while Gehrmann-Stirling fitted world g_1 values. While the A_1 fits assume R is zero, experimental extractions of g_1 typically correct for the measured R values. Based on the discussion in Section 6.2.1, an R correction is applied to the A_1 fits in order to make the comparison consistent with the longitudinal cross-section treatment in this work. In each parameterization, the leading order analysis with an assumed zero or slightly positive ΔG is chosen for consistency with the assumptions in this analysis.

A direct fit to HERMES data has also been made in this analysis, using the form of GRSV. Each quark distribution is fit according to

$$\Delta u + \Delta \bar{u}(x) = N_u x^{\alpha_u} \cdot (u + \bar{u})(x), \quad (6.34)$$

$$\Delta d + \Delta \bar{d}(x) = N_d x^{\alpha_d} \cdot (d + \bar{d})(x), \quad (6.35)$$

$$\Delta q_{\text{sea}}(x) = N_q x^{\alpha_q} (1-x)^{\beta_q} \cdot q_{\text{sea}}(x). \quad (6.36)$$

The CTEQ Low Q^2 distributions provide the unpolarized parton distributions. The resulting “Best Fit” functions are also shown in Figure 6-12; the parameters for these fits are listed in Table 6.7.2.

The HERMES data are consistent with these world parameterizations within uncertainties. The up helicity difference is slightly smaller than the existing world parameterization, but the statistical uncertainties on the down-flavor extraction are currently too large to constrain the x dependence precisely. The sea quark polarization directly extracted with purities is closer to

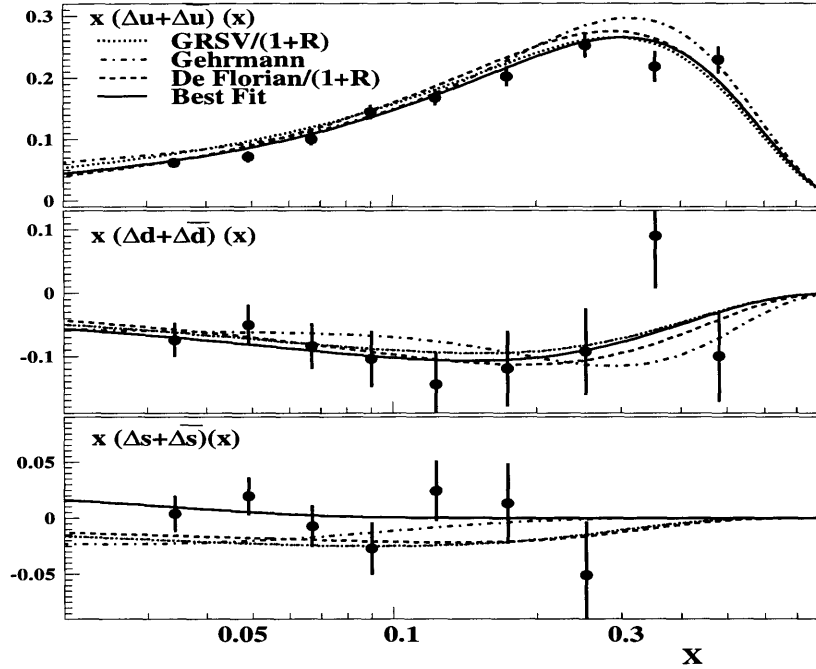


Figure 6-12: A comparison of extracted flavor symmetric polarized parton distributions at $Q^2=2.5 \text{ GeV}^2$ to parameterizations of other world data, as explained in the text. Statistical uncertainties only are shown.

zero than the world parameterization constrained by hyperon decay constants. The sea results may not be directly comparable though as the primary sea sensitivity in the extraction is $\Delta\bar{u}$, not Δs .

As semi-inclusive physics only extends inclusive analyses, the extraction presented here should be consistent with previous inclusive measurements. The consistency is best checked by examining the non-singlet polarization density, $\Delta q^{NS}(x)$, a quantity nearly independent of the properties of the sea. It can be shown to be directly related to the inclusive structure function g_1 , by

$$\Delta q^{NS}(x) = (\Delta u + \Delta\bar{u})(x) - (\Delta d + \Delta\bar{d})(x), \quad (6.37)$$

$$= 6 \left[g_1^p(x) - g_1^n(x) \right]. \quad (6.38)$$

$g_1^p(x)$ and $g_1^n(x)$ are calculated directly from the inclusive asymmetries in Figure 5-10, using Equations (5.14) and (6.22). The comparison is shown in Figure 6-13. The extracted parton distributions yield a non-singlet helicity density consistent with the inclusive structure function difference; the slight deviations arise from the additional information in semi-inclusive reactions. Within the statistics, all three world parameterization fit the data.

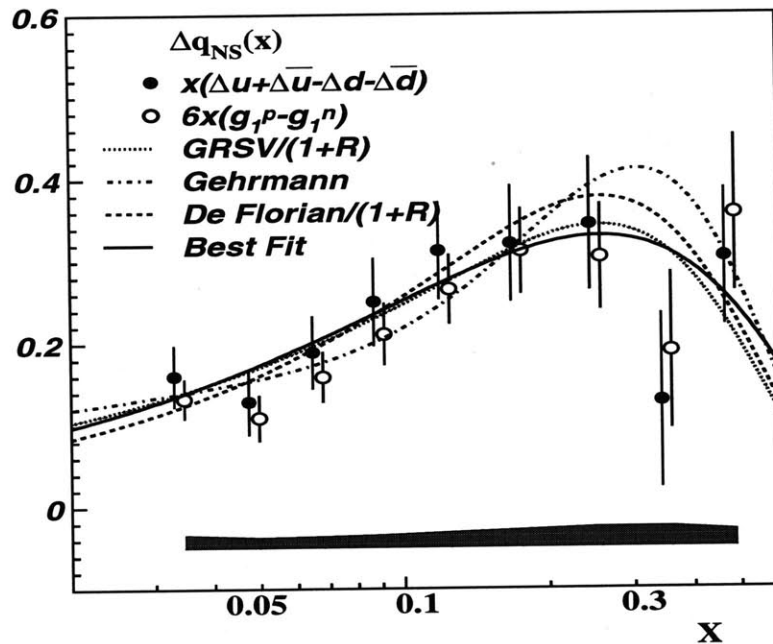


Figure 6-13: The Extracted Non-singlet Quark Distribution. The dark circles show the derived $\Delta q_{NS}(x)$ from flavor symmetric up and down quark polarized parton distributions. The same quantity derived from the inclusive structure functions are shown in the open circles. The four parameterization are explained in the text. All quantities are evaluated at $Q^2=2.5 \text{ GeV}^2$

6.7.3 Comparison of Models of the Sea

While this thesis focuses on the SU(3) symmetric polarization model of the sea, but the sensitivity to different sea models is also interesting. Figure 6-14 compares three models of sea polarization, in the valence fit: the SU(3) symmetric polarization, the SU(3) symmetric parton distribution, and the direct strange quark fit. Each symmetric sea model fits only inclusive and

semi-inclusive hadron asymmetries. In these two models, the strange quarks' polarizations or parton densities are assumed identical to the light quarks' properties; in the plot, the strange sea polarization is simply reproduced from the light quark sea polarizations. As noted above, the polarization in these models may be more constrained in practice by \bar{u} than by s or \bar{s} -quarks.

In addition, the strange quark fit adds the HERMES pion asymmetries to the vector \vec{A} in order to gain a lever arm on strangeness properties. A total of thirteen asymmetries over three years are fit, with eight representing independent physical distributions.

In comparing the SU(3) symmetric models, one sees little dependence on the sea model assumption. The purities in the two models differ mainly by the fact that $\bar{d}(x) \sim 2\bar{u}(x)$ near $x=0.18$. The extracted polarized parton distributions vary even less, which may result from the dominance of \bar{u} over \bar{d} in the sea purity construction.

The strange quark fit is both unique and interesting. While statistical uncertainties are large, the direct fit to HERMES pion data suggests the strange sea polarization is positive. A fit of $\Delta s + \Delta \bar{s}(x)$ to zero polarization using statistical uncertainties only yields a $\chi^2/\text{d.o.f}$ of 17.8/7; with the estimated systematic uncertainties, this becomes 15.3/7. The corresponding confidence that the observation is a statistical fluctuation from zero is 1.8% and 4.1% respectively. The naive interpretation of these results is that strange quarks have a large positive contribution to the nucleon spin.

However, this analysis must be attended with strong caveats. Section 6.1 discussed the disadvantage of using the purity analysis, when the purities themselves are as unknown as the investigated polarizations. In the strange quark case, the fragmentation to pions is known poorly, and is generally assumed identical to unfavored light quark fragmentation. Of more concern, however, is the possibility that light quark fragmentation is not constrained well enough for this analysis. If one rewrites the purity equation to isolate Δs , one gets

$$\frac{\Delta s}{s} = \frac{1}{P_s^h} \left(A^h - P_u^h \frac{\Delta u}{u} - P_d^h \frac{\Delta d}{d} \right). \quad (6.39)$$

P_s^h is relatively small, while the correction $(P_u^h \frac{\Delta u}{u} + P_d^h \frac{\Delta d}{d})$ is large and nearly the same size as A^h . If the uncertainty in P_u^h is underestimated by the fragmentation model variation, than a large systematic effect in the extracted strange sea polarization will be observed.

The positive strange sea has also been confirmed in an analysis based on counting rate differences [44, 43], as described in 2.1.4.1. That analysis observed that the strange sea

extraction is especially sensitive to breaking of charge conjugation symmetry in fragmentation. In contrast to Eq. 2.34, if \bar{u} -quarks produce $\sim 25\%$ more charged pions than u -quarks, $D_{\bar{u}}^{\pi^+\pi^-} \sim 1.25 D_u^{\pi^+\pi^-}$, then a false signal may be seen in the strange sea extraction. The LUND string model does predict slight violations of fragmentation symmetries in HERMES kinematics but these effects typically do not exceed 5%. A large charge conjugation symmetry breaking in fragmentation would also affect other analyses with semi-inclusive pions, including the extraction of $\frac{d_v}{u_v}$.

Another possibility is that a deficiency in the Monte Carlo acceptance model biases the extraction. Semi-inclusive pions events are more sensitive to acceptance corrections than other event classes, as Figure 5-8 demonstrates. At this time, it is not possible to rule out these effects and unambiguously measure of the strange sea polarization. Detailed investigations of these issues must wait for future HERMES data-taking. Higher statistics unpolarized data samples should provide stronger constraints on these uncertainties.

6.8 Determining Moments of the Distributions

To determine the total contribution of each quark flavor to the proton spin, the measured parton distributions must be integrated over the entire x range. This integration is usually broken into three pieces: the HERMES measured region, $0.023 < x < 0.6$; the low x region $x < 0.023$, and the high x region, $x > 0.6$.

To determine the measured region contribution to the integral, one first assumes that the quark polarizations have constant values across each kinematic bin. This is the simplest and most direct interpretation of the measurement: a fit to the x dependence of the quark polarizations may provide a more reasonable behavior in x , but subsequent results would depend implicitly on the form of the fitting function chosen.

In each bin, the n^{th} moment of the measured distribution is determined by,

$$x^n (\Delta q^{\text{measured}})_{Q^2=2.5\text{GeV}^2} = \int_{0.023}^{0.6} dx x^n (\Delta q(x))_{Q^2=2.5\text{GeV}^2} \quad (6.40)$$

$$= \sum_{i=1}^9 \left(\frac{\Delta q}{q} \Big|_i \int_{x_i}^{x_{i+1}} dx x^n (q(x))_{Q^2=2.5\text{GeV}^2} \right) \quad (6.41)$$

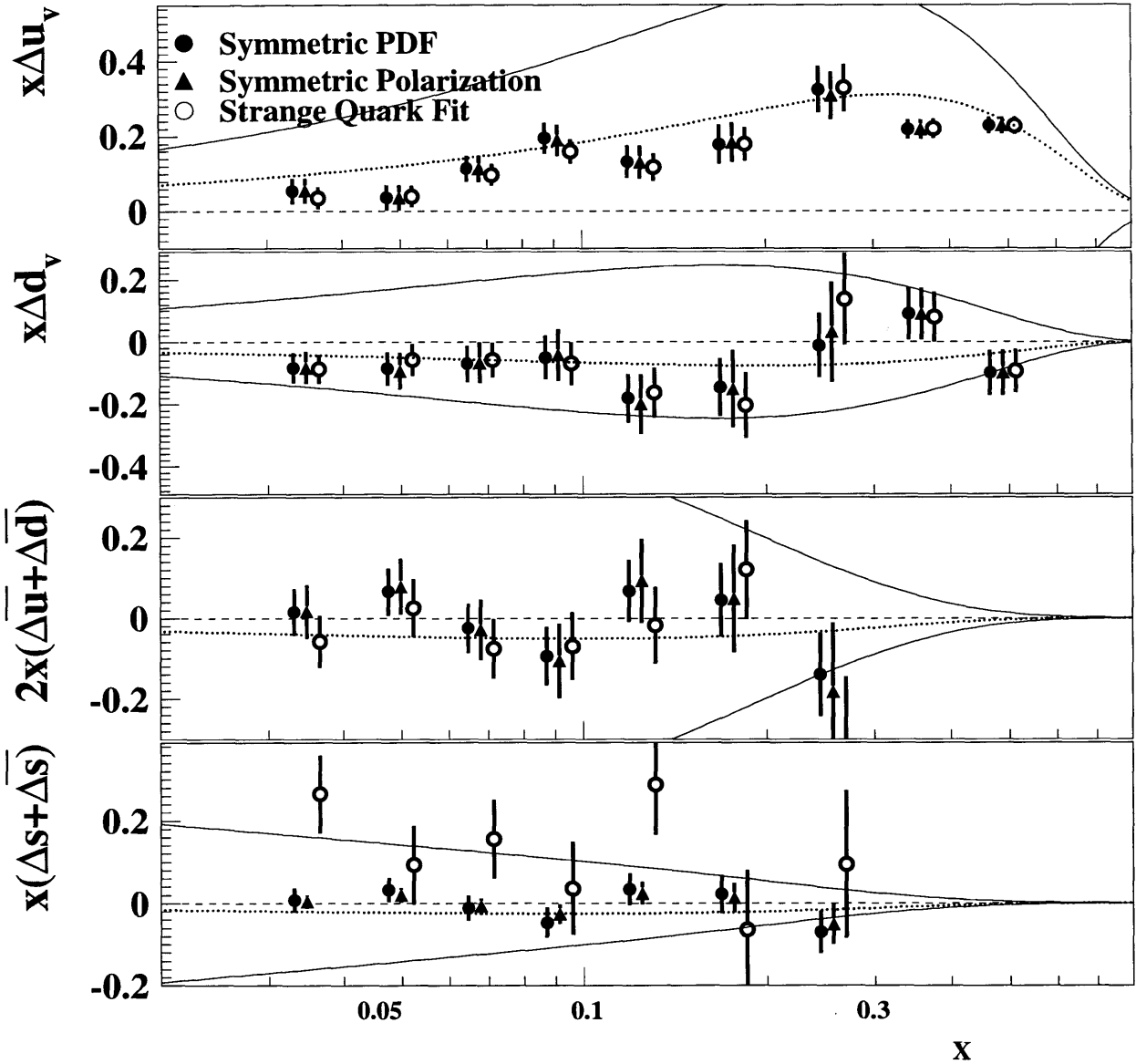


Figure 6-14: Three models of sea polarization are constrained in the Valence Fit. The SU(3) symmetric PDF and polarization fits are three parameter fits: the strange quark polarizations are reproduced from the light quark polarizations. The Strange Quark fit directly fits the strange sea, using four parameters. The solid lines show CTEQ unpolarized parton distributions and the dotted lines, the GRSV prediction. Statistical uncertainties only are shown.

Statistical uncertainties in each x bin are added in quadrature, while systematic uncertainties are assumed to be completely correlated among x bins and are added linearly.

DIS experiments attempt to measure as large an x range as possible, but extrapolation outside the measured region is necessary. Guidance from theory is required if the low x integral contribution is estimated. Unfortunately, there is no clear prediction for the behavior of polarized parton distributions at low x [57]. In the past, analyses of $g_1(x)$ have relied on Regge theory [187, 188], which predicts $x^{-\alpha}$ behavior at low x with $0.5 < \alpha < 0$ [53, 54]. The application of this theory has been questioned, as recent analyses indicate that the polarized structure functions could diverge by more negative powers at low x [57]. Also, the rise of the unpolarized structure functions at low x is steeper than Regge theory predicts [83]. In this analysis, the Regge fit has been performed in order to facilitate comparison to previous works. The α is assumed zero, and a constant value is fit to the first three bins in x for each extracted parton distribution. The lines are then integrated from 0 to 0.023. For a “systematic uncertainty,” the statistical uncertainty from determining the line is chosen.

To estimate the high x valence quark helicity integral, the quark polarization fits from Table 6.7.2 are extended to x of 1.0. The fits are then weighted with the unpolarized parton distribution and integrated from 0.6 to 1.0. The steep drop of the unpolarized parton distributions above x of 0.6 ensures the integral contribution remains small in this region. To be conservative, the value of the extrapolation has also been used as its systematic uncertainty. The polarized parton distributions of the sea above $x = 0.3$ are assumed zero, with the positivity limit providing the systematic uncertainty.

6.9 Results for the Integrals

The extracted integral values for the first and second moments of the polarized quark distributions are listed in Tables A.10 and A.11. The results here differ from Reference [149] in that all the experimental asymmetries were studied independently in this work with slight differences in ^3He data analysis; the published results are compatible with this work. A few of the key values are summarized here and are compared to determinations from other sources.

Measured region integrals of the quark distributions may be compared between different deep-inelastic scattering experiments with little theoretical uncertainty. Table 6.3 compares the results with the SMC experiment from Reference [167]. The SMC values have been evolved to

	This Thesis	SMC
Δu_{val}	$0.53 \pm 0.05 \pm 0.08$	$0.59 \pm 0.08 \pm 0.07$
Δd_{val}	$-0.23 \pm 0.10 \pm 0.14$	$-0.33 \pm 0.11 \pm 0.09$
$\Delta \bar{u}$	$0.00 \pm 0.02 \pm 0.03$	$0.02 \pm 0.03 \pm 0.02$
$\Delta \bar{d}$	$-0.01 \pm 0.03 \pm 0.05$	$0.02 \pm 0.03 \pm 0.02$
$x\Delta u_{\text{val}}$	$0.12 \pm 0.01 \pm 0.01$	$0.15 \pm 0.02 \pm 0.01$
$x\Delta d_{\text{val}}$	$-0.03 \pm 0.02 \pm 0.02$	$-0.05 \pm 0.02 \pm 0.02$

Table 6.3: The measured region integrals compared to similar values from SMC[167]. The SMC results have been evolved to a common $Q^2 = 2.5 \text{ GeV}^2$ and integrated over the HERMES x -range of $0.023 < x < 0.6$.

	This Thesis	SU(3) Analysis
$\Delta u + \Delta \bar{u}$	$0.58 \pm 0.02 \pm 0.04$	0.66 ± 0.03
$\Delta d + \Delta \bar{d}$	$-0.30 \pm 0.06 \pm 0.05$	-0.35 ± 0.02
$\Delta s + \Delta \bar{s}$	$-0.01 \pm 0.03 \pm 0.04$	-0.08 ± 0.01
a_0	$0.27 \pm 0.04 \pm 0.09$	0.23 ± 0.04
a_3	$0.89 \pm 0.07 \pm 0.07$	1.01 ± 0.05
a_8	$0.28 \pm 0.08 \pm 0.10$	0.46 ± 0.03

Table 6.4: Integrals of the quark distributions over the entire x range compared to an SU(3) symmetry analysis of inclusive data and hyperon decays[65]. All values are quoted at $Q^2 = 2.5 \text{ GeV}^2$.

the common $Q^2 = 2.5 \text{ GeV}^2$ and integrated over the HERMES measured x range in order to make a direct comparison. The determinations of the two experiments are compatible within the quoted uncertainties. The high statistics of the HERMES proton data is reflected in the lower statistical uncertainty in the measured u_{valence} quark spin fraction.

With extrapolations extending the integration over the entire x range, a comparison of the results with the hyperon decay analyses discussed in Section 2.2.6 is possible, and is shown in Table 6.4. In this table, the values in Equation (2.84) have been evolved to the quoted $Q^2 = 2.5 \text{ GeV}^2$, using the QCD corrections (2.75) and $\alpha_s(Q^2 = 2.5) = 0.3467 \pm 0.035$ [13] for three flavors. The semi-inclusive results in this thesis are compatible with the results of the SU(3) symmetry analysis. The quark polarizations tend to be slightly lower in value, with a disagreement in the sea spin fraction $\Delta s + \Delta \bar{s}$: the HERMES data suggests that sea quarks are unpolarized. In interpreting these results, one must be aware of the sea polarization

	This Thesis	Lattice QCD[100]	Q^2 (GeV ²)
Δu_{val}	$0.576 \pm 0.046 \pm 0.081$	0.841 ± 0.052	5
Δd_{val}	$-0.270 \pm 0.104 \pm 0.138$	-0.245 ± 0.015	5
$x\Delta u_{\text{val}}$	$0.134 \pm 0.009 \pm 0.017$	0.198 ± 0.008	4
$x\Delta d_{\text{val}}$	$-0.029 \pm 0.024 \pm 0.016$	-0.048 ± 0.003	4

Table 6.5: First and second moments of the valence quark distributions compared Lattice QCD. The measured values are quoted at $Q^2 = 2.5 \text{ GeV}^2$, while Q^2 of the lattice results are given in the table.

definition used. The strange quark spin fraction, $\Delta s + \Delta \bar{s}$, is constrained by the SU(3) symmetric polarization model rather than by direct measurement. If the symmetric distribution model is used instead, the sea quark polarization does not change noticeably: $\Delta s + \Delta \bar{s} = 0.01 \pm 0.04 \pm 0.05$. The present statistics are not sensitive enough to distinguish the nucleon spin structure in these models. Using Equations (2.62) and (2.58), the extracted quark polarizations may be converted to axial vector currents. Good agreement with SU(3) symmetry analysis is also seen.

A final comparison with lattice QCD results is shown in Table 6.5. The extracted first and second moments are significantly lower than the lattice predictions. This may suggest that the quenched approximation does not yield accurate predictions for nucleon spin structure.

Chapter 7

Conclusions

The first three years of HERMES data taking have yielded high statistics polarized deep-inelastic scattering data on ^3He and ^1H targets. With high purity targets, a large acceptance, and scattered particle identification, HERMES has studied inclusive and semi-inclusive DIS reactions inaccessible to previous experiments in the field. An important part of the double-spin cross-section asymmetry measurement is the determination of beam polarization; the state of the art of beam polarimetry at HERA was presented in this thesis.

The polarized measurements yield inclusive and semi-inclusive charged hadron asymmetries, which have been presented as a function of x_{Bjorken} . In the framework of the Quark-Parton Model, these asymmetries may be simultaneously fit to constrain the polarization of each species of quark inside the nucleon. The estimated helicity difference parton distributions for valence and sea quarks have been presented, and the extracted values for the measured region integrals are $\Delta u_v = 0.525 \pm 0.046 \pm 0.078$, $\Delta d_v = -0.23 \pm 0.10 \pm 0.14$, and $\Delta \bar{u} = -0.003 \pm 0.021 \pm 0.030$.

All current experimental investigations in polarized DIS have focused on either inclusive asymmetries or semi-inclusive total hadron asymmetries. A feature of the analyzed data set included clean separation of pions from other particles at high momentum. Hints of different physics accessed by this sample have been presented, with the caution that the systematics of measuring pion asymmetries have only begun to be addressed.

HERMES will soon have a new data set with high statistics on a deuterium target, which will significantly improve the precision on the d -quark helicity distribution. Before the deuterium run began, the Threshold Čerenkov was replaced with a Ring Imaging Čerenkov (RICH).

This new detector will identify π , K and p particles over nearly all momenta. Detailed investigations of fragmentation to each particle will also become possible, addressing issues in strange quark fragmentation and fragmentation symmetry. Kaon asymmetries should also provide direct sensitivity to strange quark polarizations in the nucleon. Fits of these semi-inclusive asymmetries may directly extract Δs without invoking SU(3) symmetry.

HERMES is currently alone in collecting polarized deep-inelastic data, but a new generation of experiments will start running within a few years, including the COMPASS[47] experiment at CERN and spin program at RHIC[189]. These efforts will focus study on the elusive gluon spin contribution to the nucleon spin. Hints of a large gluon polarization have already been found in HERMES photoproduction data[45]. The new measurements of sea quark and gluon polarizations will provide a more complete understanding of how the nucleon spin is composed.

Appendix A

Tables of Results

Inclusive Events							
Bin	$\langle x \rangle$	$\langle Q^2 \rangle$ (GeV ²)	$\langle W^2 \rangle$ (GeV ²)	γ	η	ϵ	$\langle D \rangle$
1	0.033	1.21	36.7	0.056	0.025	0.535	0.719
2	0.047	1.47	30.6	0.074	0.042	0.695	0.590
3	0.065	1.72	25.8	0.093	0.061	0.792	0.498
4	0.087	1.99	21.9	0.117	0.084	0.857	0.427
5	0.119	2.30	18.1	0.150	0.116	0.905	0.361
6	0.168	2.66	14.2	0.198	0.163	0.942	0.297
7	0.245	3.06	10.4	0.272	0.236	0.966	0.240
8	0.342	3.74	8.1	0.342	0.300	0.973	0.212
9	0.465	5.16	6.8	0.392	0.341	0.970	0.223

Semi-inclusive Events											
Bin	$\langle x \rangle$	$\langle Q^2 \rangle$ (GeV ²)	$\langle W^2 \rangle$ (GeV ²)	γ	η	ϵ	$\langle D \rangle$	$\langle z_{h+} \rangle$	$\langle z_{h-} \rangle$	$\langle z_{\pi+} \rangle$	$\langle z_{\pi-} \rangle$
1	0.033	1.21	36.0	0.057	0.026	0.546	0.704	0.384	0.366	0.420	0.398
2	0.047	1.45	30.1	0.075	0.044	0.716	0.579	0.396	0.379	0.472	0.459
3	0.065	1.74	26.2	0.094	0.063	0.801	0.506	0.406	0.392	0.513	0.498
4	0.087	2.13	23.4	0.116	0.083	0.850	0.462	0.416	0.397	0.544	0.527
5	0.118	2.69	21.0	0.141	0.104	0.873	0.438	0.415	0.399	0.558	0.536
6	0.167	3.66	19.4	0.169	0.126	0.880	0.433	0.410	0.392	0.570	0.544
7	0.239	5.15	17.4	0.206	0.154	0.883	0.445	0.405	0.383	0.576	0.552
8	0.339	7.20	14.9	0.241	0.177	0.874	0.452	0.396	0.378	0.585	0.561
9	0.449	9.84	12.9	0.280	0.205	0.871	0.474	0.385	0.398	0.588	0.560

Table A.1: Average values of kinematic variables for the inclusive and semi-inclusive samples. The values are quoted for the proton data. The semi-inclusive kinematic factors are calculated for positive hadron events except for the $\langle z \rangle$. Note that the semi-inclusive samples includes a $W^2 > 10 \text{ GeV}^2$ in their definition, where the inclusive sample is constrained by $W^2 > 4 \text{ GeV}^2$.

Raw ^3He Asymmetries, $\frac{A_{\parallel}}{D}$ (1995)					
$\langle x \rangle$	e^+	h^+	h^-	π^+	π^-
0.033	-0.032 ± 0.012	-0.046 ± 0.033	-0.079 ± 0.038	0.121 ± 0.101	-0.268 ± 0.114
0.047	-0.008 ± 0.014	-0.002 ± 0.034	0.033 ± 0.040	-0.058 ± 0.110	0.133 ± 0.126
0.065	-0.026 ± 0.015	-0.035 ± 0.035	-0.013 ± 0.043	0.071 ± 0.118	0.242 ± 0.141
0.087	-0.028 ± 0.018	-0.049 ± 0.040	0.025 ± 0.049	-0.255 ± 0.135	-0.126 ± 0.170
0.119	-0.037 ± 0.019	-0.017 ± 0.042	0.052 ± 0.054	-0.078 ± 0.148	-0.197 ± 0.185
0.168	-0.036 ± 0.023	0.017 ± 0.050	-0.024 ± 0.066	-0.217 ± 0.187	0.613 ± 0.245
0.245	-0.009 ± 0.030	-0.139 ± 0.067	0.049 ± 0.093	0.429 ± 0.274	0.462 ± 0.395
0.342	0.075 ± 0.051	-0.121 ± 0.137	-0.177 ± 0.195	-0.617 ± 0.778	0.423 ± 1.286
0.465	-0.039 ± 0.072	-0.189 ± 0.257	0.916 ± 0.401	1.480 ± 2.197	—
Raw Proton Asymmetries, $\frac{A_{\parallel}}{D}$ (1996)					
$\langle x \rangle$	e^+	h^+	h^-	π^+	π^-
0.033	0.086 ± 0.012	0.085 ± 0.034	0.086 ± 0.040	0.075 ± 0.044	0.044 ± 0.050
0.047	0.096 ± 0.014	0.107 ± 0.035	0.109 ± 0.043	0.113 ± 0.050	0.107 ± 0.057
0.065	0.124 ± 0.016	0.161 ± 0.037	0.068 ± 0.046	0.142 ± 0.054	0.051 ± 0.062
0.087	0.178 ± 0.018	0.186 ± 0.041	0.173 ± 0.053	0.280 ± 0.061	0.108 ± 0.076
0.119	0.231 ± 0.020	0.273 ± 0.044	0.274 ± 0.058	0.186 ± 0.067	0.242 ± 0.084
0.168	0.252 ± 0.024	0.240 ± 0.052	0.295 ± 0.072	0.282 ± 0.083	0.200 ± 0.109
0.245	0.346 ± 0.030	0.498 ± 0.068	0.280 ± 0.097	0.472 ± 0.115	0.393 ± 0.153
0.342	0.388 ± 0.050	0.238 ± 0.136	0.432 ± 0.198	0.502 ± 0.249	0.459 ± 0.338
0.465	0.584 ± 0.070	0.890 ± 0.275	0.109 ± 0.427	1.501 ± 0.554	1.261 ± 0.708
Raw Proton Asymmetries, $\frac{A_{\parallel}}{D}$ (1997)					
$\langle x \rangle$	e^+	h^+	h^-	π^+	π^-
0.033	0.077 ± 0.007	0.096 ± 0.020	0.036 ± 0.024	0.039 ± 0.027	0.017 ± 0.030
0.047	0.107 ± 0.009	0.123 ± 0.021	0.091 ± 0.026	0.079 ± 0.030	0.099 ± 0.035
0.065	0.118 ± 0.009	0.142 ± 0.022	0.070 ± 0.028	0.106 ± 0.032	0.044 ± 0.038
0.087	0.169 ± 0.011	0.201 ± 0.025	0.024 ± 0.033	0.180 ± 0.038	0.023 ± 0.046
0.119	0.205 ± 0.012	0.273 ± 0.027	0.166 ± 0.036	0.243 ± 0.042	0.079 ± 0.052
0.168	0.273 ± 0.015	0.274 ± 0.032	0.175 ± 0.044	0.374 ± 0.051	0.117 ± 0.066
0.245	0.350 ± 0.019	0.413 ± 0.043	0.201 ± 0.061	0.340 ± 0.071	0.177 ± 0.100
0.342	0.505 ± 0.031	0.497 ± 0.084	0.654 ± 0.123	0.443 ± 0.154	0.473 ± 0.217
0.465	0.649 ± 0.042	0.552 ± 0.169	0.123 ± 0.256	0.670 ± 0.333	-0.459 ± 0.484

Table A.2: The experimental asymmetries, $\frac{A_{\parallel}}{D}$, without smearing and radiative corrections for 1995, 1996, and 1997. Only statistical uncertainties are listed.

${}^3\text{He}$ Structure Function Ratio, $\frac{g_1^h}{F_1^h}$					
$\langle x \rangle$	e^+	h^+	h^-	π^+	π^-
0.033	$-0.036 \pm 0.012 \pm 0.004$	$-0.046 \pm 0.033 \pm 0.007$	$-0.079 \pm 0.038 \pm 0.008$	$0.121 \pm 0.101 \pm 0.011$	$-0.268 \pm 0.114 \pm 0.021$
0.047	$-0.012 \pm 0.014 \pm 0.003$	$-0.002 \pm 0.034 \pm 0.006$	$0.032 \pm 0.040 \pm 0.006$	$-0.058 \pm 0.109 \pm 0.007$	$0.133 \pm 0.125 \pm 0.012$
0.065	$-0.029 \pm 0.015 \pm 0.004$	$-0.034 \pm 0.035 \pm 0.006$	$-0.013 \pm 0.042 \pm 0.006$	$0.071 \pm 0.117 \pm 0.008$	$0.241 \pm 0.140 \pm 0.019$
0.087	$-0.031 \pm 0.017 \pm 0.004$	$-0.048 \pm 0.039 \pm 0.007$	$0.025 \pm 0.049 \pm 0.006$	$-0.253 \pm 0.134 \pm 0.020$	$-0.125 \pm 0.168 \pm 0.011$
0.119	$-0.040 \pm 0.019 \pm 0.004$	$-0.017 \pm 0.041 \pm 0.006$	$0.051 \pm 0.053 \pm 0.007$	$-0.077 \pm 0.147 \pm 0.008$	$-0.195 \pm 0.183 \pm 0.015$
0.168	$-0.038 \pm 0.022 \pm 0.004$	$0.017 \pm 0.049 \pm 0.006$	$-0.023 \pm 0.065 \pm 0.006$	$-0.213 \pm 0.184 \pm 0.017$	$0.604 \pm 0.241 \pm 0.044$
0.245	$-0.011 \pm 0.028 \pm 0.003$	$-0.135 \pm 0.065 \pm 0.011$	$0.048 \pm 0.090 \pm 0.006$	$0.418 \pm 0.267 \pm 0.030$	$0.450 \pm 0.385 \pm 0.032$
0.342	$0.067 \pm 0.046 \pm 0.006$	$-0.116 \pm 0.131 \pm 0.010$	$-0.169 \pm 0.187 \pm 0.013$	$-0.595 \pm 0.750 \pm 0.042$	$0.409 \pm 1.242 \pm 0.029$
0.465	$-0.032 \pm 0.063 \pm 0.007$	$-0.178 \pm 0.243 \pm 0.015$	$0.866 \pm 0.379 \pm 0.062$	$1.407 \pm 2.089 \pm 0.100$	—

Proton Structure Function Ratio, $\frac{g_1^h}{F_1^h}$					
$\langle x \rangle$	e^+	h^+	h^-	π^+	π^-
0.033	$0.076 \pm 0.006 \pm 0.005$	$0.085 \pm 0.016 \pm 0.006$	$0.048 \pm 0.020 \pm 0.004$	$0.044 \pm 0.021 \pm 0.003$	$0.024 \pm 0.025 \pm 0.002$
0.047	$0.102 \pm 0.007 \pm 0.007$	$0.110 \pm 0.017 \pm 0.008$	$0.092 \pm 0.021 \pm 0.007$	$0.082 \pm 0.024 \pm 0.006$	$0.097 \pm 0.029 \pm 0.007$
0.065	$0.116 \pm 0.008 \pm 0.008$	$0.136 \pm 0.018 \pm 0.010$	$0.065 \pm 0.022 \pm 0.005$	$0.107 \pm 0.026 \pm 0.008$	$0.043 \pm 0.031 \pm 0.003$
0.087	$0.163 \pm 0.009 \pm 0.011$	$0.182 \pm 0.020 \pm 0.013$	$0.058 \pm 0.026 \pm 0.005$	$0.190 \pm 0.030 \pm 0.014$	$0.042 \pm 0.036 \pm 0.003$
0.119	$0.194 \pm 0.010 \pm 0.013$	$0.251 \pm 0.021 \pm 0.016$	$0.178 \pm 0.028 \pm 0.012$	$0.209 \pm 0.033 \pm 0.014$	$0.113 \pm 0.041 \pm 0.008$
0.168	$0.241 \pm 0.011 \pm 0.016$	$0.247 \pm 0.026 \pm 0.017$	$0.191 \pm 0.035 \pm 0.013$	$0.326 \pm 0.041 \pm 0.022$	$0.130 \pm 0.053 \pm 0.009$
0.245	$0.306 \pm 0.014 \pm 0.020$	$0.411 \pm 0.034 \pm 0.027$	$0.211 \pm 0.049 \pm 0.014$	$0.357 \pm 0.058 \pm 0.024$	$0.228 \pm 0.080 \pm 0.015$
0.342	$0.409 \pm 0.023 \pm 0.027$	$0.401 \pm 0.068 \pm 0.026$	$0.563 \pm 0.100 \pm 0.036$	$0.440 \pm 0.126 \pm 0.028$	$0.450 \pm 0.175 \pm 0.029$
0.465	$0.551 \pm 0.032 \pm 0.036$	$0.607 \pm 0.136 \pm 0.040$	$0.112 \pm 0.207 \pm 0.008$	$0.840 \pm 0.271 \pm 0.056$	$0.081 \pm 0.379 \pm 0.017$

Table A.3: The structure function ratios $\frac{g_1^h}{F_1^h}$ for inclusive e^+ and semi-inclusive h^+ , h^- , π^+ , and π^- events.

$\langle x \rangle$	Cor (A^{e^+}, A^{h^+})	Cor (A^{e^+}, A^{h^-})	Cor (A^{e^+}, A^{π^+})	Cor (A^{e^+}, A^{π^-})
0.033	0.452	0.394	0.265	0.242
0.047	0.490	0.414	0.268	0.235
0.065	0.517	0.406	0.259	0.217
0.087	0.509	0.379	0.238	0.192
0.119	0.464	0.328	0.208	0.161
0.168	0.375	0.253	0.168	0.124
0.245	0.267	0.171	0.120	0.084
0.342	0.188	0.115	0.085	0.056
0.465	0.130	0.076	0.061	0.039
Cor (A^{h^+}, A^{h^-})	Cor (A^{h^+}, A^{π^+})	Cor (A^{h^+}, A^{π^-})	Cor (A^{h^-}, A^{π^+})	Cor (A^{h^-}, A^{π^-})
0.130	0.568	0.047	0.042	0.603
0.140	0.515	0.046	0.039	0.557
0.134	0.478	0.040	0.034	0.526
0.120	0.448	0.035	0.030	0.500
0.108	0.431	0.033	0.027	0.486
0.098	0.432	0.031	0.025	0.485
0.084	0.434	0.028	0.022	0.484
0.066	0.437	0.024	0.017	0.481
0.050	0.457	0.019	0.013	0.506

Table A.4: Correlations of asymmetries on the proton in HERMES kinematics. Note that the (A^{π^+}, A^{π^-}) correlation is nearly zero over the kinematic range.

$\langle x \rangle$	Cor (A^{e^+}, A^{h^+})	Cor (A^{e^+}, A^{h^-})	Cor (A^{h^+}, A^{h^-})
0.033	0.446	0.395	0.128
0.047	0.491	0.417	0.137
0.065	0.507	0.411	0.131
0.087	0.497	0.386	0.117
0.119	0.452	0.336	0.105
0.168	0.365	0.260	0.096
0.245	0.260	0.178	0.083
0.342	0.183	0.120	0.066
0.465	0.127	0.080	0.051

Table A.5: Correlations of ^3He asymmetries measured at HERMES.

$\langle x \rangle$	$\langle Q^2 \rangle$	$\frac{\Delta d_{\text{val}}}{d_{\text{val}}}$	$\frac{\Delta u_{\text{val}}}{u_{\text{val}}}$	$\frac{\Delta q_{\text{sea}}}{q_{\text{sea}}}$	$\chi^2/\text{d.o.f.}$
0.033	1.211	$-0.473 \pm 0.294 \pm 0.120$	$0.202 \pm 0.121 \pm 0.054$	$0.023 \pm 0.094 \pm 0.085$	0.77
0.047	1.459	$-0.433 \pm 0.268 \pm 0.123$	$0.105 \pm 0.095 \pm 0.057$	$0.118 \pm 0.103 \pm 0.028$	0.31
0.065	1.697	$-0.272 \pm 0.262 \pm 0.133$	$0.269 \pm 0.082 \pm 0.061$	$-0.048 \pm 0.122 \pm 0.025$	0.07
0.087	1.945	$-0.153 \pm 0.297 \pm 0.147$	$0.378 \pm 0.082 \pm 0.062$	$-0.200 \pm 0.173 \pm 0.071$	1.72
0.119	2.220	$-0.674 \pm 0.321 \pm 0.159$	$0.224 \pm 0.076 \pm 0.055$	$0.217 \pm 0.242 \pm 0.167$	1.63
0.168	2.524	$-0.508 \pm 0.420 \pm 0.165$	$0.281 \pm 0.081 \pm 0.049$	$0.164 \pm 0.450 \pm 0.318$	0.92
0.245	2.844	$0.129 \pm 0.633 \pm 0.175$	$0.464 \pm 0.095 \pm 0.047$	$-1.162 \pm 1.093 \pm 0.533$	1.93
0.342	3.526	$0.523 \pm 0.484 \pm 0.577$	$0.391 \pm 0.044 \pm 0.036$	—	1.58
0.465	4.964	$-1.216 \pm 0.874 \pm 0.413$	$0.666 \pm 0.063 \pm 0.039$	—	1.43

Table A.6: Extracted valence and sea quark polarizations versus x for a fit with the SU(3) sea polarization model.

$\langle x \rangle$	$\langle Q^2 \rangle$	Δd_{val}	Δu_{val}	Δq_{sea}
0.033	2.5	$-2.741 \pm 1.700 \pm 0.695$	$1.843 \pm 1.106 \pm 0.491$	$0.767 \pm 3.123 \pm 2.833$
0.047	2.5	$-2.014 \pm 1.249 \pm 0.570$	$0.799 \pm 0.727 \pm 0.437$	$2.243 \pm 1.957 \pm 0.533$
0.065	2.5	$-1.054 \pm 1.017 \pm 0.517$	$1.790 \pm 0.548 \pm 0.405$	$-0.587 \pm 1.506 \pm 0.304$
0.087	2.5	$-0.487 \pm 0.946 \pm 0.466$	$2.191 \pm 0.476 \pm 0.360$	$-1.566 \pm 1.351 \pm 0.558$
0.119	2.5	$-1.679 \pm 0.800 \pm 0.396$	$1.100 \pm 0.371 \pm 0.272$	$0.994 \pm 1.110 \pm 0.768$
0.168	2.5	$-0.894 \pm 0.740 \pm 0.290$	$1.092 \pm 0.315 \pm 0.191$	$0.371 \pm 1.019 \pm 0.720$
0.245	2.5	$0.133 \pm 0.656 \pm 0.182$	$1.259 \pm 0.256 \pm 0.127$	$-0.968 \pm 0.911 \pm 0.444$
0.342	2.5	$0.267 \pm 0.247 \pm 0.295$	$0.644 \pm 0.073 \pm 0.059$	—
0.465	2.5	$-0.197 \pm 0.142 \pm 0.067$	$0.457 \pm 0.043 \pm 0.027$	—

Table A.7: Extracted valence and sea quark distributions versus x in the symmetric sea polarization model, evolved to $\langle Q^2 \rangle = 2.5 \text{ GeV}^2$.

$\langle x \rangle$	Cor $(\frac{\Delta u_{\text{val}}}{u_{\text{val}}}, \frac{\Delta d_{\text{val}}}{d_{\text{val}}})$	Cor $(\frac{\Delta u_{\text{val}}}{u_{\text{val}}}, \frac{\Delta q_{\text{sea}}}{q_{\text{sea}}})$	Cor $(\frac{\Delta d_{\text{val}}}{d_{\text{val}}}, \frac{\Delta q_{\text{sea}}}{d_{\text{sea}}})$
0.033	0.723	-0.503	-0.403
0.047	0.715	-0.702	-0.676
0.065	0.728	-0.698	-0.676
0.087	0.746	-0.594	-0.532
0.119	0.756	-0.436	-0.315
0.168	0.770	-0.497	-0.385
0.245	0.784	-0.704	-0.647
0.342	-0.187	-	-
0.465	-0.648	-	-

Table A.8: Correlations among the extracted quark polarizations.

$\langle x \rangle$	P_B	P_T	Yield	Smear	R	g_2	RadCor	PDF	Frag	Δq_{sea}
$\frac{\Delta u_{\text{val}}}{u_{\text{val}}}$ Systematic Uncertainty Contributions										
0.033	0.0069	0.0088	0.0024	0.0012	0.0051	0.0008	0.00245	0.0046	0.0518	0.0000
0.047	0.0037	0.0057	0.0014	0.0017	0.0015	0.0009	0.00146	0.0066	0.0563	0.0000
0.065	0.0091	0.0135	0.0011	0.0004	0.0023	0.0010	0.00100	0.0079	0.0579	0.0000
0.087	0.0133	0.0177	0.0009	0.0026	0.0020	0.0010	0.00066	0.0086	0.0567	0.0000
0.119	0.0079	0.0113	0.0008	0.0010	0.0006	0.0011	0.00035	0.0087	0.0526	0.0000
0.168	0.0096	0.0112	0.0006	0.0015	0.0005	0.0012	0.00027	0.0081	0.0457	0.0000
0.245	0.0161	0.0234	0.0001	0.0025	0.0004	0.0016	0.00040	0.0070	0.0359	0.0000
0.342	0.0136	0.0199	0.0023	0.0028	0.0003	0.0026	0.00170	0.0052	0.0232	0.0109
0.465	0.0227	0.0297	0.0021	0.0028	0.0006	0.0060	0.00143	0.0028	0.0077	0.0027
$\frac{\Delta d_{\text{val}}}{d_{\text{val}}}$ Systematic Uncertainty Contributions										
0.033	0.0196	0.0251	0.0501	0.0036	0.0124	0.0056	0.04815	0.0736	0.0534	0.0000
0.047	0.0152	0.0153	0.0413	0.0060	0.0061	0.0054	0.03393	0.0721	0.0795	0.0000
0.065	0.0127	0.0216	0.0369	0.0021	0.0023	0.0062	0.02332	0.0689	0.1021	0.0000
0.087	0.0130	0.0276	0.0356	0.0028	0.0007	0.0076	0.01471	0.0640	0.1212	0.0000
0.119	0.0264	0.0315	0.0367	0.0024	0.0017	0.0096	0.00838	0.0574	0.1368	0.0000
0.168	0.0192	0.0200	0.0401	0.0017	0.0009	0.0112	0.00756	0.0491	0.1489	0.0000
0.245	0.0148	0.0422	0.0429	0.0029	0.0001	0.0090	0.01866	0.0390	0.1575	0.0000
0.342	0.0212	0.0276	0.0302	0.0016	0.0004	0.0041	0.02259	0.0273	0.1626	0.5501
0.465	0.0417	0.0439	0.0357	0.0035	0.0011	0.0780	0.02405	0.0138	0.1642	0.3628
$\frac{\Delta q_{\text{sea}}}{q_{\text{sea}}}$ Systematic Uncertainty Contributions										
0.033	0.0016	0.0025	0.0061	0.0015	0.0006	0.0019	0.00598	0.0022	0.0845	—
0.047	0.0040	0.0042	0.0062	0.0031	0.0017	0.0019	0.00536	0.0045	0.0254	—
0.065	0.0027	0.0079	0.0070	0.0012	0.0004	0.0022	0.00479	0.0107	0.0186	—
0.087	0.0088	0.0147	0.0087	0.0025	0.0011	0.0028	0.00402	0.0205	0.0643	—
0.119	0.0097	0.0117	0.0120	0.0022	0.0005	0.0041	0.00312	0.0340	0.1623	—
0.168	0.0076	0.0000	0.0188	0.0020	0.0003	0.0064	0.00415	0.0512	0.3128	—
0.245	0.0457	0.0949	0.0297	0.0077	0.0011	0.0082	0.01612	0.0721	0.5157	—

Table A.9: A separation of the individual systematic uncertainties contributing to the total uncertainty in the quark polarization extraction. The columns represent the uncertainty in the beam polarization measurement (P_B), in the target polarization measurement (P_T), in 1995 yield fluctuations (Yield), in smearing corrections (Smear), in R , in the assumption $g_2 = 0$ (g_2), in the inclusive asymmetry radiative corrections (RadCor), in the unpolarized parton distribution (PDF), in the fragmentation model (Frag), and in the unpolarized sea model assumption at high x (Δq_{sea}).

x -Range	0.023 – 0.6	0 – 0.023	0.6 – 1	0 – 1
Δu_{val}	$0.525 \pm 0.046 \pm 0.078$	0.0339	0.017	$0.576 \pm 0.046 \pm 0.081$
Δd_{val}	$-0.230 \pm 0.104 \pm 0.137$	-0.0388	-0.001	$-0.270 \pm 0.104 \pm 0.138$
$\Delta u + \Delta \bar{u}$	$0.523 \pm 0.017 \pm 0.034$	0.0393	0.0170	$0.579 \pm 0.017 \pm 0.039$
$\Delta d + \Delta \bar{d}$	$-0.260 \pm 0.060 \pm 0.050$	-0.0338	-0.0015	$-0.296 \pm 0.060 \pm 0.051$
$\Delta \bar{u}$	$-0.003 \pm 0.021 \pm 0.030$	0.002	0	$-0.001 \pm 0.021 \pm 0.030$
$\Delta \bar{d}$	$-0.016 \pm 0.035 \pm 0.045$	0.0024	0	$-0.010 \pm 0.035 \pm 0.048$
Δs	$-0.004 \pm 0.015 \pm 0.020$	0.0011	0	$-0.003 \pm 0.015 \pm 0.021$
a_0	$0.254 \pm 0.044 \pm 0.094$	0.0090	0.0047	$0.268 \pm 0.044 \pm 0.094$
a_3	$0.783 \pm 0.073 \pm 0.062$	0.073	0.037	$0.893 \pm 0.073 \pm 0.073$
a_8	$0.279 \pm 0.086 \pm 0.102$	0.001	-0.002	$0.279 \pm 0.086 \pm 0.103$
Γ_1^p	$0.101 \pm 0.002 \pm 0.010$	0.0069	0.0076	$0.116 \pm 0.002 \pm 0.012$
Γ_1^n	$-0.029 \pm 0.012 \pm 0.013$	-0.005	0.00	$-0.034 \pm 0.012 \pm 0.013$

Table A.10: The first moments of the polarized quark distributions at a fixed $Q^2=2.5 \text{ GeV}^2$. Valence quark polarizations were fit in the SU(3) symmetric polarization sea model.

x -Range	0.023 – 0.6	0 – 0.023	0.6 – 1	0 – 1
$x \Delta u_{\text{val}}$	$0.122 \pm 0.009 \pm 0.011$	0.0003	0.011	$0.134 \pm 0.009 \pm 0.016$
$x \Delta d_{\text{val}}$	$-0.029 \pm 0.024 \pm 0.015$	0	-0.0003	$-0.029 \pm 0.024 \pm 0.015$
$x \Delta u + \Delta \bar{u}$	$0.118 \pm 0.005 \pm 0.007$	0.0001	0.012	$0.130 \pm 0.005 \pm 0.014$
$x \Delta d + \Delta \bar{d}$	$-0.038 \pm 0.018 \pm 0.010$	-0.0001	-0.001	$-0.039 \pm 0.018 \pm 0.010$
$x \Delta \bar{u}$	$-0.0019 \pm 0.0034 \pm 0.0032$	0	0	$-0.0019 \pm 0.0033 \pm 0.0038$
$x \Delta \bar{d}$	$-0.0047 \pm 0.0066 \pm 0.0061$	0	0	$-0.0047 \pm 0.0066 \pm 0.0079$
$x \Delta s$	$-0.0018 \pm 0.0027 \pm 0.0026$	0	0	$-0.0018 \pm 0.0027 \pm 0.0033$
$x a_0$	$0.077 \pm 0.014 \pm 0.018$	0.0001	0.0031	$0.081 \pm 0.014 \pm 0.018$
$x a_3$	$0.161 \pm 0.023 \pm 0.013$	0.0009	0.026	$0.187 \pm 0.023 \pm 0.029$
$x a_8$	$0.089 \pm 0.020 \pm 0.019$	0	0	$0.090 \pm 0.020 \pm 0.019$
$x \Gamma_1^p$	$0.024 \pm 0.001 \pm 0.002$	0	0.0053	$0.030 \pm 0.001 \pm 0.006$
$x \Gamma_1^n$	$-0.0023 \pm 0.0038 \pm 0.0026$	0	0	$-0.0023 \pm 0.0038 \pm 0.0026$

Table A.11: The second moments of the polarized quark distributions at a fixed $Q^2=2.5 \text{ GeV}^2$. Valence quark polarizations were fit in the SU(3) symmetric polarization sea model.

	Δd_{val}	Δu_{val}	Δq_{sea}
Δd_{val}	1	0.61	-0.84
Δu_{val}	0.61	1	-0.93
Δq_{sea}	-0.84	-0.93	1

Table A.12: The correlation matrix among the second integral moments of the quark distributions.

	$x\Delta d_{\text{val}}$	$x\Delta u_{\text{val}}$	$x\Delta q_{\text{sea}}$
$x\Delta d_{\text{val}}$	1	0.2	-0.69
$x\Delta u_{\text{val}}$	0.2	1	-0.8
$x\Delta q_{\text{sea}}$	-0.69	-0.8	1

Table A.13: The correlation matrix among the second integral moments of the quark distributions.

Appendix B

Nuclear Corrections with Quark Polarizations

Chapter 6 presented formalism to extract neutron asymmetries from asymmetries on nuclear targets. This appendix presents a second, complementary approach to nuclear corrections that was not used in thesis, but may be important for future analysis of HERMES data. The second method of handling nuclear targets corrects the extracted parton distributions directly. Using the QPM identification of the inclusive structure functions, $g_1(x)$ and $F_1(x)$, in Equation 2, one may rewrite Eq. (6.22) as

$$q^A(x) = \frac{Z}{A}q^p(x) + \frac{N}{A}q^n(x), \quad (\text{B.1})$$

$$\Delta q^A(x) = P_A^p \frac{Z}{A} \Delta q^p(x) + P_A^n \frac{N}{A} \Delta q^n(x). \quad (\text{B.2})$$

$$(\text{B.3})$$

where q_f^A , q_f^p , and q_f^n are the parton distributions for flavor f in nuclei, protons, and neutrons, respectively. The conventional distributions are defined in the proton: $q \equiv q^p(x)$, and $q^n(x)$ are simply the isospin-rotated analogues.

The PEPSI Monte Carlo may be adjusted to generate purities on nuclear targets such as ^3He and ^2H . In such a case, the matrix purity equation reads,

$$\vec{\mathbf{A}}^A = \mathbf{P}^A \vec{\mathbf{Q}}^A. \quad (\text{B.4})$$

where \vec{Q}^A is a vector of quark polarizations defined inside the nucleus. Since one wishes to measure quark polarizations defined on the proton, a matrix, \mathcal{N}_Q , is required which transforms quark nuclear polarizations to the standard polarizations defined on a proton:

$$\vec{Q}^A = \mathcal{N}_Q \vec{Q}^p. \quad (\text{B.5})$$

\mathcal{N}_Q can be easily defined from the above Eq. (B.3). The form of \mathcal{N}_Q varies with choice of quark polarizations fit and the definition of the average sea; as an example, the \mathcal{N}_Q for the 3-parameter fit with SU(3) symmetric polarizations is,

$$\begin{pmatrix} \frac{\Delta u^A}{u^A} \\ \frac{\Delta d^A}{d^A} \\ \frac{\Delta q_{\text{sea}}^A}{q_{\text{sea}}^A} \end{pmatrix} = \begin{bmatrix} \frac{1}{u^A} & & 0 \\ & \frac{1}{d^A} & \\ 0 & & \frac{1}{q_{\text{sea}}^A} \end{bmatrix} \begin{bmatrix} P_A^p \frac{Z}{A} & P_A^n \frac{N}{A} & 0 \\ P_A^p \frac{N}{A} & P_A^n \frac{Z}{A} & 0 \\ 0 & 0 & \frac{ZP_A^p + NP_A^n}{A} \end{bmatrix} \begin{bmatrix} u & & 0 \\ & d & \\ 0 & & q_{\text{sea}} \end{bmatrix} \begin{pmatrix} \frac{\Delta u}{u} \\ \frac{\Delta d}{d} \\ \frac{\Delta q_{\text{sea}}}{q_{\text{sea}}} \end{pmatrix}. \quad (\text{B.6})$$

Bibliography

- [1] M. Gell-Mann, Phys. Lett. **8** (1964) 214.
- [2] G. Zweig, CERN-TH-412, Technical report, CERN, 1964.
- [3] EM Collaboration, J. Ashman et al., Nucl. Phys. **B328** (1989) 1.
- [4] M. Anselmino, A. Efremov and E. Leader, Phys. Rept. **261** (1995) 1, *Erratum-ibid.* **281** (1997) 399-400.
- [5] P. Renton, Electroweak Interactions (Cambridge University Press, Cambridge, England, 1990).
- [6] T. Pussieux and R. Windmolders, Symposium on the Internal Spin Structure of the Nucleon, p. 212, 1994.
- [7] R.L. Jaffe, Comm. Nucl. Part. Phys. **14** (1990) 239.
- [8] J.I. Friedman and H.W. Kendall, Ann. Rev. Nuc. Sci. **22** (1972) 203.
- [9] R. Feynman, Phys. Rev. Lett. **23** (1969) 1415.
- [10] J.D. Bjorken and E.A. Paschos, Phys. Rev. **185** (1969) 1975.
- [11] CTEQ Collaboration, H. Lai et al., Phys. Rev. **D126** (1997) 1280.
- [12] C.G. Callan and D.J. Gross, Phys. Rev. Lett. **22** (1969) 156.
- [13] Particle Data Group, C. Caso et al., Euro. Phys. Jour. **C3** (1998) 1.
- [14] BCDMS Collaboration, A.C. Benevenuti et al., Phys. Lett. **B223** (1989) 485.
- [15] E665 Collaboration, M.R. Adams et al., Phys. Rev. **D54** (1996) 3006.
- [16] NM Collaboration, M. Arneodo et al., Phys. Lett. **B364** (1995) 107.

- [17] L.W. Whitlow et al., Phys. Lett. **B282** (1992) 475.
- [18] CTEQ Collaboration, G. Sterman et al., Euro. Phys. Jour. **C3** (1998) 1.
- [19] G. Altarelli and G. Parisi, Nucl. Phys. **B126** (1977) 298.
- [20] V.N. Gribov and L.N. Lipatov, Sov. J. Nucl. Phys. **15** (1972) 438.
- [21] Y.L. Dokshitzer, Sov. Phys. JETP **46** (1977) 641.
- [22] S. Wong, Introductory Nuclear Physics (Prentice-Hall, Englewood Cliffs, NJ, 1990).
- [23] R. Jaffe, hep-ph/9602236.
- [24] Y.I. Azimov et al., Phys. Lett. **B165** (1985) 147.
- [25] Y.I. Azimov et al., Zeit. Phys. **C27** (1985) 65.
- [26] EM Collaboration, M. Arneodo et al., CERN-EP/86-119, 1985.
- [27] J. Binneweis, B.A. Kniehl and G. Kramer, Zeit. Phys. **C65** (1998) 1.
- [28] S. Rolli, hep-ph/9607480.
- [29] B.R. Webber, Ann. Rev. Nucl. Part. Sci. **36** (1986) 253.
- [30] R.D. Field and R.P. Feynman, Nucl. Phys. **B136** (1978) 1.
- [31] EM Collaboration, M. Arneodo et al., Phys. Lett. **B145** (1984) 458.
- [32] P. Geiger, PhD thesis, Ruprecht-Karls-University Heidelberg, 1998.
- [33] B.R. Webber, hep-ph/9411384.
- [34] P. Hoyer et al., Nucl. Phys. **B161** (1979) 349.
- [35] A. Ali et al., Phys. Lett. **B93** (1980) 155.
- [36] A. Ali et al., Nucl. Phys. **B168** (1980) 409.
- [37] B. Andersson et al., Phys. Rept. **97** (1983) 33.
- [38] B. Andersson et al., Zeit. Phys. **C9** (1981) 233.
- [39] G. Marchesi et al., Comp. Phys. Comm. **67** (1992) 465.
- [40] L.L. Frankfurt et al., Phys. Lett. **B230** (1989) 141.

- [41] F.E. Close and R.G. Milner, Phys. Rev. **D44** (1991) 3691.
- [42] S. Güllenstern et al., Phys. Lett. **B312** (1993) 166.
- [43] B. Tipton and F. Dashevskiy, HERMES Internal Note 98-073, 1998.
- [44] F. Dashevskiy, Senior Thesis, Massachusetts Institute of Technology, 1999.
- [45] HERMES Collaboration, A. Airapetian et al., Measurement of the spin asymmetry in the photoproduction of high- p_t hadron pairs at hermes, submitted to Phys. Rev. Lett., hep-ex/9907020, 1999.
- [46] J. Martin, PhD thesis, Massachusetts Institute of Technology, in preparation.
- [47] COMPASS Collaboration, CERN/SPSLC 96-14, 1996.
- [48] X. Ji, Phys. Rev. **D55** (1997) 7114.
- [49] SM Collaboration, B. Adeva et al., Phys. Rev. **D58** (1998) 112002.
- [50] SM Collaboration, B. Adeva et al., Phys. Rev. **D58** (1998) 112001.
- [51] E80 Collaboration, M.J. Alguard et al., Phys. Rev. Lett. **37** (1976) 1261.
- [52] E130 Collaboration, G. Baum et al., Phys. Rev. Lett. **51** (1983) 1135.
- [53] E142 Collaboration, P.L. Anthony et al., Phys. Rev. **D54** (1996) 6620.
- [54] E143 Collaboration, K. Abe et al., Phys. Rev. **D58** (1998) 112003.
- [55] E154 Collaboration, E.W. Hughes et al., SLAC Proposal E154, 1993.
- [56] E155 Collaboration, R.G. Arnold et al., SLAC Proposal E155, 1993.
- [57] E154 Collaboration, K. Abe et al., Phys. Rev. Lett. **79** (1997) 26.
- [58] HERMES Collaboration, K. Ackerstaff et al., Nucl. Instrum. Methods **A417** (1998) 230.
- [59] R.L. Jaffe and A. Manohar, Nucl. Phys. **B337** (1990) 509.
- [60] J.J.J. Kokkedee, The Quark Model (W.A. Benjamin, Inc., New York, 1969).
- [61] A. Chodos et al., Phys. Rev. **D9** (1974) 3471.
- [62] M. Beyer and S.K. Singh, Zeit. Phys. **C31** (1986) 421.

- [63] F.E. Close, *An Introduction to Quarks and Partons* (Academic Press, New York, 1979).
- [64] S. Brodsky and F. Schlumpf, *Phys. Lett.* **B329** (1994) 111.
- [65] J. Ellis and M. Karliner, hep-ph/9601280.
- [66] F.E. Close and R.G. Roberts, *Phys. Lett.* **B316** (1993) 165.
- [67] J. Ellis and R.L. Jaffe, *Phys. Rev.* **D9** (1974) 1444, *Erratum-ibid* **D10** 1669.
- [68] J.D. Bjorken, *Phys. Rev.* **148** (1966) 1467, *ibid.* **D1**, 1376 (1970).
- [69] A. Buras, *Rev. Mod. Phys.* **52** (1980) 200.
- [70] B. Lampe and E. Reya, hep-ph/9810270.
- [71] S.A. Larin, *Phys. Lett.* **B334** (1994) 192.
- [72] S.A. Larin, T. van Ritbergen and J.A.M. Vermaseren, *Phys. Lett.* **B404** (1997) 153.
- [73] E. Leader and M. Anselmino, *Zeit. Phys.* **C41** (1988) 239.
- [74] S.L. Adler, *Phys. Rev.* **177** (1969) 2426.
- [75] J.S. Bell and R. Jackiw, *Nuovo Cimento* **47** (1969) 61.
- [76] G. Altarelli and G. Ross, *Phys. Lett.* **B212** (1988) 391.
- [77] R.D. Carlitz et al., *Phys. Lett.* **B214** (1988) 219.
- [78] A.V. Efremov and O.V. Teryaev, Dubna report JIN-E2-88-287, 1988.
- [79] S.L. Adler and W.A. Bardeen, *Phys. Rev.* **182** (1969) 1517.
- [80] G. t'Hooft and M. Veltman, *Nucl. Phys.* **B44** (1972) 189.
- [81] G.T. Bodwin and J. Qiu, *Phys. Rev.* **D41** (1990) 2755.
- [82] P.G. Ratcliffe, *Phys. Lett.* **B192** (1987) 180.
- [83] G. Altarelli et al., *Nucl. Phys.* **B496** (1997) 337.
- [84] F.E. Close, hep-ph/9306288.
- [85] P.G. Ratcliffe, *Phys. Lett.* **B365** (1996) 383.
- [86] H.J. Lipken, *Phys. Lett.* **B337** (1994) 157.

- [87] J. Lichtenstadt and H.J. Lipken, Phys. Lett. **B353** (1994) 115.
- [88] M. Karliner and H.J. Lipken, hep-ph/9906321.
- [89] NuSea Collaboration, E.A. Hawker et al., Phys. Rev. Lett. **80** (1998) 3715.
- [90] NA51 Collaboration, A. Baldit et al., Phys. Lett. **B332** (1994) 244.
- [91] HERMES Collaboration, K. Ackerstaff et al., Phys. Rev. Lett. **81** (1998) 5519.
- [92] NuSea Collaboration, J.C. Peng et al., Phys. Rev. **D58** (1998) 092004.
- [93] E.J. Eichten, I. Hinchliffe and C. Quigg, Phys. Rev. **D45** (1992) 2269.
- [94] X. Song, J.S. McCarthy and H.J. Weber, Phys. Rev. **D55** (1997) 2624.
- [95] S. Brodsky and B. Ma, Phys. Lett. **B381** (1996) 317.
- [96] R.J. Fries and A. Schäfer, Phys. Lett. **B443** (1998) 40.
- [97] M. Peskin and D. Schroeder, An Introduction to Quantum Field Theory (Addison-Wesley, New York, 1995).
- [98] S.J. Dong, J.F. Lagae and K.F. Liu, Phys. Rev. Lett. **75** (1995) 2096.
- [99] M. Fukugita et al., Phys. Rev. Lett. **75** (1995) 2092.
- [100] M. Göckeler et al., Phys. Rev. **D53** (1996) 2317.
- [101] I.M. Ternov, Y.M. Loskutov and L.I. Korvina, Sov. Phys. JETP **14** (1962) 921.
- [102] A.A. Sokolov and I.M. Ternov, Sov. Phys. Doklady **8** (1964) 1203.
- [103] J.D. Jackson, Rev. Mod. Phys. **48** (1976) 417.
- [104] M. Dueren, Habilitation, University Erlangen-Nürnberg, 1995.
- [105] L.H. Thomas, Philos. Mag. **3** (1927) 1.
- [106] V. Bargmann, L. Michel and V.L. Telegdi, Phys. Rev. Lett. **2** (1959) 435.
- [107] J. Kewisch et al., Phys. Rev. Lett. **62** (1989) 419.
- [108] M. Boege, PhD thesis, University of Hamburg, 1994.
- [109] D.P. Barber et al., Nucl. Instrum. Methods **A329** (1993) 79.

- [110] J. Buon and K. Steffen, Nucl. Instrum. Methods **A245** (1986) 248.
- [111] D.P. Barber et al., Phys. Lett. **B343** (1995) 436.
- [112] D. De Schepper et al., Nucl. Instrum. Methods **A419** (1998) 16.
- [113] J. Stewart, Polarized gas targets and polarized beams: Seventh International Workshop, p. 69, Urbana-Champagne, USA, 1997, AIP Conf. Proc. 421.
- [114] D. De Schepper, PhD thesis, Massachusetts Institute of Technology, 1997.
- [115] B. Braun, Polarized gas targets and polarized beams: Seventh International Workshop, p. 156, Urbana-Champagne, USA, 1997, AIP Conf. Proc. 421.
- [116] H. Kolster, PhD thesis, Ludwig-Maximilians University of Munich, 1998.
- [117] T. Benisch, PhD thesis, University Erlangen-Nürnberg, 1998.
- [118] C. Baumgarten, Proc. of "13th International Symposium on High-Energy Spin Physics (SPIN98)", Protvino, Russia, 1998.
- [119] J. van der Marel, PhD thesis, Delft University, 1997.
- [120] C.A. Miller, HERMES Internal Note 95-072, 1995.
- [121] S. Bernreuther et al., Nucl. Instrum. Methods **A416** (1998) 45.
- [122] R. Kaiser, PhD thesis, Simon Fraser University, 1997.
- [123] H. Avakian et al., Nucl. Instrum. Methods **A381** (1998) 69.
- [124] U. Fano, J. Op. Soc. Am **39** (1949) 859.
- [125] N. Meyners, private communication.
- [126] D.P. Barber et al., Nucl. Instrum. Methods **A329** (1993) 79.
- [127] W. Lorenzon, private communication.
- [128] M. Ruh et al., Polarimeter Internal Note IPR-97-05, 1997.
- [129] H. Götschel, Diploma thesis, University of Hamburg, 1990.
- [130] R. Kaiser, Diploma thesis, University of Münster, 1992.
- [131] W.R. Nelson, H. Hirayama and D.W.O. Rogers, SLAC 265, 1985.

- [132] M. Lomperski, PhD thesis, University of Wisconsin, Madison, 1993.
- [133] Y.S. Derbenev and A.M. Kondratenko, *Sov. Phys. JETP* **37** (1973) 968.
- [134] A. Most, private communication.
- [135] S. Barrow et al., HERMES Internal Note 96-002, 1994.
- [136] W. Lorenzon, Polarized gas targets and polarized beams: Seventh International Workshop, p. 181, Urbana-Champaign, USA, 1997, AIP Conf. Proc. 421.
- [137] S. Barrow et al., Polarimeter Internal Note IPR-94-02, 1994.
- [138] J.E. Belz, HERMES Internal Note 96-051, 1994.
- [139] F. Zetsche, Polarimeter Internal Note IPR-98-02, 1994.
- [140] CERN-CN Division, CERN, EPIO - Experimental Physics Input Output Package, 1993.
- [141] ECP Division, CERN, ADAMO - Entity-relationship programming system, version 3.3, 1994.
- [142] W. Wander, Proceedings of CHEP '95, Rio de Janeiro, 1995.
- [143] K. Ackerstaff and M.-A. Funk, Proceedings of CHEP '95, Rio de Janeiro, 1995.
- [144] J.K. Ousterhout, *Tcl and the Tk Toolkit* (Addison-Wesley, 1994).
- [145] W. Wander, PhD thesis, University of Erlangen-Nürnberg, 1996.
- [146] M. Kolstein, PhD thesis, Free University, Amsterdam, 1998.
- [147] HERMES Collaboration, A. Airapetian et al., *Phys. Lett.* **B442** (1998) 484.
- [148] HERMES Collaboration, K. Ackerstaff et al., *Phys. Lett.* **B404** (1997) 383.
- [149] HERMES Collaboration, K. Ackerstaff et al., (1999), submitted to *Phys. Lett.*, hep-ex/9906035.
- [150] D. De Schepper, private communication.
- [151] H. Ihssen, private communication.
- [152] PhD thesis, University of Hamburg, 1998.
- [153] N. Makins, private communication.

- [154] The HERMES g_1^n Group, K. Akopov et al., HERMES Internal Note 97-007, 1997.
- [155] J. Ouyang, HERMES Internal Note 97-047, 1997.
- [156] A. Gute, private communication.
- [157] P. Geiger et al., The HERMES Monte Carlo, <http://www-hermes.desy.de/hmc/>.
- [158] CERN-CN Division, CERN, GEANT Detector Description and Simulation Tool, 1993.
- [159] M. Ferstl, PhD thesis, University of Erlangen-Nürnberg, 1997.
- [160] I.V. Akushevich and N.M. Shumeiko, *J. Phys.* **G20** (1994) 513.
- [161] I.V. Akushevich, private communication.
- [162] M. Glück, E. Reya and W. Vogelsang, *Zeit. Phys.* **C67** (1995) 433.
- [163] M. Glück et al., *Phys. Rev.* **D53** (1996) 4775.
- [164] U. Stösslein, private communication.
- [165] B. Bains et al., HERMES Internal Note 97-048, 1995.
- [166] H. Tallini, PhD thesis, University of Liverpool, 1998.
- [167] SM Collaboration, B. Adeva et al., *Phys. Lett.* **B420** (1998) 180.
- [168] E154 Collaboration, K. Abe et al., *Phys. Lett.* **B404** (1997) 377.
- [169] E155 Collaboration, P.L. Anthony et al., hep-ex/9901006.
- [170] R.H. Myers, *Classical and Modern Regression with Applications* (Duxbury Press, Boston, 1986).
- [171] J.M. Niczyporuk and E.E. W.Bruins, *Phys. Rev.* **D58** (1998) 091501.
- [172] M. Ruh, PhD thesis, University of Freiburg, 1999.
- [173] M. Veltri, MPIH-V18-1992.
- [174] G. Ingelman et al., DESY Report 96-057.
- [175] A.D. Martin, R.G. Roberts and W.J. Stirling, *Phys. Rev.* **D50** (1994) 6734.
- [176] K. Ackerstaff, PhD thesis, University of Hamburg, 1996.

-
- [177] T. Shin, PhD thesis, Massachusetts Institute of Technology, in preparation.
- [178] EM Collaboration, M. Arneodo et al., Nucl. Phys. **B321** (1989) 541.
- [179] T. Sjöstrand, Comp. Phys. Comm. **82** (1994) 74.
- [180] JADE Collaboration, W. Bartel et al., Phys. Lett. **B157** (1985) 340.
- [181] P. Geiger, private communication.
- [182] J. Friar et al., Phys. Rev. **C42** (1990) 2310.
- [183] C.C. degli Atti and G. Salme, Phys. Rev. **C48** (1993) R968.
- [184] G.D. Lafferty and T.R. Wyatt, Nucl. Instrum. Methods **A355** (1994) 541.
- [185] T. Gehrman and W.J. Stirling, Phys. Rev. **D53** (1996) 6100.
- [186] D. de Florian, O. Sampoya and R. Sassot, Phys. Rev. **D57** (1998) 5803.
- [187] R.L. Heimann, Nucl. Phys. **B64** (1973) 429.
- [188] J. Ellis and M. Karliner, Phys. Lett. **B213** (1988) 73.
- [189] PHENIX Collaboration, J.C. Gregory et al., Nucl. Phys. **A566** (1994) 287.